THÈSE

En vue de l'obtention du

DOCTORAT DE L'UNIVERSITÉ DE TOULOUSE

Délivré par :

Institut National Polytechnique de Toulouse (INP Toulouse)

Discipline ou spécialité :

Dynamique des fluides

Présentée et soutenue par :

M. FERNANDO DIOGO GROSSI

le mercredi 12 février 2014

Titre :

PHYSIQUE ET MODELISATION D'INTERACTIONS INSTATIONNAIRES ONDE DE CHOC/COUCHE LIMITE AUTOUR DE PROFILS D'AILE TRANSSONIQUES PAR SIMULATION NUMERIQUE.

Ecole doctorale :

Mécanique, Energétique, Génie civil, Procédés (MEGeP)

Unité de recherche :

Institut de Mécanique des Fluides de Toulouse (I.M.F.T.)

Directeur(s) de Thèse :

MME MARIANNA BRAZA

Rapporteurs :

M. ALAIN DERVIEUX, INRIA SOPHIA ANTIPOLIS

M. GEORGE BARAKOS, UNIVERSITY OF LIVERPOOL

Membre(s) du jury :

M. ALAIN DERVIEUX, INRIA SOPHIA ANTIPOLIS, Président

M. DIETER SCHWAMBORN, DLR GOTTINGEN, Membre

M. FRANK THIELE, TECHNISCHE UNIVERSITAT BERLIN, Membre

M. LARS DAVIDSON, CHALMERS UNIV.OF TECH. HOGSKOLA GOTEBORG, Membre

Mme MARIANNA BRAZA, INP TOULOUSE, Membre

Physics and modeling of unsteady shock wave/boundary layer interactions over transonic airfoils by numerical simulation

Fernando Grossi

Preface

The present document considers the physics and modeling of shock wave/boundary layer interactions in transonic flow by means of numerical simulations using high-fidelity turbulence modeling approaches. It constitutes a dissertation for obtaining the *Doctorat de l'Université de Toulouse* degree in Fluid Dynamics, awarded by the *Institut National Polytechnique de Toulouse* and the Doctoral School MEGeP (*Mécanique, Energétique, Génie civil, & Procédés*).

This thesis was carried out under supervision of Dr. Marianna Braza at the *Institut de Mécanique des Fluides de Toulouse* from October 2010 to September 2013. It was supported by the ANR Cosinus '*calcul intensif et simulation*' ECINADS (*Ecoulements instationnaires turbulents et adjoints par Simulation Numérique de Haute Performance*), coordinated by Dr. Alain Dervieux (INRIA, Sophia Antipolis, France). The research was also undertaken in the framework of two European projects: ATAAC (Advanced Turbulence Simulation for Aerodynamic Application Challenges), coordinated by Dr. Dieter Schwamborn (DLR, Göttingen, Germany), and TFAST (Transition Location Effect on Shock Wave Boundary Layer Interaction), coordinated by Prof. Piotr Doerffer (IMP PAN, Gdansk, Poland).

All simulations were performed with resources allocated by the french national computing centers CINES (*Centre Informatique National de l'Enseignement Supérieur*) and CALMIP (*Calcul en Midi-Pyrénées*).

Acknowledgment

First of all, I would like to express my gratitude to Dr. Marianna Braza for the opportunity and supervision during these years in France as well as for the great working environment at the Institut de Mécanique des Fluides de Toulouse.

I am very thankful to Dr. Alain Dervieux and Prof. George Barakos for having accepted the invitation to review my thesis and for their valuable contributions. I also wish to thank Dr. Dervieux for having magnificently conducted my defense and all members of the examining committee: Dr. Dieter Schwamborn, Prof. Frank Thiele, Prof. Lars Davidson and Dr. Franck Dagrau. All have contributed with questions that led to interesting discussions on turbulence modeling and aerodynamics. I would like to particularly thank Prof. Davidson for his comments and suggestions for the manuscript and for having gently received me as a visiting student at Chalmers University of Technology.

I thank Dr. Yannick Hoarau immensely for the precious assistance during the last years, and Dr. Rémi Bourguet for the many inspiring scientific discussions, fruitful ideas and friendship. I am also very grateful to Dr. Shia-Hui Peng for his kindness and advise during my stay in Sweden, and to Dr. Jan Vos and Stéphane Sanchi from CFS Engineering for the support with the NSMB code and in CFD in general.

I am deeply thankful to Prof. André Giovannini, who made my french adventure possible and opened the doors of IMFT to me. I also would like to thank Prof. Pierre Brancher and Dr. Henri Boisson as well as the recent Direction of the institute: Prof. Jaques Magnaudet, Prof. François Charru and Prof. Éric Climent.

My grateful thanks to Enrico Deri, Thibaut Deloze, Damien Szubert, Thibaud Marcel, Christophe Korbuly, Marie Cabana, Antonio Jimenez Garcia, Marc Gual Skopek, Hilde Ouvrard, Guillaumme Barbut, Gerardo Del Guercio, Bastian Nebenführ, Sebastian Arvidson, Guillaume Jourdain and all other friends and colleagues for the encouragement and enjoyable moments in Toulouse and Gothenburg. Very special thanks to my great friend Luigi Bisanti for sharing with me the everyday life of a graduate student, and to Ruddy Soeparno and Gregory Ehses for the enjoyable lunchtime and afterwork moments.

Finally, I wish to thank the unconditional support and love of my family and of my fiancée Ana, who stood beside me in all moments of difficulty and of joy throughout this journey. I love you.

Contents

List of Figures

Nomenclature

Latin symbols

a	Speed of sound
a_p	Downstream moving waves velocity
a_u	Upstream moving waves velocity
c	Chord length
c_p	Specific heat under constant pressure
c_v	Specific heat under constant volume
C_D	Drag coefficient
C_{D_f}	Friction drag coefficient
C_f	Skin-friction coefficient
C_L	Lift coefficient
C_m	Pitching moment coefficient
C_p	Pressure coefficient
C_μ	Turbulent diffusivity coefficient
d	Wall distance
e	Internal energy per unit mass; airfoil thickness
E	Total energy per unit mass
f	Transonic buffet frequency
$\vec{F}_C$	Convective flux vector
f_d	Delaying function of DDES
$\vec{F}_D$	Diffusive flux vector
g	Acceleration of gravity
h	Enthalpy per unit mass
H	Total enthalpy per unit mass
i	Grid index in the tangential direction
$\bar{\bar{I}}$	Unit tensor
j	Grid index in the normal direction
k	Turbulent kinetic energy; thermal conductivity coefficient; grid index in z
l	Turbulence length scale
l_b	Bubble separation length

L_z	Domain size in the spanwise direction
M	Mach number
$\vec{n}$	Surface normal vector
p	Static pressure
Pr	Prandtl number
q	Freestream dynamic pressure
q_t	Turbulent transport heat
Q	Q-criterion
$\vec{Q}_V$	Volume source vector
r	Transonic buffet reduced frequency; near-wall parameter
r_d	Near-wall parameter of DDES
R	Gas constant
Re	Chord-based Reynolds number
S	Stain-rate norm; control volume boundary; Sutherland's temperature
S_{ij}	Strain-rate tensor
t	Physical time
t^*	Non-dimensional time tU/c
T	Temperature; transonic buffet period
Tu	Turbulence intensity
x	Velocity in the x direction
U	Freestream velocity
u_τ	Friction velocity
v	Velocity in the y direction
$\vec{v}$	Velocity vector
V	Volume of the control volume
w	Velocity in the z direction
W	Vorticity magnitude
$\vec{W}$	State vector
x	Coordinate in the chordwise direction
x_b	Bubble separation position
x_r	Rear separation location
x_s	Shock-wave position
x_t	Transition location
y	Coordinate in the direction normal to the chord
y^+	Non-dimensional wall distance
z	Coordinate in the spanwise direction

Greek symbols

α	Angle of attack
δ	Boundary layer thickness

δ_{ij}	Kronecker delta
Δ	Grid spacing; variation
Δt	Physical time step
ϵ	Tolerance threshold
ε	Turbulence dissipation rate
γ	Specific heat ratio
κ	Kármán constant; diffusivity constant
λ	Second viscosity
μ	Dynamic molecular viscosity
μ_t	Dynamic eddy viscosity
ν	Kinematic molecular viscosity
ν_t	Kinematic eddy viscosity
$\tilde{\nu}$	Modified (undamped) eddy viscosity
ρ	Density
σ	Prandtl number; standard deviation
σ_{ij}	Viscous stress tensor
τ_{ij}	Turbulent (or Reynolds) stress tensor
$\tilde{\nu}$	Modified eddy viscosity
ω	Specific turbulence dissipation rate
Ω_{ij}	Rotation tensor

Subscripts

amb	Ambient
avg	Average
cr	Critical
∞	Relative to the freestream
max	Maximum
ref	Reference

Abbreviations

ATAAC	Advanced Turbulence Simulation for Aerodynamic Application Challenges
AUSM	Advection Upstream Splitting Method
BGK	Bauer-Garabedian-Korn
BSL	Menter's Baseline model
CC	Compressibility correction
CFD	Computational Fluid Dynamics
CFL	Courant-Friedrichs-Lewy number
DDES	Delayed Detached-Eddy Simulation

DES	Detached-Eddy Simulation
DES97	Original formulation of Detached-Eddy Simulation
EARSM	Explicit algebraic Reynolds stress model
EDW	Edwards-Chandra model
FOI	Swedish Defence Research Agency
KEC	k-ε model of Chien
MUSCL	Monotone upwind schemes for conservation law
MSD	Modeled stress depletion
LDV	Laser Doppler velocimetry
LES	Large-Eddy Simulation
LU-SSOR	Lower-upper symmetric successive overrelaxation
MSD	Modeled stress depletion
NACA	National Advisory Committee for Aeronautics
NASA	National Aeronautics and Space Administration
NPL	National Physical Laboratory
NSMB	Navier-Stokes Multiblock
OAT15A	Supercritical airfoil from ONERA
ONERA	Office National d'Etudes et de Recherches Aérospatiales
PSD	Power spectral density
RANS	Reynolds-averaged Navier-Stokes
RMS	Root mean square
SA	Spalart-Allmaras model
SALSA	Strain-adaptive linear Spalart-Allmaras model
SST	Shear Stress Transport model
SWBLI	Shock wave/boundary layer interaction
TFAST	Transition Location Effect on Shock Wave Boundary Layer Interaction
TVD	Total Variation Diminishing
URANS	Unsteady Reynolds-averaged Navier-Stokes
V2C	Laminar transonic airfoil from Dassault Aviation
WCX	Wilcox' new k-ω model
ZDES	Zonal Detached-Eddy Simulation

Chapter 1

General Introduction

Contents

1.1 Flow simulation in aeronautics

During the past decades, the continuous and fast progress of high performance computing in conjunction with the development and improvement of numerical methods and physical models for flow simulation have motivated the aeronautical industry to increasingly rely on Computational Fluid Dynamics (CFD). Nowadays, the computation of viscous flows around complex geometries such as a complete aircraft is practicable and the flexibility of CFD allows to considerably reduce the number of wind tunnel tests in the design of a new product, thus shortening its development cycle and reducing costs. In aeronautics, CFD applications are not restricted to aerodynamics. Flow simulation is also useful in other fields such as aeroelasticity, aeroacoustics and turbomachinery. Moreover, simulation data can also be used to build models for multidisciplinary design optimization. Therefore, flow simulation has become a major tool in aircraft design and is essential for improving the flight performance and minimizing the environmental impact of new aircraft.

Today, the use of CFD in industry is for the most part based on methods solving the Reynolds-averaged Navier-Stokes (RANS) equations adopting one- or two-equation eddy-viscosity models for turbulence closure. Experience has shown that the RANS approach can provide accurate results near the cruising design point, where the flow around the aircraft is usually smooth and effects such as strong adverse pressure gradients and flow separation are relatively small. In such conditions, flow unsteadiness is limited to thin boundary layers and wakes and is usually well represented by turbulence models, so that the flowfield can be regarded as 'steady' from a numerical standpoint. However, CFD reliability cannot be guaranteed throughout the whole flight envelope. As one approaches the envelope limits, nonlinear effects such as shock waves and flow separation may play a major role and cause difficulties for both modeling and numerical method. A recent discussion on the current uses and limitations of CFD and on the perspectives for flow simulation in the aeronautical industry is given by Abbas-Bayoumi and Becker [1]. Based on that paper, figure 1.1 illustrates for a typical civil transport aircraft the regions in the flight envelope where CFD techniques are most accurate and robust. An overview of the use of computational methods in aerodynamic design from a historical perspective is provided by de Resende [2].

As can be observed in figure 1.1, the region where CFD is most reliable includes the cruising point (cruising speed V_C and $1g$) and is small compared to the whole flight envelope. As one moves away from this region, numerical simulations become less accurate and are sometimes unfeasible. At low values of equivalent airspeed (EAS), a proper prediction of turbulent boundary layers in strong adverse pressure gradients and of separation onset and development is essential. Moreover, the flow around high-lift configurations creates additional challenges to turbulence modeling as the interactions between boundary layers and wakes of different airfoil elements as well as laminar-turbulent transition. Besides, low-Mach number regions such as recirculations in slat coves and flap cavities can be a problem for the solver due to their low compressibility. Such regions are illustrated

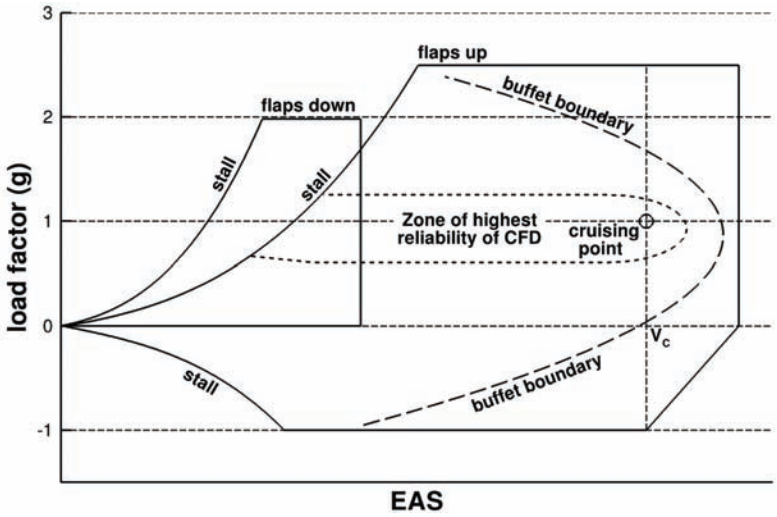

Figure 1.1: CFD reliability through the flight envelope (based on Ref. [1]).

in figure 1.2, which shows the mean streamlines around a three-element airfoil featuring separation on the flap.

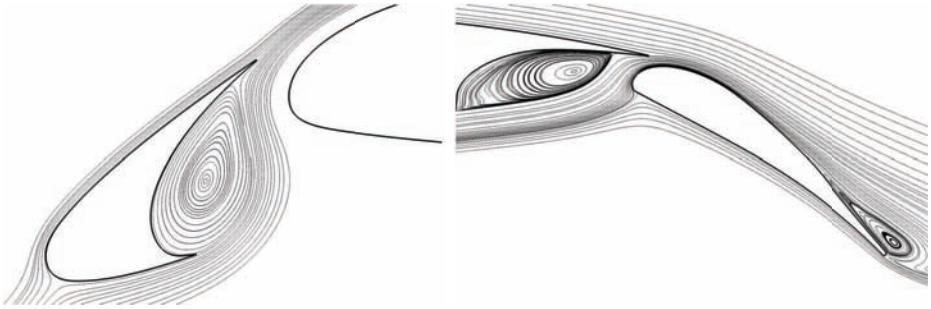

(a) Slat (b) Flap

Figure 1.2: Mean-flow streamlines around a three-element airfoil (from Nebenführ [3]).

At high speeds, the challenges for CFD come mainly from shock wave/boundary layer interaction (SWBLI). In general, inaccurate predictions of shock waves have large impact on the global aerodynamic coefficients. The proper computation of the shock-wave location and of the resulting pressure jump depends not only on the solver ability to resolve discontinuities but mostly on the accurate prediction of turbulent boundary layers, whose properties are in turn influenced by shock waves. The situation becomes more complicated when a shock is sufficiently strong to cause flow separation, which often gives rise to an unsteady SWBLI regime commonly known as transonic buffet. This condition is illustrated in figure 1.3 for a supercritical airfoil in transonic flow. In such cases, the shock wave usually oscillates in large-amplitude motions, producing strong fluctuations of forces and moments (the physics of transonic buffet will be addressed in detail in chapter 2). Therefore, since airworthiness standards require aircraft to resist up to $1.3g$ at cruising speed without significant lift loss [2], the accurate prediction of shock-induced separation is a problem of high industrial relevance.

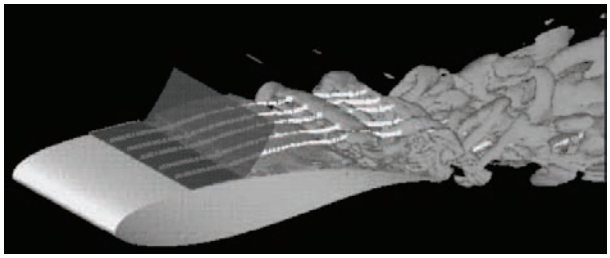

Figure 1.3: Numerical simulation of a shock-induced separation (from Deck [4]).

Either at low or high speeds, CFD reliability in aerodynamics is primarily limited by the performance of turbulence models regarding the prediction of complex flow phenomena. In cases involving shock waves or boundary layer separation, for example, the numerical solutions are often strongly model dependent. When flow unsteadiness plays an essential role as in the case of an oscillating shock wave or of massively-detached flows, satisfactory results cannot be obtained unless time-accurate simulations are performed. Moreover, some unsteady flows require that small turbulence structures be resolved in time, which is usually very costly for high Reynolds number flows. In respect to industrial applications, such simulations are frequently prohibitive due to the large number of degrees of freedom and of time steps needed.

1.2 Objectives of the thesis

This thesis aims at investigating the physics and modeling of shock wave/boundary layer interactions in transonic flow by means of numerical simulations using high performance computing. The geometries considered in the studies are a standard supercritical airfoil (the OAT15A) and an experimental laminar transonic profile (the V2C airfoil), and special attention is paid to the simulation of transonic buffet as well as to the influence of the laminar-turbulent transition location on such interactions. To do so, different levels of turbulence modeling are assessed, including URANS models commonly used in the aeronautical industry and alternative closures capable of capturing the physics of interest. The extended use of hybrid RANS-LES approaches in the simulation of shock-induced separated flows is also investigated, and improvements to the main code employed regarding the flow physics prediction and its numerical behavior for transonic flows are performed. The studies have been carried out in the framework of the ATAAC (Advanced Turbulence Simulation for Aerodynamic Application Challenges) and TFAST (Transition Location Effect on Shock Wave Boundary Layer Interaction) European projects.

1.3 Structure of the manuscript

In chapter 2, following an overview of the fundamental and technological aspects of transonic aerodynamics, the physics of shock wave/boundary layer interaction in transonic flow is addressed for both steady and unsteady (buffet) regimes. The text presents the models of shock-induced separation and gives a detailed description of transonic buffet. For the latter, the possible types of shock-wave motion are illustrated, which is followed by a broad literature review on the subject including experimental investigations, recent results from global-stability theory as well as numerical simulations. The equations governing fluid dynamics and upon which CFD is founded are presented in chapter 3, which also provides a description of the numerical codes used. A detailed presentation of all turbulence modeling approaches considered in the simulations of this thesis is given in chapter 4, which includes standard and modified eddy-viscosity models as well as turbulence-resolving methods. In chapter 5, results from two-dimensional simulations of transonic flows over the OAT15A supercritical airfoil are presented starting with preliminary steady-flow computations for the evaluation of numerical schemes and parameters as well as of various turbulence models. The implementation of a compressibility correction for one-equation models and of ambient-turbulence sustaining terms for two-equation ones is also addressed. Then, unsteady simulations of the OAT15A in the transonic buffet regime are presented and compared with experimental data. Besides the performance of turbulence models, the influence of time-stepping parameters on the buffet properties is also assessed. The best approach is then used in chapter 6 in the context of a hybrid RANS-LES simulation of the same flow by means of the Delayed Detached-Eddy Simulation (DDES) method. An in-depth analysis of the predicted flow topology and of the RANS-LES interface dynamics during buffet is provided. The chapter is concluded with a discussion on the DDES results including possible reasons for them and a comparison with literature results from a Zonal Detached-Eddy Simulation. The V2C laminar transonic airfoil is studied in chapter 7. By means of a series of simulations, the effect of the laminar-turbulent transition location on the properties of steady and unsteady transonic shock wave/boundary layer interactions is investigated. At the end of the chapter, a turbulence-resolving simulation of transonic buffet is conducted. The most important achievements and findings of the thesis are summarized in chapter 8.

Chapter 2

Shock Wave/Boundary Layer Interaction in Transonic Flow

Contents

2.1 Overview of transonic aerodynamics

In aerodynamics, a flow is said to be transonic when it simultaneously presents subsonic and supersonic regions. Typically, transonic flow may occur around aircraft flying at freestream Mach numbers ranging from $M_\infty = 0.6$ to 1.2, which covers the cruising regime of virtually all modern transport airplanes. Indeed, transonic flight is the most efficient regime for long-range aircraft [5]. The vast majority of them have a cruising Mach number between 0.74 and 0.86, which allows high speeds while keeping efficient lift-to-drag ratios. As the Mach increases further, this condition rapidly gets limited mainly due to the formation of strong shock waves. Such transonic nonlinearities lead to high wave drag values and may cause boundary layer separation, producing a sharp drag rise as the Mach number augments. Besides the flow around aircraft wings and tails, compressibility-related detrimental effects are also found in propeller aerodynamics as well as in turbomachinery flows.

At subsonic speeds, the transonic regime arises when the expansion of a fluid element along a curved streamline, caused by the presence the body in the flow, is strong enough to accelerate it up to the local speed of sound. The freestream Mach number for which the first sonic point appears around a given aerodynamic configuration is called 'critical Mach number' M_{cr} and the value of the static pressure at any sonic point in the flowfield is named 'critical pressure'. For isentropic flow, the pressure depends only on the local Mach number M, on M_∞ and on the specific heat ratio γ. Therefore, at a sonic point ($M = 1$), the critical pressure coefficient can be computed through [6]

$$C_{p_{\text{cr}}} = \frac{2}{\gamma M_\infty^2}\left[\left(\frac{2 + (\gamma - 1)\, M_\infty^2}{\gamma + 1}\right)^{\frac{\gamma}{\gamma - 1}} - 1\right]. \tag{2.1}$$

Therefore, regions of supersonic flow can be distinguished by verifying whether the local pressure coefficient $C_p = 2\,(p - p_\infty)\,/(\gamma p_\infty M_\infty^2)$ is lower than $C_{p_{\text{cr}}}$. As the Mach is further increased the sonic point becomes a supersonic pocket, which is a finite region of supersonic flow that can be terminated by a shock wave if the Mach number is sufficiently high. A sketch of the transonic flow around an arbitrary airfoil is presented in figure 2.1 for $M_\infty < 1$. It shows a region of supersonic flow ($M > 1$) over the airfoil upper surface terminated by a shock wave, whereas the flow on the lower surface remains completely subsonic.

As the Mach number increases, the supersonic pocket gets larger and shock waves become stronger and tend to move towards the trailing edge. A similar effect can be reached by increasing the angle of attack α while keeping M_∞ unchanged. Under such conditions, complex shock wave/boundary layer interaction phenomena may take place in the flow. The intense compression across a shock imposes an equally intense adverse pressure gradient to the underlaying boundary layer, which undergoes a substantial thickening.

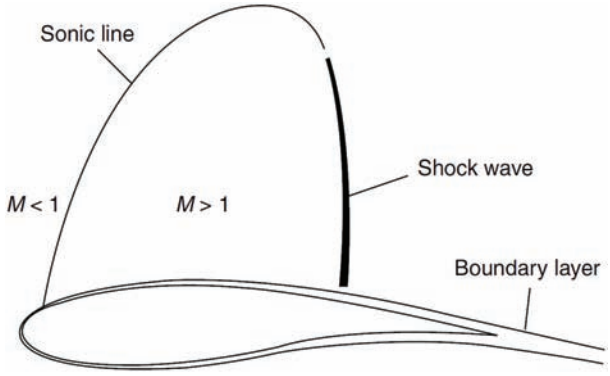

Figure 2.1: Sketch of the transonic flow around an airfoil (from Jameson [5]).

Moreover, depending on shock-wave strength, the interaction can even result in shock-induced separation. In addition to wave drag, flow separation is responsible for the 'drag divergence' phenomenon encountered by aircraft flying in the transonic range, which led to the misconception of a sound barrier during the early days of aeronautics. In regard to the flow around an airfoil, for example, the total drag can get ten times larger in the transonic regime due to the drag divergence [6]. Specific combinations of Mach number and angle of attack may also lead to an unsteady SWBLI regime commonly known as transonic buffet, which is characterized by high-amplitude shock-wave oscillations that may produce strong fluctuations of forces and moments.

In order to reduce the detrimental effects of compressibility and make transonic and supersonic flight possible and efficient, several breakthroughs had to be made in aeronautical engineering such as the swept wing of Busemann and Whitcomb's area rule. In respect to airfoil design for transonic applications, Whitcomb was also responsible for a major milestone. Departing from NACA airfoils originally designed to maximize laminar flow at low speeds but that had reasonably good performance in transonic flow, he proposed the concept of supercritical airfoil (see figure 2.2). The idea was to delay and minimize drag divergence through some basic geometrical features. A standard supercritical airfoil has a large leading-edge radius to enable rapid expansion and increase lift on the front. The upper surface is relatively flat in order to keep the flow supersonic over a pressure plateau along which the velocity may decrease gradually to generate a weaker shock wave. Rear camber is also used to provide extra lift and the trailing edge is usually thicker than in conventional airfoils in order to reduce the adverse pressure gradient in the recovery region and consequently the shock strength. Important contributions to the development of efficient transonic airfoils and particularly of 'shock-free' profiles were also made by the team of Garabedian [7, 8, 9].

Since transonic flow calculations over realistic aerodynamic configurations can only be made using CFD, progress in aerodynamic design has accompanied the evolution of numerical methods and high performance computing. Starting from schemes solving the small-disturbance potential equation [10] and then the full potential equation, the in-

(a) Whitcomb integral supercritical airfoil (b) Garabedian-Korn 'shock-free' airfoil

Figure 2.2: Examples of supercritical wing sections.

creasing computational resources has made possible the resolution of the Euler equations, which considerably improved the prediction of shock waves as they account for total pressure losses across a shock. Nowadays, viscous effects such as boundary layers, turbulence and flow separation are also included in the design process through the resolution of the RANS equations (an overview of modern aerodynamic design is given in Ref. [11]). In a recent numerical experiment, Jameson [5] replaced the original airfoils of a generic modern transonic wing [12] by modified versions of the Garabedian-Korn airfoil [13] (Fig. 2.2(b)) twisted to produce a near elliptical lift distribution at the design point ($C_L = 0.440$ at $M_\infty = 0.850$). The pressure contours obtained over the wing after solving the RANS equations for a chord-based Reynolds number of 20 million are illustrated in figure 2.3(a) and show a strong shock wave along the span. By means of an optimization process [14], an almost shock-free solution was obtained yielding a 38.5%-drag reduction. This exercise is an example of how severe compressibility effects can be in transonic aerodynamics and of the use of CFD in modern aircraft design.

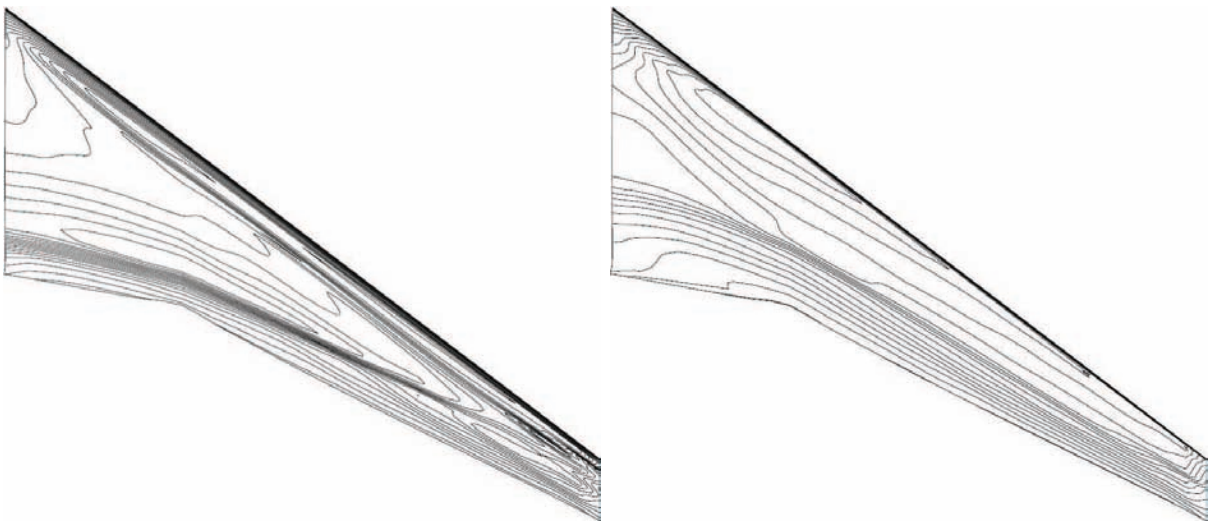

(a) Before optimization ($C_D = 0.02219$) (b) After optimization ($C_D = 0.01364$)

Figure 2.3: Pressure contours over a generic transonic wing (from Jameson [5]).

2.2 Shock wave/boundary layer interaction

2.2.1 Interaction regimes

Shock wave/boundary layer interaction is a complex subject and can give rise to multiple interaction regimes depending on the freestream Mach number, the geometry of the airfoil and the angle of attack. In the simplest case, which involves a relatively weak shock wave, the adverse pressure gradient due to the presence of the shock induces only a local thickening in the boundary layer with no separation. If the Mach or the angle of attack is high enough, the flow may feature shock-induced separation, where the shock wave can either remain stationary or oscillate at low frequencies (unsteady shocks are discussed in the next subsection).

Pearcey et al. [15] proposed a classification of the different types of shock-induced separation encountered in the transonic flow around an airfoil. Their classification considered only steady shock waves, and the possible scenarios are sketched in figure 2.4. The first is illustrated in figure 2.4(a) and consists in the formation of a separation bubble at the foot of the shock wave. Pearcey et al. named this interaction as 'model A'. The separation bubble can either remain stable, having a minor effect on the trailing edge pressure and on the circulation, or it can grow downstream, reaching the trailing edge and producing a full shock-induced separation. For thick or supercritical airfoils [16], the adverse pressure gradient on the recovery zone in conjunction with the shock wave effect can cause rear separation. By Pearcey et al. classification, interactions involving rear separation are variants of the so-called 'model B'. Figure 2.4(b) shows the case where separation bubble and rear separation coexist. Such configuration, however, is very unstable, and a full separation ranging from the foot of the shock to the trailing as illustrated in figure 2.4(c) is more likely to happen. For example, if a boundary layer is about to separate at the trailing edge, the formation of a separation bubble at the shock will favor rear separation, which will eventually merge with the bubble. Rear separation can also occur without the presence of an initial bubble and lead to full separation. Either by model A or B, full shock-induced separation strongly affects the trailing edge pressure and thus the circulation around the airfoil, causing drastic lift losses.

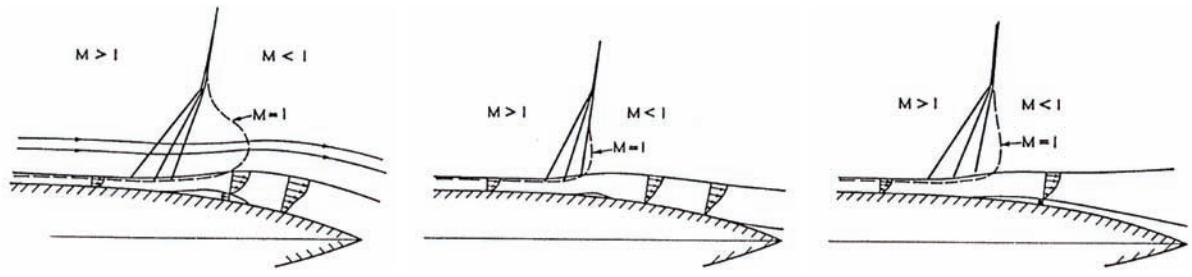

(a) Separation bubble (b) Bubble and rear separation (c) Full separation

Figure 2.4: Models of shock-induced separation (from Pearcey et al. [15]).

By measuring the unsteady surface pressure behavior around a NACA section, Mundell and Mabey [17] suggested another classification of shock wave/boundary layer interactions in transonic flow. Keeping the freestream Mach number constant, they varied the airfoil angle of attack and identified three possible SWBLI regimes, which are presented in figure 2.5 (these three regimes were also observed when fixing α and varying M_∞). They called by 'type 1' the case where a weak shock wave thickens the boundary layer without inducing any separation. This configuration is sketched in figure 2.5(a), where the numbers indicate flow regions exhibiting distinct pressure unsteadiness properties. Upstream the shock wave (1), the fluctuation levels are very low at all frequencies. Close to the shock (2), low-frequency small-scale unsteadiness can be measured. These quickly disappear as one moves downstream along the attached boundary layer (3). At slightly higher angles of attack, the shock strength becomes high enough to produce a separation bubble. Such interaction was named as 'type 2' and corresponds to model A in Pearcey et al. [15] classification. The regime is illustrated in figure 2.5(b) and is mainly characterized by low-frequency large-scale fluctuations close to the shock (2). Moreover, high-frequencies may be measured near the bubble (3) and only low levels of unsteadiness exist upstream the shock (1) and in the boundary layer downstream the bubble (4 and 5). The interaction of 'type 3' arises at higher angles of attack, where very strong shock waves induce full boundary layer separation. The resulting configuration is presented in figure 2.5(c) and is distinguished by low-frequency large-scale fluctuations over a large area downstream the separation (2). Further downstream (2A), high frequencies produced by the separated shear layer may be measured, while upstream the shock (1) the pressure fluctuations remain very low.

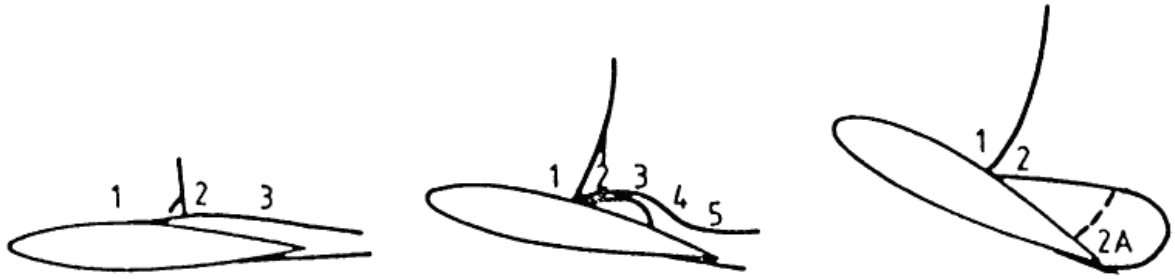

(a) Type 1 (weak shock) (b) Type 2 (stronger shock) (c) Type 3 (very strong shock)

Figure 2.5: Types of shock/boundary layer interaction (from Mundell and Mabey [17]).

2.2.2 Buffet definition and classification

In external aerodynamics, transonic buffet is an unsteady shock wave/boundary layer interaction regime characterized by low-frequency self-sustained shock-wave oscillations. For a given airfoil or wing, the phenomenon appears under specific combinations of freestream Mach number and angle of attack at transonic speeds. The shock-wave motion

is associated with full shock-induced separation, which can be permanent or intermittent, originated by the development of a separation bubble or of rear separation. Despite many experiments and numerical simulations on the subject, the mechanism of the self-sustained unsteady SWBLI is not completely understood yet. The transonic buffet is purely aerodynamic in the sense that it does not depend on a flexible structure to occur. The resulting unsteady loads, however, may produce large fluctuations of the aerodynamic forces, causing strong structural vibrations that limit the effective flight envelope. Unsteady SWBLI equivalent to transonic buffet also arises in internal aerodynamics, as in the case of supersonic intakes and of turbomachines.

The prediction of the onset conditions for transonic buffet is a problem of great interest for industry. In the design of transonic wings, the buffet boundary must be well known in order to allow a safe buffet-free margin in terms of Mach number and angle attack. In respect to airfoils, different methods have been proposed for determining buffet onset. Among them, the most widespread are based on the unsteady behavior of the global forces and pressure distribution on the surface. For flows involving shock-induced separation bubble (model A [15] or type 2 [17]), Pearcey [18] showed that the moment when the bubble arrives at the trailing edge and gives rise to a separated shear layer is accompanied by the divergence of the trailing edge pressure. Assuming that moment as the buffet boundary, good results are usually obtained for conventional airfoils. A more general way to detect buffet onset uses the divergence of the unsteady normal force, which can be measured with a balance or by unsteady pressure transducers over the surface. The buffet boundary is then defined as the moment when the variation of the fluctuating normal force with lift reaches a certain threshold. Lee [19] showed this method to produce different results from that of Pearcey when applied to Bauer-Garabedian-Korn (BGK) No. 1 supercritical airfoil. Indeed, in the paper by Roos [20], the prediction of the buffet onset over a modified Whitcomb airfoil through the divergence of the unsteady normal force resulted in better agreement with the experiments than by using the trailing edge pressure divergence method.

Different types of shock-wave motion can take place in transonic buffet. These are frequently described based on Tijdeman's classification [21] for the periodic shock-wave displacements induced by a conventional airfoil with an oscillating flap. In his study, a NACA 64A006 section at zero incidence was equipped with a trailing edge flap hinged at 0.75% of the chord. The flap oscillated sinusoidally around the zero-deflection position with an amplitude of 1° at 120 Hz (a frequency typical of the transonic buffet range). By means of shadowgraph pictures and high-speed films, Tijdeman distinguished three possible types of shock motion as the freestream Mach number varied at transonic speeds. These were named as types A, B, and C, and are illustrated in figure 2.6.

At $M_\infty = 0.90$, 'type-A' motion was obtained, which consisted of an almost sinusoidal shock-wave motion. The shocks on the upper and lower surfaces oscillated in antiphase, exhibiting a phase shift relative to the flap deflection and between the position and the

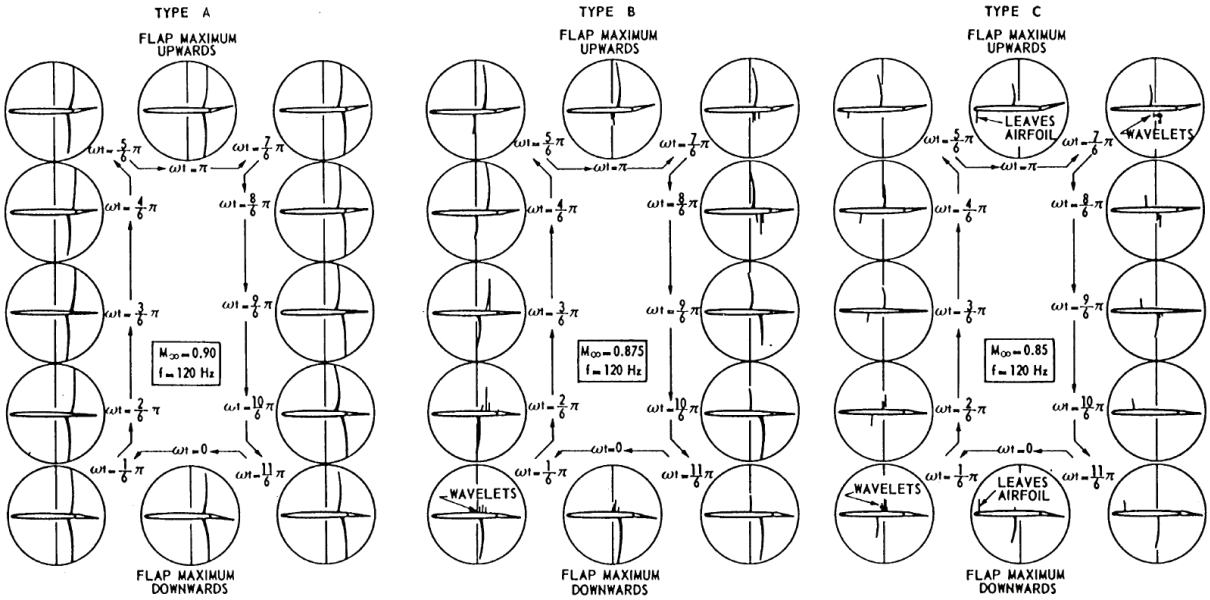

Figure 2.6: Types of periodic shock-wave motion (from Tijdeman [21]).

strength (pressure jump) of the shock wave (what was attributed to the dynamic character of the flow). The maximum strength of the shock wave appeared during the upstream motion and the minimum strength during the excursion downstream. The motion of 'type B' was described at $M_\infty = 0.875$ and was characterized by an interrupted motion of the shock, which was also almost sinusoidal but in phase with the flap deflection. During part of the downstream motion, the shock disappeared transforming into weak compression waves. The maximum shock strength arose during the upstream motion. With the flow slightly supercritical at $M_\infty = 0.85$, 'type-C' motion was characterized by upstream-moving shock waves, being considerably different from types A and B. Just after the maximum positive deflection (downwards) of the flap, the coalescence of weak compression waves formed a shock wave over the upper surface. This shock then moved upstream, leaving the airfoil from the leading edge as a free shock and vanishing in the oncoming flow. This phenomenon was also observed on the lower surface in antiphase with the upper surface.

2.3 Literature review on transonic buffet

2.3.1 Experimental investigations

2.3.1.1 Circular-arc airfoils

Despite the fact that moving shock waves have been documented since the early work of Hilton and Fowler at the NPL [22], McDevitt et al. [23] were the first to conduct an in-

depth investigation of transonic buffet [16]. During the seventies, the NASA carried out a series of experimental and numerical studies aiming at improving the performance of turbulence models in flows featuring separation. As one of such efforts, McDevitt's team analyzed the transonic flow around a symmetric circular-arc airfoil over a large range of freestream Mach and Reynolds numbers. They employed a 18%-thick profile in order to obtain shock-induced separation at a relatively low Mach number, and set airfoil at zero incidence to minimize lateral wall effects. The upper and lower walls were adapted to simulate the streamlines obtained from an inviscid computation at $M_\infty = 0.775$ in free-air. By means of a hinged mechanism, these walls could be adjusted to account for boundary layer displacements and to simulate other flow conditions. A sketch of the experimental setup is presented in figure 2.7. In the tests, the chord-based Reynolds number Re was varied between 1 million and 17 million, covering from a large laminar boundary layer extent to fully-turbulent flow. The freestream Mach number was varied from $M_{\rm cr}$ ($M_\infty \approx 0.71$) to a maximum value corresponding to a local Mach number of 1.4 immediately ahead of the shock wave, yielding weak and strong shock wave/boundary layer interaction regimes. In all cases, pressure measurements at different spanwise positions on the airfoil and oil-film visualizations showed that the flow was essentially two-dimensional.

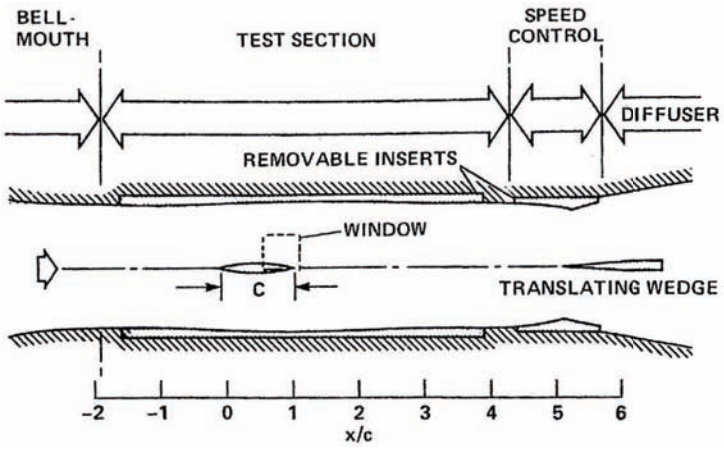

Figure 2.7: Experimental setup for the 18%-thick circular-arc airfoil (from Ref. [24]).

Although the initial goal of the study was to investigate rear and full shock-induced separation, the flowfield was found to be unsteady and periodic for certain combinations of Mach and Reynolds number. From $M_{\rm cr}$ to about $M_\infty = 0.75$, the flow remained steady, exhibiting a large pressure recovery on the rear part of the airfoil. Approximately between $M_\infty = 0.76$ and 0.78 and for values of Re above $4{\times}10^6$, the flow was shown to be unsteady with an intermittent separation line oscillating between the foot of the shock and the trailing edge. For all Reynolds numbers tested, shock-induced separation occurred through the development of rear separation. The buffet frequency was of $f = 190 \pm 3$ Hz (or a reduced frequency $r \equiv 2\pi f c/U \approx 0.49$) and was not affected by the Reynolds number. For the lower range of Re, a slightly higher Mach number was necessary to trigger buffet. Unsteady pressure transducers distributed over the airfoil showed that

the unsteadiness produced large wall pressure fluctuations. Moreover, the flows over the upper and lower surfaces were revealed to be in anti-phase. The authors explained the unsteady motion on the basis of the large changes in the displacement thickness caused by the intermittent separation on each surface. By increasing the Mach number further, steady flow was obtained again as the shocks got sufficiently strong to induce permanent boundary layer separation on both surfaces, resulting in a weak pressure recovery on the rear part. The unsteady periodic flow domain (buffet boundary) is illustrated in figure 2.8 as a function of the Mach and Reynolds numbers. The lower boundary varied considerably with M_∞ when this parameter was either increased or decreased in time. McDevitt et al. [23] attributed this hysteresis to the existence of large regions of separated flow downstream the shocks.

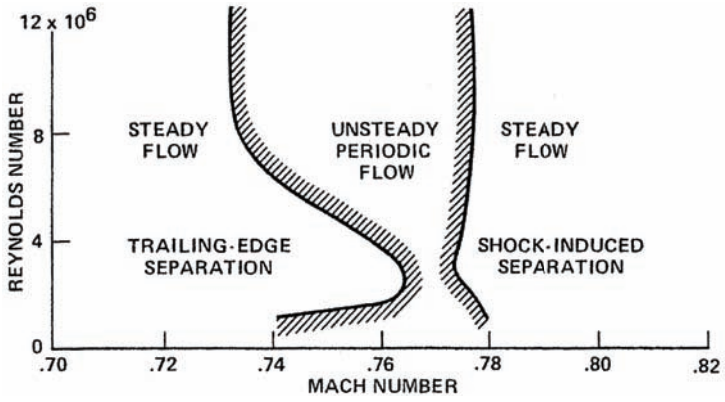

Figure 2.8: Flow domains for the 18%-thick circular-arc airfoil (from Ref. [24]).

Further investigation on NASA's circular-arc airfoil was carried out by Seegmiller et al. [24]. In order to get more detailed data of the unsteady flow regime, two-component laser velocimetry was used to characterize the velocity field. The experimental arrangement was the same of McDevitt et al. [23], shown in figure 2.7. Two freestream Mach numbers were addressed, namely $M_\infty = 0.76$ and 0.79, at a Reynolds number of $11{\times}10^6$. At $M_\infty = 0.76$, the flow was unsteady and periodic with the flows over the upper and lower surfaces in anti-phase as in Ref. [23]. The frequency of the unsteady flow was of 188 Hz and was found to be independent of the measurement position. High-speed shadowgraphs revealed the formation of a series of weak compression waves near the trailing at each period. These waves became stronger and coalesced into a shock wave that moved upstream in a way similar to Tijdeman's type-C of shock motion [21]. During the shock travel, the flow was separated from the foot of the shock to the trailing edge. The boundary layer reattached as the shock became progressively weaker until vanishing upstream. During attached flow a vortex formed at the trailing edge, causing a flow circulation towards the opposite surface where the boundary layer was separated. Depending on the degree of the flow asymmetry, alternate vortex shedding could be seen close to the trailing edge. At $M_\infty = 0.79$, the flow was steady with full shock-induced separation, yielding a thick and highly turbulent shear layer.

A deeper analysis of the unsteady flow around the same airfoil more focused on the structure of turbulence was given by Marvin et al. [25] also at $M_\infty = 0.76$ and $Re = 11\times10^6$. The mean velocity and turbulent kinetic energy and shear stress in the periodic flow were computed by means of ensemble averages of conditionally sampled data. The frequency of the periodic flow was of approximately 185 Hz, with the period exhibiting a Gaussian distribution with a standard deviation of ±2.4%. The turbulent kinetic energy and shear stress appeared to be in phase during the whole cycle. For a given point inside the shock motion range, these two quantities reached maximum values after the passage of the shock upstream. The time required for such increase depended on the shock strength and on the position along the airfoil. The local velocity then decreased, with the shear getting small and negative in regions of separated flow. After the collapse of the shock wave, the turbulent kinetic energy decreased and negative stresses could be seen at some stations inside and outside the boundary layer. At these locations, however, the measured strain rates were found to be positive. Marvin et al. attributed the generation of negative stresses to the interaction between the boundary layer and the unsteady compression waves. Since the turbulent stresses were not proportional to the local strain rates, the authors suggested that linear eddy-viscosity turbulence models would not be appropriate for the prediction of that part of the unsteady flow.

Mabey [26] studied the transonic buffet boundaries of different circular-arc airfoils with relative thickness varying between 10% and 20% for Reynolds numbers up to 6×10^5. Periodic flow was observed both with free laminar-turbulent transition and with a fully-turbulent boundary layer, which was obtained by placing a transition band near the leading edge. In cases where free transition was allowed, the shock-wave motion range was larger than in fully-turbulent cases. Mabey concluded that the unsteady periodic flow regime demanded the formation of a relatively strong shock wave and that its origin was related to viscous phenomena, requiring the occurrence of shock-induced separation. Mabey et al. [27] investigated the transonic flow around a half-wing model with an aspect ratio of two and made of a 14%-thick circular-arc section. The freestream Mach number was varied between 0.74 and 0.9 and the Reynolds number from 1 million to 7 million. At zero incidence, the flow was shown to be essentially two-dimensional at the mid-section of the wing. Between $M_\infty = 0.82$ and 0.86, the flows over the upper and lower surfaces were periodic and in anti-phase, exhibiting a mean frequency of 130 Hz. With laminar boundary layer extending from the leading edge to the shock, buffet was suppressed for Reynolds numbers from 3×10^6 to 5×10^6. Contrary to the type C motion seen by McDevitt et al. for the 18%-thick airfoil [23], Mabey et at. classified the shock-wave motion as of type B. At each period, the shock vanished during its travel upstream, which was accompanied by the reattachment of the boundary layer. Moreover, no compression waves propagating from the leading edge into the flow were seen in shadowgraphs.

Based on the results of Mabey et al. [27] for the 14%-thick circular arc airfoil, Gibb [28] proposed a model for the self-sustained shock-wave oscillations, which is presented in the sequence of figure 2.9. According to his model, as the freestream Mach number

is increased, the local Mach number just ahead of the shock wave eventually gets high enough to induce separation on one side of the airfoil as illustrated in figure 2.9(a) for the upper surface. The resulting asymmetric wake decreases the flow velocity on the separated side, inducing the shock to move upstream where it becomes weaker and allows the boundary layer to reattach. On the contrary, the flow on the opposite surface is accelerated, inducing the shock to travel downstream where it becomes strong enough to induce separation. As shown in figure 2.9(b), the flow asymmetry is then inverted and the shocks start moving in the opposite direction. In such self-sustained periodic flow, the deflections produced by the oscillating wake play a role similar to the flap used by Tijdeman [21]. If the freestream Mach number gets too high for the boundary layers to reattach, steady shock-induced separation is obtained on both surfaces as illustrated in figure 2.9(c).

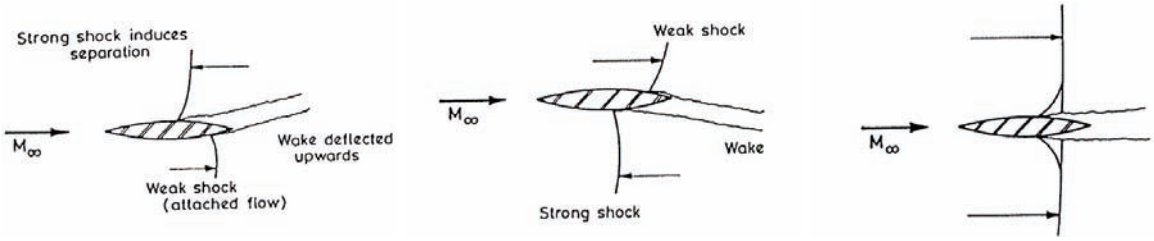

(a) (b) (c)

Figure 2.9: Self-sustained shock-wave motion over a circular-arc airfoil (from Gibb [28]).

2.3.1.2 Conventional and supercritical profiles

Regarding lifting airfoils at variable incidence, Roos [29] studied the unsteady aerodynamics of a supercritical airfoil at transonic speeds. He employed a Whitcomb profile modified to have a thick trailing edge of 1% of the chord to facilitate the installation of pressure transducers, which were placed at the mid-section over both the upper and lower surfaces. By varying the lift coefficient and the freestream Mach number, Roos detected regions of intense pressure fluctuations for which he performed spectral analyzes and computed the correlations between the unsteady pressure signals to determine the propagation directions and speeds of the pressure waves in the flowfield. In order to better understand the physics of the unsteady pressure field, Roos [20] analyzed the same Whitcomb airfoil over a larger range of M_∞ and C_L and compared its buffet characteristics with those of a conventional NACA 0012 section. The tests were conducted using 6-in models in a 2×2 ft^2 continuous wind tunnel, yielding an aspect ratio of 4. Along with pressure transducers, flowfield measurements were made using hot-film anemometry and a shock-position sensor. The study was performed varying either the freestream Mach number or the lift coefficient, around baseline conditions of $M_\infty = 0.82$ and $C_L = 0.53$ for the Whitcomb airfoil, and $M_\infty = 0.68$ and $C_L = 0.42$ for the NACA 0012. The Reynolds number was equal to 2×10^6 and the boundary layer was tripped on the upper surface

at 35% of the chord for the Whitcomb and 18% for the NACA section. The evolution of the pressure distributions around the two airfoils as the flow conditions were varied is presented in figure 2.10. For the Whitcomb profile, as the Mach number or the lift were increased, the shock moved always downstream as long as the boundary layer remained attached. When separation occurred, evolving from the tailing edge, the shock wave moved upstream. A strong buffet condition is illustrated in figure 2.10(a) through the curve for $C_L = 0.91$, which presented a large-amplitude shock-wave motion. By varying the Mach number up to 0.90, no shock-wave oscillation was detected at $C_L = 0.53$ despite the occurrence of flow separation and the divergence of the trailing edge pressure.

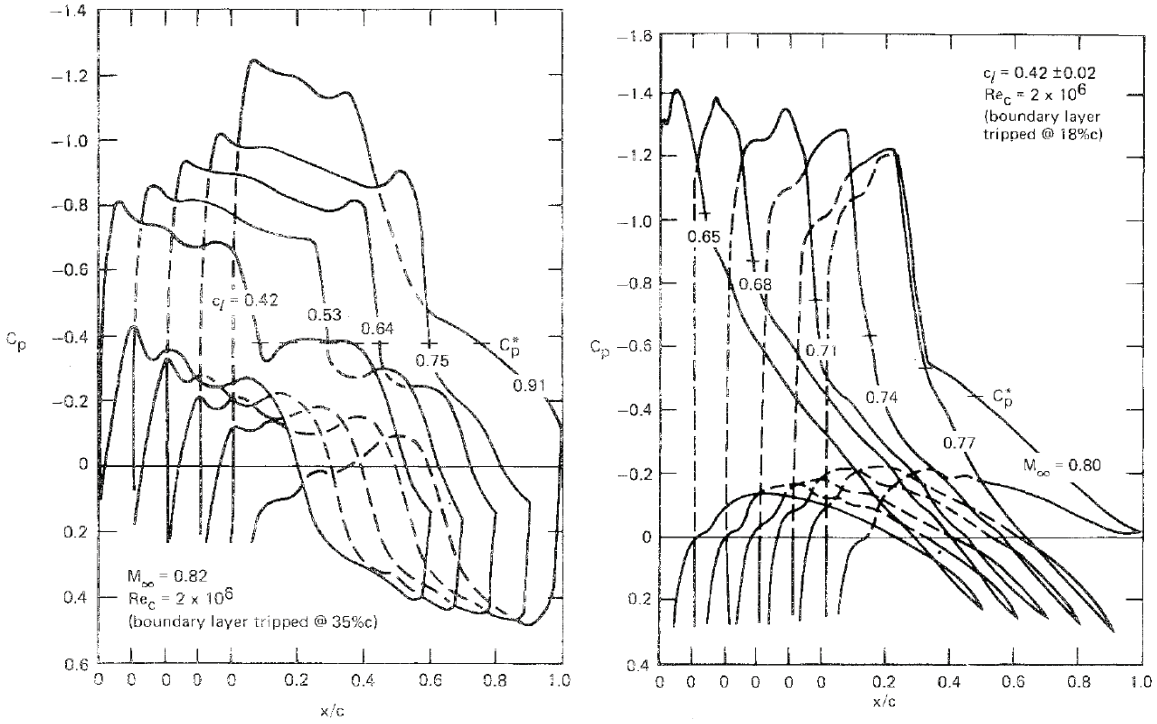

(a) Whitcomb (as a function of M_∞)

(b) NACA 0012 (as a function of C_L)

Figure 2.10: Evolution of the pressure distributions over two airfoils (from Roos [20]).

For the NACA 0012 airfoil, the variation of C_p with the Mach number at constant lift is given in figure 2.10(b). The evolution of the pressure distribution as a function of C_L at fixed Mach number was similar. For this conventional airfoil, separation occurred through a separation bubble at the foot of the shock, appearing around $M_\infty = 0.74$. As the Mach was increased, the bubble grew downstream and reached the trailing edge at approximately $M_\infty = 0.77$, yielding full shock-induced separation with strong buffeting. The behavior of the shock-wave position was similar to that for Whitcomb airfoil, but with a smaller shock-motion range in buffet conditions. The pressure transducers over the Whitcomb supercritical airfoil showed intense pressure fluctuations arising as a consequence of the development of separation. These were caused mainly by the shock-wave motion but also by the unsteadiness in the separated region. In respect to the conventional NACA 0012 airfoil, similar results were obtained, with the shock unsteadiness responsible for

the most intense fluctuations. For that airfoil, however, the pressure fluctuations grew from foot of the shock towards trailing edge, as consequence of the development of the separation bubble with increasing Mach number of lift. Measurements of the trailing edge pressure coefficient as well as of the unsteady lift coefficient and shock-wave position as a function of the freestream Mach number are presented in figure 2.10 for the two airfoils. For the Whitcomb profile, the divergences of the trailing edge pressure and of the unsteady lift did not occurred simultaneously as M_∞ was augmented, suggesting that the trailing edge pressure divergence is not a good indicator of buffet onset for that supercritical airfoil. On the contrary, these variables diverged at the same time in the case of the conventional NACA 0012 section.

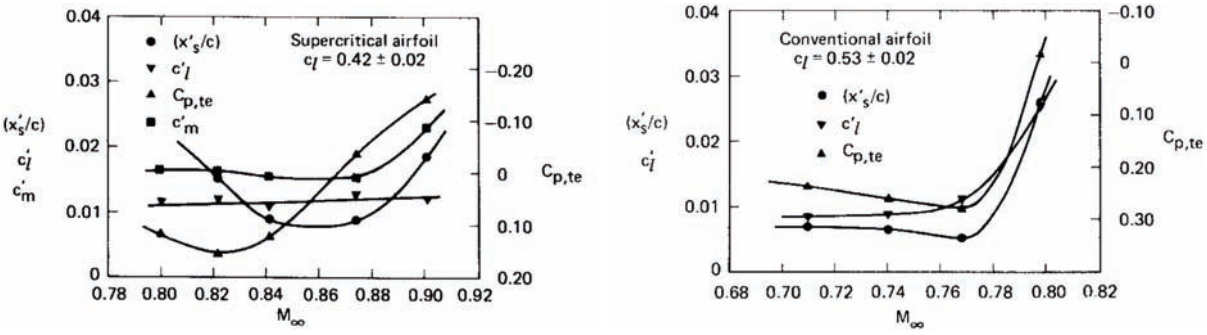

(a) Whitcomb (b) NACA 0012

Figure 2.11: Behavior of the unsteady lift and trailing edge pressure (from Roos [20]).

For both the Whitcomb and NACA 0012 airfoils, two-point correlations of the pressure transducers signals suggested similar behavior for wave propagation phenomena. With the flow completely attached, perturbations were shown to travel upstream from the trailing edge/near-wake region to the shock wave. However, when the flow was fully-separated in buffet conditions, the perturbations propagated downstream from the shock region towards the trailing edge. Correlations of the surface pressure signals with the flow velocity just downstream the trailing edge revealed that the pressure perturbations were associated with downstream moving structures. Furthermore, smaller-scale perturbations were shown to have higher propagation speeds than large-scale ones. In the case of intermittent separation, the scenario was more complex, involving both upstream and downstream moving perturbations (i.e., both acoustic and convection modes). The pressure transducers also revealed that the buffet over the Whitcomb airfoil was less periodic than for the NACA 0012 profile. The correlations of the pressure signals with the global lift showed that the shock region was responsible for most of the unsteady lift forces.

The NACA 0012 airfoil was also subject of investigation in the experimental work by McDevitt and Okuno [30]. The authors studied the airfoil in transonic flow conditions, for freestream Mach numbers varying between 0.7 and 0.8 and Reynolds numbers in the range 1-20 $\times 10^6$, with special attention towards the determination of the buffet onset boundary as a function of the flow parameters and of the angle of attack. In order to

generate a useful database for the assessment of numerical codes, techniques for obtaining two-dimensional flow such as lateral boundary layer suction were applied to the test channel to minimize interference. Besides, flexible upper and lower walls were adapted to reproduce the free air streamlines for a series of selected nominal conditions. The adaptive walls also permitted to correct for test section Mach number changes due to the sidewall mass removal and for boundary layer displacement effects. Oil visualizations revealed that natural transition occurred near the trailing edge for high Re, so that the boundary layer could be considered as fully turbulent. Buffet onset was determined by means of unsteady pressure transducers placed at $x/c = 0.5$ and 0.8 on the airfoil surface, based on the fact that the amplitude of the pressure fluctuations grew linearly with α. With increasing incidence, the shock wave position first moved downstream, until it started moving upstream close to the buffet boundary. At low Reynolds numbers, buffet was characterized by random pressure fluctuations that were first detected by the transducer located at $x/c = 0.5$. This suggested that the unsteadiness was originated somewhere closer to the airfoil midchord than to the trailing edge. For Reynolds numbers larger than 6×10^6, buffet was detected simultaneously by the two transducers, which exhibited periodic fluctuations with a well defined frequency. Shadowgraphs revealed the occurrence of intermittent shock-induced separation at buffet onset. With moderate incidence, separation occurred only on the upper surface, though the flow unsteadiness could be felt everywhere. The resulting wake deviation was similar to an upward flap deflection, tending to decrease the velocity on the upper surface so that the flow returns to its original configuration thus becoming periodic. Tests at zero incidence with increasing Mach number showed buffet to occur simultaneously on both upper and lower surfaces, with the shock waves oscillating in antiphase.

In order to get a better understanding on the aerodynamic aspects of the transonic buffet over supercritical airfoils, Lee and Ohman [31] investigated the transonic flow around the BGK No. 1 supercritical airfoil in the Mach number range from $M_\infty = 0.501$ to 0.805. In the experiments, the angle of attack was varied from $-0.36°$ to $11.74°$ at Reynolds numbers between $15{\times}10^6$ and $21{\times}10^6$. The unsteady normal force on the airfoil was measured using a sidewall balance, and fast-response unsteady pressure transducers distributed along the upper surface were used to measure the pressure fluctuations during buffet. The most severe fluctuations of the normal force were detected at freestream Mach numbers between 0.7 and 0.8, for lift coefficients ranging from 0.8 to 1.1. In this range, the shock waves were strong and the flow was permanently separated from the foot of the shock to the trailing edge. The unsteady aerodynamic forces were mainly caused by the pressure fluctuations in the separated region, and the pressure transducers indicated very high fluctuations close to the shock wave. In the separated region, the pressure fluctuations increased monotonically from the shock to the trailing edge. Power spectral densities of the normal force and of the pressure signals showed a distinct peak whose frequency increased with M_∞ and, in most cases, the first harmonic was also visible. In the region of separated flow, the experiments revealed a strong coherence between the

unsteady normal aerodynamic force and the signals from the pressure transducers.

Lee et al. [32] compared the transonic buffet properties of the BGK No. 1 and WTEA II [33] supercritical airfoils. The two profiles have been designed for similar cruising Mach numbers and lift coefficients ($M_\infty = 0.75$ and $C_L = 0.63$ for the BGK No. 1, $M_\infty = 0.72$ and $C_L = 0.6$ for the WTEA II), although their relative thickness differ considerably (16% for the BGK No. 1 and 11.8% for the WTEA II). Therefore, the effect of the airfoil thickness on the onset boundary and on the characteristics of transonic buffet could be investigated. For both airfoils, the Reynolds number was equal to 20 million and the boundary layer was allowed to develop freely. Transition was revealed to occur before 5% of the chord on the WTEA II and before 10% on the BGK No. 1 airfoil. In the tests, the freestream Mach number was varied between 0.612 and 0.792 for the WTEA II, and from 0.5 to 0.818 for the BGK No. 1 airfoil. The buffet boundaries of the two airfoils determined by means of the divergence of the unsteady normal force and expressed in terms of lift coefficient and freestream Mach number are presented in figure 2.12. Below $M_\infty = 0.71$, the two boundaries are virtually identical. As the Mach number is increased, however, buffet onset over the WTEA II arises for a lower lift coefficients than on the thinner BGK No. 1 airfoil. This difference becomes larger for higher values of M_∞. Moreover, Lee et al. showed the unsteadiness of the normal force to increase with the airfoil thickness.

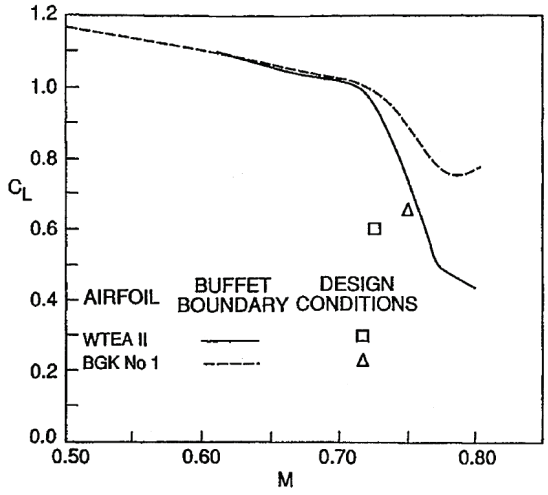

Figure 2.12: Buffet boundaries of the WTEA II and BGK No. 1 airfoils (from Ref. [32]).

For the WTEA II airfoil, the buffet frequency increased with the Mach number. Its value remained within the 50-80 Hz range from $M_\infty = 0.612$ to 0.792. As the angle of attack was increased, the shock became progressively stronger until a critical incidence. From that point on, the shock started to weaken and the buffet vanished. In the case of the BGK No. 1 airfoil, as the angle of attack was increased, the pressure transducers on the upper surface showed the transonic flow regime to change from subcritical to a weak shock wave/boundary layer interaction without separation, then to shock-induced separation bubble and finally to fully-separated buffet, where the frequency of the shock motion was

of approximately 75 Hz at $\alpha = 6.94°$. The buffet boundary of the BGK No. 1 airfoil as a function of the angle of attack for the Mach number range investigated is given in figure 2.13 based on Ref. [19]. The study also revealed that pressure waves induced by the shock motion propagated towards the trailing edge through the separated region. In cases featuring full shock-induced separation, the phase angle of the fundamental component of these waves varied almost linearly downstream the shock, so that their propagating velocity could be easily determined.

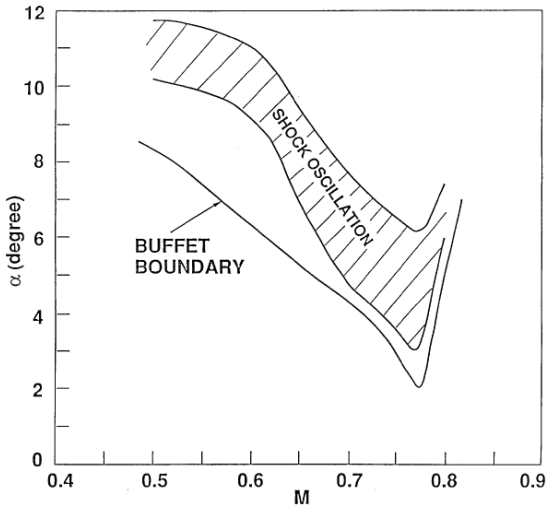

Figure 2.13: Buffet and shock oscillation boundaries for the BGK 1 airfoil (from Lee [19]).

The results for the BGK No. 1 airfoil inspired Lee [19] to elaborate a model for the self-sustained shock-wave oscillation over supercritical airfoils in cases where the flow is fully separated. The model stands on the work of Roos and Riddle [34], who revealed the presence of upstream moving waves originated at the trailing edge and in the near wake of a Whitcomb profile in transonic buffet regime. In Lee's words, the physical mechanism was described as follows: *Because of the movement of the shock, pressure waves are formed which propagate downstream in the separated flow region at velocity a_p. On reaching the trailing edge, the disturbances generate upstream moving waves at velocity a_u. These waves will interact with the shock and impart energy to maintain its oscillation* [19]. The model proposed is schematized in figure 2.14. According to Lee, the period of the shock-wave oscillation should agree with the time it takes for a disturbance to travel from the shock to the trailing edge plus the time an upstream moving wave takes to reach the shock wave from the trailing edge. Therefore, the total time T for a disturbance to complete such a loop (i.e., the buffet period) could be estimated by

$$T = \int_{\overline{x}_s}^{c} 1/a_p \, dx - \int_{c}^{\overline{x}_s} 1/a_u \, dx, \tag{2.2}$$

where x is the coordinate in the chordwise direction and $\overline{x}_s$ stands for the mean position of the oscillating shock wave. Within the buffet boundary, the unsteady pressure data from the upper surface of the BGK No. 1 airfoil showed large levels of fluctuation in the

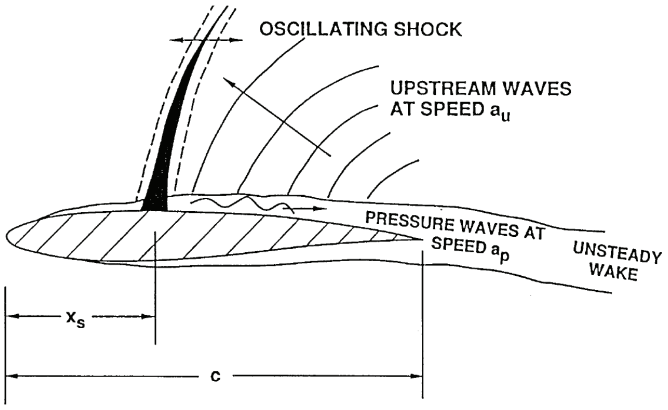

Figure 2.14: Model of self-sustained shock oscillations (from Lee [19]).

shock-wave region. These decayed rapidly and remained nearly constant in the separated region as illustrated in figure 2.15. In addition to a random turbulent motion, the fluctuations were mainly caused by a deterministic component $\tilde{p}$ resulting from the shock-wave oscillation. Therefore, Lee [19] calculated the velocity of the downstream propagating waves in the separated region a_p from a phase relation, which considered only the fundamental of $\tilde{p}$ as the magnitude of its first harmonic was too small. Besides, the velocity of the upstream moving waves was computed as $a_u = (1 - M)\, a$, where M and a stand for the local Mach number and speed of sound, respectively. Despite all the approximations made for a_p, a_u and $\overline{x}_s$, the buffet frequencies $f = 1/T$ obtained by means of this model were in good agreement with the experimental results for several values of M_∞ and angle of attack.

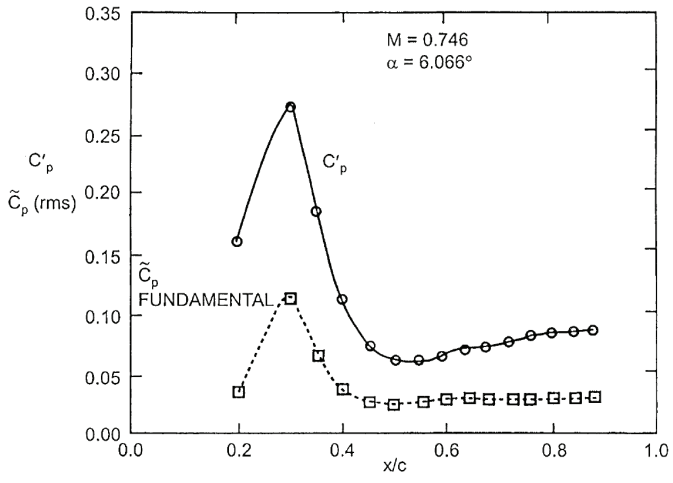

Figure 2.15: RMS values of pressure fluctuations on the BGK 1 airfoil (from Lee [19]).

Upstream moving pressure waves forming near the trailing edge and in the near-wake have been observed in many studies of transonic flows past airfoils and are commonly known as 'Kutta waves'. By means of experiments and numerical simulations, Alshabu et al. [35] showed that the generation of such waves is coupled with vortex structures

traveling downstream in the boundary layer. Alshabu and Olivier [36] investigated the nature of the Kutta waves in the transonic flow over the BAC3-11 airfoil at zero incidence for freestream Mach numbers from 0.65 to 0.80, and Reynolds numbers between 1×10^6 and 4×10^6. By means of shadowgraphs and Schlieren pictures of the flow, the waves could be observed in compressible subsonic flows even without the presence of shock waves. Numerical simulations confirmed that wave generation is coupled with vortices in the boundary layer. The wave intensity increased in regions where the airfoil was thicker and decreased again further upstream, almost vanishing near the leading edge. With increasing freestream Mach number, the waves became more intense and complex due to the interaction with the supersonic pocket. The effect of increasing the Reynolds number was similar but at a much lower degree. For the attached flow with no shock at $M_\infty = 0.71$ and $Re = 2\times10^6$, unsteady pressure transducers revealed that the wave process was periodic, exhibiting two predominant frequencies at 700 Hz and 1500 Hz. At higher Mach numbers, the supersonic region was terminated by a shock wave. For specific freestream conditions, the interaction of the pressure waves with the shock wave could attenuate and even degenerated the shock into compression waves for short time periods. Figure 2.16(a) shows a Schlieren picture of the wave/shock wave interaction at $M_\infty = 0.80$ and $Re = 3.4\times10^6$. The extension of the supersonic pocket is revealed by the Mach lines and, as it can be seen, the boundary layer undergoes a full shock-induced separation. Since the shock works as an obstacle for wave propagation, the upstream moving waves travel around the shock through the subsonic flow above it. Such wave pattern is schematized in figure 2.16(b).

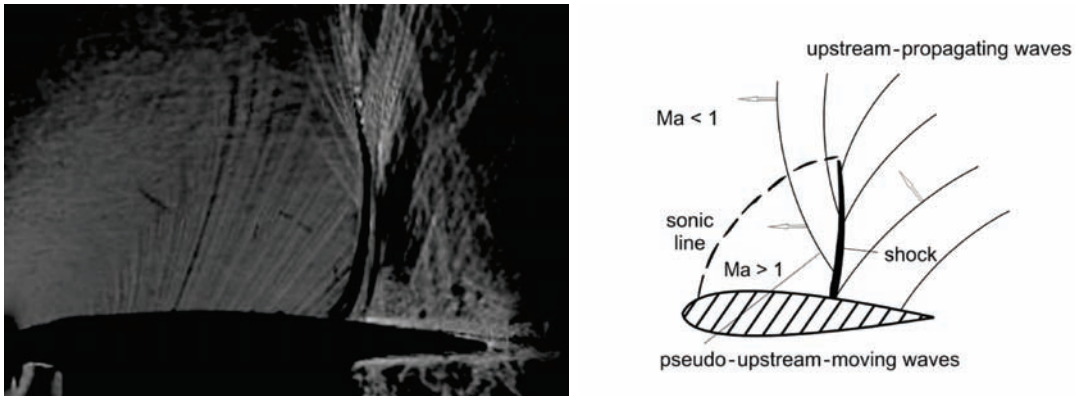

(a) Schlieren picture (b) Schematic drawing

Figure 2.16: Wave propagation and interaction with the shock wave (from Ref. [36]).

Stanewsky and Basler [37] studied the transonic buffet over the CAST7/D0A1 supercritical airfoil and the influence of parameters such as the freestream Mach number, the Reynolds number and the angle of attack on the buffet characteristics. In the experiments, boundary layer transition was imposed at 9% of the chord. At $\alpha = 3^\circ$ for freestream conditions of $M_\infty = 0.77$ and $Re = 6\times10^6$, only the upper surface presented a shock wave, which oscillated according to type A motion [21]. The evolution of the

shock-wave strength measured by the shock height h_{ss} and of the boundary layer thickness at the trailing edge δ_{TE} during buffet are shown in figure 2.17 as a function of the shock-wave position. The shock-wave strength decreased during the shock motion downstream. It started to increase only as the shock approached its most downstream position and the boundary layer thickness reached its minimum value. As the progressively stronger shock wave started moving back upstream, the boundary layer thickened continuously, separating approximately when $x_s/c = 0.48$. During its upstream travel, the shock reached its maximum strength, starting to weaken as the boundary layer reattached around $x_s/c = 0.44$. With the shock at its most upstream position, the boundary layer thickness at the trailing edge was maximal.

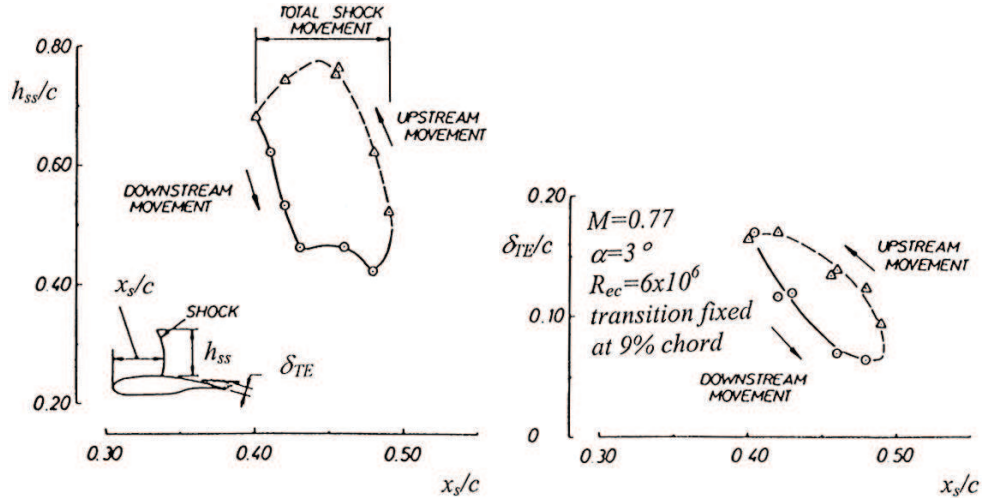

(a) Shock-wave height (b) Boundary layer thickness

Figure 2.17: Shock-wave and boundary layer properties during buffet (from Ref. [37]).

With the aim of providing a well-documented test case for CFD research, Jacquin et al. [38, 39] performed an experimental investigation of the transonic buffet around the OAT15A, a 12.3%-thick supercritical airfoil from ONERA. The tests were conducted in a continuous closed-circuit transonic wind tunnel with a square test section of 0.78×0.78 m^2 (see figure 2.18). In order to reduce wall interference, the mean flow streamlines were simulated using adaptive upper and lower walls accounting for boundary layer displacement effects. The model had a chord length of 0.23 m and a blunt trailing edge of 0.5% of the chord, giving an aspect ratio of about 3.4. Transition was triggered on both upper and lower surfaces using carborundum strips placed at $x/c = 0.07$ from the leading edge. In the experiments, the freestream Mach number could be varied from 0.70 to 0.75 with an uncertainty of $\pm 1\times10^{-4}$ and the angle of attack could be set from 2.5° up to 3.9°. The chord-based Reynolds number was equal to 3×10^6 and the total conditions for pressure and temperature were 10^5 Pa and 300 K, respectively.

Most of the results reported in Ref. [39] are for Mach 0.73. Preliminary flow visualizations with sublimating product for the steady flow at $\alpha = 2.5°$ confirmed that the boundary layer was fully turbulent downstream the tripping line. Oil flow visualizations revealed

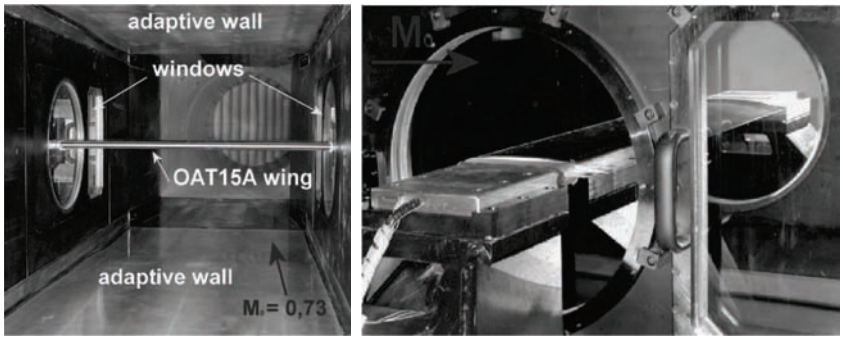

(a) General view (b) Detail of the model fixation

Figure 2.18: Experimental setup for the OAT15A supercritical airfoil (from Ref. [39]).

that the separation at the foot of the shock wave was two-dimensional over a large portion of the model span. Static pressure orifices and unsteady pressure transducers distributed over the central part of the airfoil detected no buffet at incidences equal or smaller than 3°. The flow remained steady exhibiting only weak pressure fluctuations at the foot of the shock and on the rear part of the airfoil. The first shock wave unsteadiness occurred around $\alpha = 3.1°$, being amplified at 3.25° although the shock motion was not fully established yet. Fully-developed shock-wave oscillations began only from 3.5°. At that incidence, oil flow revealed the presence of three-dimensional steady structures on the central part of the wing, though the mean separation line remained two-dimensional. The statistical pressure distributions over the airfoil as a function of the angle of attack are presented in figure 2.19. The shock-wave motion range can be identified by the spread compression area in the mean pressure profile in figure 2.19(a) as well as by the region of high pressure fluctuations in figure 2.19(b). At 3.5°, it covered approximately 20% of the chord.

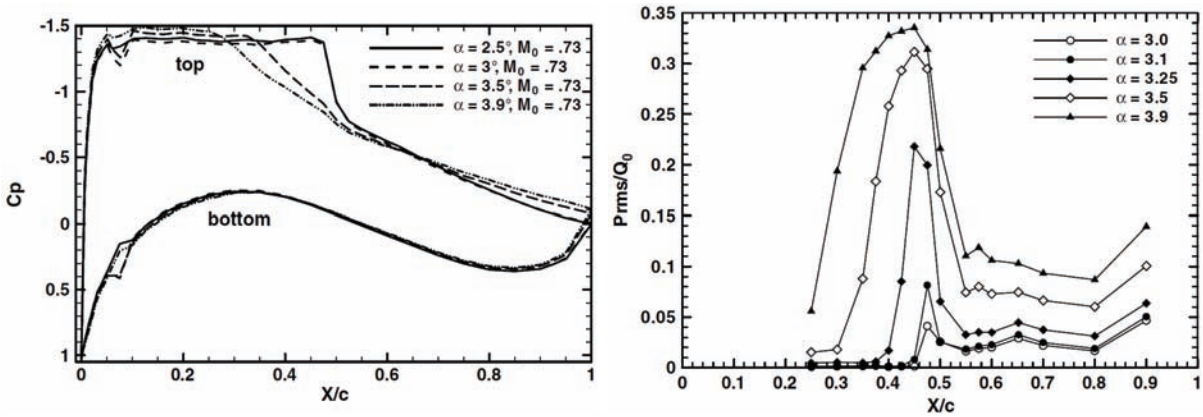

(a) Mean pressure coefficient (b) RMS values of the pressure fluctuations

Figure 2.19: Statistical pressure distributions over the OAT15A (from Ref. [39]).

High-speed Schlieren cinematography showed a lambda-shaped shock wave oscillating at a frequency close to 70 Hz, which was indicated by the spectral analysis of the transducers

signals. A posterior study at fixed angle of attack demonstrated that the buffet frequency increased with the Mach number. Velocity profiles at the trailing edge region revealed that the periodic flow over the OAT15A airfoil was characterized by an intermittent boundary layer separation process coupled with the shock-wave motion. By means of two-component laser Doppler velocimetry, the flow topology was depicted as shown in figure 2.20. When the shock was about its most upstream position, the boundary layer was separated from the foot of the shock to the trailing edge (figure 2.20(a)). As the shock started moving downstream, separation disappeared and the boundary layer remained attached during the shock excursion towards the trailing edge (figure 2.20(b)). As the shock reached its most downstream location (figure 2.20(c)), the boundary layer became progressively thicker and, as the shock started traveling back upstream, shock-induced separation occurred. During the motion (figure 2.20(d)), the size of the separated region grew until the shock arrived at its most upstream location and completed the cycle. The spectral contents from unsteady pressure transducers distributed on the upper surface in the spanwise direction at $x/c = 0.6$ were essentially two-dimensional in the central region of the model. Jacquin et al. suggested that the transonic buffet phenomenon is modal and essentially two-dimensional, despite the three-dimensional patterns detected in the flow visualizations.

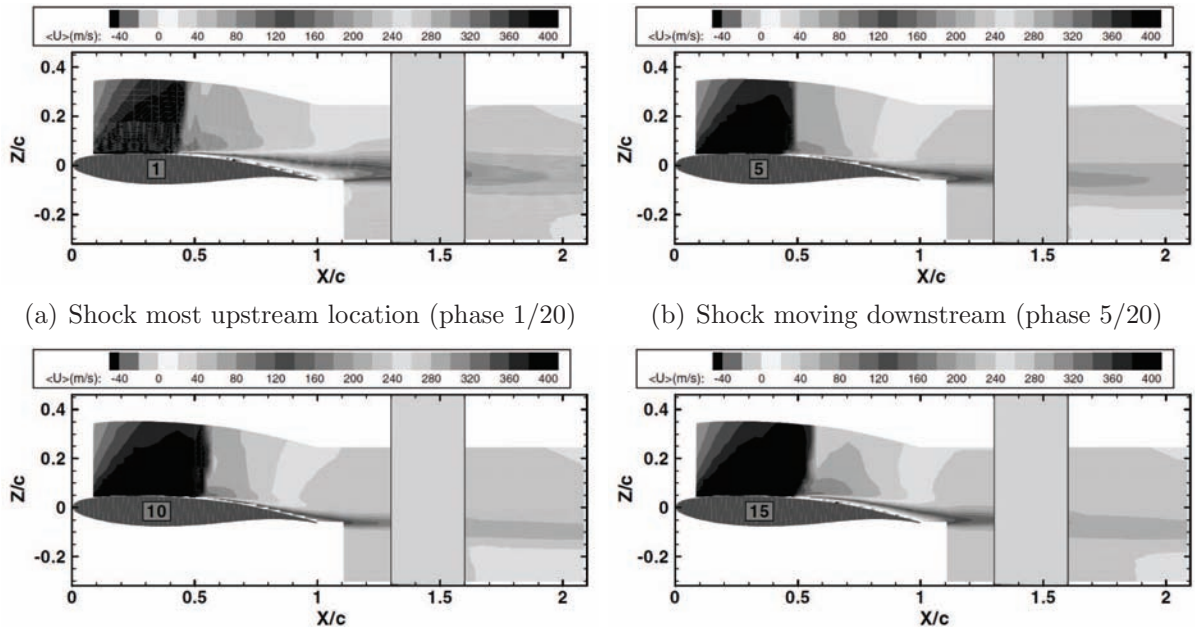

(a) Shock most upstream location (phase 1/20)

(b) Shock moving downstream (phase 5/20)

(c) Shock most downstream location (phase 10/20)

(d) Shock moving upstream (phase 15/20)

Figure 2.20: Phase-averaged velocity fields around the OAT15A (from Ref. [39]).

2.3.2 Global-stability theory

Through the past decades, several explanations for transonic buffet have been proposed as presented in the previous subsection. In these models, the physical mechanism driving

the self-sustained shock-wave oscillations is often described in terms of wave propagation phenomena or variations in the effective body caused by flow separation. Using global-stability theory, Crouch et al. [40, 41] linked the origin of transonic buffet over airfoils to the onset of a global flow instability due to a Hopf bifurcation. Their studies employed a generalized approach for the prediction of flow unsteadiness onset in high-Reynolds number compressible flows by solving an eigenvalue problem based on steady solutions of the Reynolds-averaged Navier-Stokes equations obtained numerically. The method was first used to predict vortex shedding onset in the laminar incompressible flow around a cylinder, showing excellent agreement with experimental results in respect to the critical Reynolds number. Then, it was applied at high Reynolds in conjunction with a turbulence model to predict transonic buffet onset over the NACA 0012 airfoil based on the experiments of McDevitt and Okuno [30]. For a fixed Mach number, as the angle of attack increased, the critical incidence was defined as the moment when the least stable eigenvalue crossed the real axis, penetrating into the unstable region of the complex plane (see Ref. [40] for a complete presentation of the method). By following this procedure for different Mach numbers, the predicted buffet onset boundary was in good agreement with the experiments of Ref. [30] as shown in figure 2.21, providing evidence that airfoil transonic buffet is caused by global instability.

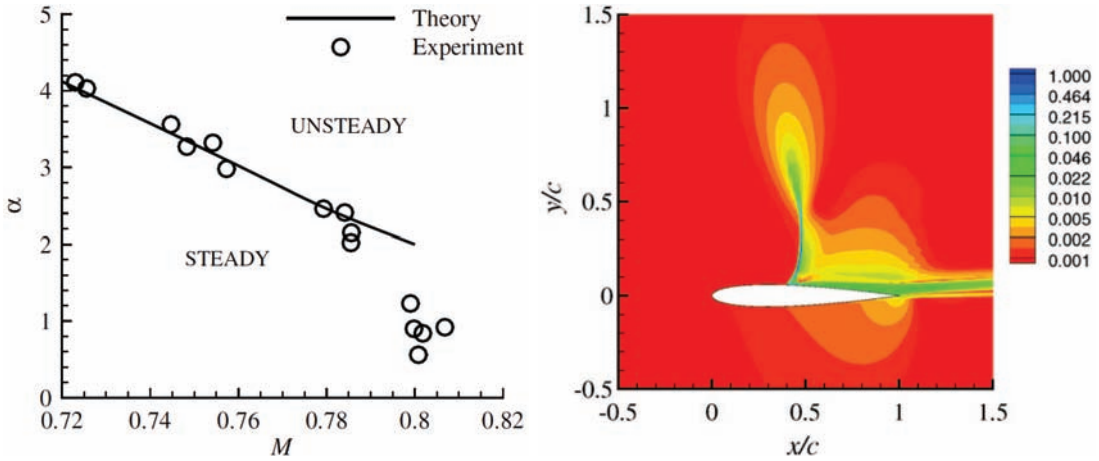

(a) Buffet boundary

(b) u-velocity for the unsteady mode

Figure 2.21: Global-stability theory results for the NACA 0012 airfoil (from Ref. [40]).

Near buffet onset, the instability growth rate varied almost linearly with the angle of attack. For higher Mach number values, the experimental buffet boundary appeared earlier than by global-stability analysis. According to Crouch et al., possible reasons for this behavior could be deficiencies in the base flow computation (e.g., turbulence modeling) or in the experiments of reference, such as tunnel unsteadiness or blockage effects. The instability mode shape was characterized by perturbations located primarily around the shock and in the shear layer downstream it, with the unsteady flow presenting a coupled modulation of these two regions in agreement with the description provided in Ref. [30]. The longitudinal velocity u for the unsteady mode is illustrated in figure

2.21(b). As the shock moved downstream, the separated shear layer moved closer to the airfoil surface, becoming thinner. The authors did not found a clear link between qualitative features of flow separation (e.g., separation bubble burst) and buffet onset [41].

In another paper, Crouch et al. [42] applied the global-stability analysis to predict the structure of the buffeting flow around the OAT15A supercritical airfoil and compared it to the experiments of Jacquin et al. [38, 39]. Again, the results from global-stability analysis showed buffet to result from a Hopf bifurcation. Figure 2.22 shows that this approach gives a good prediction of the critical angle of attack for buffet onset and of the frequency, exhibiting a consistent behavior with the experimental data as the Mach number is increased. The eigenfunction revealed that the experimental buffet flow was satisfactorily reproduced by the structure of the global instability, with the largest velocity perturbations found in the shock-wave region and in the shear layer. When the shock wave moved downstream, the shear layer oscillated in phase with it, moving closer to the airfoil surface. Comparisons with the experimental fluctuating flowfield showed that the theory provided a similar unsteady flow structure, thus supporting the global-mode description of transonic buffet.

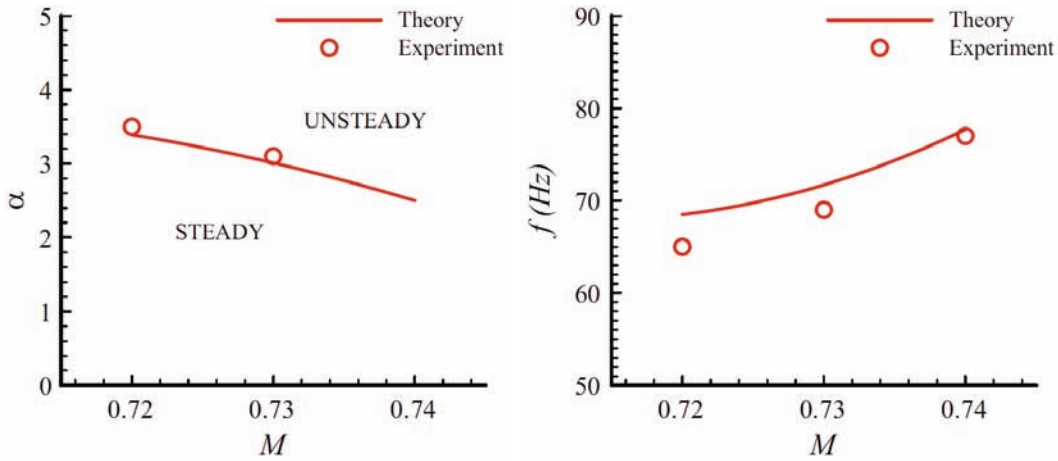

(a) Buffet boundary (b) Frequency

Figure 2.22: Global-stability theory results for the OAT15A airfoil (from Ref. [42]).

2.3.3 Numerical simulations

2.3.3.1 Pioneering studies

The first attempts to reproduce numerically the unsteady flow regime encountered in the experiments of McDevitt et al. [23] were published in the work of Levy [43]. According to that paper, that was the first time a Navier-Stokes code reproduced time-dependent unsteady turbulent flows involving weak and strong shock wave/boundary layer interac-

tions with good qualitative results. The two-dimensional RANS equations in conjunction with a primitive algebraic eddy-viscosity model were solved by means of the explicit finite-difference scheme of MacCormack [44]. Computations were run for three freestream Mach numbers ($M_\infty = 0.720$, 0.754 and 0.783) at a Reynolds number of 11×10^6, covering both weak and strong shock wave/boundary layer interaction regimes. At $M_\infty = 0.720$, the flow was steady, presenting a weak shock and trailing edge separation. The computed pressure distribution was in good agreement with experimental data over the most part of the airfoil. Nevertheless, the pressure recovery was overestimated in the separated region, which was attributed to inadequate turbulence modeling. The freestream Mach number of 0.754 lied within the zone of hysteresis reported in Ref. [23] concerning the Mach-number lower boundary of unsteadiness. The numerical simulation led to an unsteady flow alternating between shock-induced and trailing-edge separations. The mean pressure distributions were well predicted over the first half of the airfoil and the time histories of the wall pressure at $x/c = 0.50$ and 0.775 indicated that the numerical method successfully reproduced the actual wave forms. Moreover, the flowfield was asymmetric, exhibiting a 180°-phase difference between the upper and the lower surfaces and a main frequency about 20% lower than in the experiments. Figure 2.23 illustrates instantaneous Mach number contours at four different phases of the unsteady flow. It indicates that a shock wave forms near the trailing edge and increases in strength, giving rise to shock-induced separation. As the shock and the separated region move upstream, the local velocities ahead of the shock increase and the shock becomes stronger. As the latter goes further upstream into regions of lower velocities, it weakens and vanishes, and the separation point moves downstream to the trailing edge.

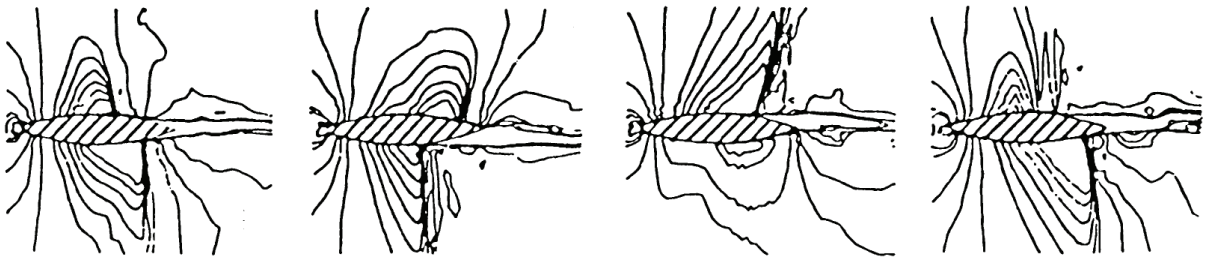

Figure 2.23: Mach contours around the circular-arc airfoil ($M_\infty = 0.754$) (from Ref. [43]).

Inviscid computations were also performed at $M_\infty = 0.754$ and resulted in a steady flow, thus revealing that the flow unsteadiness resulted from viscous effects. An additional Navier-Stokes simulation considering only half airfoil also led to steady state. Therefore, Levy concluded that besides the solid boundary that favored flow reattachment the half domain eliminated the communication of pressure waves across the airfoil. Moreover, both experimental and numerical tests revealed that a one-quarter-chord trailing edge splitter plate was sufficient to cease the flow unsteadiness. For the strong shock-wave case at $M_\infty = 0.783$ with a large region of separation, good agreement with experimental data for the mean pressure distribution upstream the shock was obtained. However, the shock location was predicted far downstream and large differences were found on the

rear part of the airfoil. Again, the results were attributed to inappropriate modeling of separation.

Seegmiller et al. [24] used the same algebraic model employed in Ref. [43] to investigate the unsteady periodic flow over the circular-arc airfoil at $M_\infty = 0.76$ and Reynolds $11{\times}10^6$. Time histories of the surface pressure at several locations revealed the numerical method to reproduce the essential flow features, with the wave forms comparing favorably with the experiments and the main frequency about 20% lower than the experimental value. As expected, the flow over the upper and lower surfaces was 180° out of phase. The magnitude of the pressure fluctuations in the separation region was two times larger than that measured in the experiments, which was consistent with an overprediction observed in the pressure recovery downstream the shock. The simulations showed that the shock formed near the trailing edge and started moving upstream. During the motion, the flow separated, reattaching near the trailing edge. As the shock continued moving upstream, a large-scale vortex shedding could be observed beyond the trailing edge. According to Seegmiller, the probable mechanism of the unsteady flow depended on a slight asymmetry between the upper and lower surfaces that would have been created either by the numerical code, by the freestream flow angle or during the model generation. Such condition would lead to a rapid development of a large separated region on one side, ranging from the foot of the shock to the trailing edge. The resulting asymmetric wake would then readjust the outer flow, creating a camber effect that would slow down the flow in the separated side while increasing the velocity on the opposite side, thus generating a stronger shock that would cause separation on that side. The period of such oscillation would depend on how much time does the flow take to adapt to the displacement effects, being primarily a function of the Mach number and of the geometry, and less sensitive to the Reynolds number. This explanation would account for the fact that the reduced frequency remained constant when changing the airfoil dimensions during the experiments.

Numerical results for the transonic flow over NASA's circular-arc airfoil at $M_\infty = 0.76$ and Reynolds 11×10^6 were also provided by Marvin et al. [25]. In that paper, the unsteady flow features were well reproduced by the simulations. However, they appeared somewhat later in the buffet period compared to the experiments. Also, the shock wave was more normal, engendering higher pressures behind it, and the shear layer dissipated faster than in the experiments. The reverse flow, reattachment and substantial thickening of the shear layer were qualitatively well reproduced, with the location and extension of the separated region as well as the maximum shear stress being slightly different from the experiments. For a given streamwise station, the velocities before the shock passage upstream were somewhat higher, whereas the subsequent velocity adjustment and the shear stress were in good agreement with the experimental data. Marvin concluded that an algebraic turbulence model developed for steady flows could qualitatively reproduce all features of that unsteady flow. Nonetheless, for a better agreement with the physics observed in the experiments, a model would have to account for the effects of turbulence

production and destruction mechanisms.

Besides the numerical method, the turbulence model is a major source of uncertainties in the numerical simulation of transonic buffet. Barakos and Drikakis [45] assessed several turbulence models against the experimental data of McDevitt and Okuno [30] concerning the buffet boundaries of a NACA 0012 airfoil. The experiments were conducted at $Re = 10^7$ for Mach numbers from 0.7 to 0.85, and incidences varying between 0° and 5°. They tested different classes of turbulence closures including the algebraic Baldwin-Lomax model [46], the one-equation Spalart-Allmaras model [47], two linear low-Reynolds number two-equation k-ε models (that of Launder and Sharma [48] and that of Nagano and Kim [49]) as well as the nonlinear k-ε model of Craft et al. [50] and its k-ω version by Sofialidis and Prinos [51]. In the nonlinear models, the Reynolds stresses were computed by means of a cubic expansion in terms of the strain-rate and rotation tensors as well as of k, ε and μ_t, where both a varying turbulent diffusivity coefficient (function of Ω_{ij} and S_{ij}) and the standard constant $C_\mu = 0.09$ were evaluated. When using a constant C_μ in conjunction with either linear or nonlinear models, the results were inaccurate with the shock-wave position predicted too far downstream and a small separation region. Better results were obtained when using the functional formulation and computations without the nonlinear formulation showed that the improvements were indeed due to the varying C_μ and to the damping functions and that the anisotropic stresses from the nonlinear formulation did not play a significant role. This conclusion was supported by the fact that the Spalart-Allmaras model provided good results comparable to those of the nonlinear models with functional C_μ. The buffet boundary as a function of the Mach number and angle of attack was determined using the various models. In general, buffet onset appeared at incidences higher than in the experiments. The linear k-ε models were unable to predict unsteady solutions for all combinations of M_∞ and α considered.

2.3.3.2 OAT15A test case

Several numerical simulations of transonic buffet have been devoted to the periodic flow over the OAT15A airfoil, which was investigated in the experimental work of Jacquin et al [39]. The aim of these studies is mainly to assess the capabilities of turbulence models in predicting unsteady shock wave/boundary layer interactions. In most cases, the freestream Mach and Reynolds numbers are 0.73 and 3×10^6 respectively and the angle of attack is of 3.5°, which is very close to the buffet onset.

Since the period of the periodic shock-wave motion in transonic buffet is much larger than the near-wall turbulence time scale, URANS appears as an attractive approach due to its relatively low computational cost. Moreover, URANS simulations using standard eddy-viscosity models have been shown to reproduce the main features of transonic buffer over different types of airfoils [45, 52, 53]. In this way, Brunet [54] carried out a study involving different URANS models and numerical schemes. The results showed that this class of

closures is capable of predicting reasonably well the main features of the transonic buffet, despite the fact that some models required an increase in the angle of attack to trigger the buffet. The Spalart-Allmaras model, for example, needed an incidence $\alpha = 4.5°$ to produce a self-sustained shock-wave motion. In the paper by Brunet [55], the SST model and the EARSM model of Shih, Zhu and Lumley [56] (SZL) were used to compute the OAT15A test case. The use of wall functions was also evaluated for both models, merging all grid cells where $y^+ < 50$ for the steady flow at $\alpha = 2.5°$. The solver employed a second-order central scheme with artificial dissipation for the Navier-Stokes equations, whereas the turbulence models equations were treated with a second-order Roe upwind scheme with TVD correction. For preliminary computations at 2.5° incidence (with no shock-wave motion), the mean pressure coefficient distributions showed that the SST model predicted better the position of the shock wave compared to the SZL. For both models, the use of wall functions placed the shock-wave further upstream and closer to the experimental data. Unsteady computations were performed at $\alpha = 3.5°$ and $\alpha = 4.0°$ adopting very small time steps ($\Delta t = 1 \times 10^{-3} c/U$ with wall functions and 2×10^{-4} without them). Sinuous-like shock-wave motions were obtained in all cases, with the SZL model exhibiting larger amplitudes and more downstream-located shocks compared to the SST model. Nevertheless, in the unsteady computations, the mean shock positions appeared further downstream when using wall functions, contrary to the steady case. The SST model with wall functions described well the mean wall pressure in the shock motion region, though the pressure of the supersonic plateau was a bit overestimated. For all models, the pressure fluctuations over the airfoil were slightly underestimated at 3.5° and overestimated at 4.0°, and power spectral densities of the signals indicated a main frequency of about 76 Hz (or a reduced frequency $r \approx 0.456$).

Thiery and Coustols [57] investigated the influence of the test-section walls in the OAT15A test case. First, several URANS models were tested in two dimensions in free air and in a confined domain which accounted for the upper and lower adaptive walls of the wind tunnel treated as viscous walls, as sketched in figure 2.24.

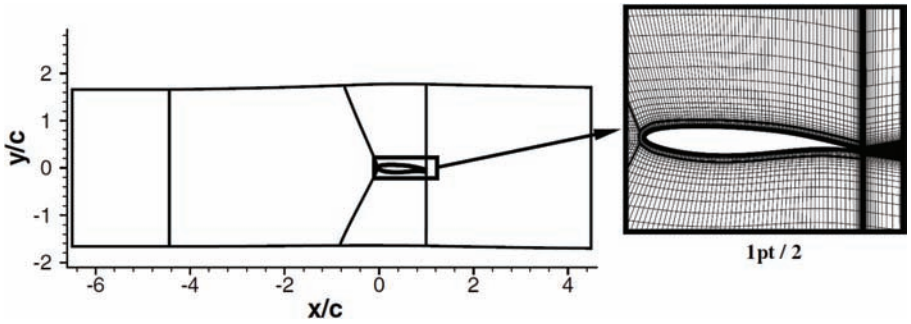

Figure 2.24: Confined domain and grid detail for the OAT15A airfoil (from Ref. [57]).

Simulations were run at the experimental angle of attack of 3.5° with the Spalart-Allmaras model, the Baseline and SST models of Menter and the k-kL model of Daris and Bézard [58]. The solver used the Jameson scheme for the mean flow and a second-order Roe

scheme with anisotropic correction for the turbulence equations. The physical time step adopted yielded about 300 steps per buffet cycle ($\Delta t \approx 5\times10^{-2}c/U$) and the flow properties were averaged during a period of 5 cycles. In free air, the Spalart-Allmaras model resulted in steady flow whereas by considering the tunnel upper and lower walls the self-sustained shock motion was obtained for that model. The SST and the k-kL models were capable of predicting buffet in both configurations, however the lift oscillations amplitudes increased by a factor of 2-2.5 when the walls were considered. The computed frequencies were slightly higher than the experimental one in free air (71-78 Hz or r = 0.43-0.47), decreasing by about 3 Hz in the confined domain whatever the model. The Baseline model led to steady results independent of the boundary conditions used. The mean pressure coefficient distributions revealed that the main differences from the experimental profile were in the region of shock motion. The prediction of pressure recovery behind that region improved when the upper and lower walls were considered. Concerning the RMS pressure, the fluctuations were well reproduced by the SST model, though slightly underestimated all over the upper surface. The k-kL model overestimated the pressure fluctuations, predicting a wider region of shock-wave motion. As for the lift coefficient, in both models, the two-dimensional confined domain was responsible for an increase in the fluctuations (see figure 2.25 for the SST). The Spalart-Allmaras model showed the best RMS distribution though the mean shock was located far too downstream. For the SST model in free air, unsteady velocity profiles were in good agreement compared with experimental phase-averaged ones at different phases of the flow. For all the models, the velocity profiles degraded for the confined domain. A three-dimensional simulation considering the whole wind tunnel was then performed for the SST model, which exhibited the best overall results. The grid was obtained by reproducing the two-dimensional confined domain grid in the spanwise direction, and the side walls were also treated with the no-slip condition. The amplitude of the lift oscillations and the frequency remained almost unchanged compared to the free air computation as shown on the upper left corner of figure 2.25. The figure also reveals that the pressure RMS distribution was very similar to that of free air as well, as if accounting for the third direction balanced the increase on the fluctuations created when considering only the upper and lower walls. The comparison of velocity profiles led to the same conclusion, being the free air profiles even closer to the experimental data. The major conclusion of the paper was that the modeling of the tunnel walls should not be essential to assess the capabilities of turbulence models in predicting the transonic buffet flow over OAT15A airfoil.

In the work by Deck [4], a zonal Detached-Eddy Simulation (ZDES) was employed to predict the transonic buffet over the OAT15A airfoil. That was one of the first attempts to apply DES-like methods to flows featuring thin-layer separation [4]. The results were compared with URANS and standard DES simulations, all three approaches based on the Spalart-Allmaras model. The motivation for the ZDES method is to eliminate the need in standard DES of having a grid spacing in the tangential direction larger than the boundary layer thickness in order to avoid grid-induced separation and/or the underes-

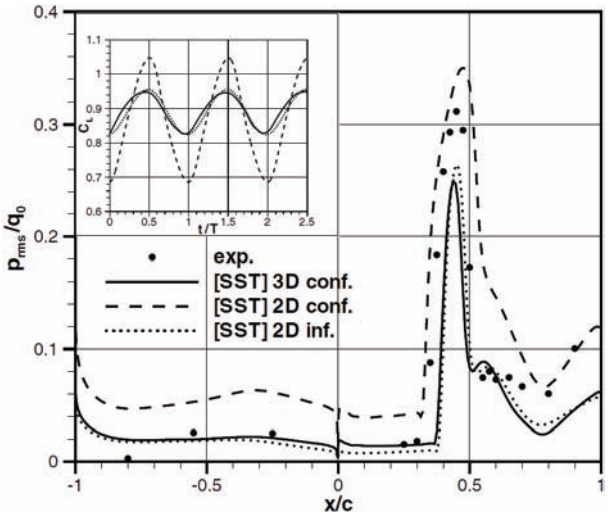

Figure 2.25: Lift evolution and RMS pressure for the OAT15A airfoil (from Ref. [57]).

timation of the skin-friction. The strategy was to force the attached boundary layer and the shock wave/boundary layer interaction to be treated in RANS by means of explicitly defined RANS and LES zones. This was reached by overriding the DES limiter so that the boundary layer separation depended only on the RANS model behavior. The approach did not reconstruct the turbulent fluctuations in the RANS/LES interfaces. In LES regions, the filter adopted was the cubic root $\Delta = (\Delta_i \Delta_j \Delta_k)^{1/3}$. Since the C_{DES} constant had the standard value of 0.65, this filter reduces the eddy viscosity compared to the standard DES method. Moreover, all near-wall functions of the SA models were removed in LES mode regions. The three-dimensional grid used in the computations was based on a planar grid of about 110.000 cells, which was extruded in the spanwise direction throughout a distance of 0.26 chord divided in 41 cells of equal length in order to keep $\Delta_i \approx \Delta k$. The airfoil span was defined based on an analogy with the flow over a backward-facing step, and is supposed to be sufficiently long to resolve the largest wave lengths in the spanwise direction. The solver used a second-order modified AUSM+ upwind scheme for the convective fluxes and central-differencing for the viscous ones, and time integration was performed by a second-order implicit formulation. The ZDES was performed only on the upper surface and in the wake, with all other regions (where the flow is essentially two-dimensional) treated in two-dimensional RANS. The time step adopted was $\Delta t = 5 \times 10^{-7}$ s (about $5 \times 10^{-4} c/U$).

The Spalart-Allmaras model led to steady state at the experimental angle of attack of 3.5° and required an increase in the incidence to 4.5° in order to give a self-sustained shock-wave motion. This result agrees with the conclusions of Refs. [54, 57]. For the standard DES, an angle of 4° was needed to yield unsteadiness, however with no shock motion. The ZDES was the only approach capable of predicting buffet at the experimental angle of attack. The mean pressure coefficient distribution was overestimated over almost all the upper surface, with the shock-wave motion region located further upstream compared to

the experiments (see figure 2.26). The pressure in the trailing edge region was lower than in the experiments, indicating an earlier an larger separation zone. The shock excursion predicted by the ZDES was narrower than in the tests, and the fluctuations of pressure and velocity in this region were overestimated. An iso-surface for a positive value of the Q-criterion obtained with the ZDES is given in figure 1.3. It shows the evolution of two-dimensional structures in the shear layer that impact the trailing edge region and break down into smaller three-dimensional eddies.

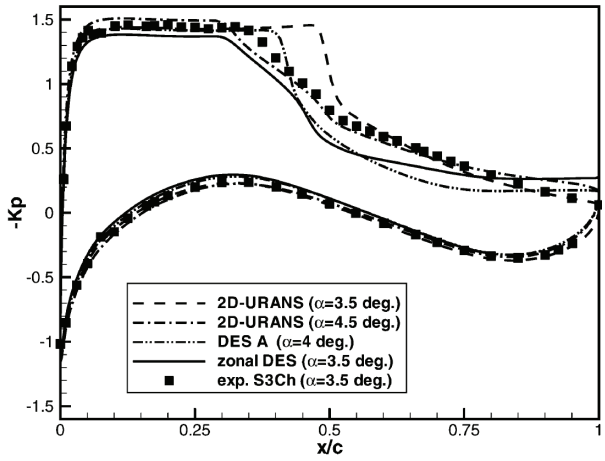

Figure 2.26: Mean pressure distributions over the OAT15A (from Deck [4]).

Due to the short duration of the computations, a parametric auto-regressive model was used to compute power spectral densities of pressure signals. Compared to URANS, ZDES spectra were closer to the experimental ones particularly at higher frequencies. The analysis of wave propagation phenomena based on the ZDES results evidenced the generation of upstream moving waves in the flowfield due to the interaction of large-scale structures of the shear layer with the sharp trailing edge. The results strongly supported the feedback mechanism proposed by Lee [19], giving a frequency of 73 Hz (about 5% error) despite all inaccuracies in computing the wave velocities and the mean shock position.

Garnier [59] tested two RANS-LES strategies in the prediction of the OAT15A flow. The first performed pure LES on the wing upper surface and in the wake, while most of the lower surface and the irrotational region far from the body were treated by two-dimensional RANS. The aft part of the lower surface close to the trailing edge was computed in three-dimensional RANS. Following this methodology, the entire boundary layer and particularly its interaction with the shock wave was treated in LES. In the second strategy, the LES zones were replaced by LES-mode regions in the framework of a zonal DES, using the Spalart-Allmaras model as subgrid-scale model. In both methodologies, the RANS regions were also computed using this model. The solver was second-order accurate in space and time, with the convective fluxes based on a modified Roe scheme. The physical time step adopted was $\Delta t = 3 \times 10^{-7}$ s (or $2 \times 10^{-4} c/U$), which is slightly smaller than that used in the ZDES in Ref. [4]. Despite the many two-dimensional RANS

areas defined, the computational costs of the simulations remained high. Therefore, two grids of small span were used, the first having a length of only 3.65% of chord in the spanwinse direction (grid A) and the second 7.30% of chord, giving 41.6 million cells (grid B). In the latter, two LES were carried out to evaluate the effect of numerical dissipation, as well as the ZDES. After a transient phase of two periods, the LES on the smaller grid (LES A) ran for one period of buffet, whereas the duration of the corresponding computation on the finer grid (LES B1) was equal to seven periods. The LES with reduced dissipation (LES B3) and the ZDES where computed upon only one buffet period. The mean pressure coefficient distributions are given in figure 2.27(a). The LES resulted in a region of shock motion located 7% of chord further downstream compared to the experimental data. By reducing the dissipation, the shock position was improved, what revealed the high influence of numerical dissipation. The ZDES predicted a much better shock location though the wall pressure was underestimated in the aft part of the motion range. The short duration of the simulation was pointed out as a possible reason for the discrepancies observed. In general, the pressure fluctuations were overestimated on the aft part shock motion and downstream the shock region for all models. The simulations on the longer span resulted in lower fluctuation levels near the trailing edge. This was attributed to two-dimensional structures of less intensity, as they were permitted to better develop three-dimensional modes. The LES velocity profiles were in good agreement with LDV data both up- and downstream the shock wave, exhibiting considerable differences from the second LES and ZDES profiles. This evidenced that the effect of numerical dissipation can be even more important than that of turbulence model. Unsteady data showed that the pressure oscillations around the airfoil were overestimated in all cases. The same behavior was found for the velocity fluctuations, which were particularly exaggerated in the wake region. Power spectral density analyzes using an auto-regressive model indicated a main frequency around 72 Hz for the LES, while that of the ZDES was estimated around 80 Hz. Finally, the LES was shown to be more periodic than the experiments since more harmonics were present in the spectra. Figure 2.27(b) shows an instantaneous iso-surface of the Q-criterion colored by the longitudinal velocity for the main LES computation.

Complex three-dimensional unsteady shock wave/boundary layer interactions in transonic flow have been investigated in few works. Brunet [55] studied the simplified configuration of a 24°-swept wing with the OAT15A profile at $M_\infty = 0.8$ and $Re = 6 \times 10^6$. Two sets of computations were performed, one considering infinite swept wing hypothesis and another for a wall-to-wall configuration with slip lateral conditions. For the later, a twist distribution was applied to the wing in order to keep a constant lift along the span as done in the experiments, which detected a small-amplitude shock-surface oscillation at a reduced frequency of $r = 2\pi fc/U \approx 0.35$ (or about 29 Hz in the experiments). The plane grid was the same used for the purely two-dimensional buffet simulations of the OAT15A airfoil [55], as well as the wall functions employed with the EARSM model of Shih, Zhu and Lumley [56]. Preliminary computations of the steady flow at 2.0° showed

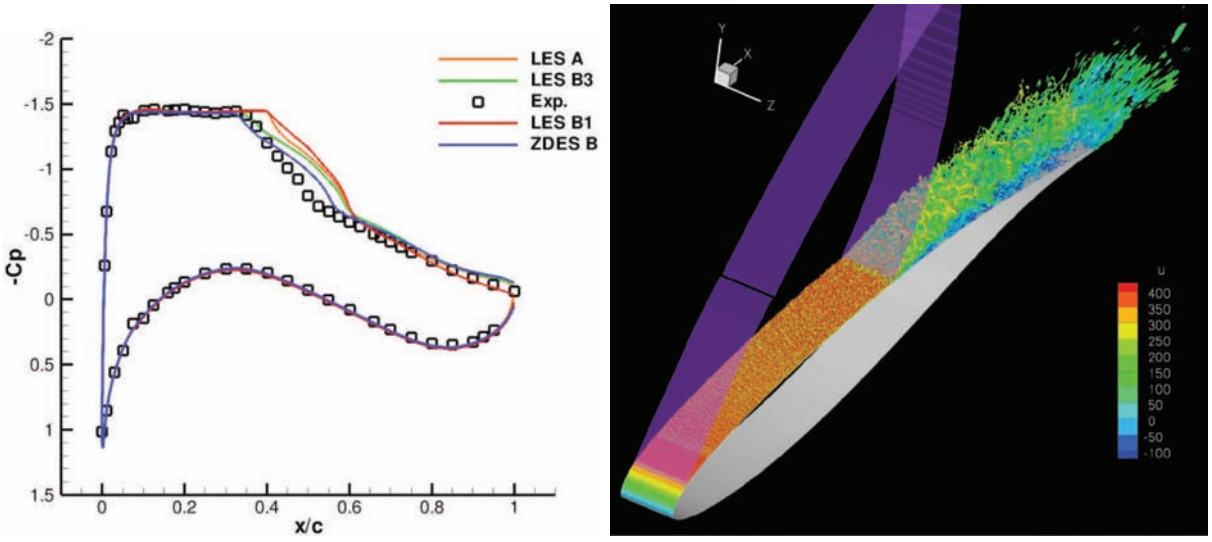

(a) Mean pressure coefficient distribution

(b) Iso-surface of the Q-criterion for the LES

Figure 2.27: LES and ZDES studies of the OAT15A buffet (from Ref. [59]).

a shock wave located too far downstream compared to the experiments, like in the two-dimensional case. Furthermore, wind-tunnel effects were evidenced by the bad agreement between numerical and experimental pressure coefficient distributions, which showed the supersonic region and the lower surface pressure diverging from the reference data. Time-accurate computations at 3.5° with a non-dimensional time step of $\Delta t\, U/c = 1.1{\times}10^{-3}$ for the infinite wing produced exaggerated unsteadiness at a frequency of 34 Hz (about 17% higher than the measured value), and did not reproduce the qualitative features of the flow, clearly showing the relevance of the three-dimensional effects created by the actual tunnel configuration. The wall-to-wall solution was basically a steady flow, with initial buffet oscillations being rapidly damped until a final solution with a very small fluctuation of the lift coefficient is reached. Compared with the two-dimensional buffet case, for which reasonable agreement was found using the same modeling approach, the results give some idea on how complex the simulation of unsteady transonic shock wave/boundary layer interactions can become when the geometry is really three-dimensional.

Chapter 3

Theory and numerical aspects

Contents

3.1 Governing equations of fluid dynamics

Fluid motion is governed by three fundamental laws: conservation of mass, of momentum and of energy. These principles can be expressed through 'conservation laws', which describe the evolution of the conserved quantities in a given domain by means of transport equations. In the governing equations of fluid dynamics the flowfield is treated as a continuous medium. This means that the mean free path of the fluid molecules is assumed to be very small compared to the length scale characteristic of the problem (e.g., the chord of an airfoil) so that the interaction between the fluid molecules is much more important than their individual motion. Therefore, the whole system can be investigated using continuum mechanics imagining a fluid particle a as very large number of fluid molecules within a small volume. All flow properties (as velocity, pressure, temperature, viscosity, etc.) are in fact mean properties which reflect the statistical motion of the fluid molecules at each point of the flowfield.

3.1.1 General transport equation

Assuming that ϕ is a scalar conserved quantity per unit volume and that V is an arbitrary control volume fixed in space, the conservation law of ϕ states that the amount of this quantity inside V can vary as a result of its net flux across the surface S enclosing V and due to volume and surface sources of ϕ only. This law can be formalized in integral form as

$$\frac{\partial}{\partial t}\int_V \phi dV = -\int_S \left(\vec{F}_C \cdot \vec{n}\right) dS - \int_S \left(\vec{F}_D \cdot \vec{n}\right) dS + \int_V Q_V dV + \int_S \left(\vec{Q}_S \cdot \vec{n}\right) dS. \quad (3.1)$$

The term on the left-hand side of equation 3.1 is the time variation of the total amount of ϕ inside V. The flux of ϕ across the volume boundaries is usually split into two components of different physical nature. $\vec{F}_C$ is the 'convective flux', which corresponds to the time rate of ϕ crossing the surface S per unit surface. Convective fluxes are directional, being proportional to and aligned with the local flow velocity $\vec{v} = [u, v, w]^T$ and are given by $\vec{F}_C = \phi\vec{v}$. The second contribution, $\vec{F}_D$, is called 'diffusive flux' and is proportional and opposite to the gradient of ϕ. It is generalized by the 'law of Flick'

$$\vec{F}_D = -\kappa\rho\vec{\nabla}\left(\frac{\phi}{\rho}\right), \quad (3.2)$$

where κ is a diffusivity coefficient. The physical mechanism of diffusion is related to molecular agitation and can have a net effect even in a fluid at rest if the distribution of ϕ is inhomogeneous. The minus signs in front of the fluxes are due to the fact that the surface normal vector $\vec{n}$ is considered positive when pointing outwards (i.e., the dot products are negative when ϕ enters the control volume). Q_V and $\vec{Q}_S$ are the volume and

surface sources, respectively. The resulting expression is a convection-diffusion equation in integral form, which allows the fluxes to be discontinuous (as in the case of shock-waves). Moreover, in the absence of volume forces, the variation of the conserved variable inside the control volume depends only on the net flux of ϕ across the boundaries.

A local differential form of the conservation law can be easily derived from the integral form. Using the divergence theorem (Gauss' theorem), the surface integrals in equation 3.1 can be replaced by volume integrals of the divergences of the fluxes and surface sources. Also, assuming that the control volume is fixed in space, the time derivative on the left-hand side of the equation can be placed inside the integral (Reynolds' transport theorem). Finally, since the integral form is written for an arbitrary control volume, the volume integrals can be dropped, yielding

$$\frac{\partial \phi}{\partial t} = -\vec{\nabla} \cdot \vec{F}_C - \vec{\nabla} \cdot \vec{F}_D + Q_V + \vec{\nabla} \cdot \vec{Q}_S, \tag{3.3}$$

which is valid at any point in the flowfield and requires the fluxes to be continuously differentiable (which is not always the case). It shows that surface sources are mathematically equivalent to fluxes and may be regarded in the same way. Moreover, if an equation is in conservative form, all the space derivative terms can be grouped as a divergence operator [60]. Substituting the expressions obtained for the fluxes and rearranging the terms, one obtains

$$\frac{\partial \phi}{\partial t} = -\vec{\nabla} \cdot (\phi \vec{v}) + \vec{\nabla} \cdot \left[\kappa \rho \vec{\nabla} \left(\frac{\phi}{\rho} \right) \right] + Q_V + \vec{\nabla} \cdot \vec{Q}_S. \tag{3.4}$$

In general, convective fluxes are non linear and yield first-order space derivatives while diffusive fluxes generate second-order ones. In the case where the conserved quantity is a vector, each component of $\vec{\phi}$ can be regarded as a scalar quantity and the above equations can be applied. Alternatively, the equations written for a scalar property can be slightly modified, replacing the fluxes and surface sources by tensors and the volume source by a vector. Hence, the integral conservation equation for a vector reads

$$\frac{\partial}{\partial t} \int_V \vec{\phi} dV = -\int_S \left(\bar{\bar{F}}_C \cdot \vec{n} \right) dS - \int_S \left(\bar{\bar{F}}_D \cdot \vec{n} \right) dS + \int_V \vec{Q}_V dV + \int_S \left(\bar{\bar{Q}}_S \cdot \vec{n} \right) dS. \tag{3.5}$$

In differential form, equation 3.5 becomes

$$\frac{\partial \vec{\phi}}{\partial t} = -\vec{\nabla} \cdot \bar{\bar{F}}_C - \vec{\nabla} \cdot \bar{\bar{F}}_D + \vec{Q}_V + \vec{\nabla} \cdot \bar{\bar{Q}}_S. \tag{3.6}$$

Using tensorial notation (for the sake of simplicity), the convective and diffusive fluxes are given by

$$(F_C)_{ij} = \phi_i u_j, \qquad (F_D)_{ij} = -\kappa \rho \frac{\partial}{\partial x_j} \left(\frac{\phi_i}{\rho} \right). \tag{3.7}$$

3.1.2 The Navier-Stokes equations

In this section, the three fundamental conservation laws that describe fluid motion are derived, namely the continuity equation, the momentum equation and the energy equation. For viscous flows, the resulting set of equations is commonly known as the 'Navier-Stokes equations'.

3.1.2.1 Continuity equation

The principle of conservation of mass in a fluid is expressed through the 'continuity equation', which states that mass cannot be created nor destroyed in the system. The transported quantity is the fluid density ρ, which is a scalar quantity and has units of mass per unity volume. The continuity equation does not present a diffusive flux term since there is no mass diffusion in a fluid at rest. By replacing ϕ by ρ in equation 3.1 and suppressing all source terms, the integral formulation of the continuity equation is obtained

$$\frac{\partial}{\partial t}\int_V \rho dV + \int_S \rho\left(\vec{v}\cdot\vec{n}\right)dS = 0 \tag{3.8}$$

The term in the left-hand side of equation 3.8 represents the time rate of change of mass inside a given control volume and the surface integral on the right side is the total mass flow across its boundaries. For the latter, negative values mean a net flux entering the control volume while positive ones correspond to an outflow. Applying Gauss' and Reynolds' theorems, the continuity equation written in differential form reads

$$\frac{\partial \rho}{\partial t} + \vec{\nabla}\cdot(\rho\vec{v}) = 0 \tag{3.9}$$

For incompressible flows, ρ is constant and equation 3.9 reduces to $\vec{\nabla}\cdot(\rho\vec{v}) = 0$.

3.1.2.2 Momentum equation

Newton's second law states that the variation of the momentum of a body is equal to the net force acting on it. By applying this fundamental principle to a fluid, one obtains the momentum equation, which expresses the conservation of momentum in the fluid system. Since the momentum of a infinitesimally small fluid element of volume dV is defined as $\rho\vec{v}dV$, the transported variable in the momentum equation is the momentum per unit volume $\rho\vec{v}$, which is a vector quantity. Alternatively, the conservation of momentum can be expressed by means of three separated transport equations for the individual components of momentum ρu, ρv and ρw. As the continuity equation, the momentum equation has no diffusive flux since, by definition, the velocity (and thus the momentum) is zero in a fluid at rest. Hence, equation 3.5 applied for the transport of momentum

yields

$$\frac{\partial}{\partial t}\int_V \rho\vec{v}dV + \int_S \rho\vec{v}\,(\vec{v}\cdot\vec{n})\,dS = \int_V \vec{Q}_V dV + \int_S \left(\bar{\bar{Q}}_S\cdot\vec{n}\right)dS, \tag{3.10}$$

where the volume sources $\vec{Q}_V$ represent all existing body forces per unit volume, which act over dV and are also called external or volume forces (e.g., Coriolis, gravitational, buoyancy, centrifugal and electromagnetic forces). The surface sources $\bar{\bar{Q}}_S$ represent the second kind of forces that act on a fluid element: the surface (or internal) forces. In this group, there are the static pressure and the viscous stresses, which have a net effect only on the boundary of the volume. The pressure p exerted by the surroundings acts in the direction normal to S, pointing inwards the fluid element. Therefore, the surface sources can be computed as $-p\bar{\bar{I}}+\bar{\bar{\sigma}}$, where $\bar{\bar{I}}$ is the unit tensor and $\bar{\bar{\sigma}}$ is the viscous stress tensor. In aerodynamics, the effect of the gravitational force on the fluid elements can be neglected and other volume sources are usually not present. Hence, the momentum equation becomes

$$\frac{\partial}{\partial t}\int_V \rho\vec{v}dV + \int_S \rho\vec{v}\,(\vec{v}\cdot\vec{n})\,dS = -\int_S p\left(\bar{\bar{I}}\cdot\vec{n}\right)dS + \int_S (\bar{\bar{\sigma}}\cdot\vec{n})\,dS, \tag{3.11}$$

or in differential form

$$\frac{\partial\rho\vec{v}}{\partial t} + \vec{\nabla}\cdot(\rho\vec{v}\times\vec{v}) = -\vec{\nabla}p + \vec{\nabla}\cdot\bar{\bar{\sigma}}. \tag{3.12}$$

Since air behaves as a Newtonian fluid, the shear stresses are proportional to the velocity gradients. Using tensorial notation, the general form of the viscous stress tensor σ_{ij} reads

$$\sigma_{ij} = \mu\left(\frac{\partial u_j}{\partial x_i} + \frac{\partial u_i}{\partial x_j}\right) + \lambda\frac{\partial u_k}{\partial x_k}\delta_{ij}, \tag{3.13}$$

where the first index in the subscript indicates the direction normal to the plane on which the stress is acting while the second one gives its direction. If $i = j$ the component is a 'normal stress' and otherwise, a 'shear stress'. Shear stresses are generated by the friction resulting from the relative motion of a body immersed in a fluid or of different fluid layers. In equation 3.13, μ is the dynamic viscosity and λ is the second viscosity of the fluid. A kinematic viscosity can also be defined as $\nu = \mu/\rho$. According to Stoke's hypothesis for a Newtonian fluid in local thermodynamic equilibrium [60]

$$\lambda + \frac{2}{3}\mu = 0. \tag{3.14}$$

This relation is called 'bulk viscosity' and is a property of the fluid. It is responsible for the energy dissipation in a fluid of smooth temperature distribution submitted to expansion or compression at a finite rate [61]. So far, there is no experimental evidence that equation 3.14 does not hold except for extremely high temperatures or pressures

[62]. Using relation 3.14, equation 3.13 becomes

$$\sigma_{ij} = \mu \left(\frac{\partial u_j}{\partial x_i} + \frac{\partial u_i}{\partial x_j} \right) - \frac{2\mu}{3} \frac{\partial u_k}{\partial x_k} \delta_{ij}. \tag{3.15}$$

Although the viscous stresses were derived as being surface sources, they play the role of diffusive fluxes of momentum (thus requiring fluid motion), with the dynamic viscosity acting as the diffusion coefficient.

3.1.2.3 Energy equation

In fluid dynamics, the conservation law for energy is obtained from the application of the first law of thermodynamics to a control volume. It expresses the fact that the time variation of the total energy inside a control volume is obtained from the balance between the work of the external forces acting on the volume and the net heat flux into it. In the energy equation, the transported quantity is the total energy per unit volume ρE, where E is the total energy per unit mass. It is defined as the sum of the internal energy per unit mass e (a state variable) and the kinetic energy per unit mass $|\vec{v}|^2/2$. The transport equation features a diffusive flux term which depends only on the gradient of e since, by definition, $\vec{v} = 0$ at rest. It accounts for the effects of thermal conduction related to molecular agitation and is given by $\vec{F}_D = -\gamma\rho\kappa\vec{\nabla}e$, where γ is the ratio of specific heat coefficients, $\gamma = c_p/c_v$. Since the internal energy can be expressed in terms of the static temperature T by $e = c_v T$, heat diffusion is more usually described using Fourrier's law

$$\vec{F}_D = -\gamma\rho\kappa\vec{\nabla}e = -k\vec{\nabla}T, \tag{3.16}$$

where k is the thermal conductivity coefficient ($k = c_p\rho\kappa$) and the negative sign accounts for the fact that heat is transferred from high- towards low-temperature regions.

Surface sources contribute to the energy equation through the work done by the pressure and viscous stresses (both normal and shear parts) acting on the boundaries of the fluid element $\vec{Q}_S = -p\vec{v} + (\bar{\bar{\sigma}} \cdot \vec{v})$. Therefore, neglecting the work done by body forces as well as that of internal energy sources (e.g., radiation, chemical reactions, etc.), the integral form of the energy equation reads

$$\frac{\partial}{\partial t} \int_V \rho E dV + \int_S \rho E \left(\vec{v} \cdot \vec{n} \right) dS = - \int_S p \left(\vec{v} \cdot \vec{n} \right) dS + \int_S (\bar{\bar{\sigma}} \cdot \vec{v}) \cdot \vec{n} dS + \int_S k \left(\vec{\nabla} T \cdot \vec{n} \right) dS, \tag{3.17}$$

which is also frequently written in terms of the total enthalpy

$$H = h + \frac{|\vec{v}|^2}{2} = E + \frac{p}{\rho}, \tag{3.18}$$

where h is the enthalpy per unit mass. This yields

$$\frac{\partial}{\partial t}\int_V \rho E dV + \int_S \rho H\left(\vec{v}\cdot\vec{n}\right) dS = \int_S \left[\left(\bar{\bar{\sigma}}\cdot\vec{v}\right)\cdot\vec{n}\right] dS + \int_S k\left(\vec{\nabla}T\cdot\vec{n}\right) dS. \tag{3.19}$$

In differential form, equation 3.17 can be rewritten as

$$\frac{\partial \rho E}{\partial t} + \vec{\nabla}\cdot\rho\vec{v}E = -\vec{\nabla}\cdot p\vec{v} + \vec{\nabla}\cdot\left(\bar{\bar{\sigma}}\cdot\vec{v}\right) + \vec{\nabla}\cdot\left(k\vec{\nabla}T\right). \tag{3.20}$$

3.1.2.4 Additional relations

In order to close the system of the Navier-Stokes equations, additional relations between the flowfield variables are needed. In aerodynamics, the air is usually modeled as a perfect gas and, therefore, a thermodynamic relation between the state variables p, ρ and T can be obtained by means of the equation of state

$$p = \rho R T, \tag{3.21}$$

where $R = c_p - c_v$ is the gas constant per unit mass (for a perfect gas, c_p, c_v and thus γ and R are constants). In compressible viscous flow, heating due to high velocity gradients is responsible for variations in the fluid viscosity. To account for such effect, a common practice in aerodynamics is to adopt Sutherland's law [63], which expresses the dynamic viscosity μ of an ideal gas as a function of temperature only as

$$\frac{\mu}{\mu_{\text{ref}}} = \left(\frac{T}{T_{\text{ref}}}\right)^{3/2}\frac{T_{\text{ref}}+S}{T+S}. \tag{3.22}$$

μ_{ref} is a reference viscosity corresponding to the reference temperature T_{ref}, and the constant S is the Sutherland's parameter (or Sutherland's temperature). Values commonly used for air are $\mu_{\text{ref}} = 1.716\times10^{-5}$ Pa.s, $T_{\text{ref}} = 273.15$ K and $S = 110.4$ K. Sutherland's Law gives reasonably good results at transonic and supersonic speeds. For hypersonic flows, however, more elaborated formulas are usually employed.

The thermal conductivity coefficient k varies with temperature in a similar way to μ. For this reason, the Reynolds' analogy is frequently used to compute k, reading

$$k = c_p\frac{\mu}{\text{Pr}}. \tag{3.23}$$

In the above equation, Pr is the Prandtl number, which is usually taken as 0.72 for air.

3.1.3 The Reynolds-averaged Navier-Stokes equations

According to 'Morkovin's hypothesis', the effect of density fluctuations on turbulent eddies in wall-bounded flows is insignificant provided that they remain small compared to the mean density [64]. Indeed, this hypothesis is verified up to Mach numbers of about five [62] and, therefore, a common approach in turbulence modeling is to apply 'Reynolds averaging' to the flow variables (otherwise one should use Favre averaging).

In Reynolds averaging, the flow variables are decomposed into two parts: a mean part and a fluctuating part. Using tensorial notation, a velocity component, for instance, is represented as $u_i = \overline{u}_i + u_i'$, where $\overline{u}_i$ is its mean value and u_i' its instantaneous fluctuation. For stationary turbulent flows, $\overline{u}_i$ is normally computed using time-averaging, which is the most common Reynolds-averaging procedure and is appropriate for a large number of engineering problems. Time-averaging can also be used for problems involving very slow mean flow oscillations that are not turbulent in nature [64], as long as the characteristic time scale of such oscillations is much larger than that of turbulence. In this way, the mean velocity is computed as

$$\overline{u}_i = \lim_{T\to\infty} \int_t^{t+T} u_i dt. \tag{3.24}$$

Also, by definition, the average of u_i' is zero. Substituting the flow variables in the Navier-Stokes equations by Reynolds-averaged ones and taking the average, one obtains in differential form

$$\frac{\partial \overline{\rho}}{\partial t} + \frac{\partial}{\partial x_i}\left(\overline{\rho}\,\overline{u}_i\right) = 0, \tag{3.25}$$

$$\frac{\partial}{\partial t}\left(\overline{\rho}\,\overline{u}_i\right) + \frac{\partial}{\partial x_j}\left(\overline{\rho}\,\overline{u}_j\,\overline{u}_i\right) = -\frac{\partial \overline{p}}{\partial x_i} + \frac{\partial}{\partial x_j}\left(\overline{\sigma}_{ij} + \tau_{ij}\right), \tag{3.26}$$

and

$$\frac{\partial}{\partial t}\left(\overline{\rho}\overline{E}\right) + \frac{\partial}{\partial x_j}\left(\overline{\rho}\,\overline{u}_j\overline{E}\right) = -\frac{\partial}{\partial x_j}\left(\overline{p}\,\overline{u}_j\right) + \frac{\partial}{\partial x_j}\left[\left(\overline{\sigma}_{ij} + \tau_{ij}\right)\overline{u}_j\right] + \frac{\partial}{\partial x_j}\left(k\frac{\partial \overline{T}}{\partial x_j} + q_{t_j}\right). \tag{3.27}$$

The only difference between the Reynolds-averaged Navier-Stokes (RANS) equations shown above and the original set of Navier-Stokes equations is the existence of a turbulent stress tensor $\tau_{ij} = -\overline{\rho u_i' u_j'}$ (also called Reynolds stress tensor) and of a turbulent transport of heat q_{t_j}. Both quantities are computed by means of additional equations (the so-called 'turbulence models') which are the subject of chapter 4. From now on in this text, the overbars in the RANS equations will be dropped for the sake of simplicity, and all flow variables should therefore be regarded as averaged quantities.

3.2 Numerical solvers

3.2.1 System of equations

The system of equations to be solved in turbulent flow computations (i.e., the Reynolds-averaged Navier-Stokes equations plus the turbulence model) can be rewritten in the form

$$\frac{\partial}{\partial t}\int_V \vec{W} dV + \int_S \left(\vec{F}_C - \vec{F}_D\right) dS = \int_V \vec{Q}_V dV, \tag{3.28}$$

or in differential form:

$$\frac{\partial \vec{W}}{\partial t} + \vec{\nabla}\cdot\left(\vec{F}_C - \vec{F}_D\right) = \vec{Q}_V. \tag{3.29}$$

In the above equations, $\vec{W}$ is the state vector and $\vec{F}_C$ and $\vec{F}_D$ are the convective and diffusive (or viscous) fluxes, respectively. These are defined as

$$\vec{W} = \begin{bmatrix} \rho \\ \rho u \\ \rho v \\ \rho w \\ \rho E \\ \dots \end{bmatrix}, \qquad \vec{F}_C = \begin{bmatrix} \rho\left(n_x u + n_y v + n_z w\right) \\ \rho u\left(n_x u + n_y v + n_z w\right) + n_x p \\ \rho v\left(n_x u + n_y v + n_z w\right) + n_y p \\ \rho w\left(n_x u + n_y v + n_z w\right) + n_z p \\ \left(\rho E + p\right)\left(n_x u + n_y v + n_z w\right) \\ \dots \end{bmatrix}, \tag{3.30}$$

and

$$\vec{F}_D = \begin{bmatrix} 0 \\ \left(\sigma_{xx} + \tau_{xx}\right) n_x + \left(\sigma_{xy} + \tau_{xy}\right) n_y + \left(\sigma_{xz} + \tau_{xz}\right) n_z \\ \left(\sigma_{yx} + \tau_{yx}\right) n_x + \left(\sigma_{yy} + \tau_{yy}\right) n_y + \left(\sigma_{yz} + \tau_{yz}\right) n_z \\ \left(\sigma_{zx} + \tau_{zx}\right) n_x + \left(\sigma_{zy} + \tau_{zy}\right) n_y + \left(\sigma_{zz} + \tau_{zz}\right) n_z \\ \Theta_x n_x + \Theta_y n_y + \Theta_z n_z \\ \dots \end{bmatrix}, \tag{3.31}$$

where

$$\begin{aligned} \Theta_x &= u\left(\sigma_{xx} + \tau_{xx}\right) + v\left(\sigma_{xy} + \tau_{xy}\right) + w\left(\sigma_{xz} + \tau_{xz}\right) + k\frac{\partial T}{\partial x} + q_{t_x}, \\ \Theta_y &= u\left(\sigma_{yx} + \tau_{yx}\right) + v\left(\sigma_{yy} + \tau_{yy}\right) + w\left(\sigma_{yz} + \tau_{yz}\right) + k\frac{\partial T}{\partial y} + q_{t_y}, \\ \Theta_z &= u\left(\sigma_{zx} + \tau_{zx}\right) + v\left(\sigma_{zy} + \tau_{zy}\right) + w\left(\sigma_{zz} + \tau_{zz}\right) + k\frac{\partial T}{\partial z} + q_{t_z}, \end{aligned} \tag{3.32}$$

and n_x, n_y and n_z are the components of the normal vector $\vec{n}$. In aerodynamics, the source term $\vec{Q}_V$ is usually taken as zero in the Navier-Stokes equations (but not in the turbulence model equations). In order to close the system, the equation of state (equation 3.21) and Sutherland's law (equation 3.22) are employed. Relations for the turbulent stresses and the turbulent heat flux are provided in chapter 4.

3.2.2 Navier-Stokes Multi Block

The main solver used in this thesis is the Navier-Stokes Multi Block [65] (NSMB), which is developed by a consortium including various European universities, institutes and industrial partners. NSMB employs the finite volume method to solve the Navier-Stokes equations on multi-block structured grids, allowing massive parallel computing. Convective fluxes can be treated by means of central-differencing schemes with adaptive artificial dissipation (scalar or matrix formulations) or upwind schemes. For the latter, a Total Variation Diminishing (TVD) version of Roe's scheme applying the Monotone Upwind Schemes for Conservation Laws (MUSCL) extrapolation is available as well as other schemes as the Advection Upstream Splitting Method (AUSM). Time integration can be performed implicitly using the Lower-Upper Symmetric Gauss-Seidel (LU-SGS) scheme (or the LU-SSOR) or explicitly by means of standard or hybrid Runge-Kutta methods. Besides local time stepping, convergence in steady flow computations can be accelerated using implicit residual smoothing and multigrid. Time accuracy in unsteady simulations can be obtained through the dual time step method and low Mach number flows can be treated with preconditioning. Several classes of turbulence models are available in NSMB including algebraic, linear and nonlinear eddy-viscosity models, different types of Reynolds stress models as well as LES and hybrid RANS-LES approaches.

3.2.3 Presentation of Edge

In the study of a laminar transonic airfoil in chapter 7, a second numerical solver has been used. Edge is a compressible finite volume CFD code developed by the Swedish Defence Research Agency (FOI) since 1997 in collaboration with industrial and academic partners. The code is open source under license agreement, and solves the Euler and Navier-Stokes equations on unstructured grids intending complex geometries and efficient scalable parallel computing. For detailed information about Edge, the reader is referred to [66] and [67]. The code formulation is edge-based using vertex-centered (or node-centered) non-overlapping control volumes. The flow equations are solved on a dual grid computed upon the primary grid given by the user by means of a preprocessor. Figure 3.1 illustrates this process for a simple two-dimensional grid formed by triangular elements.

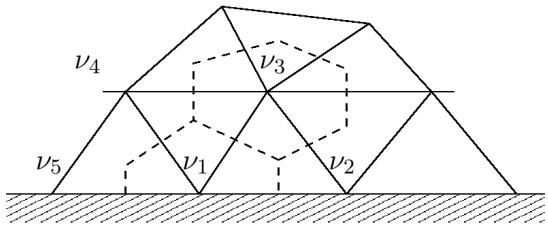

Figure 3.1: Generation of the dual grid (dashed lines) for vertices ν_1 and ν_3 of the primary grid (solid lines) in Edge (from Ref. [66]).

In Edge, the convective fluxes can be discretized using either central or upwind (Roe) schemes. Time integration can be explicit by means of a multistage Runge-Kutta method for steady solutions (allowing local time stepping) using local time stepping or implicit using dual-time stepping for time-accurate solutions. Convergence can be accelerated using multigrid and implicit residual smoothing. In multigrid, several grid levels can be obtained by the agglomeration (fusion) of control volumes in the preprocessor. In unsteady simulations, the acceleration techniques can be applied to the inner loop. The code also features preconditioning for low-Mach number flow problems. For efficient parallel computing, the input grid is split into multiple partitions so as each processor reads a different file and treats a single partition. Different turbulence models are available in Edge ranging from eddy-viscosity closures to LES, including hybrid RANS-LES models.

Chapter 4

Turbulence Models for Aerodynamics

Contents

4.1 The eddy-viscosity assumption

In section 3.1.3, the Reynolds-averaged Navier-Stokes equations were presented and the turbulent stress tensor τ_{ij} and the turbulent heat flux q_{t_j} were introduced. In this thesis, all turbulence models make use of Boussinesq hypothesis [68], which relates the turbulent stresses to the mean-flow velocity gradients by

$$\tau_{ij} = 2\mu_t S_{ij} - \frac{2}{3}\rho k \delta_{ij}, \tag{4.1}$$

where μ_t is a scalar 'eddy viscosity' (also called turbulent viscosity) and S_{ij} is the mean strain-rate tensor

$$S_{ij} = \frac{1}{2}\left(\frac{\partial u_i}{\partial x_j} + \frac{\partial u_j}{\partial x_i}\right) - \frac{1}{3}\frac{\partial u_k}{\partial x_k}\delta_{ij}. \tag{4.2}$$

The Boussinesq hypothesis assumes that the principal axes of the turbulent stress and mean strain-rate tensors are collinear and is unable to capture anisotropy effects of the normal turbulent stresses [69]. In practice, however, equation 4.1 provides accurate results for many engineering applications, including aerodynamic flows. Regarding transonic buffet simulation, Barakos and Drikakis [45] revealed that turbulence models based on the Boussinesq hypothesis can provide results comparable to models accounting for turbulence anisotropy. According to Wilcox [64], some of the applications in which the Boussinesq hypothesis fails are: flows with sudden changes in the mean strain, flows over curved surfaces, flows in rotating fluids and three-dimensional flows.

Based on the concept of eddy viscosity, the turbulent heat flux is then calculated by means of the 'Reynolds analogy':

$$q_{t_j} = -k_t \frac{\partial T}{\partial x_j} = -c_p \frac{\mu_t}{\mathrm{Pr}_t}\frac{\partial T}{\partial x_j}, \tag{4.3}$$

where k_t is the turbulent thermal conductivity coefficient and Pr_t is the turbulent Prandtl number (which for air is 0.9).

4.2 One-equation eddy-viscosity models

4.2.1 Spalart-Allmaras model

4.2.1.1 Fully-turbulent formulation

The Spalart-Allmaras (SA) model [47] is based on a single general transport equation for a modified eddy viscosity variable $\tilde{\nu}$. It was developed for aerodynamic flows based upon empiricism and dimensional analysis, using flow quantities derived from the mean

flow and that exhibit Galilean invariance. The model is local as it does not relate the turbulence length scale to some other flow parameter (e.g., the boundary layer thickness δ). Furthermore, the SA model is 'complete' since the turbulence scales are automatically provided with no need of adjustable functions or coefficients [64] (i.e., the eddy viscosity contains implicitly both the turbulence length and time scales). In its most common formulation assuming fully-turbulent behavior, the non-conservative form of the transport equation for $\tilde{\nu}$ reads

$$\frac{D\tilde{\nu}}{Dt} = c_{b1}\tilde{S}\tilde{\nu} + \frac{1}{\sigma}\frac{\partial}{\partial x_k}\left[(\nu + \tilde{\nu})\frac{\partial \tilde{\nu}}{\partial x_k}\right] + \frac{c_{b2}}{\sigma}\frac{\partial \tilde{\nu}}{\partial x_k}\frac{\partial \tilde{\nu}}{\partial x_k} - c_{w1}f_w\left(\frac{\tilde{\nu}}{d}\right)^2. \tag{4.4}$$

The eddy viscosity is then computed as

$$\nu_t = \tilde{\nu} f_{v1}, \tag{4.5}$$

where f_{v1} is a correction for the buffer and viscous layers, with $\tilde{\nu}$ joining ν_t in the logarithmic layer. This function is given by

$$f_{v1} = \frac{\chi^3}{\chi^3 + c_{v1}^3}, \qquad \text{where} \qquad \chi = \frac{\tilde{\nu}}{\nu}. \tag{4.6}$$

A similar correction is performed for the production term by means of the function f_{v2}, which is present in the quantity $\tilde{S}$:

$$\tilde{S} = S + \frac{\tilde{\nu}}{\kappa^2 d^2} f_{v2}, \qquad \text{where} \qquad f_{v2} = 1 - \frac{\chi}{1 + \chi f_{v1}}. \tag{4.7}$$

In the above equation, d represents the distance to the nearest viscous wall. The quantity S is a scalar measure of the deformation tensor $\partial u_i/\partial x_j$, which was originally chosen in Ref. [47] as the magnitude of the rotation tensor Ω_{ij}:

$$S = \sqrt{2\Omega_{ij}\Omega_{ij}}, \qquad \text{with} \qquad \Omega_{ij} = \frac{1}{2}\left(\frac{\partial u_i}{\partial x_j} - \frac{\partial u_j}{\partial x_i}\right) \tag{4.8}$$

This choice was justified by the fact that, in aerodynamic flows, turbulence mainly emanates from solid boundaries. Some implementations of the SA model use the magnitude of the strain-rate tensor S_{ij} instead.

The wall destruction term in equation 4.4 is non-viscous, depending on the wall distance and on f_w, which is a non-dimensional function that adjusts the skin-friction. It is defined as

$$f_w = g\left(\frac{1 + c_{w3}^6}{g^6 + c_{w3}^6}\right)^{1/6}, \qquad \text{with} \qquad g = r + c_{w2}\left(r^6 - r\right) \qquad \text{and} \qquad r = \frac{\tilde{\nu}}{\tilde{S}\kappa^2 d^2}. \tag{4.9}$$

The quantity r is a near-wall parameter that involves the square of the mixing length $\left(\tilde{\nu}/\tilde{S}\right)^{1/2}$. The closure coefficients of the model are

$$c_{b1} = 0.1355, \qquad c_{b2} = 0.622, \qquad \sigma = 2/3, \qquad \kappa = 0.41,$$
$$c_{w1} = \frac{c_{b1}}{\kappa^2} + \frac{1 + c_{b2}}{\sigma}, \qquad c_{w2} = 0.3, \qquad c_{w3} = 2 \qquad \text{and} \qquad c_{v1} = 7.1. \tag{4.10}$$

The SA model is robust and low-sensitive to the freestream condition of $\tilde{\nu}$. It uses trivial Dirichlet boundary conditions and allows $\tilde{\nu} = 0$ in the freestream, though non-zero values are usually preferred because of numerical issues. Spalart and Rumsey [70] suggest using $\tilde{\nu}_\infty/\nu$ between 3 and 5 in fully-turbulent computations. At solid boundaries, the condition is $\tilde{\nu} = 0$. The above formulation of the SA model can be applied to compressible flows assuming that, in slightly supersonic boundary layers, density variations have only a small influence on turbulence [47].

4.2.1.2 Treatment of laminar regions

For flows where the transition location is previously known, the Spalart-Allmaras model has additional terms to simulate laminarity as well as to ensure a smooth transition to turbulence. Since setting $\tilde{\nu} = 0$ upstream the prescribed transition line can result in convergence problems in Navier-Stokes codes [47], the production term in equation 4.4 is multiplied by $(1 - f_{t2})$, where

$$f_{t2} = c_{t3} e^{-c_{t4}\chi^2}. \tag{4.11}$$

The destruction term is also modified to include f_{t2} in order to balance the budget near the wall, becoming

$$\left(c_{w1} f_w - \frac{c_{b1}}{\kappa^2} f_{t2}\right) \left(\frac{\tilde{\nu}}{d}\right)^2. \tag{4.12}$$

The function f_{t2} has no effect inside turbulent regions and, for this reason, it is usually neglected when fully-turbulent behavior is desired. The values originally recommended in Ref. [71] for the constants c_{t3} and c_{t4} (i.e., $c_{t3} = 1.1$ and $c_{t3} = 2$) were revealed to cause premature transition in some cases [47]. Therefore, Spalart and Allmaras [47] proposed adopting $c_{t3} = 1.2$ and $c_{t3} = 0.5$ instead, which are safer especially for high Reynolds number flows.

A trip term can also be added to the right-hand side of equation 4.4 to obtain a smooth transition near the specified trip location (see Ref. [47] for more details). Nevertheless, this term is rarely used and can be replaced by alternative solutions. When computing laminar regions, the recommended inflow condition is $\tilde{\nu}_\infty/\nu < 0.1$, though $\tilde{\nu}_\infty/\nu \leqslant 0.5$ should be tolerable with the recommended values of c_{t3} and c_{t4} without disturbing the laminar region.

4.2.2 Modified Spalart-Allmaras models

4.2.2.1 Edwards-Chandra model

The paper of Edwards and Chandra [72] proposes a modified version of the Spalart-Allmaras model to fix stability problems related to the original formulation of $\tilde{S}$ (equation 4.7). The solution in the viscous sublayer gains in robustness by redefining this quantity as

$$\tilde{S} = S\left(\frac{1}{\chi} + f_{v1}\right), \qquad \text{where} \qquad S = \left[\left(\frac{\partial u_i}{\partial x_j} + \frac{\partial u_j}{\partial x_i}\right)\frac{\partial u_i}{\partial x_j} - \frac{2}{3}\left(\frac{\partial u_k}{\partial x_k}\right)^2\right]^{\frac{1}{2}}. \tag{4.13}$$

Furthermore, the near-wall parameter becomes

$$r = \frac{\tanh\left[\tilde{\nu}/\left(\tilde{S}\kappa^2 d^2\right)\right]}{\tanh 1.0}. \tag{4.14}$$

According to Edwards and Chandra [72], such modifications result in smooth and rapid convergence while retaining the near-wall accuracy of the original SA model.

4.2.2.2 Strain-adaptive linear Spalart-Allmaras model

Rung et al. [73] proposed a modification to the SA model sensitized to non-equilibrium flows, wich are frequently encountered in aerodynamics. The new closure was named Strain-adaptive linear Spalart-Allmaras (SALSA) model and is based on the following transport equation for $\tilde{\nu}$:

$$\frac{D\tilde{\nu}}{Dt} = \tilde{c}_{b1}\tilde{S}\tilde{\nu} + \frac{\partial}{\partial x_k}\left[\left(\nu + \frac{\tilde{\nu}}{\sigma}\right)\frac{\partial \tilde{\nu}}{\partial x_k}\right] + \frac{c_{b2}}{\sigma}\frac{\partial \tilde{\nu}}{\partial x_k}\frac{\partial \tilde{\nu}}{\partial x_k} - \tilde{c}_{w1} f_w \left(\frac{\tilde{\nu}}{d}\right)^2. \tag{4.15}$$

Also, the following variables are redefined:

$$\tilde{S} = S\left(\frac{1}{\chi} + f_{v1}\right), \qquad r = 1.6\tanh\left[0.7\left(\frac{\Psi}{\tilde{S}}\right)\right] \qquad \text{and} \qquad \Psi = \sqrt{\frac{\rho_0}{\rho}}\left(\frac{\tilde{\nu}}{\kappa^2 d^2}\right). \tag{4.16}$$

The choice of r was inspired by the more robust Edwards-Chandra version of the SA model. Furthermore, the S parameter adopts the magnitude of the strain-rate tensor S_{ij} (see equation 4.2), and is given by

$$S = \sqrt{2S_{ij}S_{ij}}. \tag{4.17}$$

The most important feature of the SALSA model is the modified c_{b1} coefficient, which is

no longer a constant. Instead, it becomes a function of the strain-rate and reads

$$\tilde{c}_{b1} = 0.1355\sqrt{\Gamma}, \qquad \text{where} \qquad \Gamma = \min\left[1.25, \max\left(\gamma, 0.75\right)\right], \qquad \gamma = \max\left(\alpha_1, \alpha_2\right),$$
$$\alpha_1 = \left[1.01\left(\frac{\tilde{\nu}}{\kappa^2 d^2 S}\right)\right]^{0.65} \qquad \text{and} \qquad \alpha_2 = \max\left[0, 1 - \tanh\left(\frac{\chi}{68}\right)\right]^{0.65}. \tag{4.18}$$

By consequence, the constant c_{w1} is replaced by the function $\tilde{c}_{w1} = \tilde{c}_{b1}/\kappa^2 + \left(1 + c_{b2}\right)/\sigma$. The multiplication of c_{b1} by $\sqrt{\Gamma}$ reduces production for excessive strains by means of the argument α_1, which is also related to the destruction term. The α_2 argument is used to correct undesirable wall damping. All other terms and constants are identical to those of the original Spalart-Allmaras model.

In general, the SALSA model gives results similar to those of the Edwards-Chandra model in equilibrium boundary layers and shear layers, producing a small reduction in the skin friction compared to the original SA model [73]. In respect to non-equilibrium flows, Ref. [73] shows improvements in the simulation of a large separation over a wing-body configuration, of a high-incidence airfoil and of a strong shock wave/boundary layer interaction.

4.2.2.3 Secundov's compressibility correction

As suggested by Spalart [74], the behavior of the SA model in compressible mixing layers can be improved by using Secundov's compressibility correction, which is borrowed from the ν_t-92 model [75]. Effects due to the work of compression can be taken into account by adding to the right-hand side of equation 4.4 the term

$$-c_5 \frac{\tilde{\nu}^2}{a^2} \frac{\partial u_i}{\partial x_j} \frac{\partial u_i}{\partial x_j}, \tag{4.19}$$

where a is the local speed of sound and $c_5 = 3.5$ is an empirical constant. This correction acts as a destruction term, lowering the eddy-viscosity levels in turbulent regions of high deformation to account for the reduced spreading rates of compressible shear layers [76], and can be significant in supersonic flows [74].

4.3 Two-equation eddy-viscosity models

4.3.1 Menter's k-ω models

In the early nineties, the k-ω models of Menter [77] represented a significant advance in two-equation eddy-viscosity models for aerodynamics. They were constructed upon an empirical approach and combined the best qualities of Wilcox' k-ω model [78] with those

of a standard k-ε model. The first model was called Baseline model and corrects the k-ω model sensitivity to the freestream condition of ω. The second model is an improved version of the first regarding the prediction of flow separation in strong adverse pressure gradients and was named Shear Stress Transport model.

4.3.1.1 Baseline model

The aim of the Baseline (BSL) model is to provide a robust k-ω closure free from the sensitivity to the freestream conditions exhibited by the original k-ω model as discussed in Ref. [79]. The idea behind it is to mix Wilcox' original model with a high-Reynolds k-ε model to create a closure adaptive to different flow zones. Near the wall in the inner and logarithmic regions of the boundary layer, the BSL model is identical to the original k-ω model since the latter has a better numerical stability and is more accurate than the k-ϵ one in equilibrium adverse pressure gradients and compressible flows. Furthermore, the k-ω model has no damping functions and uses trivial boundary conditions. However, in the outer region of the boundary layer and in free-shear layers, the BSL model gradually switches to the standard k-ε model (transformed into a k-ω formulation) because of the insensitivity of the k-ε formulation to freestream parameters. The transition between the two models is handled by a blending function F_1.

The transport equations of the Baseline model are obtained by multiplying those of the original k-ω model by F_1, whereas the k-ω-transformed equations of the k-ε model are multiplied by $(1 - F_1)$. In the transformation, an additional cross-diffusion term is generated in the ω equation. Then, the two sets of equations are added, resulting in the following conservative transport equations:

$$\frac{D\rho k}{Dt} = \tau_{ij}\frac{\partial u_i}{\partial x_j} - \beta^*\rho\omega k + \frac{\partial}{\partial x_j}\left[\left(\mu + \sigma_k\mu_t\right)\frac{\partial k}{\partial x_j}\right] \tag{4.20}$$

and

$$\frac{D\rho\omega}{Dt} = \frac{\gamma}{\nu_t}\tau_{ij}\frac{\partial u_i}{\partial x_j} - \beta\rho\omega^2 + \frac{\partial}{\partial x_j}\left[\left(\mu + \sigma_\omega\mu_t\right)\frac{\partial \omega}{\partial x_j}\right] + 2\left(1 - F_1\right)\rho\sigma_{\omega 2}\frac{1}{\omega}\frac{\partial k}{\partial x_j}\frac{\partial \omega}{\partial x_j}. \tag{4.21}$$

The blending function is defined as

$$F_1 = \tanh\left(\arg_1^4\right), \tag{4.22}$$

where

$$\arg_1 = \min\left[\max\left(\frac{\sqrt{k}}{0.09\omega d}, \frac{500\nu}{d^2\omega}\right), \frac{4\rho\sigma_{\omega 2}k}{\mathrm{CD}_{k\omega}d^2}\right] \tag{4.23}$$

and $\mathrm{CD}_{k\omega}$ is the cross diffusion

$$\mathrm{CD}_{k\omega} = \max\left(2\rho\sigma_{\omega 2}\frac{1}{\omega}\frac{\partial k}{\partial x_j}\frac{\partial \omega}{\partial x_j}, 10^{-20}\right). \tag{4.24}$$

The eddy viscosity is computed using the standard definition $\nu_t = k/\omega$. The blending function F_1 was designed to be equal to 1 in the viscous and logarithmic layers, resulting in the original k-ω model formulation in the near-wall region. As the wall distance increases, F_1 progressively goes to 0, resulting in the transformed k-ε model far from the walls and in the wake. The first argument in arg_1 is the ratio between the turbulence length scale and the distance to the nearest viscous wall d. The second argument forces F_1 to be 1 in the viscous sublayer whereas the third one ensures that the solution remains insensitive to the freestream. Far from any surface, all arguments vanish.

The Baseline model coefficients are local and are computed upon the constants of the k-ω and transformed k-ε models. For example, an arbitrary coefficient ϕ in the BSL model is calculated by

$$\phi = F_1\phi_1 + (1 - F_1)\,\phi_2, \tag{4.25}$$

where ϕ_1 is the corresponding constant of the k-ω model:

$$\begin{gathered}\sigma_{k1} = 0.5, \qquad \sigma_\omega 1 = 0.5, \qquad \beta_1 = 0.0750, \\ \beta^* = 0.09, \qquad \kappa = 0.41, \qquad \gamma_1 = \beta_1/\beta^* - \sigma_{\omega 1}\kappa^2/\sqrt{\beta^*}\end{gathered} \tag{4.26}$$

and ϕ_2 the equivalent for the k-ε model:

$$\begin{gathered}\sigma_{k2} = 1.0; \qquad \sigma_{\omega 2} = 0.856; \qquad \beta_2 = 0.0828, \\ \beta^* = 0.09, \qquad \kappa = 0.41, \qquad \gamma_2 = \beta_2/\beta^* - \sigma_{\omega 2}\kappa^2/\sqrt{\beta^*}\end{gathered} \tag{4.27}$$

In Ref. [77], the recommended freestream conditions are:

$$\frac{\omega L}{U} = 1\text{–}10 \qquad \text{and} \qquad k = 10^{-(2\text{–}5)}\nu\omega \tag{4.28}$$

where L is the length of the computational domain. At solid boundaries, the for ω is

$$\omega = 10\frac{6\nu}{\beta_1\left(\Delta y_1\right)^2}, \tag{4.29}$$

where Δy_1 is the first-cell height, which for k-ω models should verify $y^+ \leqslant 3$ for a correct representation of the boundary layer [77].

In general, the results obtained with the Baseline model are very similar to those with the original k-ω model with the great advantage of eliminating the undesired freestream dependency.

4.3.1.2 Shear Stress Transport model

Departing from the Baseline model, the Shear-Stress Transport (SST) model is obtained by introducing a modified formulation for the eddy viscosity. Inspired by the Johnson-King algebraic model [80], the SST model improves the prediction of flows featuring strong adverse pressure gradients by creating a 'lag effect' that accounts for the transport of the principal turbulent shear stress $-\rho\overline{u'v'}$ [77]. This is based on the assumption that the principal turbulent shear stress in a boundary layer is proportional to the turbulent kinetic energy k (which is not the case with the standard definition $\nu_t = k/\omega$). According to Menter [77], the ability of an eddy-viscosity model to predict strong pressure gradient flows is ultimately determined by the level of eddy viscosity in the wake region. Therefore, in non-equilibrium adverse pressure gradient flows (where the production of k can become much larger than its dissipation) standard two-equation models usually overpredict the eddy-viscosity levels and consequently the turbulent shear stress. To remedy this problem, the eddy viscosity in the SST model is defined as

$$\nu_t = \frac{a_1 k}{\max\left(a_1\omega, \Omega F_2\right)}, \tag{4.30}$$

where

$$F_2 = \tanh\left(\arg_2^2\right) \qquad \text{and} \qquad \arg_2 = \max\left(2\frac{\sqrt{k}}{0.09\omega d}, \frac{500\nu}{d^2\omega}\right). \tag{4.31}$$

In equation 4.30, Ω is the rotation tensor magnitude $\sqrt{2\Omega_{ij}\Omega_{ij}}$ (modern implementations use $\sqrt{2S_{ij}S_{ij}}$ instead). The F_2 function is equal to 1 in boundary layers and to 0 in free-shear regions, limiting the redefinition of the eddy viscosity to the near-wall region only. In adverse pressure gradient boundary layers, Ω is usually larger than $a_1\omega$ and the proportionality between the turbulent shear stress and k is thus preserved. For the rest of the flow, equation 4.30 reduces to the standard definition $\nu_t = k/\omega$. In the SST model, the following constants are used:

$$\sigma_{k1} = 0.85 \qquad \text{and} \qquad a_1 = 0.31. \tag{4.32}$$

The performance of the SST model in adverse pressure gradient flows is remarkably superior to those of the original k-ω model and of standard k-ε models. Indeed, the SST is nowadays the most used two-equation eddy-viscosity model in the aeronautical industry for external aerodynamics.

4.3.2 Chien's k-ε model

The k-ε was by far the most popular two-equation model until the nineties [64]. Among its many variations, the version of Launder and Sharma [48] is commonly referred to as

the 'standard' k-ε model. In aerodynamics, the k-ε model of Chien [81] is frequently used, which can be integrated to the wall. Its general approach is similar to the widespread k-ε model of Jones and Launder [82], accounting for the effects of the molecular diffusion of k and ε on the turbulence structure. In conservation form, the transport equations read

$$\frac{D\rho k}{Dt} = \tau_{ij}\frac{\partial u_i}{\partial x_j} + \frac{\partial}{\partial x_j}\left[(\mu + \mu_t)\frac{\partial k}{\partial x_j}\right] - \rho\varepsilon - \frac{2\mu k}{d^2} \tag{4.33}$$

and

$$\frac{D\rho\varepsilon}{Dt} = C_{\varepsilon 1}\frac{\varepsilon}{k}\tau_{ij}\frac{\partial u_i}{\partial x_j} + \frac{\partial}{\partial x_j}\left[\left(\mu + \frac{\mu_t}{\sigma}\right)\frac{\partial \varepsilon}{\partial x_j}\right] - C_{\varepsilon 2} f \frac{\rho\varepsilon^2}{k} - \frac{2\mu\varepsilon e^{-0.5\rho u_\tau d/\mu}}{d^2} \tag{4.34}$$

The last term in equation 4.33 represents the true finite rate of energy dissipation at the wall and serves to balance the molecular diffusion term. A similar 'wall-dissipation' term is added to equation 4.34 and the eddy viscosity is computed as

$$\mu_t = C_\mu f_\mu \rho \frac{k^2}{\varepsilon}, \tag{4.35}$$

where $C_\mu = 0.09$ is the turbulent diffusivity coefficient and the function f_μ accounts for the wall-damping effect. The latter is defined as

$$f_\mu = 1 - e^{-0.0115\rho u_\tau d/\mu}, \tag{4.36}$$

where u_τ is the friction velocity at the nearest wall (note that the model is not local). The function f in the destruction term of the ε-equation reads

$$f = \frac{0.4}{1.8} e^{-\left(k^2/6\nu\varepsilon\right)^2}. \tag{4.37}$$

The remaining constants of the model are $C_{\varepsilon 1} = 1.35$, $C_{\varepsilon 2} = 1.80$ and $\sigma = 1.3$. At solid walls, the boundary conditions are $k = 0$ and $\varepsilon = 0$ and, in the farfield, $\partial k/\partial x_i = 0$ and $\partial\varepsilon/\partial x_i = 0$.

4.3.3 Ambient-turbulence sustaining terms

For computations in free air using two-equation turbulence models, the destruction terms of the k, ω and ε equations usually cause the freestream values of these variables to suffer huge decays throughout the computational domain. The reason for such behavior is that, far from any surface and in the absence of velocity gradients, the production and diffusion terms of these equations virtually vanish and the destruction term is the only that remains non-zero. Therefore, the turbulence variables can reach extremely low and unrealistic levels as one approaches the body, even when very high freestream values are

prescribed for them. In order to remedy this undesirable behavior and keep control over the effective ambient values of the turbulence variables, the transport equations may be modified to include additional weak source terms following the recommendation of Spalart and Rumsey [70]. For the k and ω equations, for example, they read $\beta^*\omega_{amb}k_{amb}$ and $\beta\omega_{amb}^2$, respectively, where the subscript 'amb' stands for 'ambient'. The addition of these terms to the right-hand side of the transport equations results in uniform distributions of k and ω (and thus of ν_t) far from the body. Since the one-equation models presented in section 4.2 feat only wall-destruction terms, they naturally lead to uniform eddy-viscosity fields far from the body.

4.4 Hybrid RANS-LES methods

4.4.1 Motivations

RANS simulations are of widespread use in industry due to their fairly good prediction capabilities for a large range of engineering problems and their relatively low computational costs. However, as discussed in chapter 1, their accuracy and reliability are usually limited to low-incidence flows, where the boundary layers remain mostly attached. Even when time-accurate (URANS) simulations are performed in order to capture unsteady effects, the results are frequently inaccurate when flow separation is a key feature in the problem. This situation becomes especially critical for massively-detached flows, as in the case of a stalled airfoil or of bluff bodies. Such limitations are intrinsic of RANS/URANS methods and are related to the averaging of the flow properties over the whole turbulence spectrum including the energy-containing scales, which are determined by the geometry of the problem. Indeed, the success in computing separated flows is intimately related to the proper representation of those dominant structures, which can be achieved by means of time-dependent three-dimensional simulations. In respect to aeronautic applications, the typical high-Reynolds flows bounded by complex geometries make Large-Eddy Simulations prohibitive due to the extremely expensive computational costs associated and therefore an alternative solution is needed.

An interesting review on the numerical strategies currently available for the simulation of unsteady turbulent flows is given by Spalart [83]. The main conclusions of that paper concerning the applicability of the different methods to complex aerodynamic problems such as the simulation of a complete airplane or car are summarized in table 4.1. For a given method, the 'aim' row indicates if grid refinement results only in higher numerical accuracy or also in the improvement of the physical representation level. In the case of LES, for example, as the grid is refined, smaller turbulent scales are resolved since the cut-off wave number increases. The 'Re-dependence' indicates whether or not the number of grid points needed augments with the Reynolds number and '3/2D' tells if a method is inherently thee-dimensional (even for a purely two-dimensional geometry). 'Grid' and

'Steps' give estimations of the grid size and number of required time steps based on a CFL of the order of 1, assuming a simulation duration equivalent to six spans of travel in the case of an airplane. Finally, the 'Readiness' column provides a rough estimation of when such hypothetical simulation would become possible for each method as a 'Grand Challenge', assuming that computational power increases by a factor of 5 every five years.

Method	Aim	Re-dependence	3/2D	Empiricism	Grid	Steps	Readiness
2D-URANS	Numerical	Weak	No	Strong	10^5	$10^{3.5}$	1980
3D-URANS	Numerical	Weak	No	Strong	10^7	$10^{3.5}$	1995
DES	Hybrid	Weak	Yes	Strong	10^8	10^4	2000
LES	Hybrid	Weak	Yes	Weak	$10^{11.5}$	$10^{6.7}$	2045
DNS	Numerical	Strong	Yes	None	10^{16}	$10^{7.7}$	2080

Table 4.1: Numerical methods for unsteady turbulent flows (adapted from Ref. [83]).

In spite of all discussable hypotheses made to construct table 4.1, it becomes clear that a pure LES of a complete airplane will not be affordable for several decades. For this reason, significant effort has been made towards hybrid RANS-LES methods, which combine the best qualities of RANS and LES into a single turbulence model. Such methods intend to fill the gap observed in table 4.1 between URANS and LES, making the simulation of high-Reynolds unsteady separated flows feasible and compatible with the current and near-future computational resources. In this section, only the approaches directly related to the simulations in this thesis are presented. For a broad review on hybrid RANS-LES methods including various other approaches the reader is encouraged to see the text by Fröhlich and von Terzi [84]. Also, Mockett [85] gives an interesting and simple taxonomy for the categorization of hybrid methods basing on their goals.

4.4.2 Detached-Eddy Simulation

4.4.2.1 Principle

The Detached-Eddy Simulation, or simply DES, is a hybrid RANS-LES method that was first introduced by Spalart et al. [86]. The DDES is intended to high Reynolds number massively-separated flows around complex geometries and, although it is not considered 'mature' yet, its repercussion has been great in the CFD community. A recent review covering its foundations, weaknesses and numerical aspects as well as examples of application and later improvements is provided in Ref. [87].

The principle of DES is the combination of RANS and LES into a single hybrid turbulence model possessing the best properties of each approach. In its 'natural use'(according to the terminology adopted by Spalart [88]), attached boundary layers are completely treated in RANS, whereas regions of separated flow are simulated using LES. The method is constructed upon the transport equations of a baseline RANS model. The switching

between the two modes (RANS and LES) is performed by altering the turbulence length scale in the equations, switching between a RANS length scale l_{RANS} provided by the original model and a LES length scale l_{LES} computed upon the local grid size. The effective turbulence length scale l_{DES} in the DES model is then calculated as

$$l_{\mathrm{DES}} = \min\left(l_{\mathrm{RANS}}, l_{\mathrm{LES}}\right). \tag{4.38}$$

According to the above definition, in regions where $l_{\mathrm{RANS}} < l_{\mathrm{LES}}$, $l_{\mathrm{DES}} = l_{\mathrm{RANS}}$ and the DES model is identical to the original RANS model. This condition should verify in regions where the grid spacing is not fine enough for a LES. When the local grid spacing is sufficiently small, $l_{\mathrm{LES}} < l_{\mathrm{RANS}}$ and hence $l_{\mathrm{DES}} = l_{\mathrm{LES}}$. In such regions, the grid spacing acts as an implicit filter and the RANS model as a subgrid-scale model, with the eddy viscosity representing the effect of the small unresolved scales.

4.4.2.2 Original version

The first formulation of DES was proposed in 1997 by Spalart et al. [86] (it is commonly referred to as DES97, as in Ref. [89]). The Spalart-Allmaras one-equation model [47] was chosen as the baseline RANS model, with the RANS length scale provided by the distance from the closest wall d. According to Spalart, this quantity would be a natural choice for l_{RANS} because it appears explicitly in the destruction term of the SA model (see equation 4.4). Furthemore, choosing $l_{\mathrm{RANS}} = d$ harmonizes with the initial idea that attached boundary layers should be computed in RANS while detached structures far from the wall should be resolved by LES. The LES length scale is based on the larger local grid spacing $\Delta_{\max} = \max\left(\Delta_i, \Delta_j, \Delta_k\right)$, which is multiplied by a calibration constant C_{DES}. Using the maximum grid spacing in the definition of l_{LES} avoids the erroneous activation of the LES mode inside an attached boundary layer, where the grid spacing in the direction normal to the wall is usually very small compared to those in the tangential directions. Hence, the turbulence length scale in the DES97 is given by

$$l_{\mathrm{DES97}} = \min\left(d, C_{\mathrm{DES}}\Delta_{\max}\right). \tag{4.39}$$

As can be noted from equation 4.39, the switching between RANS and LES in the DES97 takes into account only the wall distance and the local grid properties. No information concerning the local flow state is evoked when computing the turbulence length scale. In LES regions, the sub-grid scale eddy viscosity was demonstrated to be proportional to the strain rate and Δ^2 (as the Smagorinsky model), assuming local turbulence equilibrium conditions [85]. As the grid is refined, destruction augments thus reducing the eddy-viscosity levels.

Figure 4.1 illustrates the original conceptual sketch of DES from Ref. [86]. It exemplifies an ideal application of the method, in which the region of separated flow is explicitly

defined by a geometry feature (i.e., the sharp edge of the spoiler over the wing). Unfortunately, such convenience is not always present in high Reynolds number massively-detached flow applications. As observed by Mockett [85], a clear disadvantage in such cases is that the separation location is dictated by the RANS model. Furthermore, it is not clear what happens in the region identified by a question mark in figure 4.1, which is part of the so-called 'gray area' [89]. In such regions, the solution is somewhere in-between RANS and LES, and the behavior of hybrid approaches is not well understood. This issue results from the fact that modeled turbulence is not immediately converted into resolved turbulence when the DES switches to LES.

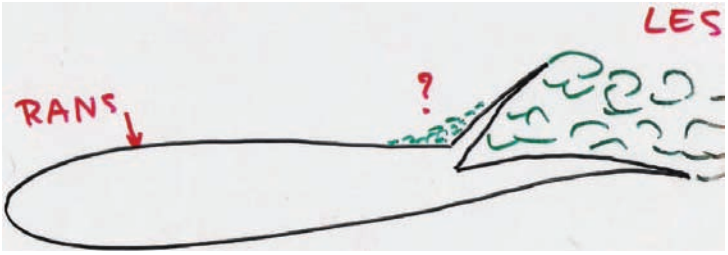

Figure 4.1: Original sketch of Detached-Eddy Simulation (from Ref. [88]).

4.4.2.3 Extension to other models

Though the initial DES studies and publications were based on the Spalart-Allmaras one-equation model (DES97), the approach can be generalized so that any RANS model may be used as the basis for a DDES. To do so, one has first to identify the turbulence length scale in the RANS model equations, which is not necessarily a simple task. This quantity is then replaced by the DES length scale l_{DES} in the model and used in equation 4.38 as l_{RANS} instead of the wall distance. While in the original DES formulation the RANS length scale d appears explicitly in the destruction term of the transport equation of $\tilde{\nu}$, in other models l_{RANS} can be present explicitly or implicitly in other terms. Furthermore, as observed by Strelets [90], there is not a unique solution regarding the choice of the RANS model terms that will receive l_{DES}.

The procedure to extend the DES approach to other RANS closures was first presented by Travin et al. [91] and Strelets [90] for Menter's SST model. As RANS length scale, a trivial replacement is to take $l_{\mathrm{RANS}} = \sqrt{k}/\left(\beta^{*}\omega\right)$, yielding

$$l_{\mathrm{DES}} = \min\left(\sqrt{k}/\left(\beta^{*}\omega\right), C_{\mathrm{DES}}\Delta_{\max}\right). \tag{4.40}$$

The authors opted for inserting l_{DES} only in the destruction term of the k-equation supported by the fact that this substitution is simple and similar to that of the original DES formulation. Also, the constant C_{DES} had to be reevaluated separately for the k-ω and k-ε branches of the SST model. In the context of a SST-based DES, equation 4.20

transforms into

$$\frac{D\rho k}{Dt} = \tau_{ij}\frac{\partial u_i}{\partial x_j} - \frac{\rho k^{\frac{3}{2}}}{l_{\mathrm{DES}}} + \frac{\partial}{\partial x_j}\left[(\mu + \sigma_k \mu_t)\frac{\partial k}{\partial x_j}\right]. \tag{4.41}$$

4.4.3 Delayed Detached-Eddy Simulation

Typical DES grids normally have the grid spacing in the direction parallel to the surface Δ_i larger than the boundary layer thickness δ as illustrated on the top of figure 4.2 for a flat plate. In some cases, however, surface grids may become excessively refined to represent some feature of the geometry or for proper resolution of a shock wave, for example. Furthermore, thick boundary layers can arise naturally as in high-incidence flows, near separation points or as a result of shock wave/boundary layer interactions. Such situations can make Δ_i become locally smaller than δ, leading to a condition of 'ambiguous grid density' for the standard DES as represented on the left side of figure 4.2. Such condition can induce an erroneous activation of the LES mode inside an attached boundary layer even if the grid is not sufficiently fine for turbulence resolution (for comparison, a typical LES grid is sketched on the right side of figure 4.2). By consequence, the effective length scale in the turbulence model equations is abruptly reduced, lowering the eddy viscosity and thus the modeled Reynolds stresses without the generation of the corresponding LES content. This issue is known as 'modeled-stress depletion' (MSD) and was already anticipated in the first publications of the DES method. MSD may potentially reduce the skin-friction and in some cases even cause premature separation as reported by Menter and Kuntz [92], who described the phenomenon as a 'grid-induced separation'.

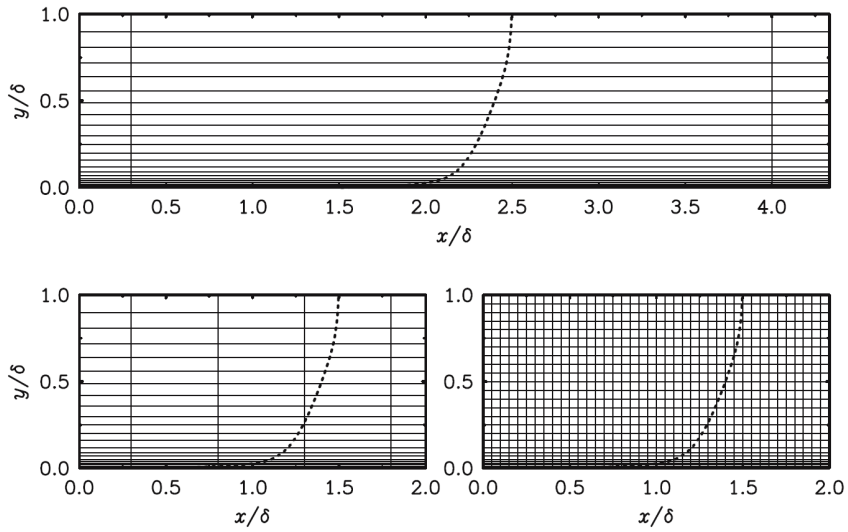

Figure 4.2: Typical grids for a boundary layer on a flat plate (from Ref. [89]). Top: DES grid ($\Delta_i > \delta$). Left: ambiguous grid ($\Delta_i < \delta$). Right: LES grid ($\Delta_i \ll \delta$).

A general solution to MSD simple enough to be applied to any eddy-viscosity model was proposed by Spalart et al. [89]. The improved model detects and 'shields' attached

boundary layers delaying the activation of the LES mode even on ambiguous grids and, for this reason, it was named Delayed Detached-Eddy Simulation (DDES). The core of the DDES is the near-wall parameter r from the Spalart-Allmaras model (see equation 4.9). This quantity can be easily implemented and extended to other eddy-viscosity models and serves as an indicator of whether a grid point is located inside a boundary layer. In the context of the DDES approach, the parameter r was renamed r_d and was slightly modified, reading

$$r_d \equiv \frac{\nu_t + \nu}{S\kappa^2 d^2}, \qquad \text{where} \qquad S = \sqrt{\frac{\partial u_i}{\partial x_j}\frac{\partial u_i}{\partial x_j}}. \tag{4.42}$$

The subscript d stands for 'delayed'. r_d is equal to 1 in the logarithmic layer and goes to zero as one approaches the boundary layer edge. The scalar S was chosen as the norm of the whole deformation tensor in order to gain in robustness in irrotational regions [89]. The introduction of the molecular viscosity in the numerator of r_d corrects the very near-wall behavior keeping r_d far from zero. In the case of a DDES based on the SA model, $\nu_t + \nu$ can be replaced by $\tilde{\nu}$.

The r_d parameter is used to design the delaying function f_d, which is capable of distinguishing RANS and LES regions. This function is defined as

$$f_d \equiv 1 - \tanh\left[(8r_d)^3\right], \tag{4.43}$$

and is equal to 1 in LES regions ($r_d \ll 1$) and to zero in all other zones. Finally, the DDES length scale is computed by

$$l_{\text{DDES}} \equiv d - f_d \max\left(0, l_{\text{RANS}} - l_{\text{LES}}\right). \tag{4.44}$$

Taking the SA model as example, equation 4.44 becomes

$$l_{\text{SA-DDES}} = d - f_d \max\left(0, d - C_{\text{DES}}\Delta\right). \tag{4.45}$$

Contrary to the DES97 (where the length scale depends only on the wall distance and on the grid size), in the DDES formulation the switching between RANS and LES also depends on the turbulence state by means of the eddy viscosity. Therefore, the effective turbulence length scale is influenced by the flow physics and can vary both in space and time. Furthermore, the transition between the two modes becomes more rapid, reducing the size of the gray area [89].

Compared to the DES method, tests for a boundary layer on a flat plate [89] showed that the DDES avoids undesired switching to LES when using ambiguous grids, keeping the eddy-viscosity levels comparable to RANS computations. In simulations involving coarse grids, the DDES provided results very similar to those from standard DES. A positive side effect of DDES is that the approach minimizes problems arising from inappropriate user intervention, although it does not eliminate them. For instance, proper grid design

is still required (best practice guidelines on grid generation for DES-family methods can be found in Ref. [93]).

Several other solutions to the MSD issue have been proposed. In the 'zonal DES' approach, for example, RANS and LES regions are explicitly determined by the user (see Ref. [4] for example). Other strategies aim at using other grid parameters (e.g., the cell aspect ratio) to 'flag' the presence of a boundary layer. However, such alternatives are not robust enough to be applied to any type of grid or may become too complicated for real-life geometries.

Chapter 5

Two-Dimensional Simulations of a Supercritical Airfoil

Contents

5.1 Motivations

In this chapter, steady and unsteady simulations of two-dimensional transonic shock wave/boundary layer interactions over the OAT15A supercritical airfoil are performed. The studies employ linear eddy-viscosity turbulence models commonly used in aerodynamics and the results are compared with the experimental data of Jacquin et al. [38, 39]. As a preparatory step for the simulation of transonic buffet, preliminary computations adopting local time stepping are carried out for a steady attached flow condition. The idea is to extract the maximum of useful information for the more expensive unsteady simulations regarding the selection of suitable numerical parameters and the performance of turbulence models. Furthermore, the computations allow to check the implementation of Secundov's compressibility correction for one-equation models (see section 4.2.2.3) and of the ambient turbulence sustaining terms for two-equation closures (see section 4.3.3), as well as to assess the effects produced by these two features on the results. The optimal set of parameters is then used in conjunction with the most promising turbulence models to simulate the transonic buffet over the OAT15A at flow conditions close to the instability onset boundary. The results provide an understanding of the strengths and weaknesses of the various turbulence models in respect to the prediction of the unsteady flow properties. Furthermore, the simulations help choosing the most appropriate baseline model for a three-dimensional simulation of the same flow in the context of a scale-resolving approach (chapter 6). The influence of time-stepping parameters on the prediction of the transonic buffet properties is also investigated.

5.2 Preliminary steady flow computations

5.2.1 Test case and numerical grid

The unsteady shock wave/boundary layer interaction over the OAT15A airfoil was summarized in section 2.3.1. The profile has a thickness-to-chord ratio of 12.3%, and the wind tunnel model used in the experiments had a blunt trailing edge measuring 0.5% of the chord. At $M_\infty = 0.73$ and $Re = 3 \times 10^6$, buffet onset was detected at $\alpha \approx 3.1°$, with large-scale periodic shock-wave oscillations being established only at 3.5° incidence. However, experimental data such as the C_p distribution is also available for angles of attack below the buffet onset boundary. In those cases, the shock wave was stationary and the boundary layer remained mostly attached, so that the flow can be treated as 'steady'. Due to the high quality of the data, a steady flow case has then been selected for the assessment of numerical parameters and turbulence models for the following simulations of this thesis. The tests are all conducted at $\alpha = 2.5°$, where the boundary layer is attached over the entire airfoil except by a small separation bubble at the foot of the shock wave. As in the unsteady flow case, the freestream conditions are $M_\infty = 0.73$ and $Re = 3 \times 10^6$,

for a total pressure of 10^5 Pa and a total temperature of 300 K. In the experiments, the boundary layer was tripped at $x/c = 0.07$ on both upper and lower surfaces using carborundum strips. The effect of simulating such portion of laminar boundary layer in contrast with a fully-turbulent computation is also investigated.

The numerical grid employed in the computations has a C-H topology and is a finer version of the grid provided by ONERA in the framework of the ATAAC European project. The latter has approximately 109,000 cells and results from a drag extraction study by Esquieu [94], being also used by Deck [4] as planar grid in the three-dimensional simulation of the transonic buffet over the OAT15A airfoil using the ZDES method. The gridlines of the ONERA grid in the vicinity of the airfoil are illustrated in figure 5.1(a). In the present grid, the total number of cells has been increased to about 130,000, resulting in the gridlines shown in figure 5.1(b). As for the ONERA grid, the farfield is located at a distance of 80 chords from the airfoil in all directions. The reason for creating a finer grid is that it will serve as basis for the generation of a three-dimensional grid to be used in conjunction with a hybrid RANS-LES method in chapter 6, thus allowing the resolution of smaller flow structures. For efficient parallel computing, both the ONERA and present grids have been split into 16 blocks of approximately same number of cells each. A comparison between the two grids in steady transonic flow is presented in the next subsection.

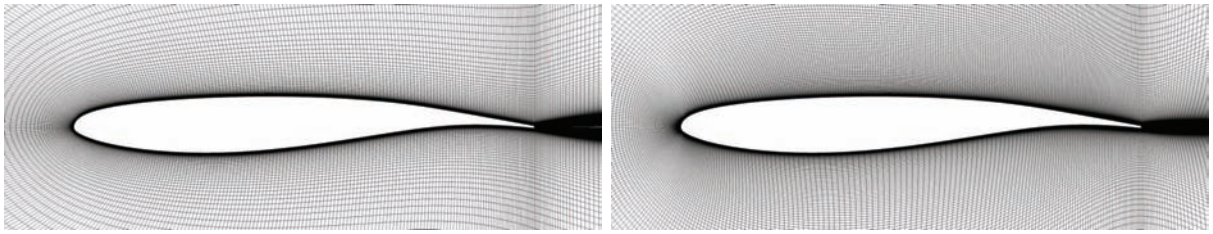

(a) ONERA grid ($\approx 109,000$ cells) (b) Present grid ($\approx 130,000$ cells)

Figure 5.1: Detail of the planar grids of the OAT15A airfoil.

5.2.2 Convergence criterion and grid check

Before evaluating numerical schemes and turbulence-related issues, a first test is conducted in order to define a convergence criterion for the steady flow computations, in which the flowfield is initialized with freestream properties. To do so, a tolerance threshold ϵ is progressively decreased to determine how many orders of magnitude of reduction in the norm of the density residual are necessary for the solution to be considered as converged. The computations are performed using the Spalart-Allmaras model with the freestream condition for the modified eddy viscosity set as $\tilde{\nu}/\nu = 3$, as recommended in Ref. [70]. The convective fluxes are computed using the second-order TVD formulation of the Roe scheme with van Leer limiters. For simplicity, fully-turbulent behavior is allowed.

Table 5.1 presents the evolution of the global aerodynamic coefficients as a function of ϵ, where the pitching moment coefficient C_m is calculated at the leading edge. The results reveal that reducing the tolerance threshold from 10^{-6} to 10^{-7} yields a variation smaller than 0.1% for all coefficients. The convergence of the numerical solution is evidenced by the surface pressure coefficient distributions shown in figure 5.2(a). Further reduction in the value of ϵ results in absolutely negligible changes in the flowfield. Therefore, all steady computations in this thesis assume the solution as converged after a relative decrease of six orders of magnitude in the density residual.

ϵ	10^{-3}	10^{-4}	10^{-5}	10^{-6}	10^{-7}	10^{-8}
C_L	1.0936	0.93149	0.90778	0.90934	0.90918	0.90914
$C_D \times 10^2$	4.7806	3.1542	2.9826	2.9934	2.9922	2.9921
C_m	-0.46088	-0.36798	-0.35580	-0.35660	-0.35654	-0.35652
ΔC_L (%)	–	-14.82	-2.55	0.17	-0.02	0.00
ΔC_D (%)	–	-34.02	-5.44	0.36	-0.04	0.00
ΔC_m (%)	–	-20.16	-3.31	0.22	-0.02	-0.01

Table 5.1: Influence of the convergence criterion on the global coefficients.

By computing the same steady flow case at $\alpha = 2.5°$ using the Spalart-Allmaras model, Deck [4] showed that the C_p distribution obtained with the ONERA grid was very similar to that with a coarser grid having 65,000 cells. The latter resulted from a grid convergence study by Brunet [54] on transonic buffet and, in both cases, the non-dimensional wall distance y^+ of the first cell was everywhere smaller than the unity. Despite these results, a comparison between the ONERA and present grids adopting exactly the same numerical and physical parameters is performed to ensure grid independence. The pressure coefficient distributions obtained with the two grids are illustrated in figure 5.2(b) and the global aerodynamic coefficients are provided in table 5.2. As expected, the C_p curves are virtually identical and the variations in the forces and moment are small. The maximum y^+ values found for the two grids are also very similar.

Grid	C_L	$C_D \times 10^2$	C_m	$y^+_{\max}$
ONERA	0.91455	3.0439	-0.35922	0.593
Present	0.90934	2.9934	-0.35660	0.588
Δ (%)	-0.57	-1.66	-0.73	–

Table 5.2: Global coefficients and wall coordinates for different grids.

5.2.3 Convective scheme and flux limiters

In the simulation of compressible flows featuring shock waves, the discretization of the convective fluxes must be made using a proper spatial scheme capable of capturing such flow discontinuities. Moreover, the scheme should provide an accurate resolution of thin boundary layers as typical of high-Reynolds flows using as few points as possible. In

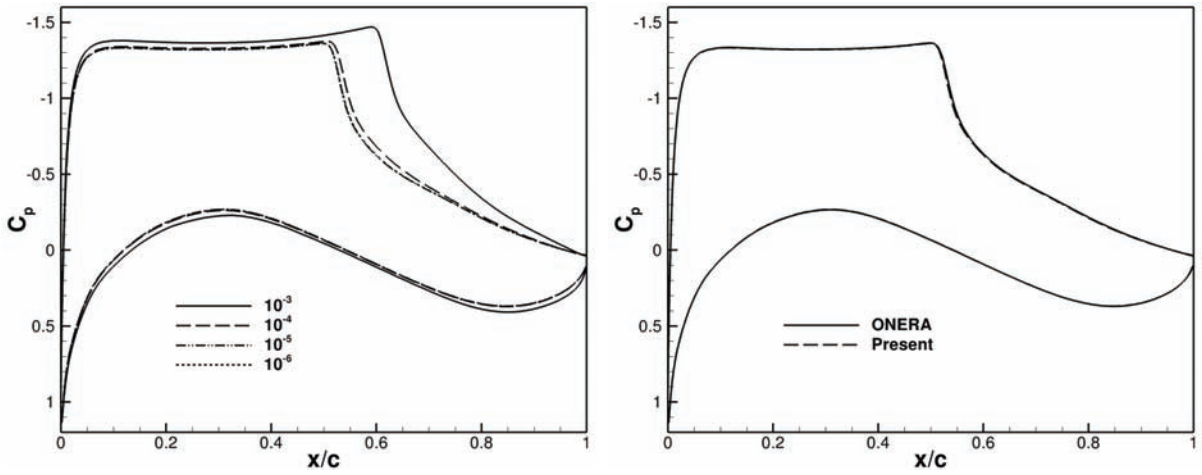

(a) Tolerance threshold

(b) Computational grid

Figure 5.2: Surface pressure distributions for different tolerances and grids.

this way, a series of tests is conducted in order to select a convective scheme for the following steady and unsteady two-dimensional simulations. Among the options available in the NSMB code, the second- and third-order accurate Roe and AUSM+ schemes as well as the second- and fourth-order central schemes with scalar artificial dissipation are considered. The C_p distributions obtained with the different schemes are shown in figure 5.3. Because the computations with the second-order AUSM+ scheme had convergence issues, no results are presented for that scheme. In figure 5.3(a), it is difficult to note any difference between the five profiles. Therefore, the shock-wave region is rescaled in figure 5.3(b) to facilitate the visualization of the small variations presented by the curves. As can be seen, the shock-wave resolution as well as the solution behavior are satisfactory whatever the spatial scheme, yielding a sharp compression through the shock with no spurious oscillations. Nevertheless, the central schemes seem to result in slightly more numerical diffusion than the upwind ones.

The influence of the numerical scheme on the computation time and on the number of iterations needed to achieve convergence is presented in table 5.3. For convenience, the results are normalized by the values relative to the second-order Roe scheme. In all cases, the minimum reduction in the residuals has been for the modified eddy viscosity $\tilde{\nu}$. Therefore, the final relative residuals of this variable are given on the bottom of the table. Regarding the two Roe schemes, the third-order version requires slightly more computation time and iterations than the second-order one, keeping the same computational cost per iteration. The third-order AUSM+ scheme demands a higher computational effort than the two Roe schemes but provides a much smaller maximum residual. However, no noticeable improvements in the resolution of the shock wave are obtained as seen in figure 5.3. With central schemes, the computation time drops considerably compared to the upwind ones, with the total number of iterations remaining almost the same. This result is expected as central schemes with scalar dissipation usually have a simpler formulation

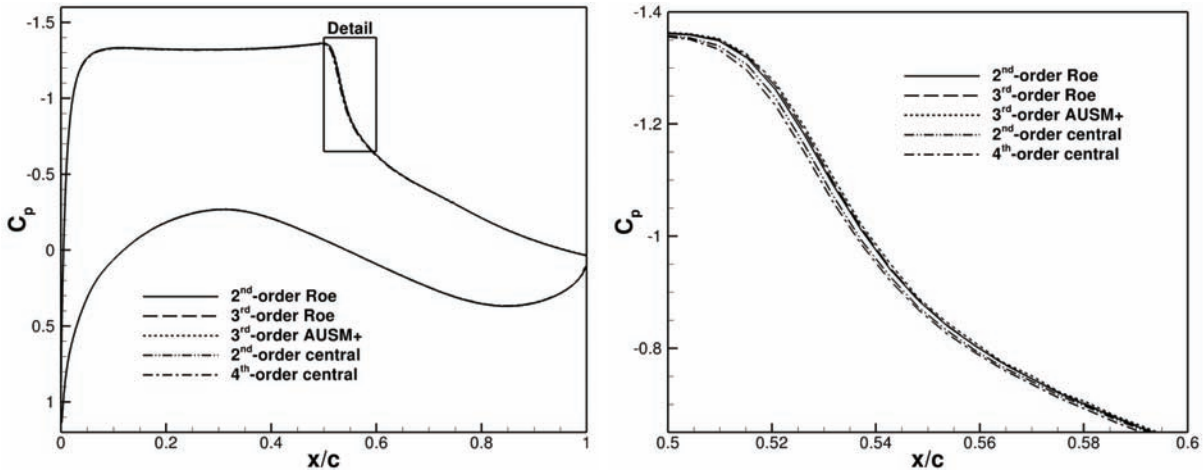

(a) Overview (b) Detail of the shock-wave region

Figure 5.3: Influence of the convective scheme on the pressure distribution.

and do not use flux limiters. Nevertheless, because of their higher numerical diffusion, they will not be employed in the following simulations. For the reasons discussed above and because it provides a solution virtually identical to that of its third-order relative, the second-order Roe scheme is retained for the two-dimensional transonic flow simulations of the present thesis.

Scheme Accuracy	Roe 2nd order	Roe 3rd order	AUSM+ 3rd order	Central 2nd order	Central 4th order
Normalized computation time	1.00	1.08	1.27	0.69	0.64
Normalized iterations	1.00	1.08	1.20	1.00	0.90
Maximum residual $\times 10^4$	1.33	1.15	0.585	1.37	4.20

Table 5.3: Effect of the convective scheme on computational parameters.

Having selected a second-order upwind scheme for the discretization of the convective fluxes, multiple choices are available in the NSMB code for the flux limiters. Therefore, a second set of computations is performed in order to compare the van Leer, minmod 1, minmod 2 and superbee limiters. From surface pressure distributions (not shown here) it is very hard to note any difference between the results. Table 5.4 summarizes the computational parameters for each limiter, where the computation time and the number of iterations are normalized by the values relative to the van Leer limiters. As can be seen in the table, the differences are also very small. Since the flux limiters appear to have only minor effect on the computations, the van Leer limiters (which are continuously differentiable) are chosen for the following simulations.

Limiter	van Leer	Minmod 1	Minmod 2	Superbee
Normalized computation time	1.00	0.95	0.96	1.09
Normalized iterations	1.00	1.00	1.01	1.07
Maximum residual $\times 10^4$	1.33	0.849	2.00	1.35

Table 5.4: Effect of the flux limiter on computational parameters.

5.2.4 Turbulence sustaining terms

In the context of this thesis, the ambient-turbulence sustaining terms discussed in section 4.3.3 have been implemented in the NSMB code. These should allow uniform ambient turbulence levels for models based on the transport of the turbulent kinetic energy k and of a scale-determining variable given by ε or ω. The aim is to avoid numerical issues due to inappropriate values of these variables near the body caused by their free decay through the domain. Therefore, following the recommendation of Spalart and Rumsey [70], extra source terms have been added to the transport equations of k, ω and ε, being available in all linear and nonlinear eddy-viscosity closures as well as in all explicit algebraic Reynolds stress models. Moreover, the ambient terms should also be compatible with future implementations of turbulence models based on these variables. The coding has been validated for all models in the version 6.04 of the code, providing uniform distributions of k, ε and ω far from viscous surfaces and for any freestream conditions of k/U^2 and ν_t/ν. Some results for standard two-equation models obtained in the present test case are shown in table 5.5, which gives the number of iterations needed to achieve convergence according to the criterion adopted in subsection 5.2.2 for three cases: ambient terms turned off (free decay), ambient terms turned on using the NSMB default freestream conditions ($k/U^2 = 0.001$ and $\nu_t/\nu = 0.01$ except for Chien's k-ε model, for which $\nu_t/\nu = 1.0$) and ambient terms turned on adopting the freestream/ambient conditions recommended in Ref. [70] (i.e., $k/U^2 = 1\times10^{-6}$ and $\nu_t/\nu = 2\times10^{-7}Re$).

Turbulence model	BSL	KEC	WCX	SST
Ambient turbulence off	–	18,357	17,758	17,689
Ambient turbulence on (def.)	7,775	9,028	12,982	17,681
Ambient turbulence on (rec.)	7,768	12,635	12,649	17,680

Table 5.5: Effect of the ambient turbulence terms on convergence.

For Menter's Baseline k-ω model (BSL), with the ambient turbulence terms deactivated, convergence has stalled before reaching the prescribed tolerance threshold ($\epsilon = 10^{-6}$). For that model, the turbulence sustaining terms have shown to be indispensable and have resulted in rapid convergence if compared to the other models listed. The convergence histories for the BSL model are presented in figure 5.4(a). As can be noted, the default and the recommended boundary/ambient conditions yield very similar convergence behaviors. In the case of Chien's k-ε model (KEC), drastic improvements have been obtained adopting the turbulence sustaining terms. When using the default NSMB boundary conditions,

the number of iterations has been reduced in more than 50%. For Wilcox' revisited k-ω model (WCX), the ambient turbulence has yield almost 30% of reduction in the computational cost, with a slightly faster convergence with the recommended ambient values. Menter's Shear Stress Model (SST) has been the only closure insensitive to the use of the source terms with recommended or default boundary conditions. Regarding the final flow solution, as one may expect, the differences in the surface pressure distribution, shock-wave location and global forces are very small, especially for the SST model. This was already expected since in near-wall regions the additional terms should remain small compared to the other terms in the transport equations. This is particularly true for the SST model, which has produced virtually identical C_p distributions with the sustaining terms turned on and off. However, some models have been slightly affected by the ambient turbulence terms as exemplified in figure 5.4(b), which compares the surface pressure distributions obtained using the WCX model with experimental data. Nevertheless, in all cases, the solutions obtained with the turbulence sustaining terms were closer to the experimental results than with free decay.

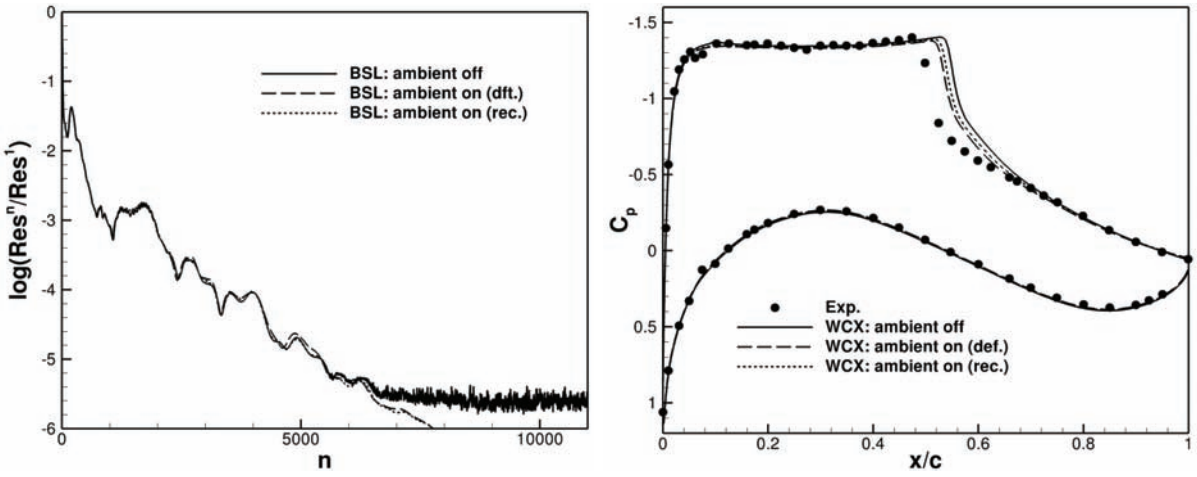

(a) Convergence history for the BSL model

(b) Pressure distributions for the WCX model

Figure 5.4: Effect of the ambient turbulence terms on two-equation models.

Although in table 5.4 the SST model appears as insensitive to the ambient turbulence terms, it does not mean that any values of k and ω can be used when these terms are turned on. For example, in the experiments of Ref. [39] for the OAT15A, the freestream turbulence intensity measured during the tests was of approximately 1%. In theory, this value could be used to set the inflow/ambient conditions for k, yielding $k/U^2 = 1.5{\times}10^{-4}$. Concerning the condition for ω, the relation suggested by Spalart and Rumsey [70] (i.e., $\omega = 5U/c$) ensures that this variable will not diffuse and influence the interior of the boundary layer. Therefore, such values of k and ω result in a freestream/ambient eddy-viscosity ratio ν_t/ν of $3 \times 10^{-5} Re$, which gives $\nu_t/\nu = 90$ for the OAT15A test case. This value, however, has been revealed to be too high for the SST model, resulting in a convergence stall due to an irregular eddy-viscosity distribution around the leading edge as illustrated in figure 5.5. The reason for this undesired behavior is that, in the SST

model, high values of k make the two arguments in the eddy viscosity limiter (see equation 4.30) become comparable near the leading edge, resulting in a random switching between them. To avoid this problem, instead of prescribing freestream/ambient conditions based on the experimental turbulence intensity, the values recommended in Ref. [70] are adopted in this thesis, namely $k/U^2 = 1\times10^{-6}$ and $\nu_t/\nu = 2\times10^{-7}Re$. Besides a regular eddy-viscosity field, the recommended inflow conditions ensure good convergence as shown in figure 5.5(b).

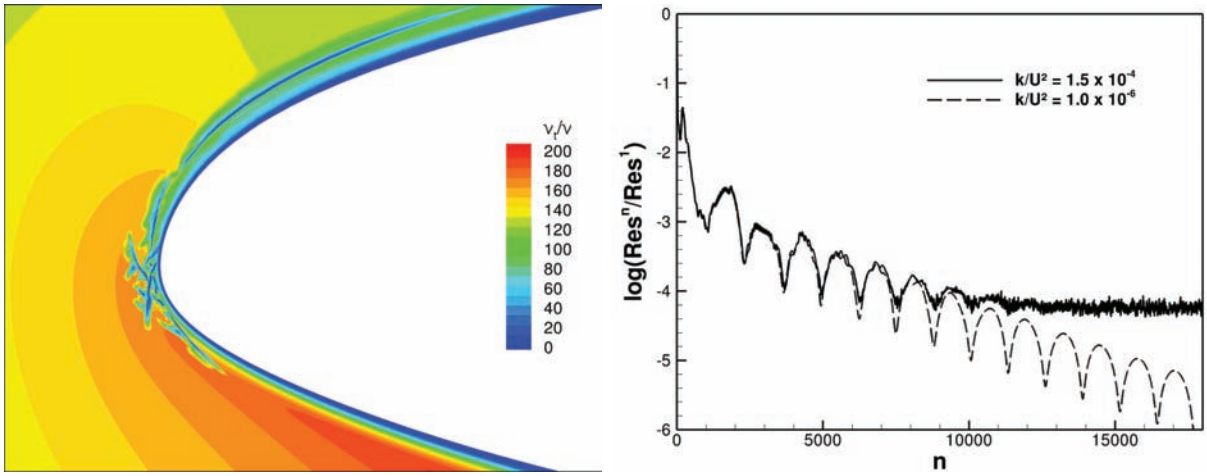

(a) Eddy-viscosity field for $k/U^2 = 1.5\times10^{-4}$ (b) Convergence histories for different k/U^2

Figure 5.5: Effect of the ambient turbulent kinetic energy on the SST model.

5.2.5 Assessment of turbulence models

After having defined the basic numerical parameters, the behavior of several one- and two-equation linear eddy-viscosity models commonly used in aerodynamics is investigated for the steady transonic flow at 2.5° incidence. All turbulence models considered in the study were described in detail in chapter 4. The conclusions regarding their performance for such configuration will serve to restrict the more expensive unsteady simulations of transonic buffet to the most promising models. The one-equation models selected are the original Spalart-Allmaras model (SA), the Edwards-Chandra modified SA model (EDW) and the Strain-Adaptive Linear Spalart-Allmaras model (SALSA). As presented in section 4.2.2.3, in the context of this thesis, the compressibility correction of Secundov has been implemented to all turbulence models in the NSMB code that are based on a single transport equation for the modified eddy viscosity $\tilde{\nu}$. In order to validate the coding and assess the effects produced by this correction in the transonic flow over the OAT15A airfoil, additional computations are performed using the SA and EDW as baseline models. The resulting closures are identified by a +CC following the original model abbreviation. In respect to two-equation models, computations are conducted for Menter's Baseline (BSL) and Shear Stress Transport (SST) models, for the new k-ω model of Wilcox (WCX)

and for the k-ε model of Chien (KEC). In all cases, the ambient turbulence source terms are turned on. For the OAT15A test case, the recommended ambient value for ν_t/ν corresponds to a modified eddy viscosity of $\tilde{\nu}/\nu \approx 4$. This value is within the range suggested by Spalart and Rumsey [70] for one-equation models, allowing the comparison of the two classes of turbulence models with a same background eddy-viscosity level.

Figure 5.6 compares the pressure coefficient distributions obtained with each turbulence model with the experimental results. The curves for the one-equation models are plotted in figure 5.6(a) and those for the two-equation models in figure 5.6(b). On the upper surface, after the rapid expansion around the leading edge, the pressure profiles exhibit an almost flat region terminated by a sudden compression caused by the shock wave. This pressure plateau results from supersonic flow over the nearly flat upper surface of the OAT15A airfoil. Downstream the shock, the pressure increases progressively along the recovery region, which extends to the trailing edge. The flow over the lower surface is everywhere subsonic, exhibiting a pressure distribution characteristic of supercritical airfoils. Although most of the experimental pressure distribution is reasonably well predicted by the turbulence models, the two figures reveal that the shock-wave position is highly model-dependent. Furthermore, in all cases the shock wave is located too far downstream the experimental position.

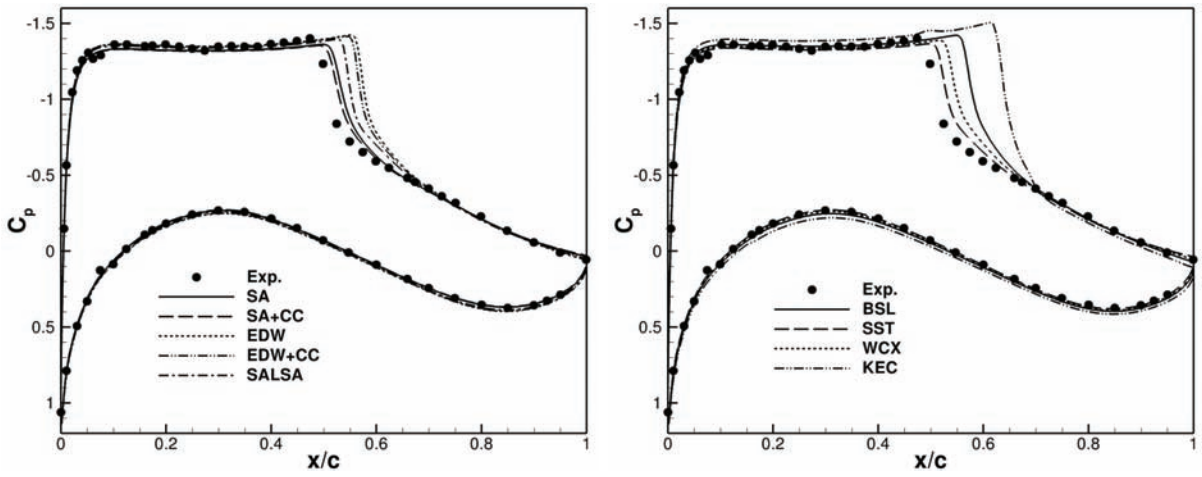

(a) One-equation models

(b) Two-equation models

Figure 5.6: Pressure distributions in steady flow for various turbulence models.

Concerning the one-equation closures, figure 5.6(a) shows that the SA model gives the most accurate prediction of the shock-wave position. The results are improved by adding the compressibility correction of Secundov (at 2.5° the local Mach number immediately before the shock wave is around 1.3). The same positive effect is observed for the EDW+CC model. As one may expect, in both cases the compressibility correction affects only the shock-wave region, where the turbulent boundary layer interacts with strong velocity gradients. Figure 5.7 illustrates the eddy-viscosity ratio distributions obtained with the one-equation models around the rear part of the OAT15A airfoil. By comparing

the SA and SA+CC fields, it can be seen that the compressibility correction slightly reduces the overall eddy-viscosity levels in the near wake. Compared to the SA model, the EDW model seems to delay the production of eddy viscosity. This difference may explain why the latter has predicted the shock-wave location further downstream. The adaptive production term of the SALSA model considerably reduces the eddy-viscosity levels compared to the EDW model, bringing the shock further upstream.

For a better understanding about the effect of the turbulence model on the shock-wave position, the longitudinal velocity and eddy-viscosity profiles on the upper surface at $x/c = 0.50$ are presented in figure 5.9. This station corresponds to approximately the experimental shock-wave position, being located upstream the shock waves and the adverse pressure gradient region. In respect to one-equation models, two groups of velocity profiles can be distinguished in figure 5.9(a), the first being composed by the SA and SA+CC models and the second by the EDW, EDW+CC and SALSA models. In terms of turbulence modeling, the fundamental difference between the two groups is in the definition of the strain-rate norm $\tilde{S}$ and of the near-wall parameter r. While the models in the first group employ the original formulation of the Spalart-Allmaras model, those in the second groups adopt the modifications proposed in the Edwards-Chandra model (see section 4.2.2.1 or Ref. [72]). Within each group, the differences between the models become more clear when comparing the eddy-viscosity profiles, which indicate that the compressibility correction effectively decreases the eddy viscosity near the shock. Moreover, the figure reveals that the strain-adaptive production coefficient $\tilde{c}_{b1}$ of the SALSA model yields a dramatic reduction in the eddy-viscosity production.

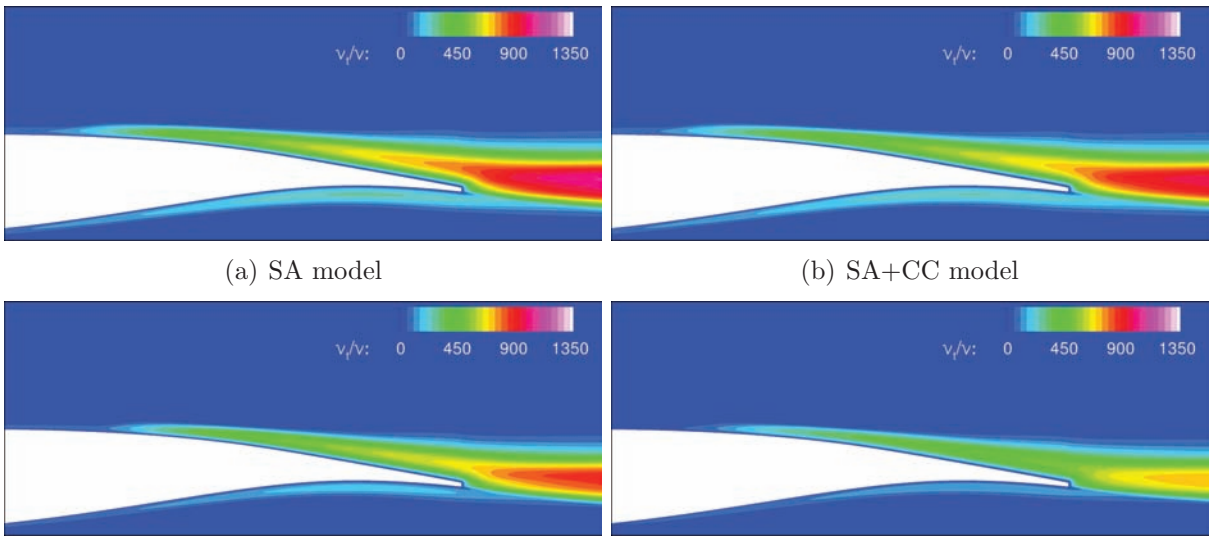

(a) SA model (b) SA+CC model

(c) EDW model (d) SALSA model

Figure 5.7: Eddy-viscosity distributions for one-equation models.

Regarding the two-equation models, figure 5.6(b) shows the improvements obtained in the shock-wave position prediction by means of the eddy-viscosity redefinition in the SST model (equation 4.30) in contrast with the standard definition (i.e., $\nu_t = k/\omega$) of the BSL

model. Using exactly the same transport equations with few modified constants, the stress limiter introduced in the SST model considerably lowers the eddy-viscosity levels on the rear part of the airfoil, where strong adverse pressure gradients take place. Such reduction is clearly seen when comparing the eddy-viscosity fields illustrated in figure 5.8 as well as the profiles at $x/c = 0.50$ presented in figure 5.9(b). The WCX model also results in great improvement in the prediction of the shock-wave location compared to the BSL model, which can be assumed as equivalent to the standard k-ω model of Wilcox without the sensitivity to the freestream values of ω. The differences in the results are probably related to the stress limiter introduced in the revisited k-ω model. It should be mentioned, however, that the two models that make use of stress limiters (i.e., SST and WCX) generate disturbances in the eddy-viscosity field as revealed by figures 5.8 and 5.9(b). The KEC model predicts the shock wave too far downstream and gives inaccurate results for the supersonic plateau, the recovery zone and even for the pressure distribution on the lower surface. As evidenced by figure 5.9(b), the boundary layer development at $x/c = 0.50$ is completely delayed. To some extent, the results reflect the inferiority of standard k-ε models in the computation of wall-bounded aerodynamic flows.

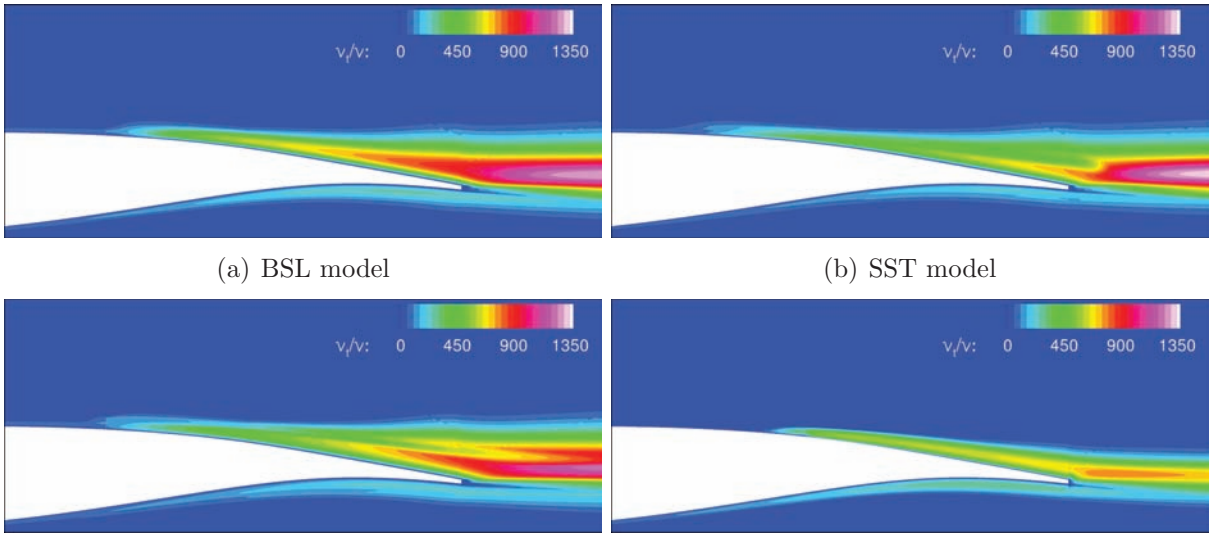

(a) BSL model

(b) SST model

(c) WCX model

(d) KEC model

Figure 5.8: Eddy-viscosity distributions for two-equation models.

5.2.6 Influence of transition

High-Reynolds-number aerodynamic flows are most frequently computed as fully turbulent. In general, this approximation is reasonable as, in such flows, transition usually occurs quickly and laminar flow normally plays a minor role. Besides, in order to simulate the laminar part of the boundary layer, prior knowledge about the transition location must be available, which is rarely the case. As already mentioned, in the OAT15A test case the boundary layer was tripped at $x/c = 0.07$ on both surfaces using a carborundum

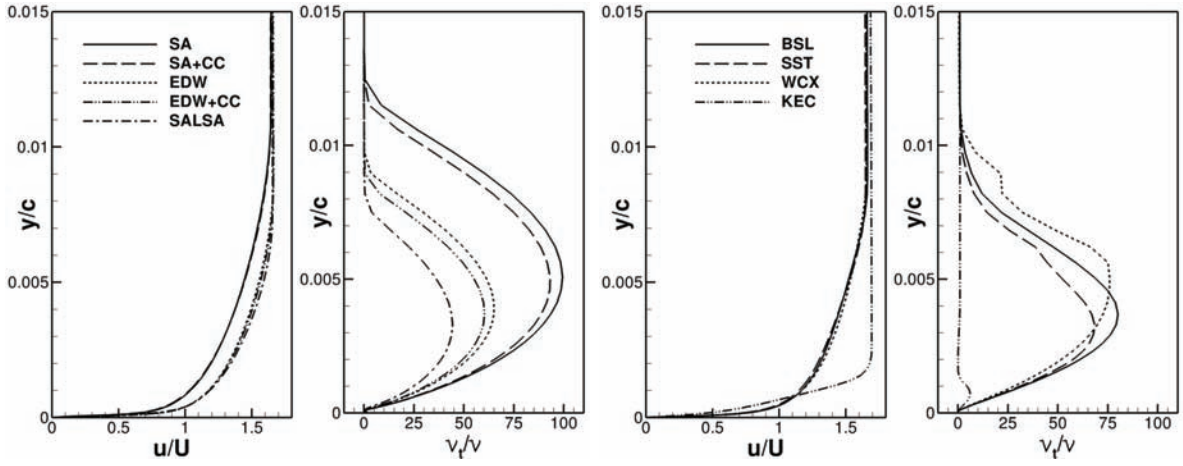

(a) One-equation models (b) Two-equation models

Figure 5.9: Longitudinal velocity and eddy-viscosity profiles at the mid-chord.

technique. To verify if the effect of the laminar boundary layer on the flowfield properties and particularly on the shock-wave position can indeed be neglected, additional computations have been run for all turbulence models. Although the complete SA model features an additional tripping term, the solution adopted for simulating laminarity has been to impose $\nu_t = 0$ upstream the tripping line, since it can be applied to all turbulence models in the same way.

Figure 5.10(a) illustrates for the SA model the resulting eddy-viscosity distribution when considering transition. As expected, turbulence starts to develop only from the prescribed tripping location. Compared to the fully-turbulent computations, for all turbulence models the shock-wave location x_s shifts slightly downstream when accounting for transition. The reason for this behavior is that the overall boundary layer thickness decreases when the laminarity is simulated, resulting in a thinner effective body. Nevertheless, the shift in the shock position is in all cases smaller than 1% of the airfoil chord, as presented in table 5.6. The influence of the laminar boundary layer on the pressure coefficient distribution is exemplified in figure 5.10(b) for the SA model, which has shown the largest changes. As can be noted, the variations produced in the C_p are small and can thus be neglected. Despite that, the laminar part of the boundary layer will be considered in the simulations of transonic buffet in order to get as close as possible to the experimental setup. Furthermore, at this stage, it cannot be stated yet whether the unsteady shock wave/boundary layer interaction will be influenced by the laminar boundary layer.

Model	SA	SA+CC	EDW	EDW+CC	SALSA	BSL	SST	WCX	KEC
$\Delta x_s/c \times 10^2$	0.80	0.77	0.31	0.30	0.27	0.66	0.68	0.90	0.51

Table 5.6: Influence of transition on the shock-wave location.

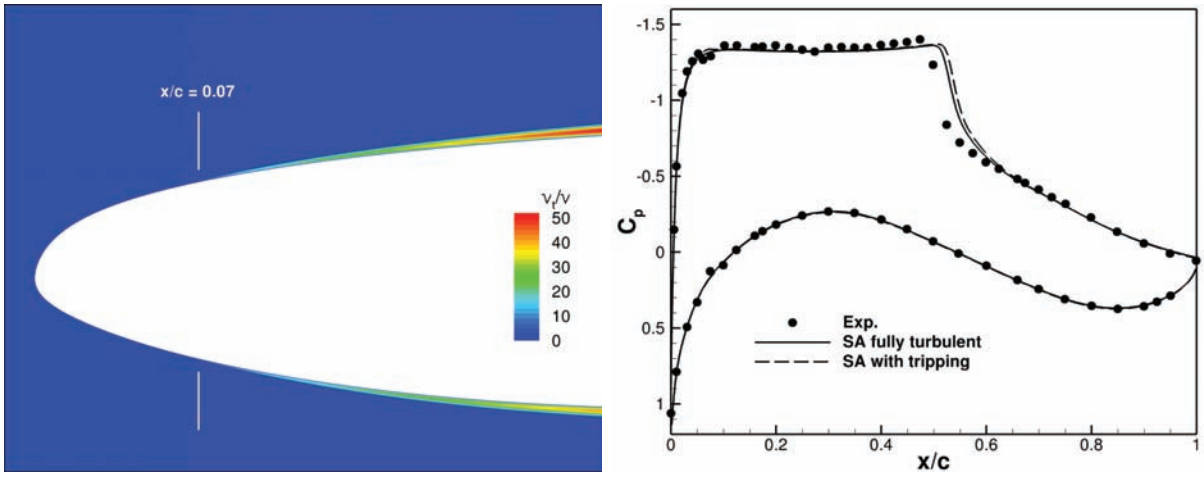

(a) Eddy-viscosity ratio

(b) Pressure coefficient distribution

Figure 5.10: Effect of transition on the steady flow results.

5.3 Unsteady simulations in the buffet regime

5.3.1 Brief test case description

After having performed conclusive preliminary studies for a steady flow case below the buffet onset boundary, the more complex unsteady shock wave/boundary layer interaction over the OAT15A airfoil is addressed. To do so, the angle of attack is increased to 3.5° to enter the buffet regime, keeping $M_\infty = 0.73$ and $Re = 3 \times 10^6$. This incidence is close to the instability onset boundary, which is at approximately 3.1° at this M_∞ though in the experiments periodic flow was not detected below $\alpha = 3.25°$ [39]. Jacquin et al. [39] described the unsteady shock wave/boundary layer interaction at 3.5° as essentially two-dimensional. The shock-wave oscillation was coupled with an intermittent boundary layer separation process, occurring at a frequency of approximately 69 Hz (or a reduced frequency $2\pi fc/U \approx 0.41$). According to that paper, the periodic flow can be summarized as follows: when the shock wave is located at its most upstream position, the boundary layer is separated from the foot of the shock to the trailing edge. As the shock starts moving downstream, the boundary layer reattaches. When the shock reaches its most downstream position, the boundary layer undergoes a progressive thickening until it separates again. The shock then starts moving upstream thus completing the cycle. Because of the flow conditions close to the buffet onset boundary and of the resulting intermittent shock-induced separation, the OAT15A test case is particularly challenging for CFD.

5.3.2 Methodology

Following the results of section 5.2.3 for the steady flow case, in the unsteady simulations the convective fluxes are discretized using the second-order TVD formulation of the Roe scheme with van Leer limiters. Time integration is performed implicitly using a second-order backward scheme in the context of the dual time-stepping method. The linear system is solved by means of the LU-SSOR scheme with 3 Gauss-Seidel sweeps and a tolerance of 10^{-3} is defined as convergence criterion. This means that the norm of the density residual is reduced by three orders of magnitude from its initial value at each time step. The physical time increment adopted is of 5×10^{-6} s, which corresponds to a non-dimensional time step of approximately 5.2×10^{-3} c/U. This value is smaller than the one used in Ref. [57] and is fairly enough for URANS simulations. The influence of the time-stepping parameters on the buffet characteristics is presented at the end of the chapter. To simulate the laminar part of the boundary layer, the eddy viscosity is set to zero upstream $x/c = 0.07$. Additional tests are also conducted to assess the effect of transition on the unsteady flow properties.

The strategy adopted in the simulations is as follows: initial flowfields are obtained from non-converged steady computations departing from an uniform field initialized with freestream properties. Such computations run for 6000 iterations, which is long enough to produce a stalled and periodic convergence history in cases where the flow unsteadiness is successfully captured. The solutions are then used to initialize the unsteady simulations, where the transient period is computed during 0.05 s of physical time. This is equivalent to about 3.5 buffet cycles and is long enough for the global forces fluctuations to reach constant amplitudes. Compared to initializations with an uniform flowfield, the procedure adopted reduces the transient period duration by about 50%. Finally, with the periodic flows well established, the physical time is reset to zero and the samplings of the flow statistics are computed for about 300 convective time scales c/U, being deliberately terminated to yield a round number of flow cycles. This results in about 20-22 buffet periods depending on the turbulence model used and is largely sufficient for the flow statistics to get converged.

5.3.3 Results for various turbulence models

5.3.3.1 Time history of lift

From the results for the steady flow at $\alpha = 2.5°$, one may expect the SA and SST turbulence models to be the best in simulating the transonic buffet over the OAT15A airfoil. Contrary to this possible misconception, both models fail in predicting the self-sustained shock-wave motion at $\alpha = 3.5°$. The time evolution of the global lift coefficient is presented in figure 5.11(a) for these models. Initially, the curves exhibit large-amplitude lift fluctuations caused by shock-wave oscillations. These are gradually damped until vanish-

ing and leading to steady flow states. Figure 5.11(b) compares the final pressure coefficient distributions obtained around the airfoil with experimental data. The spread aspect of the experimental distribution in the shock-wave region results from time-averaging. As can be noted in the figure, the shock waves predicted by the numerical simulations are straight, characteristic of steady flow. Moreover, the SST model gives a shock located more upstream than that of the SA model, which explains the lower lift obtained with the SST.

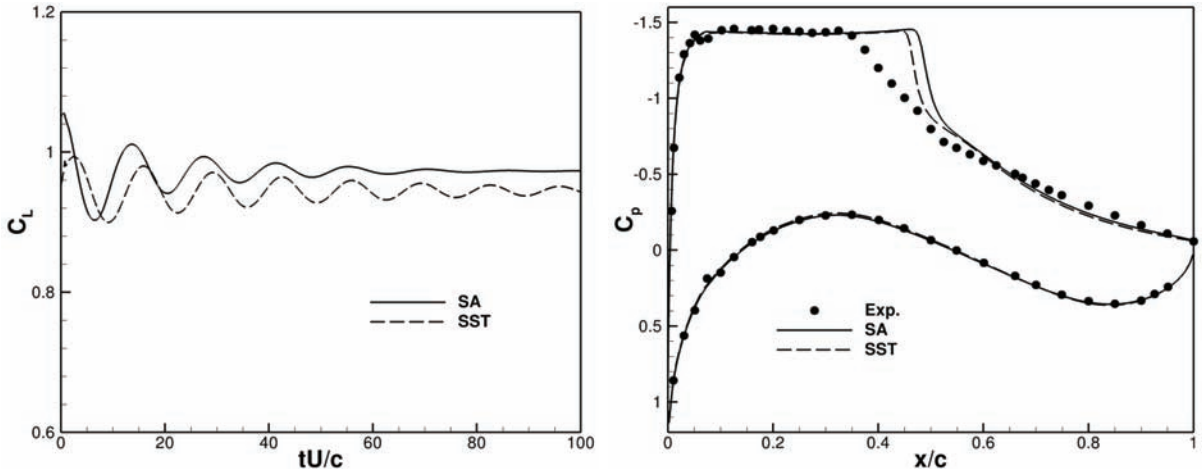

(a) Transient lift coefficient evolution

(b) Final pressure distributions

Figure 5.11: Unsteady simulation results for the SA and SST models.

The results suggest that turbulence models widely used in the aerospace industry mainly in the computation of steady flows may not be appropriate for the prediction of transonic buffet (at least close to the instability onset boundary). This limitation probably results from the hypotheses made in the development of such models and the test cases used for their calibration, which motivates the search for alternative closures more sensitive to flow unsteadiness. Regarding the SA model, the use of Secundov's compressibility correction appears as a potential candidate as it acts as a destruction term for the eddy viscosity in turbulent zones of high velocity gradients (such as the SWBLI region). By lowering the eddy-viscosity levels, the dissipative character of the turbulence model is also reduced, which may help capturing flow instabilities. As shown for the SA and EDW models for the steady flow computations at $\alpha = 2.5°$, the addition of the compressibility correction slightly lowers the eddy-viscosity levels in the boundary layer and in the near wake, tending to move the shock wave further upstream. Unfortunately, the SA+CC model has exhibited an unstable behavior during the unsteady simulation at $\alpha = 3.5°$, causing divergence. Several modifications to the time-marching method have been tried out in order to solve this issue, but no improvements have been obtained. Since the same behavior has been encountered with the original SA model at a higher angle of attack of 3.9° (and even at 3.5° depending on the numerical parameters), the problem seems to be inherent to the original SA model formulation and not related to the implementation of the compressibility correction. Moreover, when used in conjunction with

other one-equation closures such as the EDW and SALSA models (which are based on the Edwards-Chandra modification), the compressibility correction has led to rapid and smooth convergence. Indeed, the Edwards-Chandra model first appeared in a study of flows involving shock-induced separation (see Ref. [72]) to remedy stability problems related to the near-wall singular behavior of the quantity $\tilde{S}$ in the original SA model. Also, in the numerical computation of the flow around an aircraft near buffet onset conditions, Rumsey et al. [95] used a modified formulation of the SA model in order to prevent the source term from becoming negative.

On the basis of the above considerations, three models adopting the more robust Edwards-Chandra formulation of the SA model have been selected for the unsteady simulations of the present test case, namely the EDW, EDW+CC and SALSA models. Although the shock waves predicted by the EDW and EDW+CC models in the steady flow case were located too far downstream the experimental position, these models performance in the buffet regime cannot be anticipated. Furthermore, in addition to evaluating the influence of the compressibility correction in unsteady flow, the simulation with the standard EDW model also allows to assess the effect of the strain-adaptive production term of the SALSA model. Regarding two-equation closures, the WCX model has also been considered in the simulations. Assuming that the original k-ω model behaves similarly to the BSL model, one may expect it to not predict the self-sustained shock-wave motion as in tests conducted with the BSL model the solution has quickly reached a steady state.

All the four turbulence models considered in the second set of simulations have successfully predicted periodic flow. Figure 5.12(a) presents the time history of the lift coefficient obtained with each model after the transient period. The WCX model has required a transient period about three times longer than the other models for the amplitude of the fluctuations to become constant. For comparison purposes, all curves have been phased at $t = 0$ at instants of minimum lift. The figure shows quasi-sinusoidal lift curves whose main parameters are summarized in table 5.7. While the mean values and amplitudes are strongly model-dependent, the frequency of the fluctuations vary much less from one model to another.

Model	$\overline{C_L}$	ΔC_L (%)	f (Hz)	r
EDW	1.024	2.16	77.3	0.464
EDW+CC	0.9583	29.4	73.2	0.439
SALSA	0.9047	42.4	70.0	0.420
WCX	0.9727	6.45	79.9	0.479

Table 5.7: Influence of the turbulence model on the lift fluctuations.

The differences between the curves for the EDW and EDW+CC models are particularly remarkable. While with the standard model the peak-to-peak variation of lift is of about only 2%, the compressibility-corrected version of the model yields fluctuations almost 15 times larger. Such variation is a consequence of a slight reduction in the eddy-viscosity production at flow conditions close to the buffet-onset boundary, causing the flow to

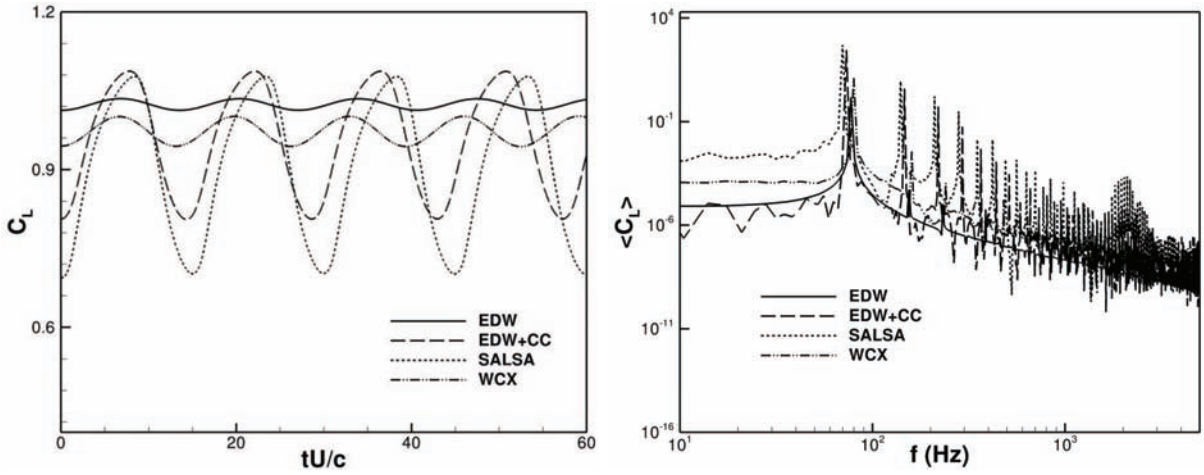

(a) Permanent lift fluctuations

(b) Power spectral densities

Figure 5.12: Time histories and spectra of the lift fluctuations for various models.

penetrate further into the instability domain. The SALSA model predicts even larger lift fluctuations compared to the EDW+CC. This effect is mainly related to the strain-adaptive production term of the SALSA model, which drastically reduces the overall eddy-viscosity levels as illustrated in figure 5.7. Finally, the WCX model results in low-amplitude lift oscillations. Compared to the steady solution produced by the BSL model, the unsteady flowfield is probably due to the use of a stress limiter in the WCX model, yielding a less dissipative k-ω model more sensitive to flow instabilities. Power spectral densities (PSD) of the lift coefficient signals after around 20 buffet periods are given in figure 5.12(b) and the main frequencies computed are indicated in table 5.7. The differences between the frequencies found for the various models are relatively small, with all values close to the experimental value ($\approx$ 69 Hz). This strongly suggests that, in all cases, the unsteadiness detected indeed corresponds to the transonic buffet phenomenon. Due to its strongly periodic character, the low-frequency instability appears well defined in the spectra. For the SALSA model, a small 'bump' can be identified around 2 kHz. The latter is actually caused by an alternate vortex shedding arising when the flow is separated and will be discussed in more detail in chapter 6.

5.3.3.2 Statistical pressure distributions

In many aspects, the ability of a turbulence model in simulating transonic buffet can be evaluated from statistical surface pressure distributions. Therefore, the mean pressure coefficient profiles for the models that have predicted unsteady flow are given in figure 5.13(a). In the experimental distribution, the spread shock-wave region indicates the actual shock-wave travel. As can be seen in the figure, the EDW and WCX models give almost straight shocks not very different from the steady profiles in figure 5.11. These are related to small shock-wave motion amplitudes, which explains the small lift fluctua-

tions observed in figure 5.12(a) for these two models. The EDW+CC and SALSA models predict shock-wave oscillation amplitudes compatible with the experimental data. For the former, the shock excursion is particularly well predicted in terms of length, covering about 20% of the chord. This suggests that the amplitude of the lift fluctuation obtained with this model should be close to the actual one. However, the shock-motion region is located somewhat downstream the experimental one, what probably overestimates the mean lift. Nevertheless, the supersonic plateau, the pressure recovery zone between the shock-wave region and the trailing edge as well as the pressure distribution on the lower surface are particularly well predicted by this model. Figure 5.14 illustrates the instantaneous Mach number fields around the airfoil obtained with the EDW+CC model with the shock wave at its most upstream and downstream positions. A detailed analysis of the buffet cycle will be given in section 5.3.4. In the shock-motion region, the SALSA model predicts a steeper distribution caused by a shock excursion which is too large. Compared to the experiments, the amplitude of the shock-wave oscillations is overestimated, resulting in very strong lift fluctuations as seen in figure 5.12(a). It is important to note that, although the SALSA model gives the best results in terms of frequency among the models considered (see table 5.7), it does not give the best prediction of the mean pressure distribution. Hence, it can be concluded that the frequency of the shock-wave motion is not necessarily the best indicator of a turbulence model ability to predict transonic buffet.

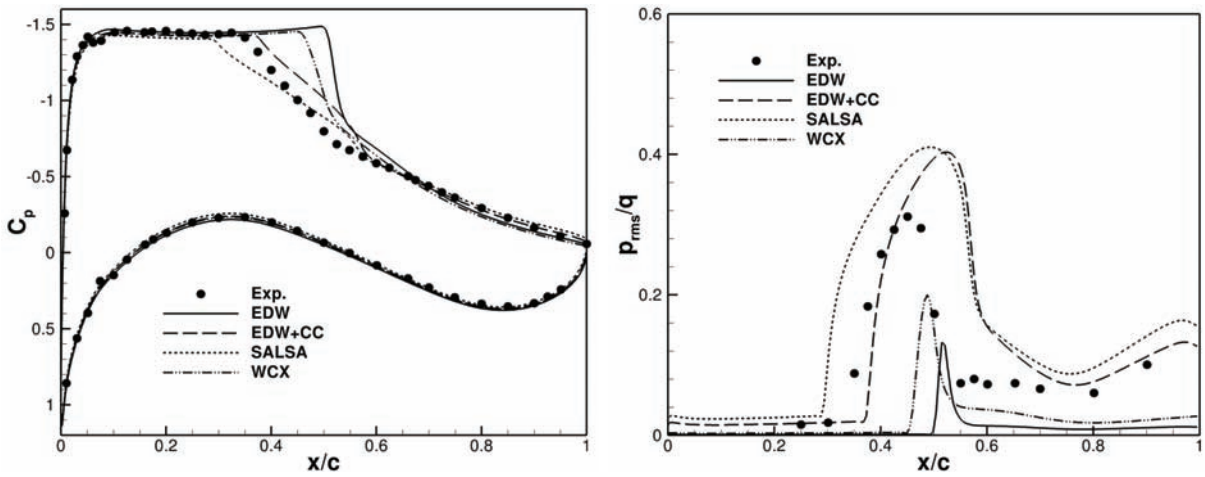

(a) Mean pressure coefficient

(b) RMS pressure on the upper surface

Figure 5.13: Statistical pressure distributions around the OAT15A airfoil.

Besides the mean surface pressure, a turbulence model suitable for unsteady flows must provide a satisfactory prediction of the unsteady pressure. Therefore, the distributions of the root mean square (RMS) of the pressure fluctuations on the upper surface of the airfoil are presented in figure 5.13(b). In the experimental data, the zone of high fluctuations is caused by strong pressure jumps caused by the shock wave passage. It also indicates the length of the shock-wave motion region. Ahead of it, nearly-constant low fluctuations levels can be observed, which are well captured by the EDW+CC model

and slightly overestimated by the SALSA model. With the latter, the shock wave goes too far upstream compared to the experiments, whereas the EDW+CC model predicts the upstream shock-motion limit much closer to the experimental data. These two models reach approximately the same peak value, overestimating the experiments by about 25%. Besides, the rear limits of the shock excursion are also very similar, being located too far downstream the experimental position. Whereas the experiments indicate an almost flat distribution just downstream the shock motion range, the turbulence models tend to overpredict the fluctuations levels in that area. The progressive increase in the pressure fluctuations along the rear part of the upper surface is mainly caused by flow separation phenomena. This region is reasonably well predicted by both the EDW+CC and SALSA models, with the former being more accurate. For the EDW and WCX models, the pressure fluctuation distributions are everywhere far from the experimental profile. Both closures give virtually zero fluctuations ahead of the shock, quite narrow shock-wave motion ranges with low peak levels and weak activity between the shock and the trailing edge. The results clearly indicate that, for the present test case, the transonic buffet phenomenon is not well predicted by these two models, which will be therefore no longer considered in the present thesis.

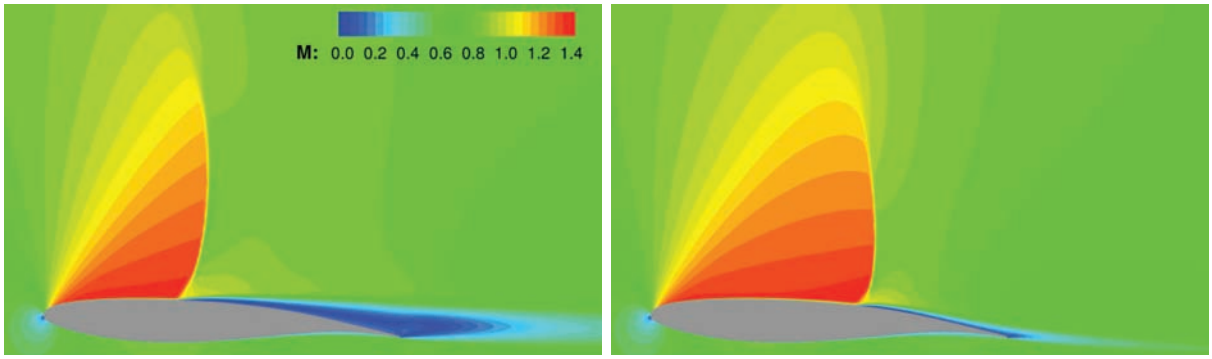

(a) Shock wave at its most upstream position (b) Shock wave at its most downstream position

Figure 5.14: Instantaneous Mach number fields during transonic buffet.

5.3.3.3 Statistical velocity profiles

In addition to the surface pressure properties, the statistical velocity fields in the vicinity of the airfoil may provide conclusive information for the assessment of turbulence models. In this way, the mean longitudinal velocity profiles at four different stations along the upper surface are presented in figure 5.15. In the figure, the y-coordinate is measured from the surface in the direction normal to the chord at each station. From now on, only the EDW+CC and SALSA models are considered as only they have provided satisfactory prediction of the experimental statistical pressure distributions. The first station is located at $x/c = 0.28$ from the leading edge (measured along the chord line) and remains always ahead of the shock wave during buffet. At that position, the boundary layer is

always attached and there are no appreciable differences between the velocity profiles obtained with the EDW+CC and SALSA models, which are in good agreement with the experiments. The station at $x/c = 0.45$ is located close to the experimental mean shock-wave position ($x/c \approx 0.44$). For both turbulence models, this station also lies within the shock-motion range, so that the unsteady shock wave can move either upstream or downstream. At that position, the outer velocity of the SALSA model is somewhat lower than the experimental one, whereas the EDW+CC gives a more accurate value. For the latter, the mean boundary layer is slightly thinner than in the experiments as the shock-wave motion occurs somewhat downstream. Because with the SALSA model the shock wave goes too far upstream, the thickness of the mean boundary layer at that position is larger than in the experiments. The third station is located at $x/c = 0.60$, which is always behind the shock wave during buffet. Whereas both turbulence models give the correct outer flow velocity, they underestimate the height of the mean recirculation. Overall, the EDW+CC model is superior to the SALSA model, especially between $y/c = 0.02$ and 0.04. The last profiles are for $x/c = 0.75$, where both models predict reasonably well the experimental profile. Nevertheless, the EDW+CC model is remarkably closer to the experiments than the SALSA over the whole range of measurements.

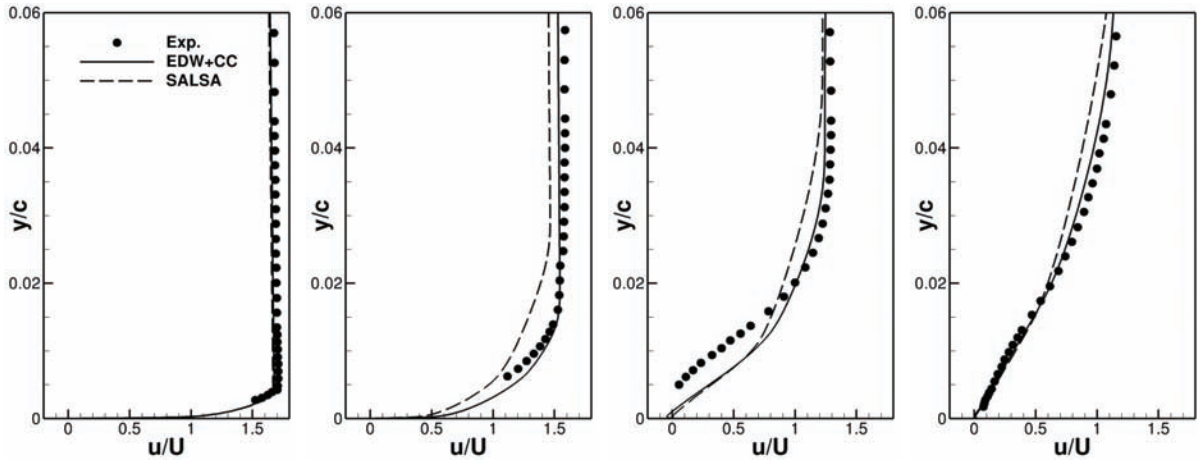

(a) $x/c = 0.28$ (b) $x/c = 0.45$ (c) $x/c = 0.60$ (d) $x/c = 0.75$

Figure 5.15: Mean longitudinal velocity profiles on the upper surface.

The RMS profiles of the longitudinal velocity fluctuations at the same four stations are shown in figure 5.16. At $x/c = 0.28$, both the EDW+CC and SALSA models give virtually zero fluctuations. The experimental profile, however, exhibits a certain level of unsteadiness in the boundary layer, as can be seen in the lower part of the figure. This may be related to disturbances created by the transition strips placed upstream or may be due to turbulence or wave propagation in the boundary layer. Within the shock-wave motion range at $x/c = 0.45$, the turbulence models tend to overestimate the fluctuation levels. Nevertheless, the EDW+CC model is much closer to the experimental data than the SALSA model. At $x/c = 0.60$ and $x/c = 0.75$, the profiles for the EDW+CC model are in good agreement with the measurements. The agreement at $x/c = 0.75$ is remarkably

good. On the contrary, the SALSA model keeps overestimating the fluctuations, though the experimental profiles are qualitatively well predicted.

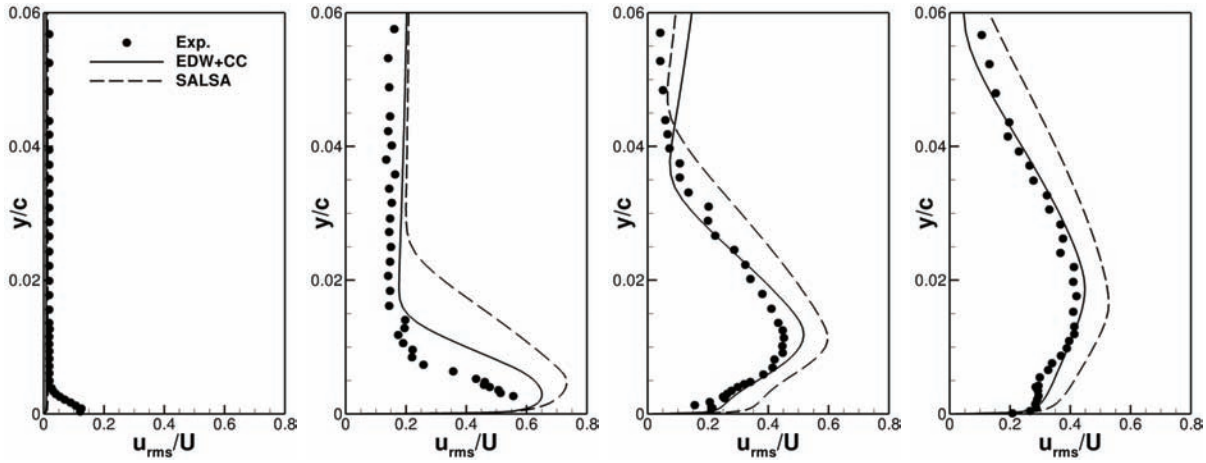

(a) $x/c = 0.28$ (b) $x/c = 0.45$ (c) $x/c = 0.60$ (d) $x/c = 0.75$

Figure 5.16: RMS profiles of the longitudinal velocity fluctuations.

5.3.4 Analysis of the shock wave/boundary layer interaction

The experiments of Jacquin et al. [39] showed that, at $M_\infty = 0.73$ and $\alpha = 3.5°$, the transonic buffet over the OAT15A airfoil was characterized by a coupling between the shock-wave motion and the intermittent boundary layer separation. Therefore, the EDW+CC model has been selected for an investigation of the unsteady flowfield topology as predicted numerically because of its superiority in the prediction of the statistical pressure distributions and velocity profiles. Following the procedure adopted in the experiments, the periodic flow is split in 20 phases where phase 1 corresponds to the moment when the shock wave is at its most upstream position. Since in the numerical simulation all turbulence scales are modeled and the resulting flow is strictly periodic, it is reasonable to assume an instantaneous flowfield as equivalent to a phase-averaged one. In this way, the instantaneous Mach number distributions and streamlines for a few selected flow phases are illustrated in figure 5.17. At phase 1, the shock wave has zero velocity and the boundary layer is separated from the foot of the shock to the trailing edge as evidenced by the large separation bubble in figure 5.17(a). As the shock starts moving downstream, the boundary layer reattaches and, at phase 5 (figure 5.17(b)), there is only a small region of rear separation near the trailing edge. This condition agrees with the phase-averaged LDV measurements in Ref. [39]. At phase 9 (figure 5.17(c)), the shock wave is still moving downstream and the boundary layer is completely attached. The shock then reaches its most downstream position and the boundary layer undergoes a progressive thickening until the flow separates again. The analysis of the instantaneous streamlines and velocity profiles indicates that separation develops from the shock towards the trailing edge through the continuous growth of the separation bubble originated at the foot of the

shock wave. Figure 5.17(d) shows an intermediate state of this process, which is already concluded in phase 13 (figure 5.17(e)). In the simulation, during the shock-wave motion towards the leading edge, the recirculation zone steadily increases but never transforms into a separated shear layer and no vortex shedding nor trailing edge instability is noticed. The shock then arrives at its most upstream position thus completing the cycle.

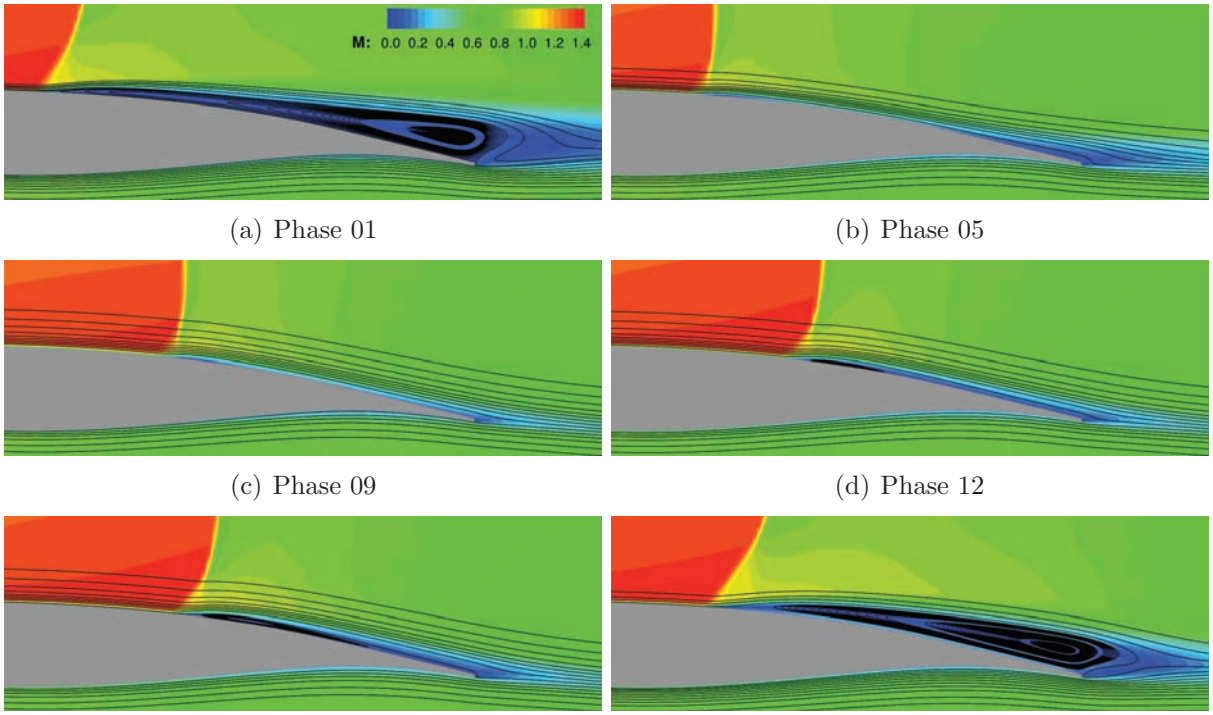

(a) Phase 01 (b) Phase 05

(c) Phase 09 (d) Phase 12

(e) Phase 13 (f) Phase 17

Figure 5.17: Mach number fields and streamlines at different flow phases.

The instantaneous velocity profiles at $x/c = 0.60$ on the upper surface at five different phases are compared with experimental phase-average LDV measurements in figure 5.18. As expected, for phases 01, 13 and 17, the boundary layer is locally separated as in the experiments. However, the turbulence model fails in predicting the correct size of the recirculation, which is particularly underestimated at phase 13. For the latter, the outer velocity strangely diverges from the experimental value above $y/c = 0.04$. At phase 17, however, the agreement between simulation and experiment is excellent over the whole curve. When the flow is attached (phase 05 and 09), the profiles describe qualitatively well the phase-averaged ones. Nevertheless, differences in the boundary-layer thickness and outer velocities can be observed. Generally speaking, the discrepancies observed in the profiles can be explained by the fact that, compared to the experiments, the shock-wave motion region in the numerical simulation is located somewhat downstream.

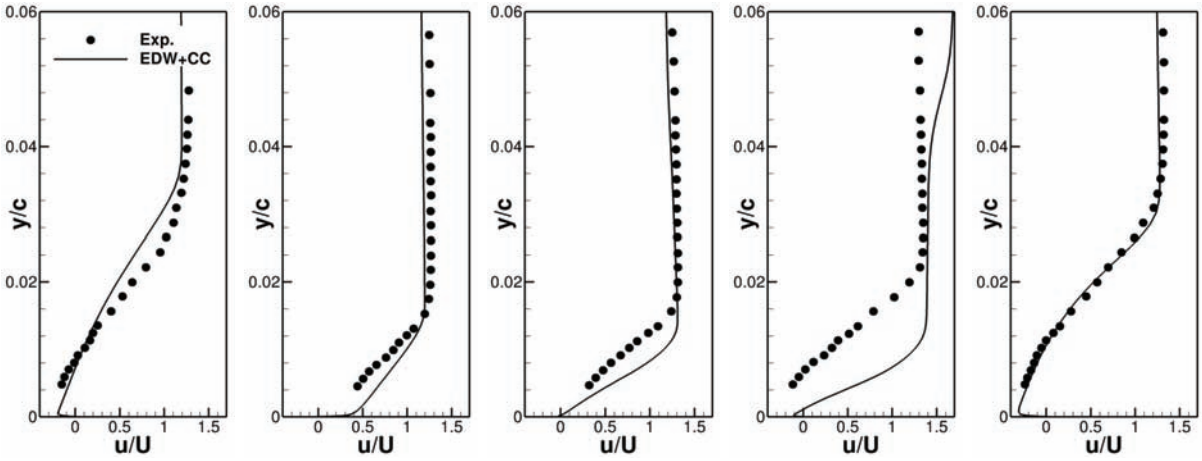

(a) Phase 01 (b) Phase 05 (c) Phase 09 (d) Phase 13 (e) Phase 17

Figure 5.18: Phase-averaged and instantaneous velocity profiles.

5.3.5 Effect of time-stepping parameters and of transition

In subsection 5.3.2, a physical time step of 5×10^{-6} s ($\approx 5.2\times10^{-3}\ c/U$) has been adopted and assumed as sufficiently small for the two-dimensional simulations using linear eddy-viscosity models. This choice was supported by other studies in literature on the same configuration (see, for instance, Ref. [57]). Similarly, based on experience, a tolerance threshold of 10^{-3} has been prescribed for the convergence criterion of the dual time-stepping method with no further justifications. The aim of the present section is to evaluate the suitability of both choices by investigating the influence of these parameters on the transonic buffet properties. Besides, the effect of simulating laminar boundary layer ahead of the experimental tripping line is examined for the present unsteady flow case.

Figure 5.19(a) presents the time histories of the lift coefficient obtained with different convergence criteria based on tolerance thresholds varying from 10^{-1} to 10^{-4}. All simulations adopt the same time step ($\Delta t = 5\times10^{-6}$ s) and are initialized with the same flowfield obtained from a non-converged steady computation (with local time stepping) using the EDW+CC model. The figure shows that, for the given time step, a threshold $\epsilon = 10^{-1}$ is too large for the shock-wave oscillations to be self sustained. Although a value of 10^{-2} results in periodic flow, it is clearly not small enough for the amplitude of the lift fluctuations (and therefore of the shock-wave motion) to be fully captured. From the figure, it can be noted that a threshold of 10^{-3} results in lift oscillations very similar to those obtained with $\epsilon = 10^{-4}$. Hence, the choice made in subsection 5.3.2 is justified. By that convergence criterion, the typical number of inner iterations required at each time step varies from 30 to 50 during buffet depending on whether the flow is attached or separated.

The time histories of lift after the transient period obtained for $\epsilon = 10^{-3}$ with three

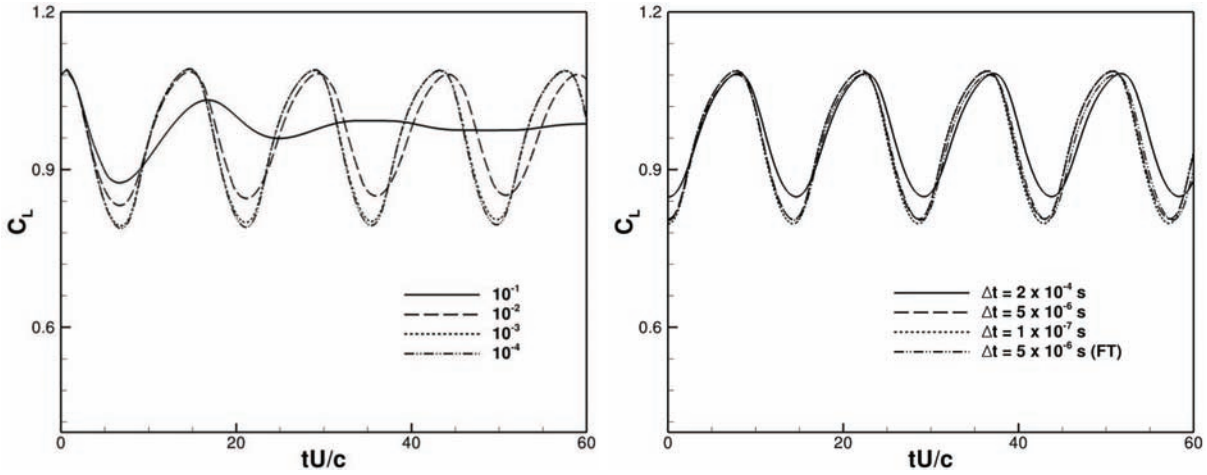

(a) Inner loop tolerance

(b) Physical time step

Figure 5.19: Influence of time-stepping parameters on the lift fluctuations.

different physical time steps are presented in figure 5.19(b). In addition to the time step adopted in the previous simulations (i.e., 5×10^{-6} s or $\approx 5.2 \times 10^{-3}$ c/U), the values $\Delta t = 2 \times 10^{-4}$ s ($\approx 2.1 \times 10^{-1}$ c/U) and $\Delta t = 1 \times 10^{-7}$ s ($\approx 1.0 \times 10^{-4}$ c/U) are also considered. An extra simulation for $\Delta t = 5 \times 10^{-6}$ s assuming fully-turbulent behavior (i.e., no boundary layer tripping) is also performed, being identified by the acronym FT. For the sake of comparison, all curves are reset in time so that $t = 0$ correspond to an instant of minimum lift. The distributions of the mean pressure coefficient and of the pressure RMS for each simulation are given in figures 5.20(a) and 5.20(b), respectively. As can be noted, the large-scale shock-wave motion is successfully predicted even when adopting the largest time step, which gives about only 70 time steps per buffet period. In that case, however, as revealed by figures 5.19(b) and 5.20(a), the amplitudes of the shock-wave oscillations and lift fluctuations are smaller than when using finer time steps, resulting in less intense pressure fluctuations as evidenced by figure 5.20(b). Nevertheless, such behavior cannot be attributed only to the time step adopted as the inner-loop convergence criterion has been shown to have an equally-important effect on the buffet properties, being the ideal tolerance threshold itself time-step dependent. The differences between the C_L and C_p curves for $\Delta t = 5{\times}10^{-6}$ s and $1{\times}10^{-7}$ s are too small to justify the adoption of the smallest time step. Hence, the temporal resolution used in this chapter can be considered as sufficiently small for URANS simulations of transonic buffet. This conclusion is also supported by the power spectral densities of the lift signals (not shown here).

The comparison between the results obtained for the fully-turbulent and tripped cases confirms that accounting for the laminar boundary layer ahead $x/c = 0.07$ is not crucial for the present configuration. Indeed, the effect of this short laminar region on the unsteady shock wave/boundary layer interaction downstream is negligible and is similar to that of the steady flow case presented in subsection 5.2.6, slightly shifting the whole

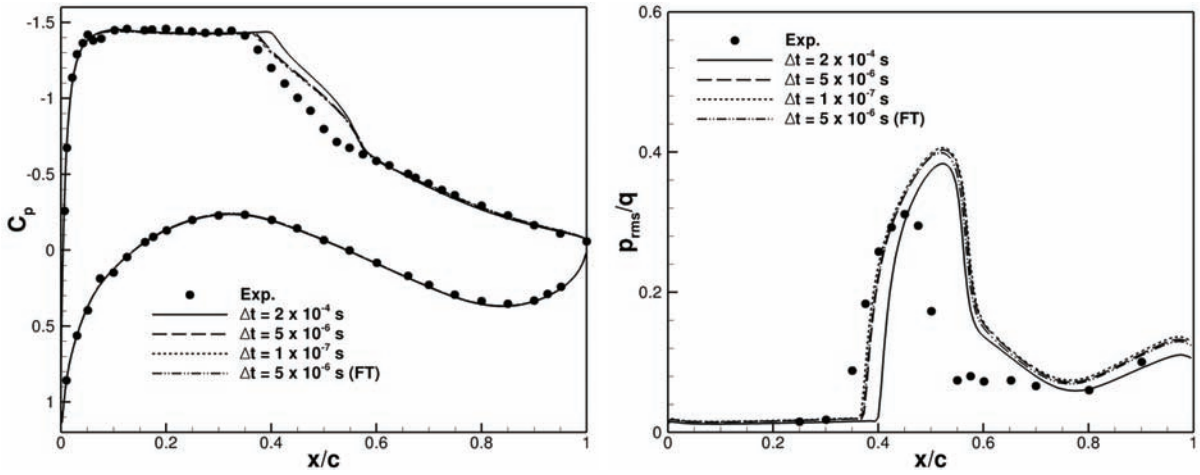

(a) Mean pressure coefficient

(b) RMS pressure on the upper surface

Figure 5.20: Effect of the time step on the statistical pressure distributions.

shock-wave motion region downstream.

Chapter 6

Turbulence-Resolving Simulation of Transonic Buffet

Contents

6.1 Introduction

In chapter 5, two-dimensional simulations of transonic flows over the OAT15A supercritical at incidences below and above the buffet onset boundary were presented. Results for various one- and two-equation linear eddy-viscosity turbulence models commonly used in aerodynamics showed that the flow properties in the shock wave/boundary layer interaction region are highly model-dependent. In the buffet regime, the best agreement with the experiments was obtained using the one-equation model of Edwards and Chandra with compressibility correction (EDW+CC). The closure provided a good prediction of the basic features of the unsteady flowfield, including the shock-wave motion amplitude. In the present chapter, a three-dimensional simulation of the transonic buffet over the OAT15A airfoil is performed with the aim of assessing the suitability of turbulence-resolving approaches to the present test case. The method of choice is the Delayed Detached-Eddy Simulation (DDES) of Spalart et al. [89], which was presented in detail in section 4.4.3. Since DES-type approaches are originally intended to massively separated flows, the OAT15A test case should be considered as an extended application of the DDES method as it features an intermittent separation that remains restricted to a thin layer whose size is comparable to the airfoil thickness. Since the performance of a hybrid RANS-LES method is intimately related to the behavior of the underlying RANS model, the present DDES is based on the EDW+CC model as it has provided a good prediction of the transonic buffet properties.

6.2 Turbulence modeling approach

6.2.1 Motivations

The choice of the DDES approach for the present study is justified by some of the same issues that motivated its creators to improve the standard Detached-Eddy Simulation (DES) method. In the case of the Spalart-Allmaras model and of other one-equation closures based on its transport equation such as the EDW and SALSA models, the original DES formulation takes the RANS length scale as the wall distance (see equation 4.39). Therefore, the switching between RANS and LES is dictated only by local grid parameters (i.e., Δ and d), being independent of any flow variable and consequently unvarying in time (at least for static grids). The problem with this formulation is that, for grids considerably refined in the tangential direction, the RANS mode may be reduced to a very thin layer around the body. This can result in the modeled-stress depletion issue (MSD) [89] discussed in section 4.4.3, which in the most critical cases can lead to grid-induced separation [92]. For a proper resolution of the moving shock wave on the upper surface, the present planar grid is considerably finer than the RANS grids typically used in industry for airfoil computations. Furthermore, in the OAT15A test case, the boundary

layer gets substantially thick during buffet, especially when the shock is about its most downstream position just before separation occurs. Therefore, the boundary layer may become much thicker than the RANS region from a standard DES, which can result in the erroneous activation of the LES mode near the surface without the appropriate spatial resolution. On the contrary, the DDES method should detect and shield the boundary layer from LES by means of the redefined model length scale using the function f_d (see equation 4.43), thus forcing the whole shock wave/boundary layer interaction to be treated in RANS.

6.2.2 Model formulation

The proposed approach is a Delayed Detached-Eddy Simulation based on the Edwards-Chandra modified Spalart-Allmaras model with the compressibility correction of Secundov. It uses a single transport equation for the modified eddy viscosity $\tilde{\nu}$ taken from the EDW model (section 4.2.2.1), to which the compressibility correction term (equation 4.19) is added on the right-hand side, yielding:

$$\frac{D\tilde{\nu}}{Dt} = c_{b1}\tilde{S}\tilde{\nu} + \frac{1}{\sigma}\frac{\partial}{\partial x_k}\left[(\nu+\tilde{\nu})\frac{\partial\tilde{\nu}}{\partial x_k}\right] + \frac{c_{b2}}{\sigma}\frac{\partial\tilde{\nu}}{\partial x_k}\frac{\partial\tilde{\nu}}{\partial x_k} - c_{w1}f_w\left(\frac{\tilde{\nu}}{l}\right)^2 - c_5\frac{\tilde{\nu}^2}{a^2}\frac{\partial u_i}{\partial x_j}\frac{\partial u_i}{\partial x_j}. \quad (6.1)$$

The eddy viscosity is computed by

$$\nu_t = \tilde{\nu}f_{v1}, \qquad \text{where} \qquad f_{v1} = \frac{\chi^3}{\chi^3 + c_{v1}^3} \qquad \text{and} \qquad \chi = \frac{\tilde{\nu}}{\nu}. \quad (6.2)$$

The remaining functions read:

$$\tilde{S} = S\left(\frac{1}{\chi} + f_{v1}\right), \qquad S = \left[\left(\frac{\partial u_i}{\partial x_j} + \frac{\partial u_j}{\partial x_i}\right)\frac{\partial u_i}{\partial x_j} - \frac{2}{3}\left(\frac{\partial u_k}{\partial x_k}\right)^2\right]^{\frac{1}{2}}, \quad (6.3)$$

$$f_w = g\left(\frac{1+c_{w3}^6}{g^6+c_{w3}^6}\right)^{1/6}, \qquad g = r + c_{w2}\left(r^6 - r\right). \quad (6.4)$$

and

$$r = \frac{\tanh\left[\tilde{\nu}/\left(\tilde{S}\kappa^2 l^2\right)\right]}{\tanh 1.0} \quad (6.5)$$

The model length scale l appears in the destruction term both explicitly and implicitly by means of the function f_w (through the near-wall parameter r). Instead of computing l as the wall distance d as in the RANS model, the DDES length scale is adopted to allow for LES far from the surface:

$$l = l_{\text{DDES}} = d - f_d \max\left(0, d - C_{\text{DES}}\Delta_{\max}\right). \quad (6.6)$$

In the subgrid length scale, $\Delta_{\max} = \max(\Delta_i, \Delta_j, \Delta_k)$ is the largest local grid spacing. Based on the study by Shur et al. [96] with the SA model in decaying homogenous isotropic turbulence, the constant C_{DES} is taken as 0.65 (far from the wall, the EDW and SA models become equivalent). The delaying function f_d is defined as:

$$f_d = 1 - \tanh\left[(8r_d)^3\right], \qquad \text{where} \qquad r_d = \frac{\nu_t + \nu}{S_d \kappa^2 d^2} \qquad \text{and} \qquad S_d = \sqrt{\frac{\partial u_i}{\partial x_j}\frac{\partial u_i}{\partial x_j}}. \quad (6.7)$$

The constants of the model are taken as:

$$c_{v1} = 7.1, \qquad c_{b1} = 0.1355, \qquad c_{b2} = 0.622, \qquad \sigma = 2/3, \qquad \kappa = 0.41,$$
$$c_{w1} = \frac{c_{b1}}{\kappa^2} + \frac{1 + c_{b2}}{\sigma}, \qquad c_{w2} = 0.3, \qquad c_{w3} = 2 \qquad \text{and} \qquad c_5 = 3.5. \quad (6.8)$$

6.3 Grid and numerical aspects

Turbulence-resolving simulations have no meaning unless the computational domains are three-dimensional, even for purely two-dimensional geometries such as an airfoil of infinite span. Besides, the domain size and the number of grid cells in the third direction must be sufficiently large for reproducing the three-dimensional character of turbulence (according to Spalart [88], a proper DES must have at least ≈ 25 grid cells in each direction). Ideally, a numerical simulation of a wind tunnel experiment should consider a computational domain as close as possible to the actual tunnel dimensions. In practice, however, this usually leads to prohibitive grid sizes, so that an alternative solution has to be searched. A common approach for two-dimensional geometries is to consider a reduced domain extent in the third direction and treat the lateral boundaries with periodic conditions. In the OAT15A test case, this approximation seems to be reasonable as the experiments showed the flow in the central portion of the airfoil to be essentially two-dimensional [39]. Therefore, because the low frequency associated with transonic buffet makes scale-resolving simulations of the phenomenon very expensive, the present study is based on a simplified three-dimensional domain.

The first step in the grid generation is to define the airfoil span length L_z. This task is not trivial as, at this stage, it is difficult to estimate the scales of the three-dimensional flow. In the present work, the choice of the span length follows the analogy made by Deck [4] between the thickness of an airfoil and the height H of a backward-facing step. According to Deck, in the case of the flow over a step, a domain width of $4H$ is a minimum to capture the largest transverse wavelengths. Assuming that in the case of an airfoil at low angle of attack the maximum height of the separation region is of about a half of the airfoil thickness e, then $L_z \approx 2e$ would be a minimum span length to simulate the largest flow scales. Since for the OAT15A airfoil $e = 0.123\,c$, this corresponds to $L_z = 0.246\,c$. Hence, a span of $L_z = 0.26\,c$ has been adopted in the present simulation. The three-dimensional

grid is then obtained by distributing equally-spaced copies of the planar grid presented in section 5.2.1 in the spanwise direction. In DES-like methods there is no reason for adopting a transverse grid spacing Δ_k much smaller than Δ_i as the subgrid length scale in the LES mode is based on the largest local grid spacing. Therefore, to obtain $\Delta_k \approx \Delta_i$ over the rear part of the airfoil and in the near wake, 64 grid cells have been generated in the spanwise direction, resulting in a three-dimensional grid with approximately 8.3-million cells (the planar grid has 130.000 cells). The final airfoil geometry and the detail of the surface grid near the trailing edge are illustrated in figure 6.1. Because the present three-dimensional simulation is very demanding in terms of computational resources, the grid has been split into 512 blocks for efficient parallel computing. Due to the reduced span length considered, periodic conditions are prescribed for the lateral boundaries. The present grid has been classified as 'mandatory' in the ATAAC European project.

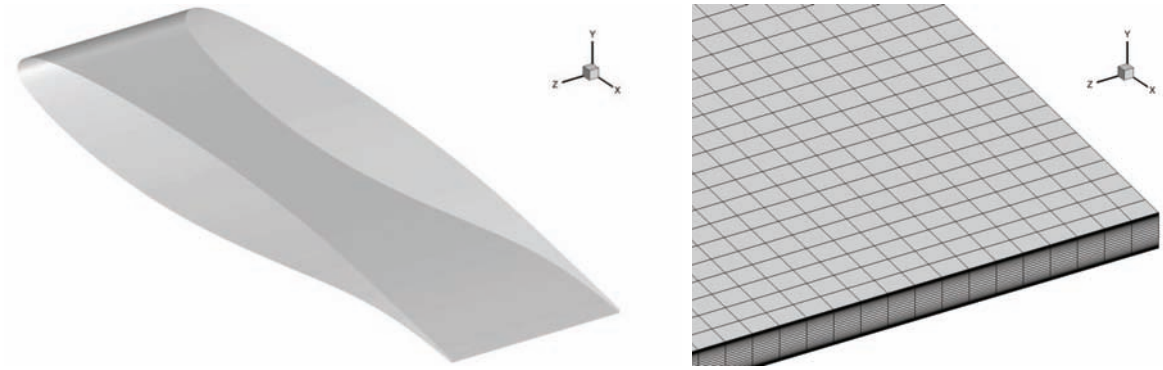

Figure 6.1: Airfoil geometry and surface grid near the trailing edge.

The numerical method of the three-dimensional simulation is similar to that of the two-dimensional simulations in chapter 5 (see section 5.2.1 for details). As one of the few differences, the accuracy of the Roe scheme with van Leer limiters is increased to third order to improve the resolution of the flow structures. The time integration procedure remains unchanged except by the reduction of the physical time step to $1{\times}10^{-7}$ s ($\approx 1{\times}10^{-4}$ c/U), which is five times smaller than the time increment adopted by Deck [4] for the ZDES of the same flow. In terms of CFL number, the present time step corresponds to values varying between 1 and 2.5 during buffet. At each time step, convergence is reached when the norm of the density residual is reduced by three orders of magnitude. Laminar boundary layer is imposed upstream $x/c = 0.07$ by setting $\nu_t = 0$ to simulate the tripping technique used in the experiments of Ref. [39]. The strategy of simulation is also very similar to that in chapter 5. First, 6000 iterations in steady mode (with local time stepping) are performed departing from an uniform flowfield with freestream properties in order to obtain a shorter transient. Then, the time-accurate computation of the transient period is conducted, which in the present case has required about 5 to 6 buffet cycles for the phenomenon to get fully developed. The physical time is then reset to zero and for the sampling of the flow statistics in the permanent unsteady regime. Contrary to the two-dimensional simulations of chapter 5, which have run for physical times equivalent

to around 300 convective time scales c/U, the three-dimensional simulation has run for a time of approximately 120 c/U. More precisely, 9 buffet periods have been simulated instead of 21 as for the EDW+CC model in two dimensions. Nevertheless, this duration has been proven to be long enough to guarantee the convergence of the statistical flow properties. This reduction has been necessary due to the high computational cost of the simulation and the resources available. In order to better evaluate the hybrid RANS-LES approach, the results are compared to those of the two-dimensional simulation using the EDW+CC model and the same time step (1×10^{-7} s). For convenience, in all figures the three-dimensional simulation is simply denoted by 'DDES' and the two-dimensional one by 'URANS'.

6.4 Simulation results

6.4.1 Time history of lift

As expected, the present hybrid simulation has predicted the self-sustained large-scale shock-wave motion at the experimental angle of attack of 3.5°. The time histories of the lift coefficient after the transient period for both the DDES and URANS simulations are presented in figure 6.2(a). For comparison purposes, the time scales have been intentionally reset to zero at instants of maximum lift. Compared to the URANS simulation, the DDES is less regular and exhibits secondary fluctuations at higher frequencies during the lift fall in each cycle. These are related to a strong vortex shedding during separation and are discussed in section 6.4.2. As it can be noted, the amplitude of the fluctuations also varies from one cycle to the other. The mean lift coefficient obtained with the DDES is somewhat lower than that of the URANS simulation, decreasing from 0.956 to 0.934. This variation suggests that the mean shock-wave position in the DDES is located somewhere upstream that of the URANS simulation. Besides, a slight drop in the average amplitude of the lift fluctuations is also observed.

The power spectral densities of the two lift coefficient signals are given in figure 6.2(b). Because the DDES signal is shorter and less periodic, the peaks in the spectrum associated to the buffet frequency and its harmonics are not as well defined as in the case of the URANS simulation. The analysis indicates for the DDES a main frequency of $f = 80.5$ Hz, which is higher than that of the URANS computation (73.2 Hz) and than the experimental frequency (≈ 69 Hz). Besides, the PSD of the DDES signal presents a 'bump' at high frequencies generated by the secondary fluctuations seen in the lift curve. This bump is centered at approximately $35f$ and suggests that the vortex shedding frequency varies in time.

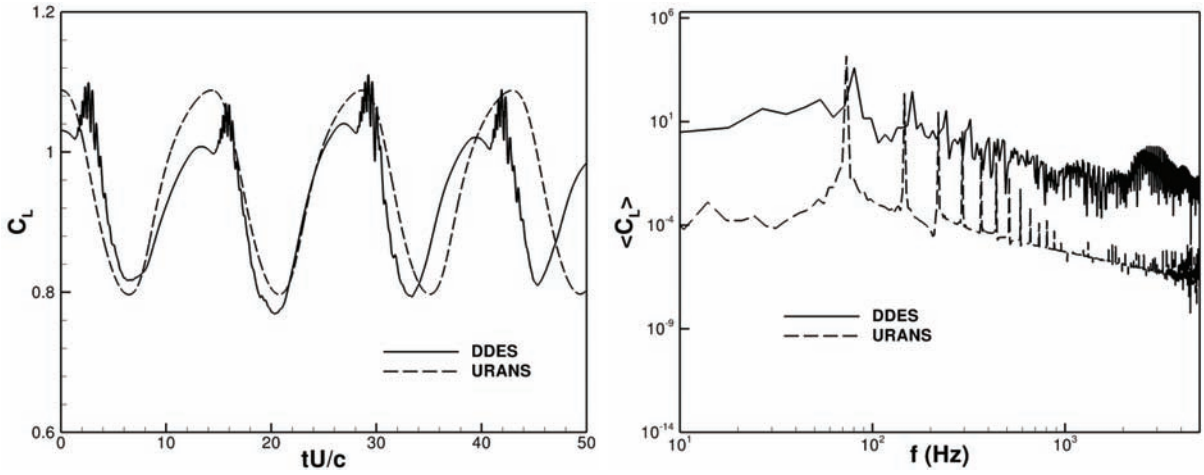

(a) Permanent lift evolutions

(b) Power spectral densities

Figure 6.2: Time histories and spectra of the lift coefficient.

6.4.2 Flow topology analysis

6.4.2.1 Global buffet dynamics

In chapter 5, the flowfield evolution during buffet was described for the URANS simulation by means of instantaneous Mach number fields, streamlines and boundary layer profiles for a few selected flow phases. For the DDES, the transonic buffet dynamics is analyzed with the help of two series of snapshots. Figure 6.3 presents for a given buffet period the fields of transverse vorticity on the mid-plane at several instants. For a better visualization of the three-dimensional flow features especially of the eddies resolved by the DDES, the corresponding isosurfaces of vorticity magnitude for $Wc/U = 10$ are given in figure 6.4. In the two sets of figures, $t^* = tU/c$ is a non-dimensional time scale where $t^* = 0$ has been arbitrarily chosen as an instant of maximum lift. At that moment, the shock wave is at its most downstream position as illustrated in figures 6.3(a) and 6.4(a) and, besides the separation bubble at the foot of the shock, a small area of rear separation also exists. These two grow simultaneously until they eventually fuse into a large separation extending from the shock wave to the trailing edge, which is followed by the initial stages of the shock-wave travel upstream, represented in figures 6.3(b) and 6.4(b). The figures also show the amplification of the von Kármán instability, which quickly gives rise to alternate vortex shedding where the coherent structures are initially two-dimensional as seen in figure 6.4(c). Although the experiments of Jacquin et al.[39] do not mention such vortices, this kind of phenomenon has been reported in several works on subsonic compressible flows over slender bodies [36]. Kármán vortices become particularly important at lower Reynolds numbers as revealed in the direct simulation of transonic buffet by Bourdet et al. [97].

During the shock motion towards the leading edge, the height of the separated region

increases causing a dramatic fall in lift and the wake develops a spanwise undulation. The early stage of this process is seen in figure 6.4(d), and, in figures 6.4(e) and 6.4(f), the wake is already strongly three-dimensional. Besides the eddies resulting from the breakdown of the primary vortices, small resolved structures can also be observed in the separated region. Figures 6.3(e) and 6.4(e) correspond to the instant when the shock wave is located at its most upstream position during buffet. At that moment, the boundary layer is still separated but the instant of minimum lift arises only during the shock travel upstream at the instant illustrated in figures 6.3(g) and 6.4(g). During the motion, the size of the separation decreases again until the boundary layer completely reattaches at some instant between those depicted in figures 6.3(g) and 6.3(h). As the shock moves further downstream, the boundary layer thickness gets progressively smaller and the von Kármán instability is damped, causing the vortex shedding to vanish as seen from figures 6.3(i) to 6.3(l). When the shock wave is about its most downstream position, the wake appears to be steady as observed in figures 6.3(l) and 6.4(l). The shock then reaches the end of its travel and the flow cycle restarts.

In the transonic buffet over the OAT15A airfoil, the alternate vortex shedding when the flow separates is sufficiently strong to affect even the global lift. Indeed, the effect of such vortices can be seen in the time history of lift presented in figure 6.2(a) in the form of secondary oscillations of higher frequency. These become especially visible during the lift falls due to separation. Within a given buffet period, the size of the vortex cores as well as the distance between two consecutive vortices vary considerably. This phenomenon can be noticed when comparing the vortex streets of figures 6.3(b) and 6.3(i), for example. It is intimately related to the changes in the height of the separation caused by the moving separation point. In other words, the airfoil and the transforming viscous regions around it compose an effective body seen by the flow whose signature also evolves in time. From a spectral point of view, this effect is responsible for the 'bump' observed at higher frequencies in the PSD of the lift signal shown in figure 6.2(b). The frequency range of the bump indicates the different frequencies assumed by the von Kármán instability as the geometry of the effective body varies during buffet. Such bumps may actually appear even in the spectra of URANS simulations as seen in figure 5.12(b) for the SALSA model, where the trailing edge instability has yielded no vortex shedding.

In respect to the transition to three-dimensional flow, the initially two-dimensional coherent structures appear to develop a secondary instability according to a preferential spanwise wavelength. The phenomenon is similar to the wake transition investigated experimentally by Williamson [98] and numerically in the direct simulations of Persillon et al. [99] for a circular cylinder in incompressible flow. Regarding transonic flow around wings, the phenomenon has also been studied in the direct numerical simulation of Bourdet et al. [97]. Navier-Stokes computations of transonic buffet and shock-vortex interaction have also been performed by Bouhadji and Braza at moderate Reynolds numbers [100, 101]. Figure 6.5 gives a series of snapshots of the surface pressure in the area behind the shock wave and shows how the patters transform from strictly two-dimensional

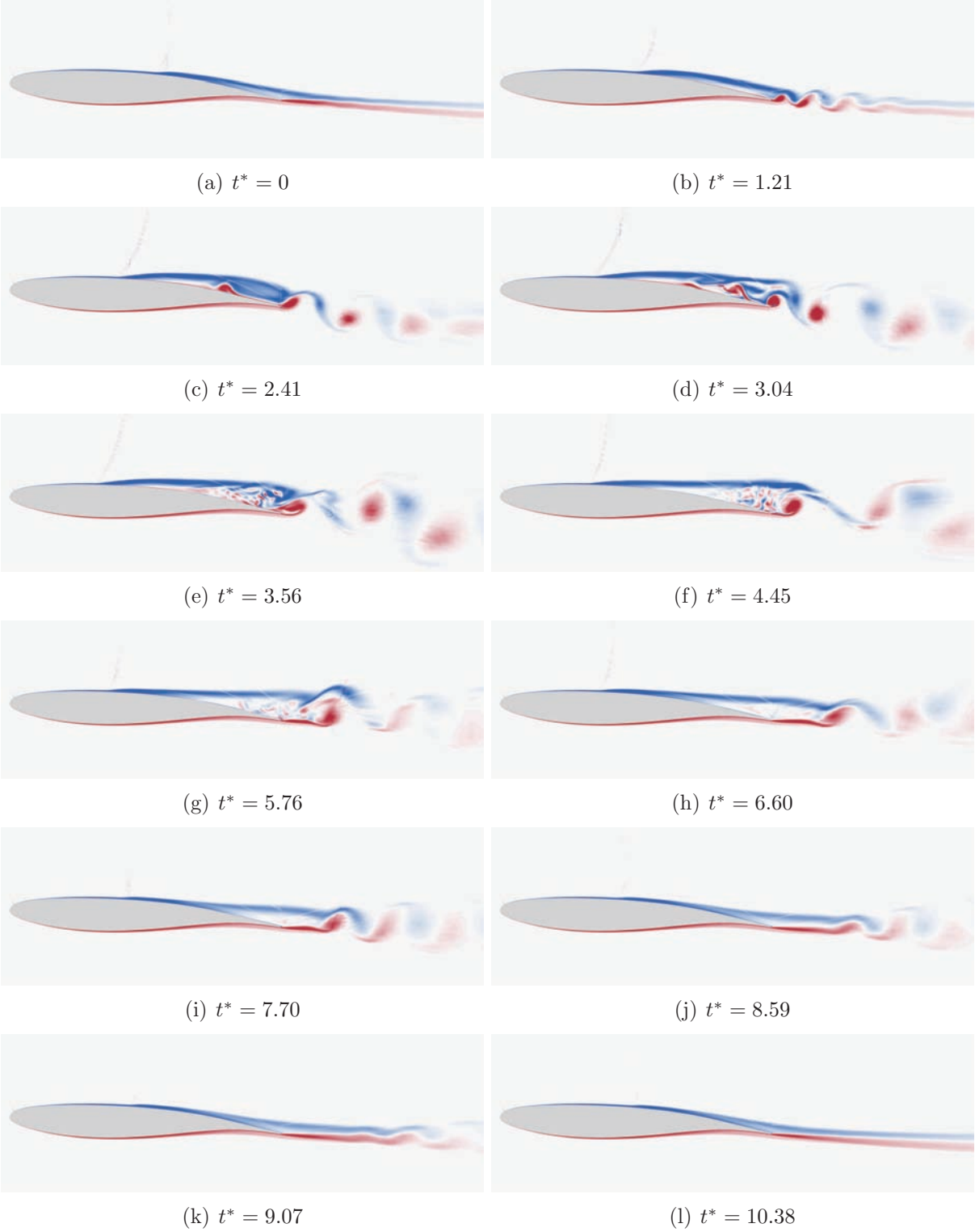

(a) $t^* = 0$ (b) $t^* = 1.21$

(c) $t^* = 2.41$ (d) $t^* = 3.04$

(e) $t^* = 3.56$ (f) $t^* = 4.45$

(g) $t^* = 5.76$ (h) $t^* = 6.60$

(i) $t^* = 7.70$ (j) $t^* = 8.59$

(k) $t^* = 9.07$ (l) $t^* = 10.38$

Figure 6.3: Instantaneous transverse-vorticity distributions in the mid-plane.

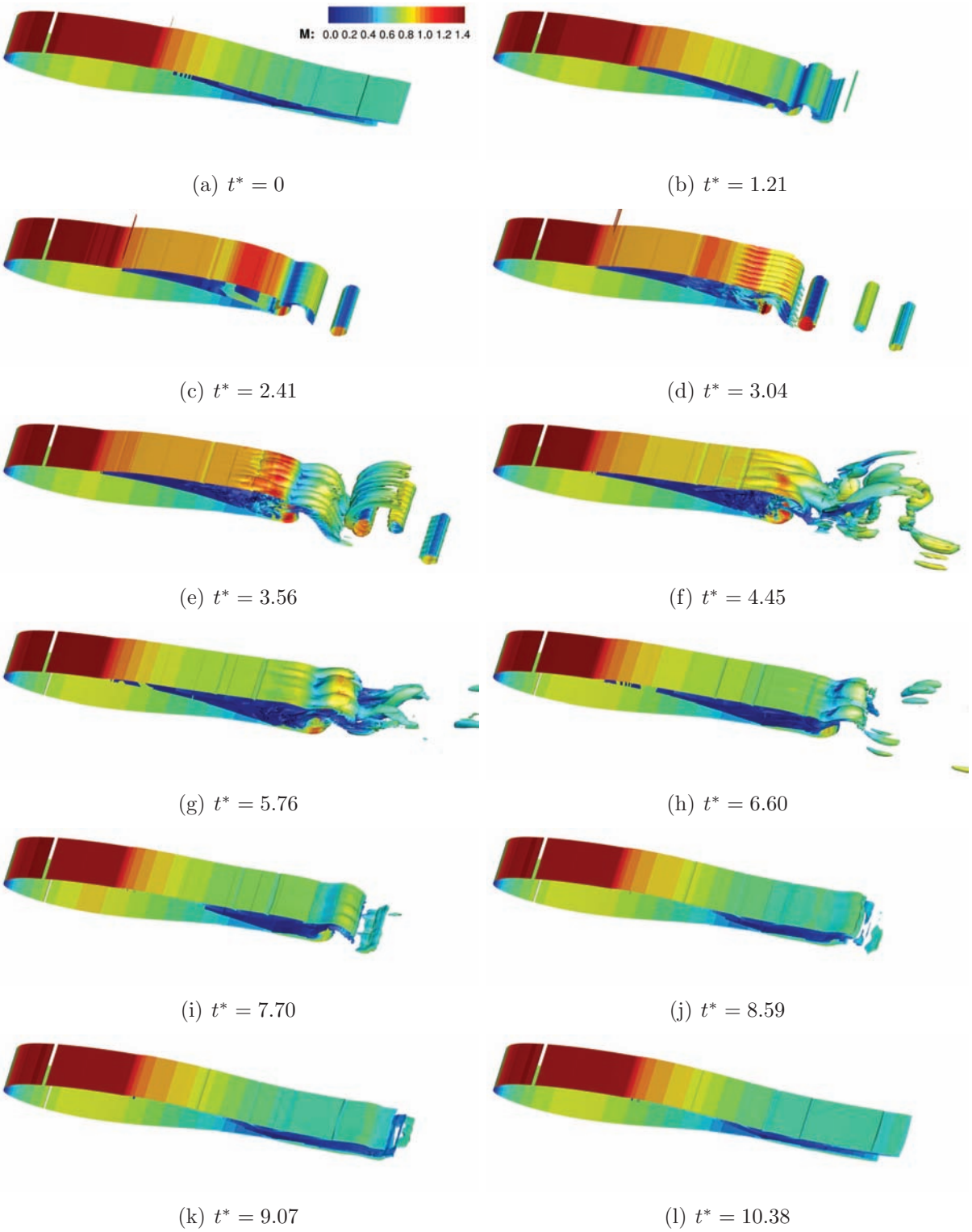

(a) $t^* = 0$ (b) $t^* = 1.21$

(c) $t^* = 2.41$ (d) $t^* = 3.04$

(e) $t^* = 3.56$ (f) $t^* = 4.45$

(g) $t^* = 5.76$ (h) $t^* = 6.60$

(i) $t^* = 7.70$ (j) $t^* = 8.59$

(k) $t^* = 9.07$ (l) $t^* = 10.38$

Figure 6.4: Vorticity-magnitude isosurfaces colored with the Mach number ($Wc/U = 10$).

to three-dimensional. Since the spanwise extent of the computational domain allows for the resolution of eight wavelengths of the secondary instability, its actual wavelength can be estimated between $0.029-0.037$ chord.

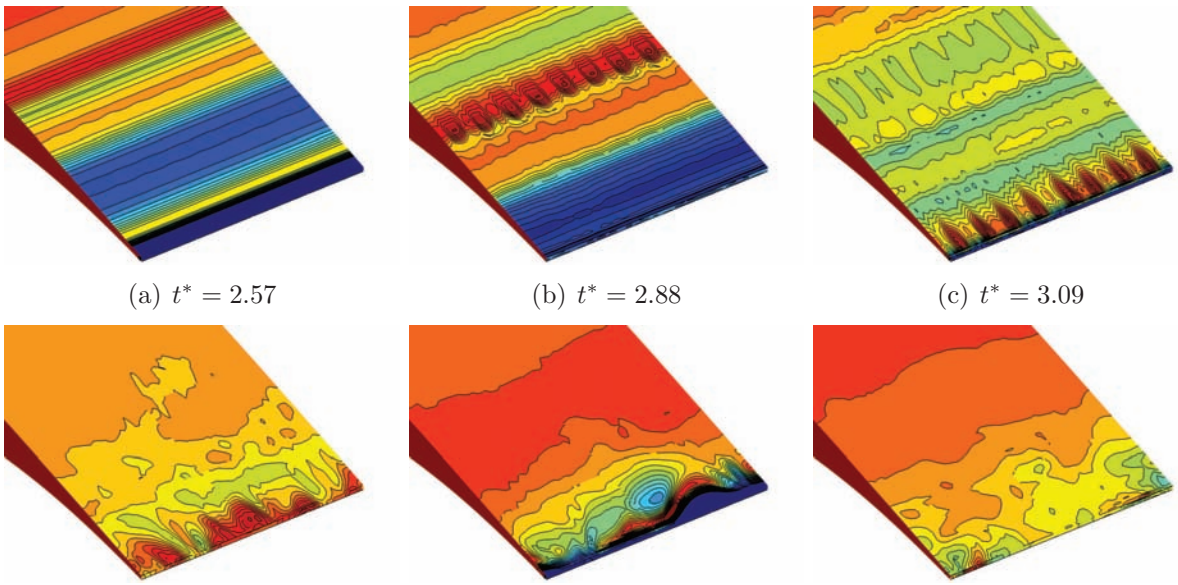

(a) $t^* = 2.57$ (b) $t^* = 2.88$ (c) $t^* = 3.09$

(d) $t^* = 3.51$ (e) $t^* = 3.83$ (f) $t^* = 4.24$

Figure 6.5: Instantaneous pressure distributions near the tailing edge (qualitative).

6.4.2.2 Mapping of flow separation

To help understanding the flow topology, the intermittent separation/reattachment process that takes place over the upper surface of the OAT15A airfoil is analyzed in more detail. Figure 6.6 presents maps of flow separation as predicted by the URANS and DDES approaches during transonic buffet. The abscissa gives the position on the upper surface parallel to the chord line and the ordinate represents the non-dimensional time normalized by the buffet period T, which is different in each case. Contrary to the convention adopted in figures 6.3 and 6.4, in the separation maps $t = 0$ corresponds to instants of minimum lift, which occur slightly after the instants when the shock wave reaches its most upstream position. The flow state at a given point and instant has been determined by evaluating the sign of the transverse vorticity component at the wall (for the DDES, this quantity has been computed on the mid-plane). The dark areas correspond to separated flow, whereas the white ones indicate that the boundary layer is locally attached. Because the URANS simulation has resulted in strongly-periodic flow, the separation map shown in figure 6.6(a) exhibits insignificant changes from one period to another. On the contrary, the DDES distribution given in figure 6.6(b) refers to a specific buffet period. Nevertheless, the behavior illustrated in that figure is representative of all other periods, which might present only small quantitative variations.

At minimum lift ($t = 0$) the shock wave is in the early stages of its travel downstream. At that instant, while the URANS simulation predicts a fully-separated flow behind the shock, the DDES gives an almost completely attached flow over the same area. During the shock-wave motion towards the trailing edge, the boundary layer remains attached in both simulations except by the separation bubble at the foot of the shock, which seems to be smaller in URANS. The side-by-side comparison reveals that the shock travel downstream is relatively longer in the DDES, taking approximately one-third of the buffet period while in URANS it takes about one half of the cycle. Such difference arises from a more rapid separation process in the DDES and may explain the higher buffet frequency found for that model. As the shock wave approaches its most downstream position, a fundamental difference between the two simulations regarding the development of the separated region is observed. As already mentioned in section 5.3.4 and illustrated in the sequence of figure 5.17, in the URANS simulation case, the separation evolves from the foot of the shock towards the trailing edge. This behavior is confirmed by the cartography of figure 6.6(a). On the contrary, figure 6.6(b) clearly shows the simultaneous growth of the separation bubble and of the rear separation in the DDES. The two separation fronts join each other at about $x/c = 0.75$ and form a large region of separated flow behind the shock. Such mechanism seems to be related to the tendency of the DDES to produce trailing edge separation as seen in figure 6.9.

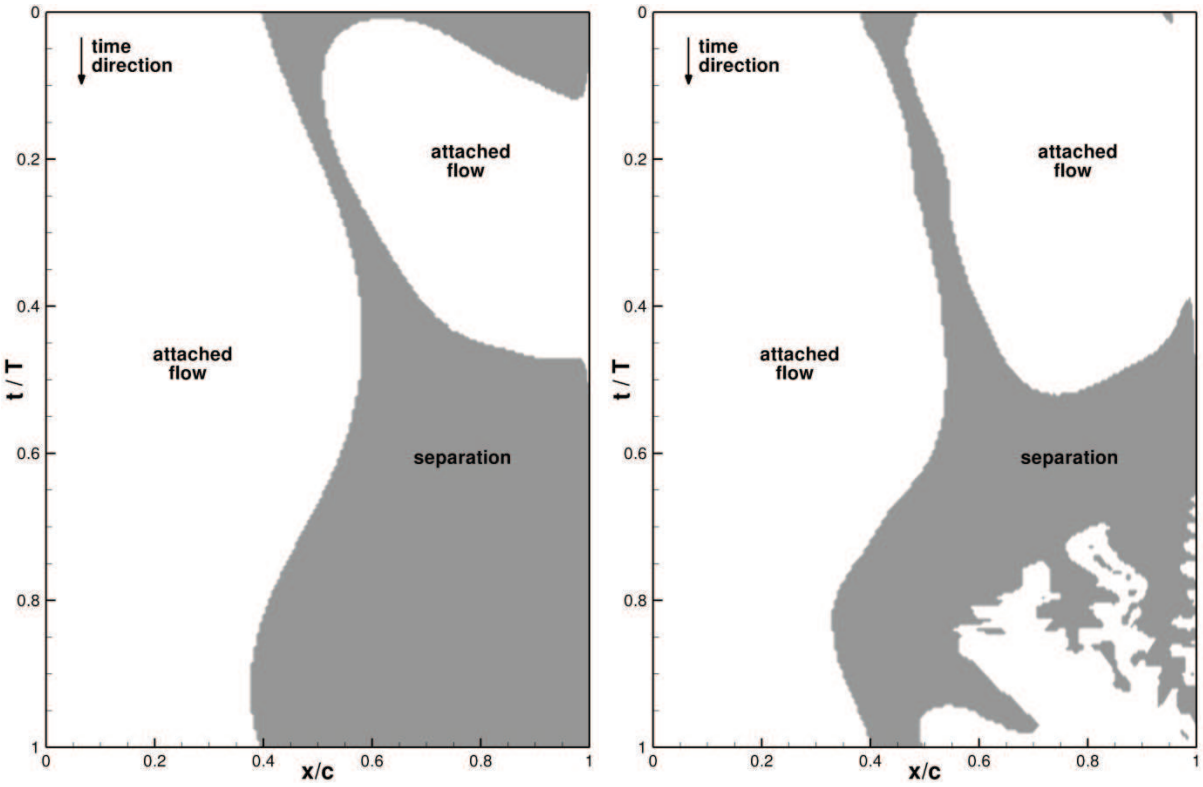

(a) URANS (b) DDES

Figure 6.6: Spatio-temporal evolution of flow separation during buffet.

The size of the separated area over the airfoil increases as the shock wave moves back upstream. During the motion, the signature of the alternate vortices can be observed near $x/c = 1$ in figure 6.6(b). The increasing size and spacing of the white areas result from the evolving properties of such structures as discussed previously.

6.4.3 Unsteady pressure

Figure 6.7(a) compares the computed time histories of the surface pressure at $x/c = 0.45$ on the upper surface with experimental data. This location is close to the mean shock-wave position observed in the experiments and in the DDES. As can be seen in the figure, while the URANS simulation produces regular and smooth wall-pressure oscillations, the DDES successfully captures the high-frequency fluctuations observed in the experimental signal. Such secondary fluctuations arise when the shock wave is upstream the location considered and have frequencies in the same range of the 'bump' seen in figure 6.2(b). Seiler and Srulijes [102] reported that the formation of trailing edge vortices in transonic flows is associated with the emission of upstream-moving waves [36]. Indeed, as shown in the experimental work of Alshabu and Olivier [36], the generation of such waves is coupled with downstream-propagating disturbances in the boundary layer.

The wall-pressure histories near the trailing edge at $x/c = 0.90$ are presented in figure 6.7(b) for the two numerical simulations. When the flow separates, a sudden pressure fall is felt at that position and secondary fluctuations can be distinguished in the DDES signal. As in the shock-motion region, at $x/c = 0.90$ the wall-pressure fluctuations predicted by the URANS simulation are regular and smooth. Because flow separation is less dramatic than in the DDES case, the amplitude of the fluctuations is much smaller in URANS. The position of all monitoring points available for the OAT15A airfoil are shown in figure 6.8 and their coordinates are provided in table 6.1.

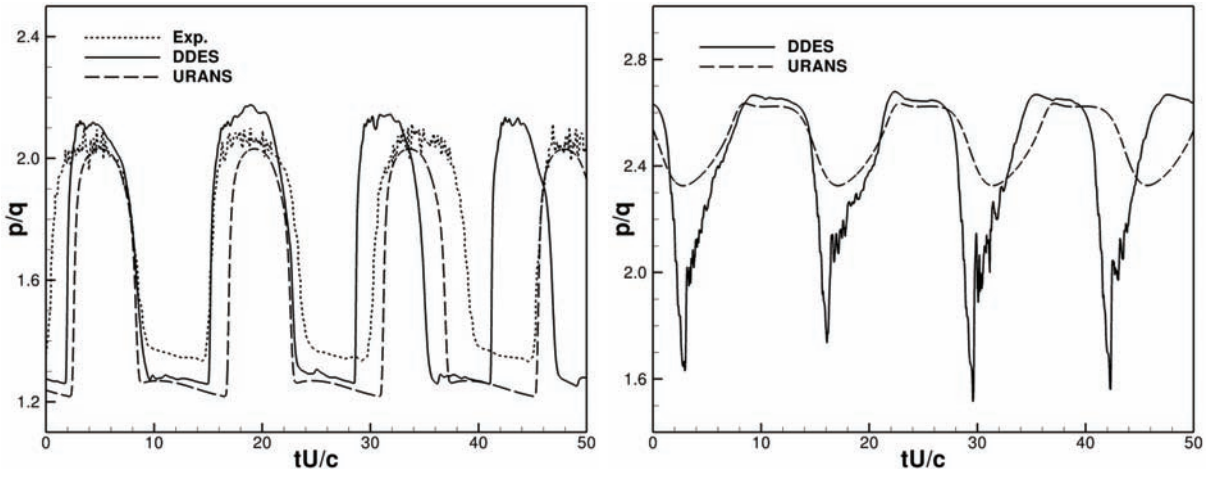

(a) $x/c = 0.45$ (b) $x/c = 0.90$

Figure 6.7: Time histories of pressure on the upper surface.

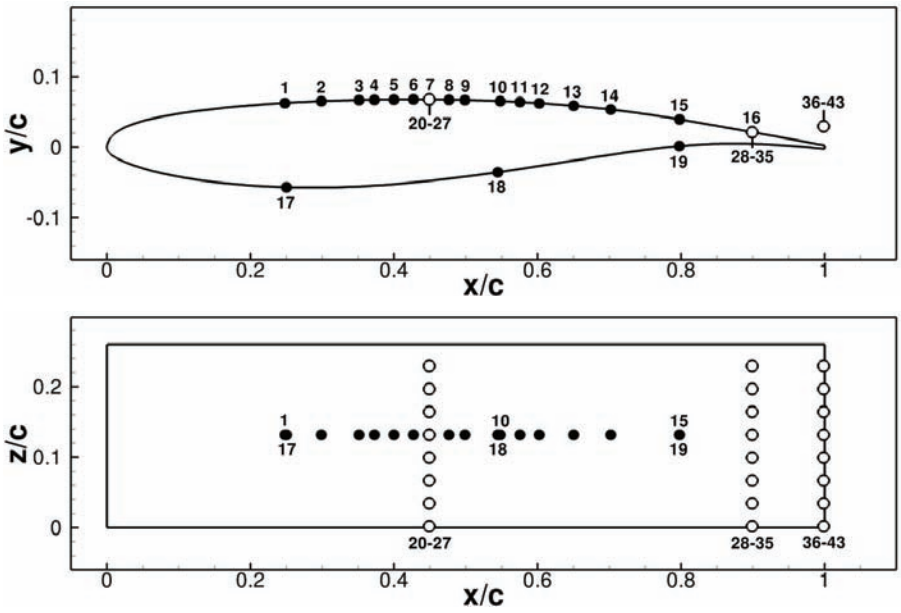

Figure 6.8: Monitor points locations for the OAT15A airfoil.

#	x/c	y/c	z/c	#	x/c	y/c	z/c	#	x/c	y/c	z/c
1	0.248	wall	0.132	18	0.545	wall	0.132	35	0.899	wall	0.002
2	0.299	wall	0.132	19	0.798	wall	0.132	36	0.999	0.030	0.230
3	0.351	wall	0.132	20	0.449	wall	0.230	37	0.999	0.030	0.197
4	0.373	wall	0.132	21	0.449	wall	0.197	38	0.999	0.030	0.165
5	0.400	wall	0.132	22	0.449	wall	0.165	39	0.999	0.030	0.132
6	0.427	wall	0.132	23	0.449	wall	0.132	40	0.999	0.030	0.100
7	0.449	wall	0.132	24	0.449	wall	0.100	41	0.999	0.030	0.067
8	0.477	wall	0.132	25	0.449	wall	0.067	42	0.999	0.030	0.035
9	0.499	wall	0.132	26	0.449	wall	0.035	43	0.999	0.030	0.002
10	0.548	wall	0.132	27	0.449	wall	0.002	44	2.001	0.089	0.230
11	0.575	wall	0.132	28	0.899	wall	0.230	45	2.001	0.089	0.197
12	0.602	wall	0.132	29	0.899	wall	0.197	46	2.001	0.089	0.165
13	0.650	wall	0.132	30	0.899	wall	0.165	47	2.001	0.089	0.132
14	0.702	wall	0.132	31	0.899	wall	0.132	48	2.001	0.089	0.100
15	0.798	wall	0.132	32	0.899	wall	0.100	49	2.001	0.089	0.067
16	0.899	wall	0.132	33	0.899	wall	0.067	50	2.001	0.089	0.035
17	0.250	wall	0.132	34	0.899	wall	0.035	51	2.001	0.089	0.002

Table 6.1: Monitor points coordinates for the OAT15A airfoil.

6.4.4 Statistical pressure distributions

As discussed in section 5.3.3.2, the statistical wall pressure data provides valuable information concerning the prediction of transonic buffet. Figure 6.9(a) presents the mean pressure coefficient distributions obtained with the DDES and URANS approaches and compares them with experimental results from Ref. [39]. The spread compression after the supersonic plateau on the upper surface gives an idea about the range of the shock-wave motion. In that area, the slopes of the curves for the DDES and URANS simulation are similar, suggesting equivalent shock oscillation amplitudes. Nevertheless, the mean shock-wave position of the DDES is located somewhat upstream that of URANS, being closer to the experiments. However, in the case of the DDES, the pressure recovery region downstream the shock gets flattened and the mean trailing edge pressure is lower than in the experiments. On the lower surface where the flow remains always attached and subcritical during buffet, both models provide accurate solutions.

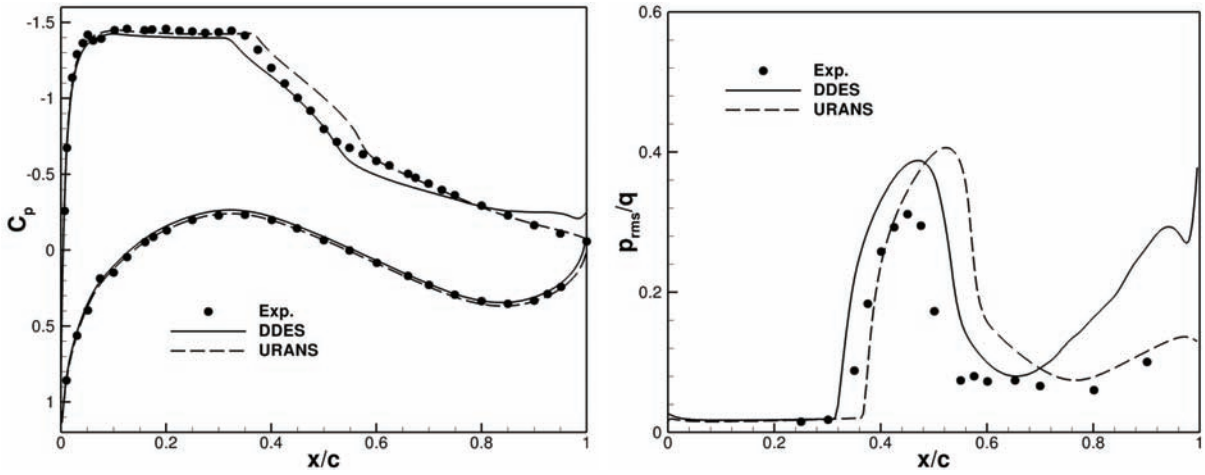

(a) Mean pressure coefficient

(b) RMS pressure on the upper surface

Figure 6.9: Statistical wall pressure distributions.

Figure 6.9(b) shows the distributions of the RMS values of the pressure fluctuations along the upper surface of the OAT15A airfoil. The region of intense fluctuations is caused by the shock-wave motion and also indicates the amplitude of the shock oscillations, with the peaks roughly corresponding to the mean shock position. As already observed in the C_p profiles, the figure indicates that the shock-wave motion range predicted by the DDES is closer to the experiments. The peak level is also better predicted by the hybrid method, yielding a slightly lower value than in the URANS simulation. Upstream the shock-motion region, the fluctuation levels are very low and agree well with the experimental data in both cases. A more precise estimate of the mean shock-wave position based on unsteady pressure signals extracted at different stations along the airfoil surface is given in section 6.4.3. Between the shock-wave motion area and $x/c = 0.8$, the experimental distribution is almost flat, which is not reproduced by any of the simulations. As one approaches the trailing edge, the fluctuations predicted by the DDES highly overestimate

the experiments whereas the URANS simulation shows a more coherent behavior. Such intense fluctuations are mainly caused by the interaction of large-scale structures resolved in the DDES with the rear part of the airfoil.

6.4.5 Statistical velocity field

To complement the analysis made for the pressure, the statistical velocity field resulting from the transonic buffet phenomenon is addressed. Figure 6.10 shows the mean longitudinal velocity profiles at four locations distributed on the upper surface. At each station, the y coordinate is measured from the wall and in the direction normal to the chord. At $x/c = 0.28$, the boundary layer is always attached and ahead of the shock wave during buffet, and both the DDES and the URANS computations give good predictions of the experimental profile. The station at $x/c = 0.45$ lies well inside the shock-wave motion region and is located close to the mean shock position of the DDES and the experiments. An outer velocity deficit can be observed for the DDES, which also exhibits a mean boundary layer that is thicker than the experimental one. The URANS simulation shows a better agreement with the experiments despite a somewhat downstream shock-wave motion region. The point at $x/c = 0.60$ remains always downstream the unsteady shock wave. At that position, both numerical results fail in reproducing the experimental behavior below $y/c = 0.02$. The DDES does not capture the mean reverse flow seen in the experiments and the URANS profile is only slightly separated. As the wall distance increases, the URANS results approach better the experimental distribution but a small deficit in the outer velocity is still visible. Further downstream at $x/c = 0.75$ both simulations predict well the experimental data, with the URANS profile showing a remarkably good agreement with the data.

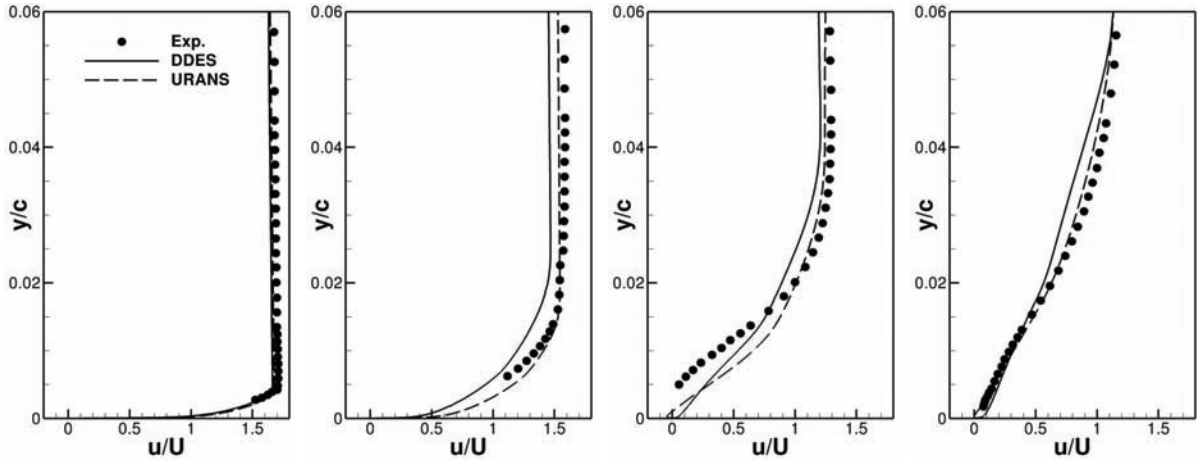

(a) $x/c = 0.28$ (b) $x/c = 0.45$ (c) $x/c = 0.60$ (d) $x/c = 0.75$

Figure 6.10: Mean longitudinal velocity profiles on the upper surface.

The RMS values of the longitudinal velocity at the same four stations are presented in the

profiles of figure 6.11. At $x/c = 0.28$, both the DDES and the URANS method lead to virtually zero unsteadiness. In the shock-wave motion region at $x/c = 0.45$, the numerical results overpredict the fluctuation levels seen in the experiments over the whole profile. This evidences how the features of shock-wave/boundary layer interactions are difficult to be reproduced by turbulence models. Nonetheless, the URANS curve is considerably closer to the experimental data if compared to the DDES. Downstream the interaction, the overall performance of the turbulence models gets improved. At $x/c = 0.60$, for example, the RMS velocity becomes less overestimated and the URANS approach predicts reasonably well the fluctuations below $y/c = 0.04$. The DDES, however, does not exhibit the divergence found in the outer velocities of the URANS distribution. As observed for the mean profiles, the agreement between the URANS results and the experiments at $x/c = 0.75$ is remarkably good.

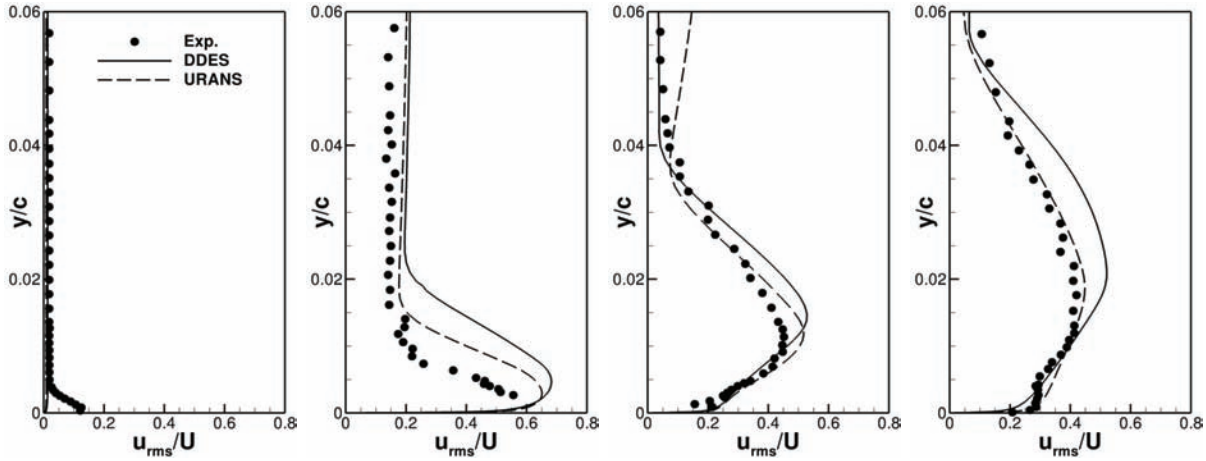

(a) $x/c = 0.28$ (b) $x/c = 0.45$ (c) $x/c = 0.60$ (d) $x/c = 0.75$

Figure 6.11: RMS longitudinal velocity profiles on the upper surface.

Figure 6.12 illustrates the statistical fields of the longitudinal velocity fluctuations around the OAT15A for the two modeling approaches. Compared to URANS, the DDES shows a slight decrease in the fluctuation levels in the shock-motion region above the shear layer. The distributions reveal that the peak RMS values take place in the shock wave/boundary layer interaction region. The figure also helps to illustrate the tendency seen in figures 6.9(b) and 6.11 of the DDES to enhance the flow fluctuations in the area downstream the interaction, which is particularly visible in the near wake. Such phenomenon becomes more clear when plotting the distributions of the vertical velocity fluctuations as shown in figure 6.13. The large differences at the trailing edge and in the wake are mainly caused by the strong vertical velocity fluctuations due to the alternate vortex shedding, which is not observed in the URANS results.

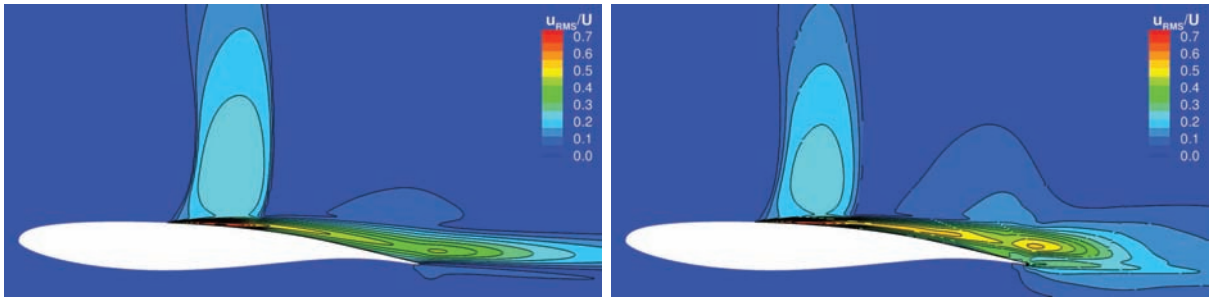

(a) URANS (b) DDES

Figure 6.12: RMS longitudinal velocity fields around the OAT15A airfoil.

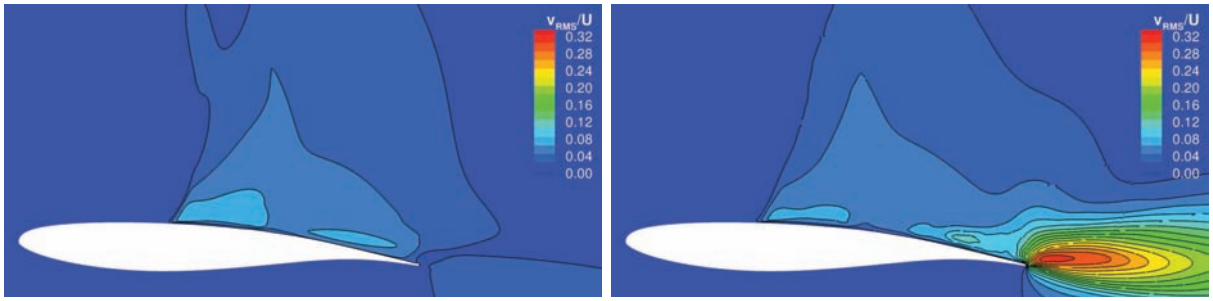

(a) URANS (b) DDES

Figure 6.13: RMS vertical velocity fields around the OAT15A airfoil.

6.5 Analysis of the DDES behavior

6.5.1 RANS and LES modes distributions

A fundamental question that must be investigated is how the DDES method switches between RANS and LES as the flow topology varies between attached flow and shock-induced separation. RANS- and LES-mode regions can be readily distinguished by plotting the distribution of the f_d function, which determines the effective length scale in the DDES methods (see equation 6.6). This function was specially designed to have a value close to 0 in RANS and to 1 in LES, also providing a rapid change between the two modes. Therefore, figure 6.14 illustrates the distributions of the function $(1 - f_d)$ in the vicinity of OAT15A airfoil during buffet at three different instants: at maximum lift with the shock wave at its most downstream position, with the shock at its most upstream position and at minimum lift. By the grayscale adopted, black regions are computed in RANS while the external white areas are treated in LES. Any shade of gray in-between is located within the transition zone. For comparison purposes, figure 6.14(d) gives the mode distribution that would be obtained with the standard DES method on the present grid. The latter would remain unaltered during buffet and is independent of the flow physics. As can be noted, RANS-mode layer provided by the DDES around the airfoil is much thicker than that by the standard DES, especially in the region between the

shock wave and the trailing edge, where the attached boundary layer is submitted to the effects of the interaction with the shock and of the adverse pressure gradient. When the shock wave is located at its most downstream position (figure 6.14(a)), the flow over the OAT15A is mostly attached. The resulting f_d distribution is smooth and correctly follows the boundary layer thickening on both surfaces due to the formulation adopted for the near-wall parameter r_d in equation 6.7.

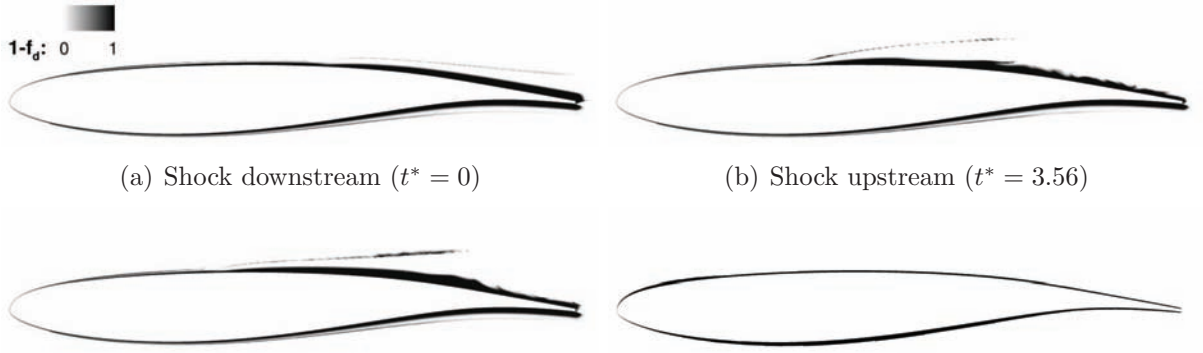

(a) Shock downstream ($t^* = 0$)

(b) Shock upstream ($t^* = 3.56$)

(c) Minimum lift ($t^* = 5.76$)

(d) Standard DES

Figure 6.14: RANS and LES regions during transonic buffet (function $1 - f_d$).

In figure 6.15, the instantaneous wall-profiles of the f_d function, eddy-viscosity ratio μ_t/μ and velocity are provided at four different locations on the upper surface. For comparison, the position where a standard DES would switch from RANS to LES (i.e., where $l_{\mathrm{RANS}} = l_{\mathrm{LES}}$) for the present grid is indicated by horizontal dash-dot-dot lines. In the figure, one can immediately notice that all stations exhibit disturbances in the f_d distributions. These appear just outside the boundary layer, where the deformation tensor magnitude becomes very small and abruptly increases r_d. As the wall distance increases further, r_d then tends to zero and, as desired, the f_d function smoothly approaches 1. Indeed, the disturbances in the f_d distributions can be observed even in figure 6.14, appearing in the form of thin black layers exterior to the viscous regions over the upper and lower surfaces. Since they arise only outside the boundary layer, they have no appreciable effect on the eddy-viscosity distribution as seen in the wall profiles, thus not being problematic. As a general result, the profiles indicate that the DDES effectively ensures that near-wall regions where high velocity gradients occur are treated in RANS. In fact, upstream the shock wave at $x/c = 0.28$, the DES approach would also perform a proper switching to LES in terms of the wall distance. At $x/c = 0.45$, however, the latter would activate the LES mode inside the boundary layer, whereas the DDES yields a satisfactory mode transition in the outer part of it. The differences between the two approaches become larger at $x/c = 0.60$, which lies well inside the separation bubble. A critical case for the standard DES is found at $x/c = 0.75$, where the boundary layer is especially thick and the tangential grid spacing is relatively small. At that station, the DES would switch to LES at a very low distance from the wall, which would result in a typical case of MSD. On the contrary, the DDES method ensures that the major part of

the boundary layer is treated in RANS.

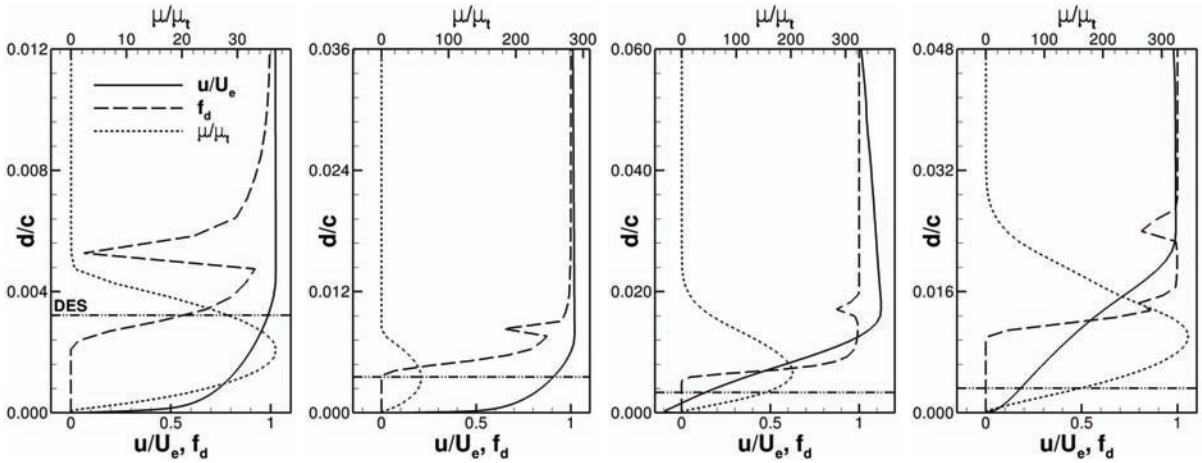

(a) $x/c = 0.28$ (b) $x/c = 0.45$ (c) $x/c = 0.60$ (d) $x/c = 0.75$

Figure 6.15: Wall profiles with the shock at its most downstream location ($t^* = 0$).

Figure 6.14(b) illustrates the distribution of RANS and LES modes when the shock wave is at its most upstream position (i.e., with the largest extent of separation). At that instant, the flow is fully separated downstream the shock wave, which is located approximately at $x/c = 0.32$. An estimate of the height of the separated region is given by the disturbances in the f_d distribution, which appear just above the shear layer. As one may expect, the bulk of that region is treated in LES as desired. Figure 6.16 reveals that, at $x/c = 0.28$, the wall profiles are very similar to those of when the shock wave is at its most downstream position as the boundary layer remains always attached at that location. For the three other stations considered, the velocity profiles confirm that the flow is separated. Besides, the heights of the RANS-mode layers around the airfoil are larger than in figure 6.15 for the attached flow condition and than in the standard DES. In all cases, however, the f_d function provides rapid transitions to LES. In respect to the DDES behavior at minimum lift conditions, the wall distributions of figure 6.17 support the previous conclusions. Indeed, the distributions are similar to those of figure 6.14(b) for the shock at its most upstream position.

6.5.2 Discussion of results

The results obtained with the DDES method differ substantially from those of the URANS simulations using the same baseline model. Remarkable differences exist in the shock wave/boundary layer interaction region, in the zone of intermittent separation over the rear part of the airfoil and particularly near the trailing edge, where the DDES overestimates the flow properties fluctuation levels. More specifically, the statistical pressure distributions in figure 6.9 show that the DDES tends to depart from the experimental data as one approaches the trailing edge, whereas the URANS results maintain a good

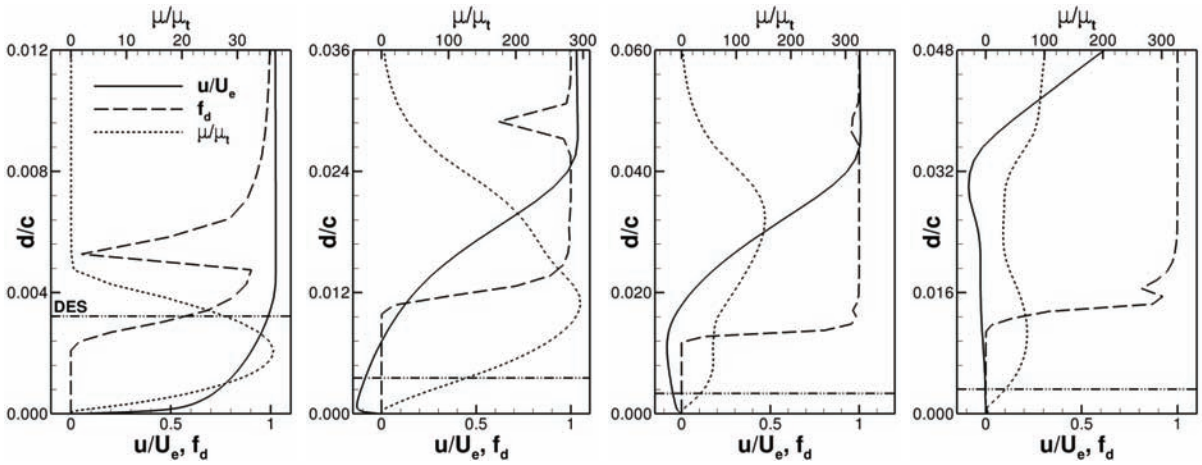

(a) $x/c = 0.28$ (b) $x/c = 0.45$ (c) $x/c = 0.60$ (d) $x/c = 0.75$

Figure 6.16: Wall profiles with the shock at its most upstream location ($t^* = 3.56$).

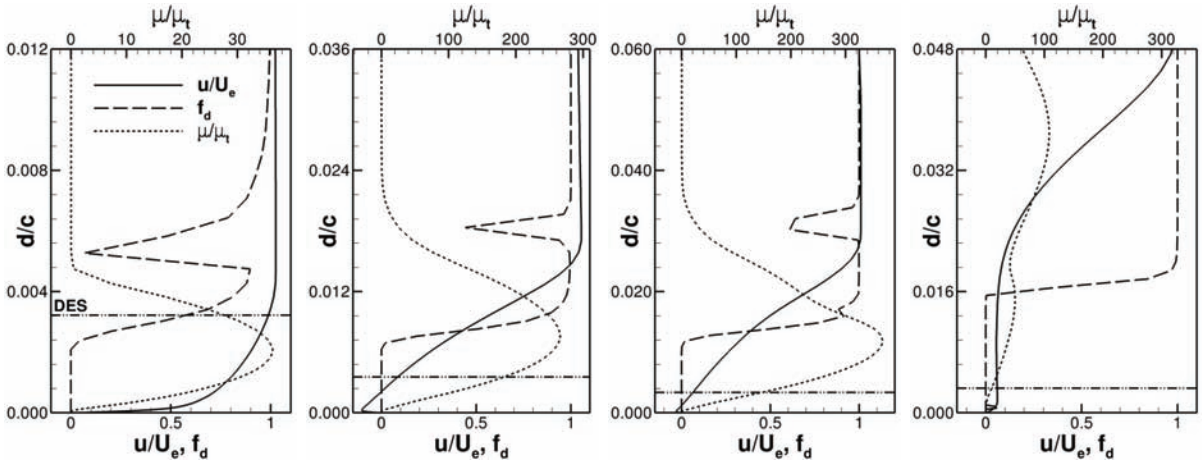

(a) $x/c = 0.28$ (b) $x/c = 0.45$ (c) $x/c = 0.60$ (d) $x/c = 0.75$

Figure 6.17: Wall profiles at minimum lift ($t^* = 5.76$).

behavior. Nevertheless, the analysis of the RANS and LES modes distribution during buffet indicates that the DDES is effective in preventing MSD even when the boundary layer gets very thick before the onset of separation.

In the sequence of flow snapshots presented in figure 6.3, it can be noted that resolved structures in the shear layer and in the separated region arise only over the rear part of the airfoil. This phenomenon is seen more clearly in figure 6.18, which illustrates isosurfaces of the Q-criterion, $Q = \frac{1}{2}\left(|\Omega|^2 - |S|^2\right)$, for two instants during separation. Despite the shock-induced separation occurring on the first half of the upper surface, a long distance is required for the formation of small eddies in the flowfield. Such effect may have been intensified in the DDES as the RANS-mode layer around the airfoil remains relatively thick during separation, which can be noted by comparing the f_d-function distributions of figures 6.15 and 6.16. Hence, one possible reason for the results obtained is that, when the flow separates, the turbulent content in LES regions is not sufficiently rich due to a severe gray area. Such delay in the generation of resolved turbulence would result in a more unstable flowfield and appears to be at least partially responsible for the generation of the strong and regular alternate vortex structures when the flow separates. These are intimately related to the high flow unsteadiness levels observed in figures 6.9(b) and 6.13 near the trailing edge.

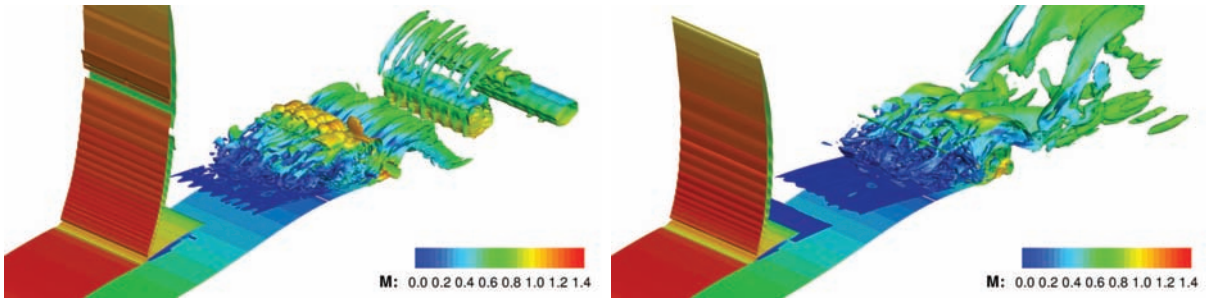

(a) $t^* = 3.56$ (b) $t^* = 4.45$

Figure 6.18: Instantaneous Q-criterion isosurfaces during separation ($Q(c/U)^2 = 100$).

In hybrid RANS-LES methods, the 'gray area' issue can become especially critical in flows where separation occurs over smooth geometries instead of being triggered by some geometry feature such as the edge of a backward-facing step or in the case of a spoiler, for example. Because of the intermittent separation in the present transonic buffet case, the gray area issue may have been more serious as the RANS-LES interface evolves over time. Therefore, a given point in the flowfield can be treated by both RANS and LES modes during buffet depending on the flow phase. To some extent, another possible contribution to the lack of small resolved structures may have been the dissipation resulting from the use of a third-order upwind scheme. The global grid refinement may also have influenced the results as it is not clear whether the cutoff length scale remains always within the inertial subrange of the turbulence spectrum. The three-dimensional flow patterns reported in the experiments of Jacquin et al. [39] may also be mentioned. However, they

do not seem to explain the DDES results since the URANS predictions near the trailing edge are in good agreement with the wind tunnel measurements.

Some results of the Zonal Detached-Eddy Simulation (ZDES) of the same test case performed by Deck [4] are compared with the present DDES in figure 6.19 and support the previous considerations. Both approaches guarantee a proper switching between RANS and LES during buffet. In the case of that particular ZDES, MSD was avoided by explicitly imposing RANS-mode (using the original SA model) in regions where the grid spacing in the direction normal to the wall was smaller than that in the spanwise direction. This ensured that the whole shock wave/boundary layer interaction was treated in RANS. Besides, the LES mode adopted the standard subgrid length-scale formulation of LES (i.e., $\Delta = (\Delta_i \Delta_j \Delta_k)^{1/3}$) and suppressed all near-wall functions of the SA model. Despite the many differences in the modeling approaches, numerical methods, time steps and grids, the mean pressure distributions in figure 6.19(a) present the same basic characteristics, showing large separation regions compared to the experiments and low trailing-edge pressures. The present DDES provides a better prediction of both the shock-wave motion range and the pressure recovery region. In fact, the method is closer to the experimental data over the whole mean pressure distribution. Nevertheless, because of the aforementioned differences in the simulation conditions, this result should not be regarded as the affirmation of the superiority of one approach over the other. Figure 6.19(b) reveals that the maximum pressure fluctuation levels predicted by the DDES and ZDES are very similar despite the somewhat different shock-wave motion ranges and mean locations. In the trailing edge region, the fluctuations obtained with the DDES are more intense than those with the ZDES. This result might be related to the fact that, in that ZDES, the hybrid model formulation was not used around the lower surface, which was completely treated in RANS mode. Therefore, the overall trailing-edge unsteadiness is attenuated, potentially preventing the development of alternate vortex shedding.

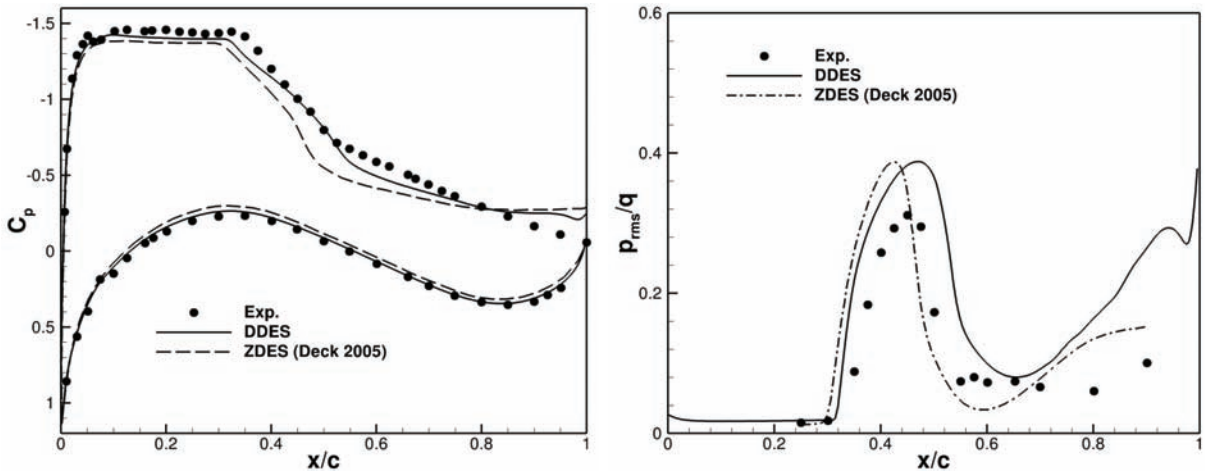

(a) Mean pressure coefficient

(b) RMS pressure on the upper surface

Figure 6.19: Comparison between the Delayed- and Zonal-DES methods.

Chapter 7

Numerical Study of a Laminar Transonic Airfoil

Contents

7.1 The V2C profile

To achieve faster cruising speeds and reduce emissions, new generation aircraft will need to have high performance, which will require the association of advanced aerodynamic design with more efficient propulsion systems and materials. Regarding the contribution of aerodynamics, performance can be improved by means of efficient lift generation and by maintaining drag as low as possible. For the latter, an obvious way to minimize parasite drag is to reduce its skin-friction component by obtaining a maximum extent of laminar flow. However, as the freestream Mach number increases in the transonic range, the generation and progressive strengthen of shock waves may lead to detrimental effects as discussed in chapter 2. In such scenario, laminar boundary layers are less resistant to shock-induced separation than turbulent ones and, for this reason, it is desirable that transition occurs upstream the shock to avoid laminar separation. This can be achieved through proper airfoil design for natural transition or by means of some boundary layer tripping method. Therefore, it is important to know how shock wave/boundary layer interaction properties such as the shock strength, the separation position and flow unsteadiness (e.g., buffet) are affected by the transition location.

A particular question addressed in the TFAST Project is how far from the shock must transition occur for the interaction to exhibit a purely turbulent behavior. Concerning the application to transonic wings, the project has selected a two-dimensional 'laminar' airfoil developed by Dassault Aviation as one of its test cases. The profile has been specifically designed in such a way that laminar flow is supposed to be maintained from the leading edge to the shock wave on the upper surface up to buffet onset. The technique employed was based on the e^N method for transition prediction (see, for instance, Ref. [103]) and the airfoil surface was generated in such a way that the N-factor remains small for low-to-moderate turbulence intensity levels, thus providing laminar flow. The design was validated numerically by Dassault by means of RANS computations for various angles of attack at freestream Mach numbers of 0.70 and 0.75, yielding chord-based Reynolds numbers of approximately 3.245×10^6 and 3.378×10^6 respectively. The study was performed using a compressible Navier-Stokes code (see Ref. [104] for details) adopting a two-layer k-ε model, with the transition location being determined from the fully-turbulent flowfield using a three-dimensional compressible boundary-layer code (see Ref. [105]) by means of the N-factor amplification with a parabola method (see Ref. [106]). The analysis of the flowfield around the airfoil indicated that the boundary layer is supposed to remain laminar up to the shock wave for angles of attack between 1° and 7°. At Mach 0.70, the flow separated between $\alpha = 6°$ and 7°. The amplification factor N was shown to be smaller than 3 up to the shock wave, thus guaranteeing laminar flow. At Mach 0.75, the value of N remained smaller than 2 up to $\alpha = 7°$. The final profile was named 'V2C' and is sketched in figure 7.1 (solid line), which compares it with the OAT15A supercritical airfoil (dashed line).

Unlike standard transonic airfoils, the upper surface of the V2C profile is not flat and the

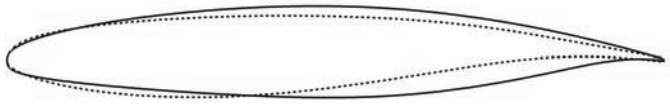

Figure 7.1: Geometries of the V2C (solid line) and OAT15A (dashed line) airfoils.

maximum thickness is located around the mid-chord, yielding a long region of favorable pressure gradient. As in supercritical airfoils, a slight camber exists in the rear part of the V2C to produce additional lift.

7.2 Grid generation

From the geometry provided by Dassault, two- and three-dimensional multiblock structured grids have been generated for the V2C airfoil adopting the same strategy as in the simulations of the OAT15A airfoil in chapters 5 and 6. First, a two-dimensional grid suitable for RANS computations has been designed, presenting a refinement along the upper surface for a proper resolution of potentially moving shock waves. Since this grid is also used as the basis for the design of the three-dimensional one, additional care has been taken for obtaining near-isotropic elements over the rear part of the airfoil and in the near wake. Therefore, three C-H planar grids with different refinement levels have been generated and evaluated. For each grid, the distribution of cells on the upper and lower surfaces, in the trailing edge, in the direction normal to the airfoil and in the wake direction is given in table 7.1.

Grid	Upper surf.	Lower surf.	T. edge	Normal	Wake	Total	1st-cell height	$y^+_{\max}$
1	156	128	28	128	128	72,704	$6.5\times10^{-6}\,c$	1.160
2	234	192	42	192	192	163,584	$3.4\times10^{-6}\,c$	0.554
3	312	256	56	256	256	290,816	$2.9\times10^{-6}\,c$	0.488

Table 7.1: Properties of the planar grids of the V2C airfoil.

Grid convergence has been investigated by means of steady computations (with local time stepping) for the flow at $M_\infty = 0.70$ and $\alpha = 4.0°$ using Menter's SST model and assuming fully-turbulent behavior. This flow condition is sufficiently critical for the formation of a relatively strong shock wave on the upper surface and the rapid and smooth reduction observed in the residuals have suggested the absence of transonic buffet. The final distributions of pressure and skin friction coefficients in the shock region are presented in figure 7.2. As can be noted, grid 2 gives a much sharper shock wave than grid 1 and yields results very similar to those of grid 3. In all other regions not shown in the figure the distributions obtained with the three grids are virtually identical. In respect to the non-dimensional wall distance y^+, the last column in table 7.1 provides the maximum values found in each case. For grid 2, a maximum value of about 0.55

has been obtained, which is adequate for the integration to the wall of the SST model. For the above reasons, grid 2 has been retained for the simulations in this chapter. The generation of the corresponding three-dimensional grid is straightforward and the details are provided in section 7.5.

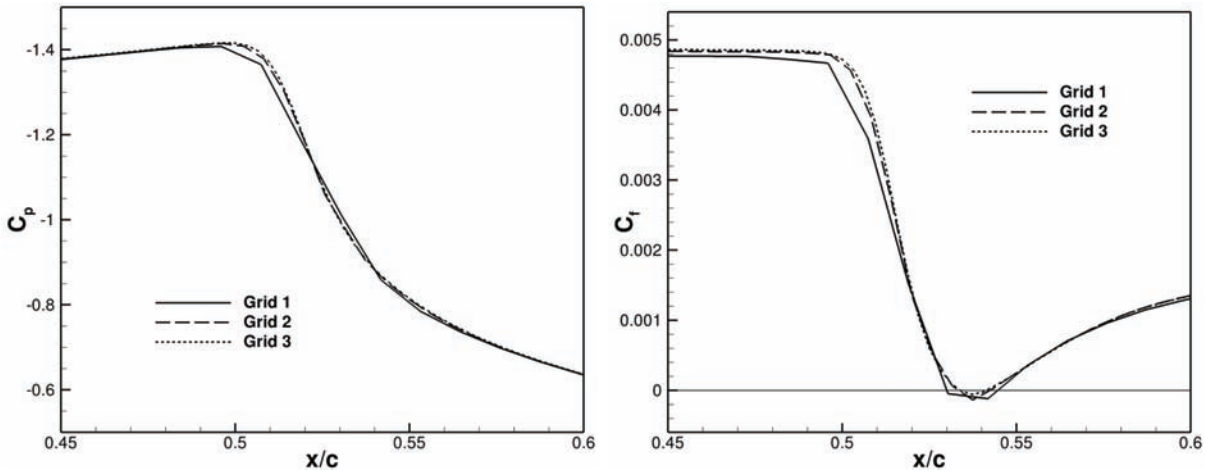

(a) Pressure coefficient

(b) Skin friction coefficient

Figure 7.2: Grid convergence results in the shock-wave region.

7.3 Preliminary investigation

As presented in section 7.1, the V2C airfoil was designed numerically considering two values of freestream Mach number (i.e., $M_\infty = 0.70$ and 0.75) and Reynolds numbers of about 3 million. Nevertheless, little information about its aerodynamic performance is known as the simulations were limited to RANS computations and did not provide further detail on the flow topology and particularly about unsteady effects. Therefore, the objective of this section is to perform an aerodynamic characterization of the V2C airfoil in the design range by means of URANS simulations. The aim is to detect the conditions for shock-wave formation, bubble and rear separations and buffet onset in order to select a few interesting configurations for a numerical investigation of transition effects on SWBLI as well as for a three-dimensional simulation of an unsteady flow case. Besides, the study might help to indicate the most promising flow conditions for wind tunnel experiments in TFAST. To increase the confidence and thus the simulations usefulness, a code-dependence study is also conducted and is presented at the end of this section using the Edge code (see section 3.2.3). The numerical method for the NSMB code is the same employed in chapter 5 for the OAT15A airfoil, which was validated for conditions very similar to those investigated here. The simulations have been run for total conditions of 10^5 Pa and 290 K. In all cases the turbulence model of choice is Menter's SST model because of its high code-independence, robustness and low sensitivity to the freestream

turbulence variables values. It should be noted, however, that this model might produce some delay in the buffet onset for a given Mach number as revealed in chapter 5.

7.3.1 Freestream Mach number 0.70

In order to characterize the aerodynamics of the V2C airfoil at $M_\infty = 0.70$, the angle of attack is varied with increments of 1° from 1° up to 7°, which is the maximum angle of attack for which the V2C airfoil is supposed to remain laminar. Initially, the computations adopt local time stepping. From the experience acquired with the OAT15A airfoil in chapter 5, if convergence is not reached (i.e., a relative reduction of 10^{-6} in the residual), time-accurate simulations with a time step of 5×10^{-6} s ($\approx 5 \times 10^{-3}\ c/U$) are then performed. Once an unsteady shock wave is obtained, the angle of attack is decreased by 0.5° in order to refine the buffet boundary.

Figure 7.3 shows the final distributions of the pressure and skin-friction coefficients for incidences up to 5°. For those angles of attack the flow is steady and rear separation is always present. As can be noted in figure 7.3(a), which also provides the critical C_p value, the flow over the upper surface is always supercritical and the shock wave can already be distinguished at 2°. As the angle of attack is further increased, the shock initially moves downstream. However, from 3° on, it goes upstream as α is augmented. As seen in figure 7.3(b), bubble separation appears and develops from $\alpha = 4°$ and the amount of rear separation steadily increases with the angle of attack.

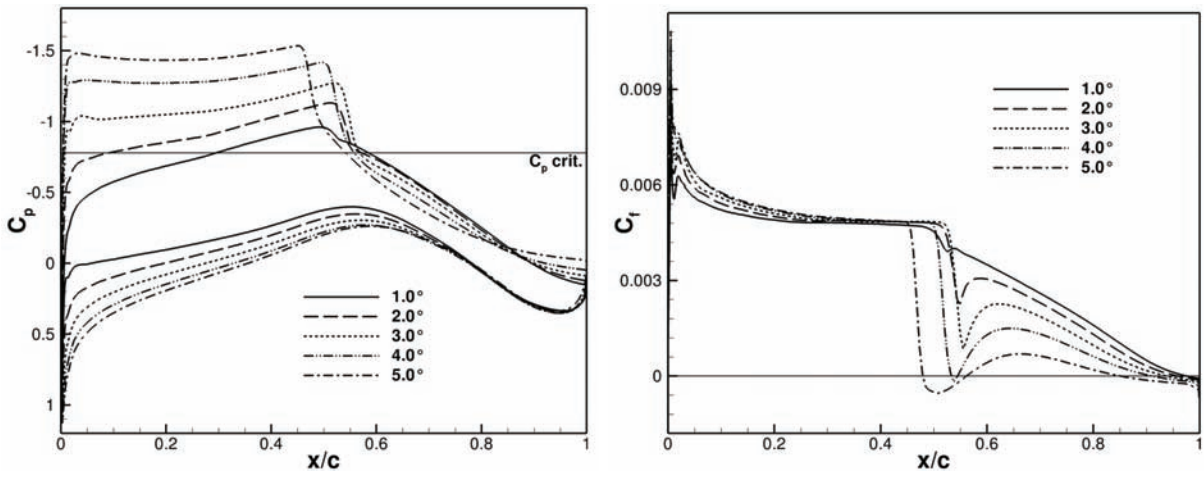

(a) Pressure coefficient

(b) Skin-friction coefficient

Figure 7.3: Steady surface distributions for the V2C airfoil at $M_\infty = 0.70$.

Since flow unsteadiness has been detected at 6°, an additional computation has been performed for $\alpha = 5.5°$, which has also led to unsteady flow (the same has occurred at 7°). In such conditions, the flow is characterized by a moving shock wave oscillating in an almost harmonic pattern (type-A shock motion according to Tijdeman's classification).

The overall buffet properties are similar to those of the OAT15A test case studied in chapters 5 and 6, with the main frequency increasing with incidence in the range of 80-82 Hz. The mean pressure coefficient and the RMS values of the pressure fluctuations on the upper surface are presented in figure 7.4. The statistical distributions have been computed after 5 buffet periods of sampling after the transient. From the simulations of the OAT15A airfoil, it has been seen that this is long enough for URANS simulations to converge in such type of strongly-periodic buffeting flows. At 5.5° the amplitude of the shock-wave motion is still small, resulting in a slight slope in the C_p curve. At 6° the buffet phenomenon seems to be fully established as the shock-motion range and the maximum fluctuation levels in the shock region and near the trailing edge are very similar to the case $\alpha = 7°$. For the latter, the whole SWBLI is somewhat shifted upstream, yielding a shorter supersonic plateau and a larger separation region.

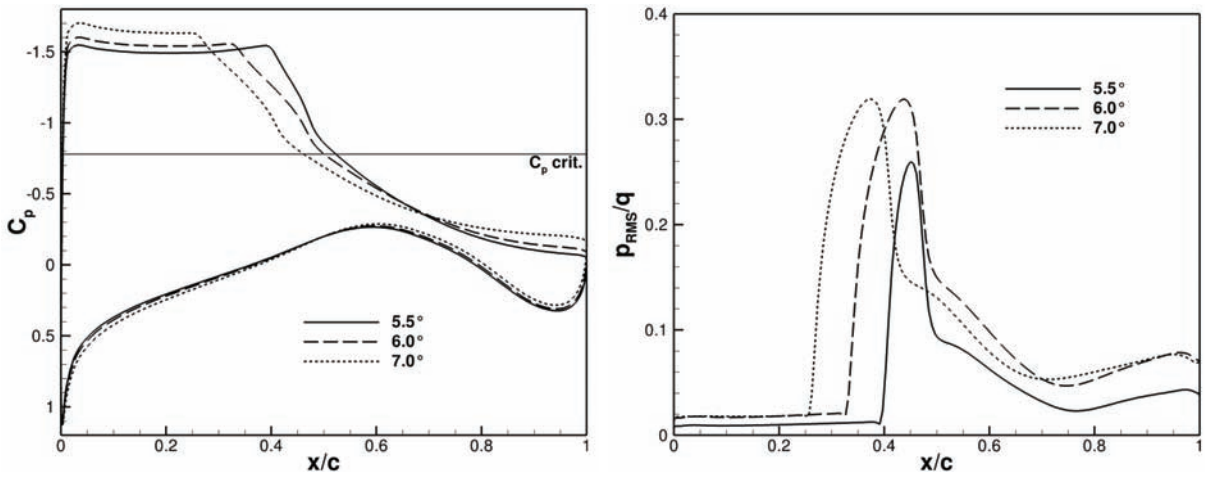

(a) Mean pressure coefficient

(b) Pressure RMS on the upper surface

Figure 7.4: Statistical pressure distributions over the V2C airfoil at $M_\infty = 0.70$.

7.3.2 Freestream Mach number 0.75

At $M_\infty = 0.75$, a strong shock wave already exists at $\alpha = 1°$ as evidenced by the C_p and C_f distributions in figures 7.5(a) and 7.5(b), respectively. The flow also features bubble separation at the foot of the shock, which rapidly turns to full shock-induced separation as the angle of attack is increased. This makes the shock and consequently the separation location move upstream, leaving a progressively larger wake behind. In the range of angle of attack investigated, no oscillating shock waves have been observed. However, high-frequency fluctuations of the global flow properties have been detected around 2 kHz at incidences of 6° and 7°. These have been found to be related to wake fluctuations caused by the von Kármán instability and are illustrated in figures 7.6(a) and 7.6(b) by means of instantaneous velocity fields for the case $\alpha = 7°$.

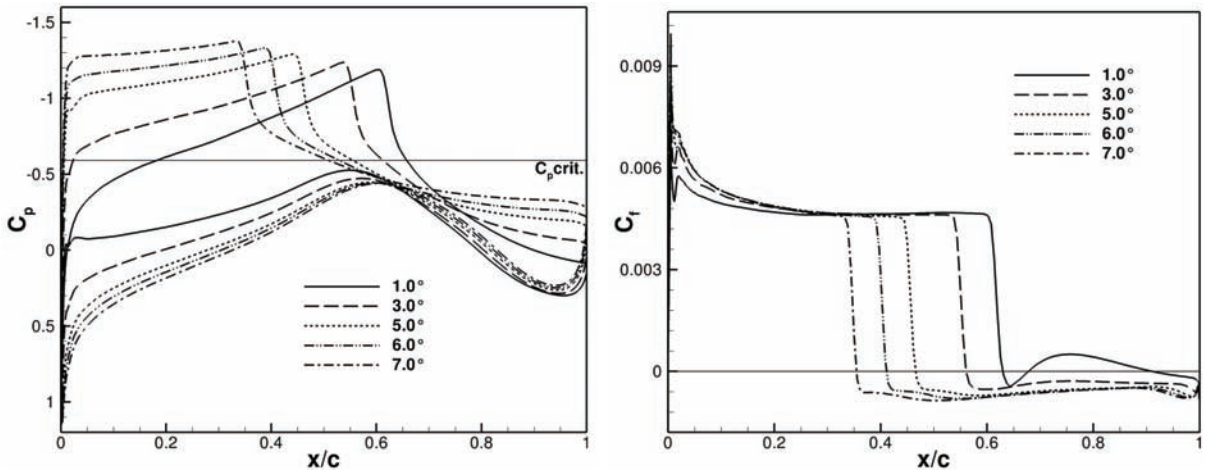

(a) Pressure coefficient (b) Skin-friction coefficient

Figure 7.5: Surface distributions for the V2C airfoil at $M_\infty = 0.75$.

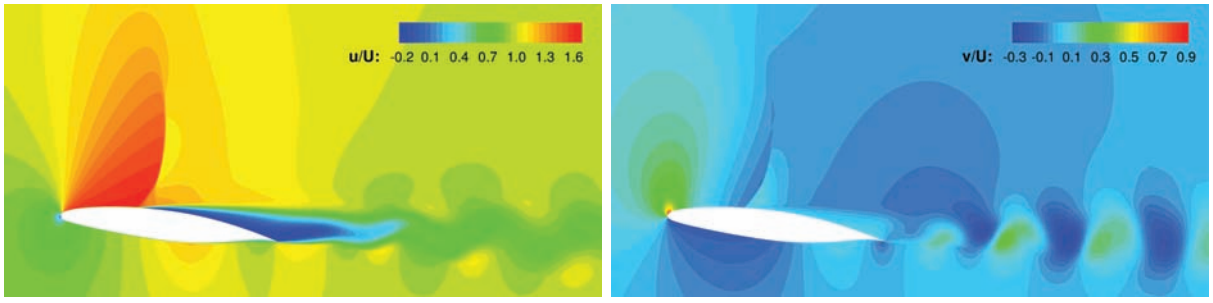

(a) Longitudinal velocity (b) Vertical velocity

Figure 7.6: Instantaneous velocity fields at $M_\infty = 0.75$ and $\alpha = 7.0°$.

7.3.3 Code-dependence study

Having performed a basic investigation of the flow regimes encountered by the V2C airfoil at $M_\infty = 0.70$ and 0.75 with the NSMB code, an extra set of simulations is conducted using the non-structured Navier-Stokes solver Edge, which was presented in section 3.2.3. Because there was no experimental results available for the V2C profile at the moment when the present study was being performed, such comparison helps to increase the reliability of the numerical simulations by reducing code-dependence issues. Besides, it helps choosing the most interesting angles of attack for studying the influence of the transition location on SWBLI. Since no unsteady shock waves have been observed at $M_\infty = 0.75$, the code comparison is made only for $M_\infty = 0.70$ considering several angles of attack ranging from 0° up to 7° with special attention to buffet onset and development.

The numerical method adopted in Edge has been as close as possible to that used in NSMB, which was described in chapter 5. For a complete description of the numerics involved, the reader is encouraged to see Ref. [66]. The convective fluxes have been discretized with a mixed differencing scheme composed by a central part plus a second-order Roe flux-difference splitting upwind dissipation term using van Leer limiters for both linear and nonlinear fields. For time-accuracy, implicit time integration has been performed with the dual time-stepping technique based on a second-order accurate backward differencing scheme, which is A-stable. The outer time step adopted has been the same as in NSMB (i.e., $5{\times}10^{-6}$ s) and the subiterations have been computed explicitly by means of a three-stage Runge-Kutta integrator employing a three-level W-cycle multigrid technique. 100 inner iterations have been prescribed in each time step in order to ensure convergence of all forces and moments.

The mean pressure coefficient distributions obtained in permanent regime for a few selected angles of attack are given in figure 7.7(a) for the two codes and the complete lift and drag polars are presented in figure 7.7(b). Up to 4°, no appreciable differences are observed between the codes in the lift curve, which exhibits a linear behavior. At those incidences, there is only a small amount of rear separation, which is equally predicted by the two codes. Once bubble separation occurs around 5°, nonlinear effects become significant and the first differences can be noted. Figure 7.7(b) shows how the drag force dramatically increases due to wave drag and shock-induced separation, which also limits the generated lift. While the drag curves remain almost identical, the NSMB code predicts a slight loss of lift caused by unsteady phenomena. As can be seen by the slope in the shock region in figure 7.7(a), transonic buffet with a small shock-motion amplitude already exists in the NSMB simulation at 5.5°, whereas the Edge code gives a straight shock wave resulting from a steady state (despite an initial oscillation yielding a long transient period). At 6°, the Edge code also gives a moving shock wave. As the transonic buffet instability becomes well developed, the statistical pressure distributions obtained with the two codes get very similar again, as shown for $\alpha = 7°$. At that angle of attack, the shock-wave motion range seems to be slightly wider in Edge. Figure 7.8 presents the

fields of the RMS values of the pressure fluctuations at 7°. The side-by-side comparison also suggests that the shock-motion amplitude predicted with Edge is somewhat larger than that with NSMB. Moreover, the Edge code also results in higher levels of pressure fluctuations in the shock region and in the near wake.

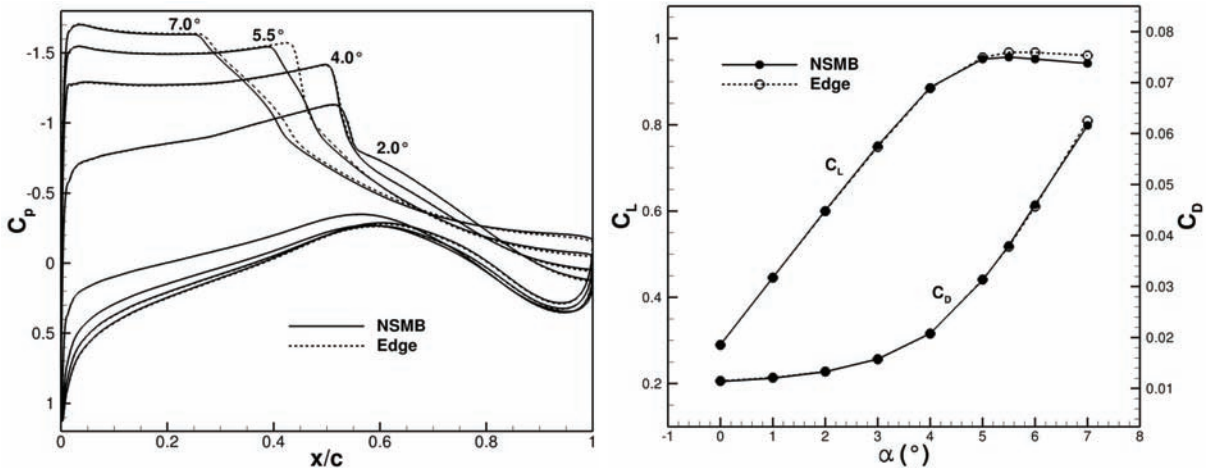

(a) Mean pressure coefficient

(b) Lift and drag polars

Figure 7.7: Code comparison results for the V2C airfoil.

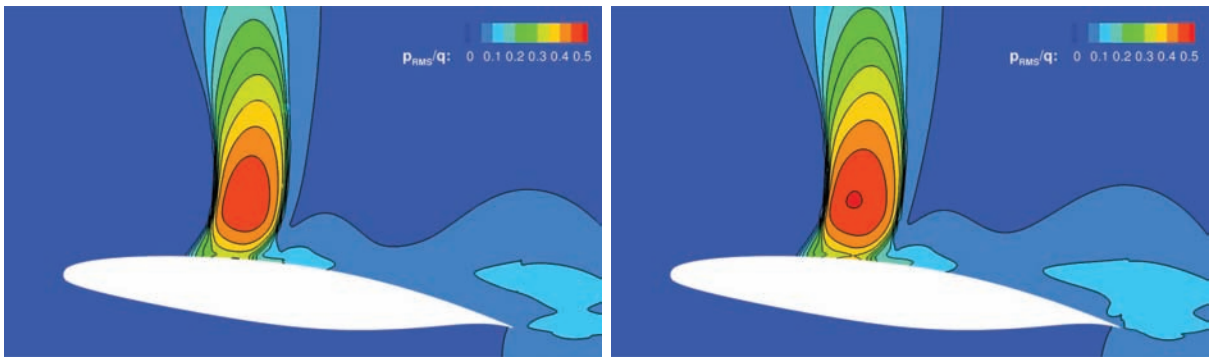

(a) NSMB

(b) Edge

Figure 7.8: RMS pressure fields at $M_\infty = 0.70$ and $\alpha = 7.0°$.

7.4 Effect of the transition location

The code comparison presented in the last section showed a lot of similarity between the flows predicted by the NSMB and Edge codes for a large range of angle of attack. Such results encourage further investigation of the V2C airfoil relying only on numerical simulations, as the uncertainties may be expected to be mostly related to the turbulence model. In this way, two flow conditions have been selected for a numerical investigation of the transition location effect on the shock wave/boundary layer interaction due to their interesting flow physics and to the remarkable similarity between the results obtained with

the two codes. First, the steady interaction arising at $\alpha = 4.0°$ is addressed, featuring a reasonably strong shock just below the critical angle of attack for buffet onset. The second flow condition is the fully-established buffet regime at $\alpha = 7.0°$, which presents a large shock-wave motion region that was similarly predicted by the numerical codes.

In chapter 5, the transition effect on steady and unsteady shock wave/boundary layer interactions was evaluated for the OAT15A airfoil, resulting in only a small shift downstream in the shock-wave region in both regimes. In that test case, however, the tripping point was at $x/c = 0.07$ and the laminar boundary layer was too short to substantially alter the properties of the SWBLI. In the present investigation, the transition location is varied from the leading edge up to as close as possible to the shock wave, providing long extents of laminar boundary layer upstream it. The influence of the tripping point over the selected steady and unsteady transonic flowfields is presented in the following sections.

7.4.1 Pre-buffet condition

The preliminary simulations in section 7.3 showed that, at 4° and $M_\infty = 0.70$, the fully-turbulent flow over the V2C airfoil is near critical with respect to transonic buffet. At that incidence, the shock wave is strong enough to induce a small separation bubble and the adverse pressure gradient over the rear part of the airfoil causes rear separation at about $x/c = 0.91$. The same flow condition has been recomputed considering different transition locations x_t from the leading edge up to the mid-chord, remaining steady in all cases. The pressure and friction coefficients distributions over the upper surface are provided in figure 7.9 for some selected values of x_t. The effect of the transition location on the shock-wave position x_s, on the location x_b and length l_b of the separation bubble as well as on the rear separation position x_r are quantified in table 7.2 for the complete set of simulations.

In figure 7.9(b), the tripping points can be easily identified by the sudden and drastic increase in the wall shear when the boundary layer becomes turbulent. They can also be distinguished in figure 7.9(a) in the form of slight pressure disturbances in the supersonic region. As can be noted in the figures, as the transition location is shifted downstream, the shock wave also moves downstream as a result of the reduction in the boundary layer displacement thickness. This produces higher Mach number levels in the supersonic pocket associated with lower pressures in that region, resulting in a stronger compression through the shock. This effect is illustrated in figure 7.10, which compares the Mach number fields in the shock-wave region for the fully-turbulent and $x_t/c = 0.50$ cases. As the laminar region increases, the progressively stronger shock wave makes the separation bubble grow continuously as indicated by table 7.2 and by the C_f distribution. Conversely, the rear separation gets smaller, yielding a larger pressure recovery and eventually vanishing for $x_t/c \approx 0.5$.

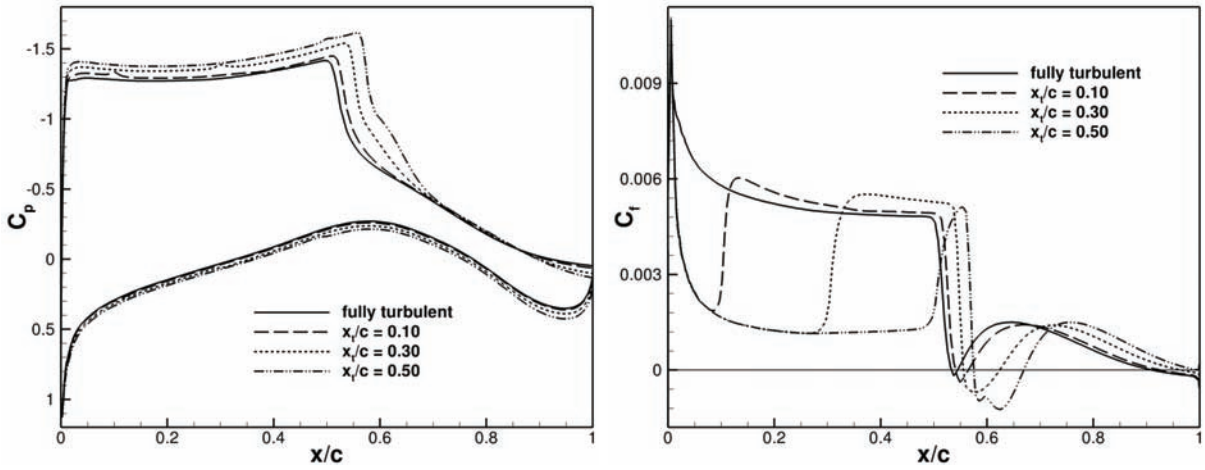

(a) Pressure coefficient (b) Skin-friction coefficient

Figure 7.9: Transition location effect on the surface distributions at $\alpha = 4.0°$.

x_t/c	Fully turb.	0.10	0.20	0.30	0.40	0.50
x_s/c	0.523	0.532	0.541	0.552	0.564	0.574
x_b/c	0.533	0.541	0.547	0.556	0.566	0.575
l_b (%)	1.1	2.4	4.7	6.8	8.5	9.4
x_r/c	0.911	0.925	0.946	0.965	0.981	–

Table 7.2: Transition location effect on the shock position and on separation.

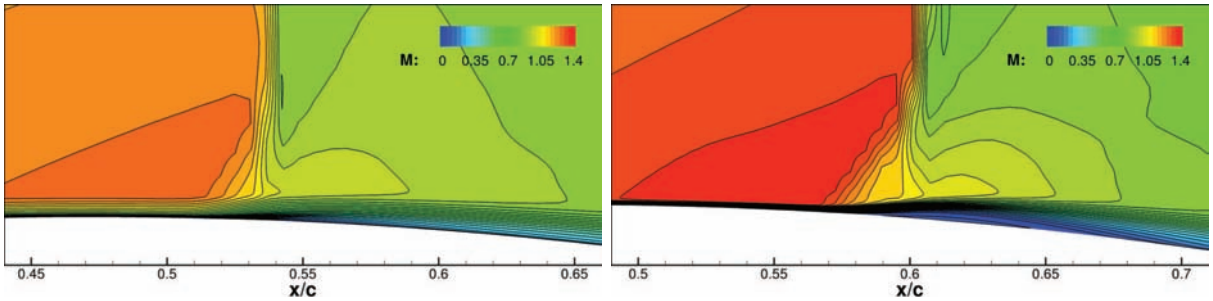

(a) Fully turbulent (b) $x_t/c = 0.50$

Figure 7.10: Mach number fields in the shock-wave region.

Table 7.3 provides the changes in the force and moment coefficients as the tripping point is varied. Moment is evaluated at the leading edge and, for a better understanding of the drag components, the friction drag coefficient C_{D_f} is also given in the table. As the transition location and thus the shock wave position move downstream, the lift augments due to an increasing pressure difference between the upper and lower surfaces. Such augmentation is accompanied by an increase in the magnitude of the pitching moment. As one may expect, the friction-drag component steadily decreases as the extent of laminar boundary layer becomes larger, yielding lower shear stresses upstream the shock. Nevertheless, such decrease does not necessarily mean a reduction in drag since the global drag tends to increase after an initial reduction observed for $x_t/c = 0.10$. This effect makes the transition location for optimal lift-to-drag ratio to appear near $x_t/c = 0.3$.

x_t/c	Fully turb.	0.10	0.20	0.30	0.40	0.50
C_L	0.8873	0.9174	0.9556	0.9919	1.029	1.061
$C_{D_f} \times 10^2$	0.610	0.574	0.510	0.460	0.396	0.334
$C_D \times 10^2$	2.080	2.069	2.102	2.171	2.268	2.365
L/D	42.7	44.3	45.5	45.7	45.4	44.9
$C_m \times 10^2$	-7.277	-7.749	-8.445	-9.195	-10.04	-10.83

Table 7.3: Transition location effect on the global aerodynamic coefficients.

7.4.2 Fully-developed unsteady regime

As discussed in the beginning of this chapter, the effect of the transition location on shock wave/boundary layer interactions is still an open question. This is particularly the case for unsteady flows such as transonic buffet. Therefore, an initial study has been conducted to assess the influence of the transition point on the properties of the well-developed buffeting flow at 7°. As for the preliminary simulations of section 7.3, a physical time step of 5×10^{-6} s has been adopted. The sampling of the flow statistics has also followed the procedure described in that section. Besides the fully-turbulent case, three tripping locations have been considered: $x_t/c = 0.09$, 0.16 and 0.24. For the latter, the most upstream position of the shock wave during buffet has been of about $x_t/c = 0.25$. This limits the displacement of the tripping point since imposing $\nu_t = 0$ inside the shock-motion region would not be an acceptable approximation.

Figure 7.11 presents the statistical pressure distributions obtained for each boundary layer tripping position. While the most upstream shock position is not much sensitive to the transition location, its most downstream position is strongly affected by the boundary layer state. As seen for the case $\alpha = 4°$, a larger extent of laminar boundary layer tends to place the shock wave further downstream by altering the displacement thickness distribution around the airfoil. In fact, this effect can also be observed in the unsteady case regarding the mean shock-wave position, which roughly corresponds to the point of

maximum pressure unsteadiness in figure 7.11(b). As the tripping point moves downstream, the shock-motion range becomes wider, increasing the fluctuation levels in the shock-wave region as well as the trailing edge unsteadiness. This can be observed in the series presented in figure 7.12, which illustrates the statistical pressure fluctuation fields for each transition case. Compared to the fully-turbulent simulation, with the tripping point placed at $x/c = 0.24$, the pressure unsteadiness increases by approximately 20% in the shock region and gets nearly two times larger near the trailing edge. The continuous growth of the shock-motion area is also clear in the figures.

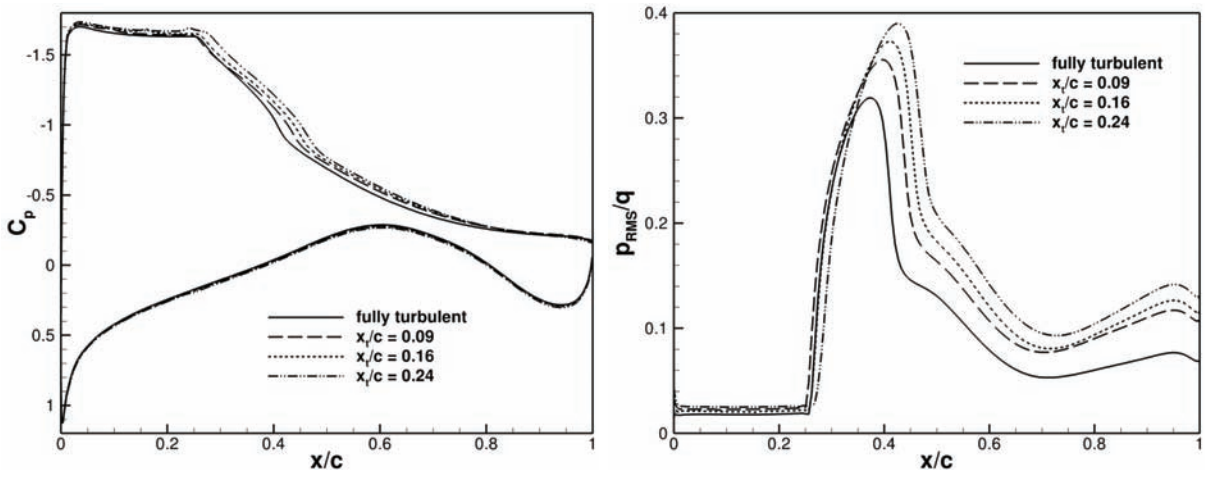

(a) Mean pressure coefficient

(b) RMS pressure on the upper surface

Figure 7.11: Transition location effect on the statistical wall pressure at $\alpha = 7.0°$.

Table 7.4 gives the average lift, drag and pitching moment coefficients for the three transition cases as well as for the fully-turbulent computation. The standard deviation σ of the aerodynamic forces is also presented. As for the steady flow at 4°, the values listed show an increase in the mean lift and in the moment magnitude as the triggering location moves towards the trailing edge. A slight augmentation in the mean drag is also noticed. As a result of the increasing shock-motion amplitude and of the overall flow unsteadiness, the standard deviations of the lift and drag coefficients also become larger as the extent of laminar boundary layer augments.

x_t/c	Fully turb.	0.09	0.16	0.24
$\overline{C_D}\times10^2$	6.163	6.501	6.604	6.715
$\sigma(C_D)\times10^2$	0.9419	1.250	1.384	1.533
$\overline{C_L}$	0.9423	0.9718	0.9927	1.018
$\sigma(C_L)$	0.0854	0.1047	0.1132	0.1204
$\overline{C_m}\times10^2$	-4.223	-4.932	-5.267	-5.676

Table 7.4: Transition location effect on the unsteady global coefficients.

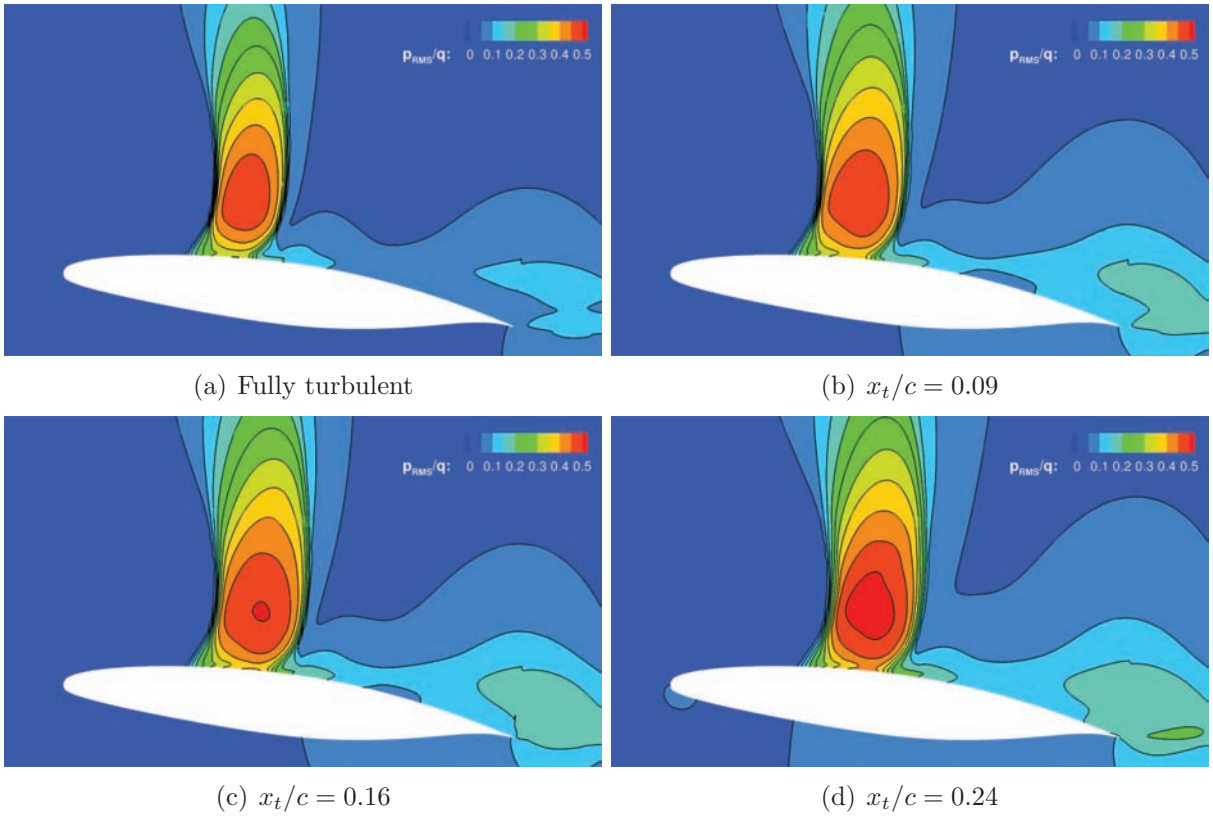

(a) Fully turbulent (b) $x_t/c = 0.09$

(c) $x_t/c = 0.16$ (d) $x_t/c = 0.24$

Figure 7.12: RMS pressure fields for different transition locations at $\alpha = 7.0°$.

7.5 Scale-resolving simulation

7.5.1 Introduction

In chapter 6 the Delayed Detached-Eddy Simulation approach was used to simulate the transonic flow over the OAT15A supercritical airfoil at conditions of angle of attack just above the buffet onset boundary. In that case, the predicted shock-wave motion region was in good agreement with the experiments and the solution exhibited a rich content of resolved flow structures. Nevertheless, the DDES was shown to produce too-intense pressure and velocity fluctuations in the region downstream the oscillating shock wave, which was probably caused by a long delay in the formation of resolved structures in LES regions. In this section, the DDES method is applied to the well-developed transonic buffet occurring over the V2C airfoil at $M_\infty = 0.70$ and $\alpha = 7.0°$. The objective is to investigate whether the same issues detected in the OAT15A test case exist for a stronger shock-induced separation by comparing the DDES results with those of the previous URANS simulations. In this way, an SST-based DDES has been carried out adopting the same numerical scheme and time step as in chapter 6 ($\Delta t = 1\times10^{-7}$ s, or 9.1×10^{-5} c/U). Due to the high computational cost of the simulation and for simplicity, only the fully-turbulent configuration is addressed. The three-dimensional grid has been obtained

by copying the planar grid used in the URANS simulations in the spanwise direction over a distance $L_z/c = 0.33$ (which is larger than in the OAT15A case). To obtain $\Delta_i \approx \Delta_k$, 59 cells have been distributed along the span keeping a constant spacing, resulting in a final grid with about 9.65 M cells.

Contrary to the DDES of chapter 6 where the RANS length scale was given by the wall distance d, in the SST-based DDES the turbulence length scale provided by the RANS part is computed using local turbulence properties and is given by $\sqrt{k}/(\beta^*\omega)$. In the SST model, this quantity exists implicitly in the dissipation term of the k-equation (see equation 4.20) and is replaced by the DDES length scale defined in equation 4.44. Hence, in the SST-based DDES the model length scale is calculated as

$$l_{\text{SST-DDES}} = d - f_d \max\left(0, \sqrt{k}/(\beta^*\omega) - C_{\text{DES}}\Delta\right), \tag{7.1}$$

where the C_{DES} constant is locally computed by blending the constants for the k-ω and k-ε branches of the SST model, that is

$$C_{\text{DES}} = F_1 C_{k\text{-}\omega} + (1 - F_1 C_{k\text{-}\varepsilon}) \tag{7.2}$$

In equation 7.2, F_1 is the blending function of the SST model defined in equation 4.22. The values that have been adopted for the two constants are $C_{k\text{-}\omega} = 0.78$ and $C_{k\text{-}\varepsilon} = 0.61$ based on the calibration by Travin et al. [91] against homogeneous isotropic turbulence. With the above definition, the RANS mode in an SST-based DDES is not necessarily restricted to the near-wall region.

7.5.2 Flowfield dynamics

The time history of lift after the transient period is presented in figure 7.13 for both the DDES and the fully-turbulent URANS computation. While in URANS the lift coefficient oscillates quasi-harmonically at a frequency of approximately 82 Hz, the DDES produces sharp and much stronger lift fluctuations whose period vary from one cycle to another. The sharp aspect of the curve indicates that the shock-wave speed is relatively high, especially during the lift fall when the flow separates and the shock moves towards the leading edge. This may explain, at least partially, the somewhat higher buffet frequency found for the DDES (approximately 106 Hz). Moreover, the larger amplitude of the fluctuations suggests that the shock-wave motion range is wider than in URANS.

The series of flow snapshots presented in figure 7.14 help understanding the dynamics of the flow predicted by the DDES. For one period of buffet, the figures illustrate instantaneous isosurfaces of vorticity magnitude for $Wc/U = 10$ colored with the Mach number as a function of the non-dimensional time $t^* = tU/c$, where $t^* = 0$ is an instant

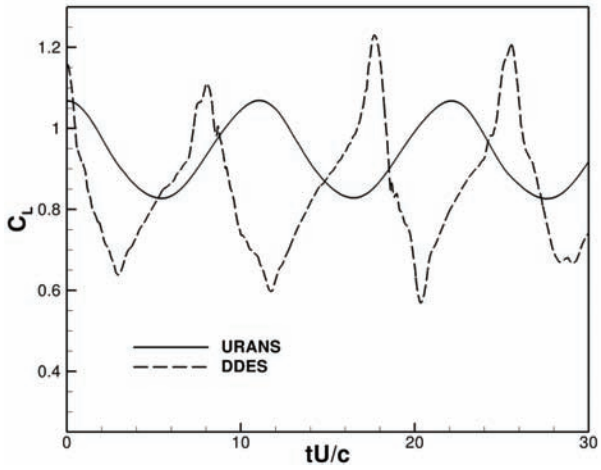

Figure 7.13: Time histories of lift at $M_\infty = 0.70$ and $\alpha = 7.0°$.

of maximum lift. During the shock travel upstream (figures 7.14(a) and 7.14(b)), alternate vortex shedding can be seen at the trailing edge. Contrary to the OAT15A case (see figure 6.4), the primary structures are always three-dimensional. As the shock approaches the leading edge, the flow over the upper surface gets fully separated and the shear layer becomes unstable (figures 7.14(c) to 7.14(e)). Such dramatic separation generates a large wake combining the eddies produced in the shear layer and the trailing edge structures. As the shock and the separation point move downstream again, the height and size of the separation region decrease and the amount of resolved flow structures reduces as seen in the sequence from figures 7.14(e) to 7.14(h). Unlike in URANS, a considerable amount of separation always exists on the rear part of the airfoil. While the shear layer becomes stable as the shock wave approaches its most downstream position, the alternate vortex shedding at the trailing edge is always present during buffet (figures 7.14(i) to 7.14(l)).

To evaluate the ability of the present SST-based DDES to switch between RANS and LES during buffet, the distribution of the two modes has been monitored. Similarly to the OAT15A case, the analysis shows the existence of a RANS-mode layer covering the near-wall region around the V2C airfoil. However, the overall height of this layer seems to be relatively smaller than in the DDES of the OAT15A flow, where l_{RANS} was dictated by the wall distance. This might cause some degree of MSD due to the erroneous penetration of the LES mode into attached boundary layers, which facilitates separation. The instantaneous distributions of the function $1 - f_d$ at four phases of buffet are given in figure 7.15. The figures are very similar to figure 6.14 and the irregular black areas over the upper surface indicate large regions of separation. Indeed, figure 7.15(a) confirms that even when the shock is at its most downstream position a large amount of rear separation exists on the upper surface.

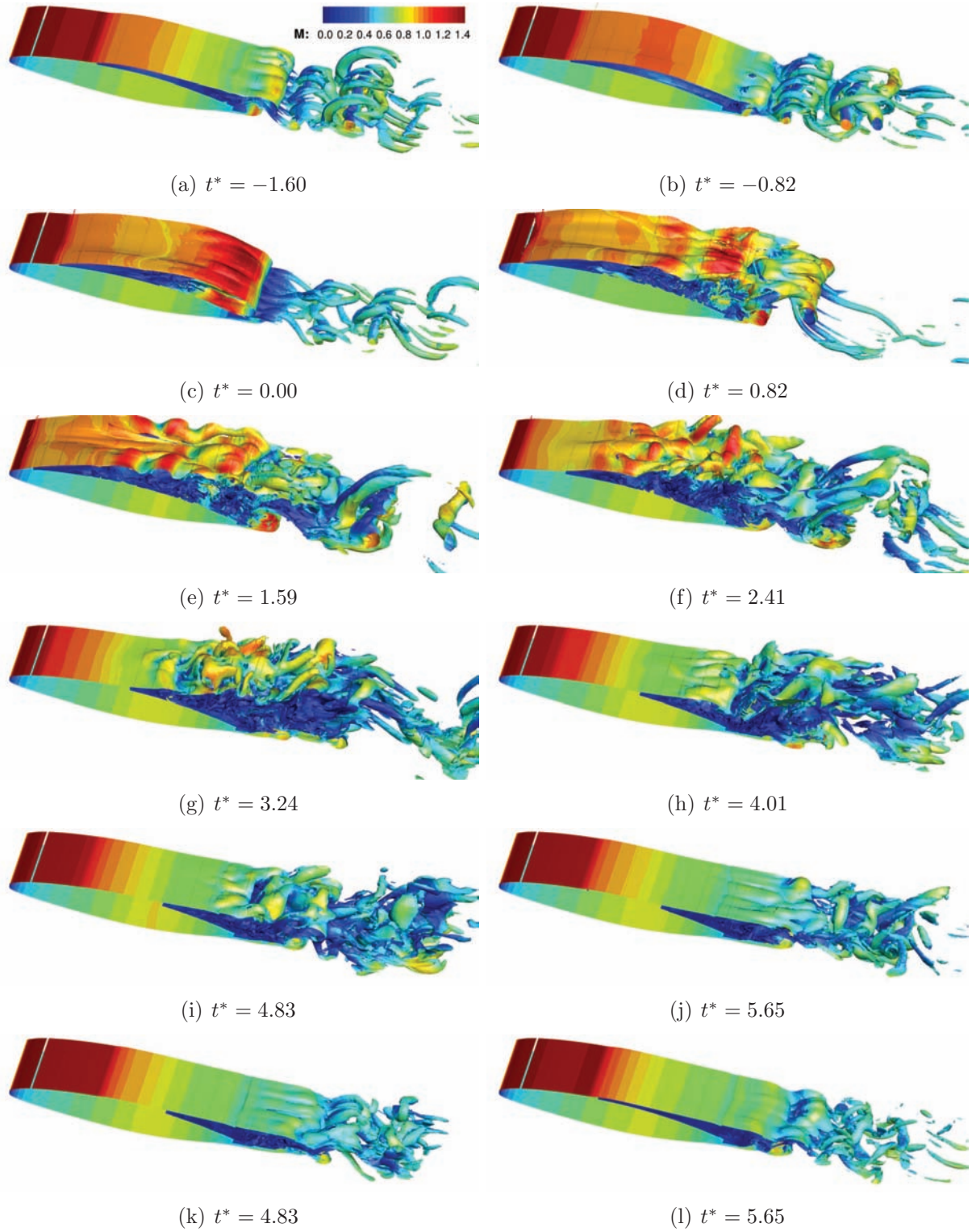

(a) $t^* = -1.60$ (b) $t^* = -0.82$

(c) $t^* = 0.00$ (d) $t^* = 0.82$

(e) $t^* = 1.59$ (f) $t^* = 2.41$

(g) $t^* = 3.24$ (h) $t^* = 4.01$

(i) $t^* = 4.83$ (j) $t^* = 5.65$

(k) $t^* = 4.83$ (l) $t^* = 5.65$

Figure 7.14: Instantaneous vorticity magnitude isosurfaces for $Wc/U = 10$.

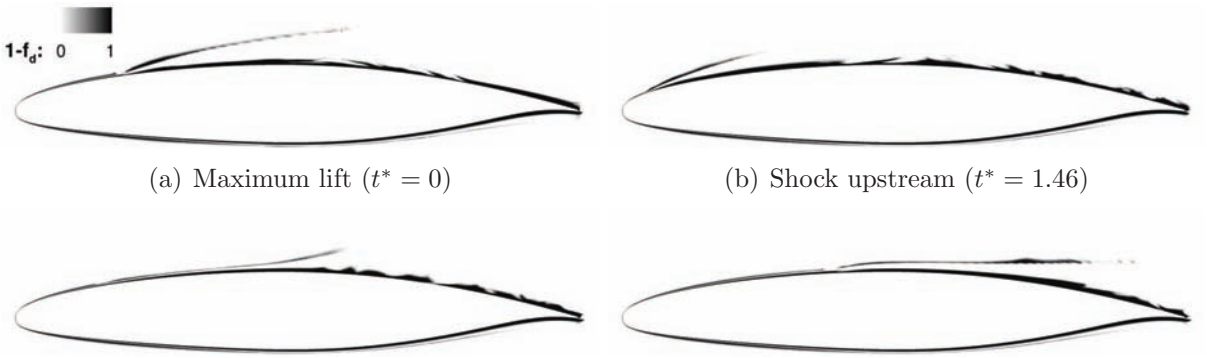

(a) Maximum lift ($t^* = 0$)

(b) Shock upstream ($t^* = 1.46$)

(c) Minimum lift ($t^* = 2.96$)

(d) Shock downstream ($t^* = 6.02$)

Figure 7.15: RANS and LES regions around the V2C airfoil (function $1 - f_d$).

7.5.3 Statistical flow properties

The mean pressure distributions for the DDES and URANS simulations are presented in figure 7.16(a). The differences between the results are large. First, the lack of a supersonic plateau in the DDES indicates that the shock wave and thus the separation point reach the leading edge in their travel upstream. The shock-motion range is much wider than in URANS, covering about 40% of the chord, and the flattened aspect downstream the shock-motion region suggests the occurrence of a large amount of separation. As can be seen in the RMS pressure distributions shown in figure 7.16(b), the maximum unsteadiness levels in the shock region are lower than in the URANS computations, whereas over the rear part of the airfoil the pressure fluctuations predicted by the DDES are considerably higher. Such behavior near the trailing edge seems very similar to that observed in the OAT15A test case, where the DDES was shown to overestimate the fluctuations measured in the experiments. This result suggests that, even for a shock-induced separated flow at a relatively high angle of attack, the lack of resolved turbulence arising from the 'gray area' issue remains critical in DDES.

The conclusions made based on the wall-pressure distributions are confirmed when looking at the RSM fields of the velocity components. Figure 7.17 illustrates the fluctuating longitudinal velocity, showing the large differences in the amplitude of the shock-wave motion and in the unsteadiness of the separated region. The vertical velocity fluctuations are given in figure 7.18, which is very similar to figure 6.13. As can be seen, the discrepancies at the trailing edge are large, being primarily caused by alternate vortex structures. Although such phenomenon might indeed exist, its strength and stability is probably overestimated in the simulation similarly to the OAT15A test case.

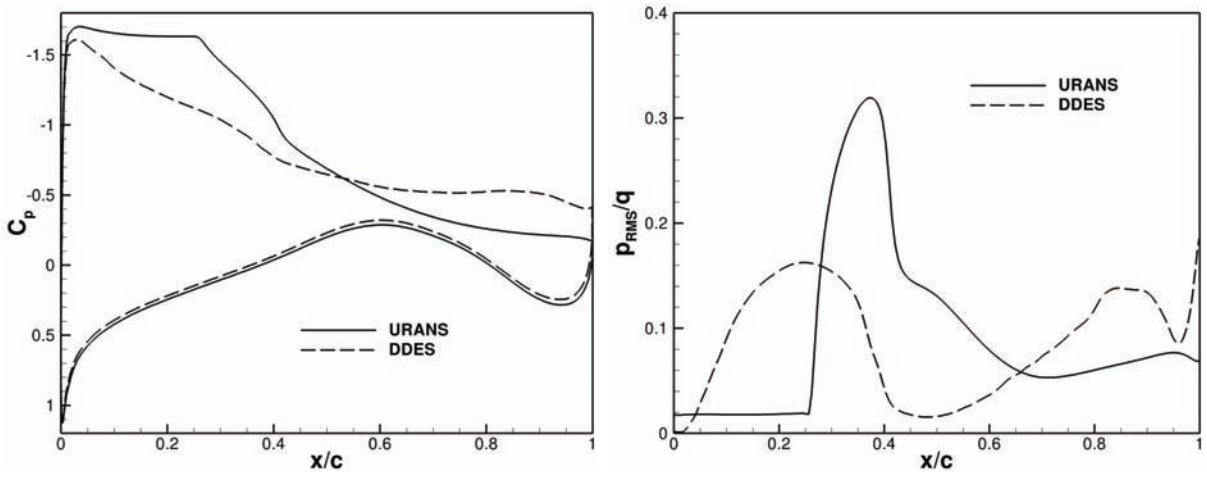

(a) Mean pressure coefficient

(b) RMS pressure on the upper surface

Figure 7.16: URANS and DDES statistical pressure distributions at $M_\infty = 0.70$.

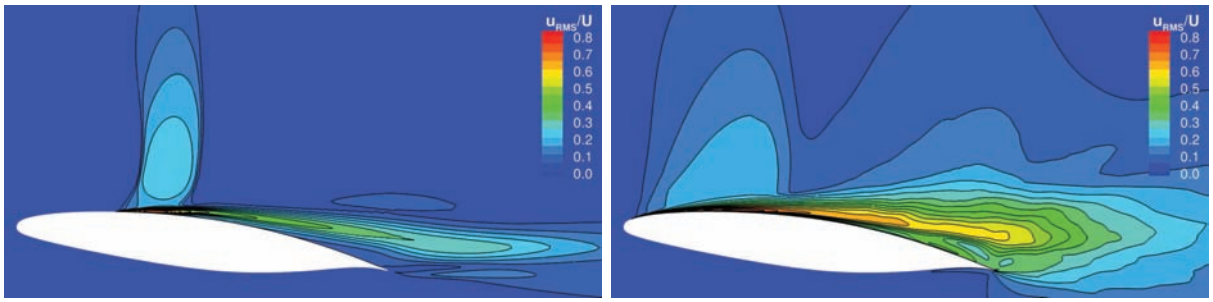

(a) URANS

(b) DDES

Figure 7.17: RMS longitudinal velocity fields around the V2C airfoil.

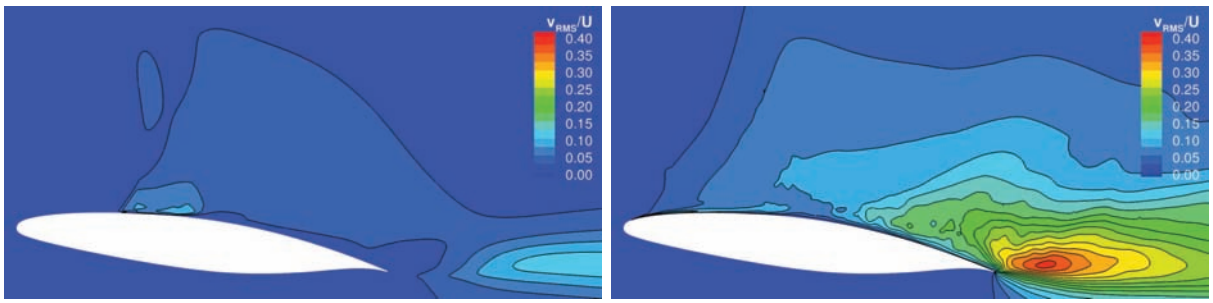

(a) URANS

(b) DDES

Figure 7.18: RMS vertical velocity fields around the V2C airfoil.

Chapter 8

Conclusions

Contents

In this thesis, the physics and modeling of shock wave/boundary layer interactions occurring in the transonic flow over airfoils were addressed using different levels of turbulence modeling and high performance computing. The most important achievements and findings of this work are summarized in the following sections.

8.1 Contributions to the NSMB code

This thesis contributes with the implementation of two turbulence-modeling features new to the NSMB code, namely Secundov's compressibility correction for compressible mixing layers and ambient-turbulence sustaining terms to prevent the free decay of the transported turbulence variables. The compressibility correction was implemented and validated for all one-equation models in the code based on a transport equation for the modified eddy viscosity. The correction was shown to reduce the overall eddy-viscosity levels in turbulent flow regions of high deformation such as shock wave/boundary layer interactions. In the steady transonic flow over the OAT15A supercritical airfoil, the correction slightly improved the shock-wave location prediction. The sustaining terms for ambient turbulence were included in all linear, nonlinear and EARSM models based on the transport of k and ω or ε. The source terms effectively produced constant fields of these variables, allowing the control of the eddy-viscosity level in the vicinity of the body. Moreover, their use should accelerate and improve convergence provided that proper boundary/ambient conditions are prescribed for the turbulence variables. In the case of the SST model, for example, high levels of turbulent kinetic energy were demonstrated to limit convergence.

8.2 Two-dimensional simulations of transonic flows

Several RANS/URANS simulations of transonic flows over airfoils were performed in two dimensions. For the OAT15A airfoil, the selected flow conditions were particularly challenging, including a steady case featuring a relatively-strong shock wave and a transonic buffet case close to the instability-onset boundary. The steady computations served to test and establish appropriate numerical schemes and parameters for the time-accurate simulations of buffet as well as to assess the performance of various linear eddy-viscosity models in transonic flow. It was shown that the shock-wave position is highly model-dependent and that the models tend to predict it too far downstream. Among the standard closures considered, the Shear Stress Transport and Spalart-Allmaras models provided the best predictions of the steady flowfield.

Still in two dimensions, the turbulence models were used to simulate the unsteady shock wave/boundary layer interaction occurring close to the buffet boundary. The best closures in the steady flow case (i.e., the SST and SA models) failed in predicting unsteady flow,

leading to steady solutions after short transient periods. Therefore, alternative URANS models were investigated and revealed that the amplitude of the shock-wave oscillation as well as the mean shock position are strongly model-dependent, whereas the buffet frequency varies much less from one model to another. The results suggest that the frequency is not the best indicator of the ability of a turbulence model in predicting transonic buffet, which should rather be evaluated upon the statistical pressure and velocity fields. It was also demonstrated that the use of the compressibility correction may significantly alter the behavior of one-equation models near the buffet onset boundary. The best results were provided by the robust Edwards-Chandra modified SA model with compressibility corrections. For that model, statistical pressure distributions and velocity profiles revealed that the shock-wave motion range and the flow fluctuations in the vicinity of the airfoil were in good agreement with the experiments. Moreover, the investigation of the flow topology during buffet by phase-averaged boundary layer profiles and by a mapping of flow separation showed that the main unsteady flow features including the onset and development of the intermittent separation were well reproduced in the simulation. A study on the influence of time-stepping parameters on the buffet properties ensured that the adopted outer time step and convergence criterion were adequate. The most successful approach was then used in the context of a hybrid RANS-LES simulation of the same flow.

The knowledge obtained through the simulations of the OAT15A airfoil was applied in the numerical investigation of the V2C laminar transonic airfoil. By means of a series of unsteady simulations, the airfoil aerodynamics was characterized, revealing the different flow phenomena occurring around the airfoil for various angles of attack and two values of freestream Mach number. Supported by a second set of simulations using the Edge code, two flow conditions were selected for a study on the transition location effects on steady and unsteady shock wave/boundary layer interactions as well as for a scale-resolving simulation of transonic buffet.

8.3 Hybrid simulations of transonic buffet

The transonic buffet over the OAT15A supercritical airfoil was also simulated using the Delayed Detached-Eddy Simulation approach based on the Edwards-Chandra model with compressibility corrections. As in URANS, the method successfully predicted the self-sustained shock-wave motion coupled with an intermittent large-scale separation. The monitoring of the RANS- and LES-mode regions during buffet showed that the DDES effectively avoided modeled-stress depletion even when the boundary layer was relatively thick. The method also captured secondary flow fluctuations which were not predicted by URANS. These were mainly related to a regular alternate vortex shedding arising during separation, which caused strong flow fluctuations near the trailing edge that affected even the integrated forces. Nevertheless, considerable differences were observed comparing the

results of the DDES and URANS simulations, including in the onset and development of separation. While the shock-wave motion range and the mean-shock location predicted by the DDES were in good agreement with the experiments, the method produced a flattened pressure recovery region with a too-low trailing-edge pressure. Contrary to URANS, the flow unsteadiness levels over the rear part of the airfoil were overestimated. Such effects seem to result from a long delay observed in the formation of resolved flow structures in the shear layer and in the separated region, which suggests that the 'gray area' is particularly severe in the modeling of transonic buffet. Indeed, the lack of resolved turbulence in LES regions seems to be responsible for the too-regular Kármán vortices and the overestimation of the flow fluctuations near the trailing edge.

A scale-resolving simulation was also performed for the transonic buffet over the V2C airfoil at a relatively high angle of attack. In that case, the DDES approach was based on the SST model and the results exhibited a richer content of resolved flow structures compared to the simulation of the OAT15A airfoil. Nonetheless, the DDES predictions were very different from the reference URANS simulations. This included the mean-shock location and amplitude of the shock-wave oscillations, which indicated that the shock reached the leading edge during buffet. Overall, the RANS-mode layer around the airfoil was relatively thinner than in the OAT15A test case, which may have caused some degree of MSD and thus facilitated separation. The simulation also presented a delay in the generation of resolved structures and, similarly to the OAT15A case, the pressure and velocity fluctuations over the rear part of the airfoil were much higher than in URANS. This result also suggests the gray area issue as critical, despite the higher incidence and the existence of more eddies in the flowfield.

8.4 Transition effects on transonic interactions

The influence of the laminar-turbulent transition location on the properties of steady and unsteady shock wave/boundary layer interactions was addressed by means of two-dimensional simulations. In the OAT15A test case, the experimental tripping point was placed close to the leading edge and the numerical results indicated that the resulting short extent of laminar boundary layer had only a minor effect on the flowfield. As in the steady-shock case, in the transonic buffet regime the whole shock-wave motion region moved slightly downstream when laminarity was considered due to a globally smaller boundary layer thickness. No changes in the shock wave-motion amplitude and frequency were observed.

Broader investigation of the transition location effect on shock wave/boundary layer interactions was conducted for the V2C airfoil, where different tripping positions from the leading edge up to just before the shock wave were considered. The results indicated that the properties of such interactions may be strongly influenced by the incoming boundary layer state when large regions of laminar flow exist. For the steady flow configuration, the

transition point was moved up to the mid-chord, having a significant effect on the shock-wave location and on the position and size of the separation bubble and rear separation. The computations also revealed that, despite a continuous reduction in the friction drag, the total drag tended to augment after a small initial decrease and the optimal lift-to-drag ratio was obtained for an intermediate tripping position. In the transonic buffet regime, the transition location strongly influenced the shock-motion amplitude, which increased as the laminar boundary layer extent was larger. An enhancement of the flow fluctuations in the shock region as well as over the rear part of the airfoil was also observed.

Bibliography

[1] Abbas-Bayoumi, A. and Becker, K., "An Industrial View on Numerical Simulation for Aircraft Aerodynamic Design," *Journal of Mathematics in Industry*, Vol. 1, No. 10, 2011, pp. 1–14.

[2] de Resende, O. C., "The Evolution of the Aerodynamic Design Tools and Transport Aircraft Wings at Embraer," *Journal of the Brazilian Society of Mechanical Sciences and Engineering*, Vol. 26, No. 4, 2004, pp. 379–390.

[3] Nebenfür, B., *Aerodynamic and Aeroacoustic Analysis of a Multi-Element Airfoil using Hybrid RANS/LES Modeling Approaches*, Licentiate thesis, Department of Applied Mechanics, Chalmers University of Technology, 2012.

[4] Deck, S., "Numerical Computation of Transonic Buffet over a Supercritical Airfoil," *AIAA Journal*, Vol. 43, No. 7, 2005, pp. 1556–1566.

[5] Jameson, A., "Paul Garabedian's Contributions to Transonic Airfoil and Wing Design," Note of the Aerospace Computing Laboratory, Department of Aeronautics and Astronautics, Stanford University, 2010.

[6] Anderson, Jr., J. D., *Fundamentals of Aerodynamics*, McGraw-Hill Series in Aeronautical and Aerospace Engineering, McGraw-Hill, 4th ed., 2007.

[7] Bauer, F., Garabedian, P., and Korn, D., *Supercritical Wing Sections I*, Vol. 66 of *Lecture Notes in Economics and Mathematical Systems*, Springer-Verlag, 1972.

[8] Bauer, F., Garabedian, P., Korn, D., and Jameson, A., *Supercritical Wing Sections II*, Vol. 108 of *Lecture Notes in Economics and Mathematical Systems*, Springer-Verlag, 1975.

[9] Bauer, F., Garabedian, P., and Korn, D., *Supercritical Wing Sections III*, Vol. 150 of *Lecture Notes in Economics and Mathematical Systems*, Springer-Verlag, 1977.

[10] Murman, E. M. and Cole, J. D., "Calculation of Plane Steady Transonic Flows," *AIAA Journal*, Vol. 9, No. 1, 1971, pp. 114–121.

[11] Jameson, A., "Re-Engineering the Design Process Through Computation," *Journal of Aircraft*, Vol. 36, No. 1, 1999, pp. 36–50.

[12] Vassberg, J. C., DeHaan, M. A., Rivers, M. S., and Wahls, R. A., "Development of a Common Research Model for Applied CFD Validation Studies," AIAA Paper 2008-6919, 2008.

[13] Jameson, A. and Vassberg, J. C., "Further Studies of Mesh Refinement: Are Shock-Free Airfoils Truly Shock Free?" AIAA Paper 2011-3983, 2011.

[14] Jameson, A., "Aerodynamic Design via Control Theory," *Journal of Scientific Computing*, Vol. 3, No. 3, 1988, pp. 233–260.

[15] Pearcey, H. H., Osborne, J., and Haines, A. B., "The Interaction Between Local Effects at the Shock and Rear Separation - A Source of Significant Scale Effects in Wind-Tunnel Tests on Aerofoils and Wings," AGARD-CP-35, Transonic Aerodynamics, AGARD, 1968.

[16] Lee, B. H. K., "Self-sustained shock oscillations on airfoils at transonic speeds," *Progress in Aerospace Sciences*, Vol. 37, 2001, pp. 147–196.

[17] Mundell, A. R. G. and Mabey, D. G., "Pressure Fluctuations Caused by Transonic Shock/Boundary Layer Interaction," *Aeronautical Journal*, Vol. 90, No. 897, 1986, pp. 274–282.

[18] Pearcey, H. H., "A Method for the Prediction of the Onset of Buffeting and Other Separation Effects from Wind Tunnel Tests on Rigid Models," AGARD-R-223, AGARD, 1958.

[19] Lee, B. H. K., "Oscillatory Shock Motion Caused by Transonic Shock Boundary-Layer Interaction," *AIAA Journal*, Vol. 28, No. 5, 1990, pp. 942–944.

[20] Roos, F. W., "Some Features of the Unsteady Pressure Field in Transonic Airfoil Buffeting," *Journal of Aircraft*, Vol. 17, No. 11, 1980, pp. 781–788.

[21] Tijdeman, H., "Investigation of the Transonic Flow Around Oscillating Airfoils," NLR TR 77090, NRL, 1977.

[22] Hilton, W. F. and Fowler, R. G., "Photographs of Shock Wave Movement," NPL R&M 2692, NPL, 1947.

[23] McDevitt, J. B., Levy, Jr., L. L., and Deiwert, G. S., "Transonic Flow About a Thick Circular-Arc Airfoil," *AIAA Journal*, Vol. 14, No. 5, 1976, pp. 606–613.

[24] Seegmiller, H. L., Marvin, J. G., and Levy, Jr., L. L., "Steady and Unsteady Transonic Flow," *AIAA Journal*, Vol. 16, No. 12, 1978, pp. 1262–1270.

[25] Marvin, J. G., Levy, Jr., L. L., and Seegmiller, H. L., "Turbulence Modeling for Unsteady Transonic Flows," *AIAA Journal*, Vol. 18, No. 5, 1980, pp. 489–496.

[26] Mabey, D. G., "Oscillatory Flows from Shock-Induced Separations on Biconvex Airfoils of Varying Thickness in Ventilated Wind Tunnels," AGARD-CP-296, Boundary Layer Effects on Unsteady Airloads, AGARD, 1980.

[27] Mabey, D. G., Welsh, B. L., and Cripps, B. E., "Periodic Flows on a Rigid 14% Thick Biconvex Wing at Transonic Speeds," TR 81059, Royal Aircraft Establishment, 1981.

[28] Gibb, J., "The Cause and Cure of Periodic Flows at Transonic Speeds," in "Proceedings of the 16th Congress of the International Council of the Aeronautical Sciences," , 1988, pp. 1522–1530.

[29] Roos, F. W., "Surface Pressure and Wake Fluctuations in a Supercritical Airfoil Flowfield," AIAA Paper 75-66, 1975.

[30] McDevitt, J. B. and Okuno, A. F., "Static and Dynamic Pressure Measurements on a NACA 0012 Airfoil in the Ames High Reynolds Number Facility," NASA TP 2485, NASA, 1985.

[31] Lee, B. H. K. and Ohman, L. H., "Unsteady Pressures and Forces During Transonic Buffeting of a Supercritical Airfoil," *Journal of Aircraft*, Vol. 21, No. 8, 1984, pp. 439–441.

[32] Lee, B. H. K., Ellis, F. A., and J., B., "Investigation of the Buffet Characteristics of Two Supercritical Airfoils," *Journal of Aircraft*, Vol. 26, No. 8, 1989, pp. 731–736.

[33] Lee, B. H. K. and Tang, F. C., "Transonic Buffet of a Supercritical Airfoil and Trailing-Edge Flap," *Journal of Aircraft*, Vol. 26, No. 5, 1989, pp. 459–464.

[34] Roos, F. W. and Riddle, D. R., "Measurements of Surface Pressure and Wake Flow Fluctuations in the Flowfield of a Whitcomb Supercritical Airfoil," NASA TN D-8443, NASA, 1977.

[35] Alshabu, A., Olivier, H., and Klioutchnikov, I., "Investigation of Upstream Moving Pressure Waves on a Supercritical Airfoil," *Aerospace Science and Technology*, Vol. 10, 2006, pp. 465–473.

[36] Alshabu, A. and Olivier, H., "Unsteady Wave Propagation Phenomena on a Supercritical Airfoil," *AIAA Journal*, Vol. 46, No. 8, 2008, pp. 2066–2073.

[37] Stanewsky, E. and Basler, D., "Experimental Investigation of Buffet Onset and Penetration on a Supercritical Airfoil at Transonic Speeds," AGARD-CP-483, Aircraft Dynamic Loads Due to Flow Separation, AGARD, 1990.

[38] Jacquin, L., Molton, P., Deck, S., Maury, B., and Soulevant, D., "Experimental Study of the 2D Oscillation on a Transonic Wing," AIAA Paper 2005-4902, 2005.

[39] Jacquin, L., Molton, P., Deck, S., Maury, B., and Soulevant, D., "Experimental Study of Shock Oscillation over a Transonic Supercritical Profile," *AIAA Journal*, Vol. 47, No. 9, 2009, pp. 1985–1994.

[40] Crouch, J. D., Garbaruk, A., and Magidov, D., "Predicting the Onset of Flow Unsteadiness Based on Global Instability," *Journal of Computational Physics*, Vol. 224, 2007, pp. 924–940.

[41] Crouch, J. D., Garbaruk, A., Magidov, D., and Travin, A., "Origin of transonic buffet on aerofoils," *Journal of Fluid Mechanics*, Vol. 628, 2009, pp. 357–369.

[42] Crouch, J. D., Garbaruk, A., Magidov, D., and Jacquin, L., "Global Structure of Buffeting Flows on Transonic Airfoils," in "Proceedings of the IUTAM Symposium on Unsteady Separated Flows and their Control," , 2009, pp. 297–306.

[43] Levy, Jr., L. L., "Experimental and Computational Steady and Unsteady Transonic Flows about a Thick Airfoil," *AIAA Journal*, Vol. 16, No. 6, 1978, pp. 564–572.

[44] MacCormack, R. W., "An efficient numerical method for solving the time-dependent compressible Navier-Stokes equations at high Reynolds number," NASA TM X-73 129, NASA, 1976.

[45] Barakos, G. and Drikakis, D., "Numerical simulation of transonic buffet flows using various turbulence closures," *International Journal of Heat and Fluid Flow*, Vol. 21, 2000, pp. 620–626.

[46] Baldwin, B. S. and Lomax, H., "Thin-Layer Approximation and Algebraic Model for Separated Turbulent Flows," AIAA Paper 78-257, 1978.

[47] Spalart, P. R. and Allmaras, S. R., "A one-equation turbulence model for aerodynamic flows," *La Recherche Aérospatiale*, Vol. 1, 1994, pp. 5–21.

[48] Launder, B. E. and Sharma, B. I., "Application of the Energy-Dissipation Model of Turbulence to the Calculation of Flow Near a Spinning Disk," *Letters in Heat and Mass Transfer*, Vol. 1, No. 2, 1974, pp. 131–137.

[49] Nagano, Y. and Kim, C., "A Two-Equation Model for Heat Transport in Wall Turbulent Shear Flows," *Journal of Heat Transfer*, Vol. 110, No. 3, 1988, pp. 583–589.

[50] Craft, T. J., Launder, B. E., and Suga, K., "Development and Application of a Cubic Eddy-Viscosity Model of Turbulence," *International Journal of Heat and Fluid Flow*, Vol. 17, 1996, pp. 108–115.

[51] Sofialidis, D. and Prinos, P., "Development of a Non-Linear Strain-Sensitive k-ω Turbulence Model," in "Proceedings of the 11th Symposium on Turbulent Shear Flows," , 1997, pp. 89–94.

[52] Xiao, Q. and Tsai, H. M., "Numerical Study of Transonic Buffet on a Supercritical Airfoil," *AIAA Journal*, Vol. 44, No. 3, 2006, pp. 620–628.

[53] Iovnovich, M. and Raveh, D. E., "Reynolds-Averaged Navier–Stokes Study of the Shock-Buffet Instability Mechanism," *AIAA Journal*, Vol. 50, No. 4, 2012, pp. 880–890.

[54] Brunet, V., "Computational Study of Buffet Phenomenon," AIAA Paper 2003-3679, 2003.

[55] Brunet, V., "Numerical Investigation of Buffet Phenomenon with URANS Equations," in "European Conference for AeroSpace Sciences (EUCAS)," , 2005.

[56] Shih, T., Zhu, J., and Lumley, J., "A Realizable Reynolds Stress Algebraic Equation Model," NASA TM 105993, NASA, 1992.

[57] Thiery, M. and Coustols, E., "Numerical prediction of shock induced oscillations over a 2D airfoil: influence of turbulence modelling and test section walls," *International Journal of Heat and Fluid Flow*, Vol. 27, 2006, pp. 661–670.

[58] Bézard, H. and Daris, T., "Calibrating the length scale equation with an algebraic Reynolds stress constitutive relation," in Rodi, W., ed., "Engineering Turbulence Modelling and Experiments," Elsevier, Vol. 6, 2005, pp. 76–86.

[59] Garnier, E. and Deck, S., "Large-eddy simulation of transonic buffet over a supercritical airfoil," in "Direct and Large-Eddy Simulation VII," Vol. 13, part 8 of *ERCOFTAC*, 2010, pp. 549–554.

[60] Hirsch, C., *Numerical Computation of Internal and External Flows - The Fundamentals of Computational Fluid Dynamics*, Vol. 1, Butterworth-Heinemann, 2nd ed., 2007.

[61] Schlichting, H. and Gersten, K., *Boundary Layer Theory*, Springer, 8th rev. and enl. ed., 2000.

[62] Blazek, J., *Computational Fluid Dynamics: Principles and Applications*, Elsevier, 2nd ed., 2005.

[63] Sutherland, W., "The viscosity of gases and molecular force," *Philosophical Magazine, Series 5*, Vol. 36, No. 223, 1893, pp. 507–531.

[64] Wilcox, D. C., *Turbulence Modeling for CFD*, DCW Industries, 3rd ed., 1986.

[65] Vos, J. B., Rizzi, A. W., Corjon, A., Chaput, E., and Soinne, E., "Recent Advances in Aerodynamics Inside the NSMB (Navier Stokes Multi Block) Consortium," AIAA Paper 98-0225, 1998.

[66] "Edge Theoretical Formulation," FOI dnr 03-2870 5.2, FOI, 2011.

[67] "Edge User Guide," FOI dnr 03-2870 5.2, FOI, 2011.

[68] Boussinesq, J., "Essai sur la théorie des eaux courantes," *Mémoires présentés par divers savants à l'Académie des Sciences*, Vol. XXIII, No. 1, 1877, pp. 1–680.

[69] Bradshaw, P., "Effects of Streamline Curvature on Turbulent Flow," AGARD-AG-169, AGARD, 1973.

[70] Spalart, P. R. and Rumsey, C. L., "Effective Inflow Conditions for Turbulence Models in Aerodynamic Calculations," *AIAA Journal*, Vol. 45, No. 10, 2007, pp. 2544–2553.

[71] Spalart, P. R. and Allmaras, S. R., "A One-Equation Turbulence Model for Aerodynamic Flows," AIAA Paper 92-0439, 1992.

[72] Edwards, J. R. and Chandra, S., "Comparison of Eddy Viscosity-Transport Turbulence Models for Three-Dimensional, Shock-Separated Flowfields," *AIAA Journal*, Vol. 34, No. 4, 1996, pp. 756–763.

[73] Rung, T., Bunge, U., Schatz, M., and Thiele, F., "Restatement of the Spalart-Allmaras Eddy-Viscosity Model in Strain-Adaptive Formulation," *AIAA Journal*, Vol. 41, No. 7, 2003, pp. 1396–1399.

[74] Spalart, P. R., "Trends in Turbulence Treatments," AIAA Paper 2000-2306, 2000.

[75] Shur, M., Strelets, M., Zaikov, L., Gulyaev, A., Kozlov, V., and Secundov, A., "Comparative Numerical Testing of One- and Two-Equation Turbulence Models for Flows with Separation and Reattachment," AIAA Paper 95-0863, 1995.

[76] Forsythe, J. R., Hoffmann, K. A., Cummings, R. M., and Squires, K. D., "Detached-Eddy Simulation With Compressibility Corrections Applied to a Supersonic Axisymmetric Base Flow," *Journal of Fluids Engineering*, Vol. 124, No. 4, 2002, pp. 911–923.

[77] Menter, F. R., "Two-Equation Eddy-Viscosity Turbulence Models for Engineering Applications," *AIAA Journal*, Vol. 32, No. 8, 1994, pp. 1598–1605.

[78] Wilcox, D. C., "Reassessment of the Scale-Determining Equation for Advanced Turbulence Models," *AIAA Journal*, Vol. 26, No. 11, 1988, pp. 1299–1310.

[79] Menter, F. R., "Influence of Freestream Values on k-ω Turbulence Model Predictions," *AIAA Journal*, Vol. 30, No. 6, 1992, pp. 1651–1659.

[80] Johnson, D. A. and King, L. S., "A Mathematically Simple Turbulence Closure Model for Attached and Separated Turbulent Boundary Layers," *AIAA Journal*, Vol. 30, No. 6, 1985, pp. 1651–1659.

[81] Chien, K.-Y., "Predictions of Channel and Boundary-Layer Flows with a Low-Reynolds-Number Turbulence Model," *AIAA Journal*, Vol. 20, No. 1, 1982, pp. 33–38.

[82] Jones, W. P. and Launder, B. E., "The Prediction of Laminarization with a Two-Equation Model of Turbulence," *International Journal of Heat and Mass Transfer*, Vol. 15, No. 2, 1972, pp. 301–314.

[83] Spalart, P. R., "Strategies for turbulence modelling and simulations," *International Journal of Heat and Fluid Flow*, Vol. 21, 2000, pp. 252–263.

[84] Fröhlich, J. and von Terzi, D., "Hybrid LES/RANS methods for the simulation of turbulent flows," *Progress in Aerospace Sciences*, Vol. 44, 2008, pp. 349–377.

[85] Mockett, C., *A comprehensive study of detached-eddy simulation*, Ph.D. thesis, Institute of Fluid Mechanics and Engineering Acoustics, Technische Universität Berlin, 2009.

[86] Spalart, P. R., Jou, W.-H., Strelets, M., and Allmaras, S. R., "Comments on the feasibility of LES for wings, and on a hybrid RANS/LES approach," in Liu, C. and Liu, Z., eds., "Advances in LES/DNS," Greyden Press, Louisiana Tech University, First AFOSR International Conference on DNS/LES, 1997, pp. 137–147.

[87] Spalart, P. R., "Detached-Eddy Simulation," *Annual Review of Fluid Mechanics*, Vol. 41, 2009, pp. 181–202.

[88] Spalart, P., "The uses of DES: natural, extended, and improper," in "DESider Hybrid RANS-LES Symposium," Stockholm, Sweden, 14th-15th July 2005.

[89] Spalart, P. R., Deck, S., Shur, M. L., Squires, K. D., Strelets, M. K., and Travin, A., "A new version of detached-eddy simulation, resistant to ambiguous grid densities," *Theoretical and Computational Fluid Dynamics*, Vol. 20, 2006, pp. 181–195.

[90] Strelets, M., "Detached eddy simulation of massively separated flows," in "Proceedings of the 39th AIAA Aerospace Sciences Meeting and Exhibit," , 2001.

[91] Travin, A., Shur, M., Strelets, M., and Spalart, P., "Physical and numerical upgrades in the detached-eddy simulation of complex turbulent flows," in "Proceedings of the 412th Euromech Colloquium on LES and Complex Transitional and Turbulent Flows," , 2000.

[92] Menter, F. R. and Kuntz, M., "Adaptation of Eddy-Viscosity Turbulence Models to Unsteady Separated Flows Behind Vehicles," in McCallen, R., Browand, F., and Ross, J., eds., "The Aerodynamics of Heavy Vehicles: Trucks, Buses, and Trains," Springer, Vol. 41 of *Lecture Notes in Applied and Computational Mechanics*, 2004.

[93] Spalart, P. R., "Young-Person's Guide to Detached-Eddy Simulation Grids," CR-2001-211032, NASA, 2001.

[94] Esquieu, S., "Numerical Simulation and Drag Extraction Using Patched Grid Calculations," AIAA Paper 2003-1238, 2003.

[95] Rumsey, C. L., Allison, D. O., Biedron, R. T., Buning, P. G., Gainer, T. G., Morrison, J. H., and Rivers, S. M., "CFD Sensitivity Analysis of a Modern Civil Transport Near Buffet-Onset Conditions," NASA TM-2001-211263, NASA, 2001.

[96] Shur, M., Spalart, P., Strelets, M., and Travin, A., "Detached-eddy simulation of an airfoil at high angle of attack," in "Engineering Turbulence Modelling and Experiments," Elsevier, Vol. 4, 1999, pp. 669–678.

[97] Bourdet, S., Bouhadji, A., Braza, M., and Thiele, F., "Direct Numerical Simulation of the Three-Dimensional Transition to Turbulence in the Transonic Flow around a Wing," *Flow, Turbulence and Combustion*, Vol. 71, 2003, pp. 203–220.

[98] Williamson, C. H. K., "Three-dimensional wake transition," *Journal of Fluid Mechanics*, Vol. 328, 1996, pp. 345–407.

[99] Persillon, H. and Braza, M., "Physical analysis of the transition to turbulence in the wake of a circular cylinder by three-dimensional Navier-Stokes simulation," *Journal of Fluid Mechanics*, Vol. 365, 1998, pp. 23–88.

[100] Bouhadji, A. and Braza, M., "Organised modes and shock-vortex interaction in unsteady viscous transonic flows around an aerofoil: Part I: Mach number effect," *Computers & Fluids*, Vol. 32, No. 9, 2003, pp. 1233–1260.

[101] Bouhadji, A. and Braza, M., "Organised modes and shock-vortex interaction in unsteady viscous transonic flows around an aerofoil: Part II: Reynolds number effect," *Computers & Fluids*, Vol. 32, No. 9, 2003, pp. 1261–1281.

[102] Seiler, F. and Srulijes, J., "Vortices and Pressure Waves at Trailing Edges," in "Proceedings of the 16th International Congress on High Speed Photography and Photonics," , 1984.

[103] Crouch, J. D. and Ng, L. L., "Variable N-Factor Method for Transition Prediction in Three-Dimensional Boundary Layers," *AIAA Journal*, Vol. 38, No. 2, 2000, pp. 211–216.

[104] Chalot, F., Mallet, M., and Ravachol, M., "A Comprehensive Finite Element Navier-Stokes Solver for Low- and High-Speed Aircraft Design," AIAA Paper 94-0814, 1994.

[105] Courty, J. C., Bulgubure, C., and Arnal, D., "Laminar Flow Investigation: Computations and Flight Tests at Dassault Aviation," AGARD-CP-547, Recent Advances in Long Range and Long Endurance Operation of Aircraft, AGARD, 1993.

[106] Arnal, D., "Boundary Layer Transition: Prediction, Application to Drag Reduction," AGARD-R-786, Special Course on Skin Friction Drag Reduction, AGARD, 1992.

Abstract

Shock wave/boundary layer interactions arising in the transonic flow over airfoils are studied numerically using different levels of turbulence modeling. The simulations employ standard URANS models suitable for aerodynamics and hybrid RANS-LES methods. The use of a compressibility correction for one-equation closures is also considered. First, the intermittent shock-induced separation occurring over a supercritical airfoil at an angle of attack close to the buffet onset boundary is investigated. After a set of URANS computations, a scale-resolving simulation is performed using the best statistical approach in the context of a Delayed Detached-Eddy Simulation (DDES). The analysis of the flow topology and of the statistical wall-pressure distributions and velocity fields show that the main features of the self-sustained shock-wave oscillation are predicted by the simulations. The DDES also captures secondary flow fluctuations which are not predicted by URANS. An examination of the unsteady RANS-LES interface shows that the DDES successfully prevents modeled-stress depletion whether the flow is attached or separated. The gray area issue and its impact on the results are also addressed. The conclusions from the supercritical airfoil simulations are then applied to the numerical study of a laminar transonic profile. Following a preliminary characterization of the airfoil aerodynamics, the effect of the boundary layer transition location on the properties of two selected shock wave/boundary layer interaction regimes is assessed. In transonic buffet conditions, the simulations indicate a strong dependence of the shock-wave motion amplitude and of the global flow unsteadiness on the tripping location.

Keywords: shock wave/boundary layer interaction; transonic buffet; numerical simulation; turbulence modeling; hybrid RANS-LES methods; URANS

Résumé

L'interaction onde de choc/couche limite en écoulement transsonique autour de profils aérodynamiques est étudiée numériquement utilisant différentes classes de modélisation de la turbulence. Les approches utilisées sont celles de modèles URANS et de méthodes hybrides RANS-LES. L'emploi d'une correction de compressibilité pour les fermetures à une équation est aussi évalué. Premièrement, la séparation intermittente induite par le choc sur un profil supercritique en conditions d'incidence proches de l'angle critique d'apparition du tremblement est analysée. Suite à des simulations URANS, la modélisation statistique la mieux adaptée est étudiée et utilisée dans l'approche DDES (Delayed Detached-Eddy Simulation). L'étude de la topologie de l'écoulement, des pressions pariétales et champs de vitesse statistiques montrent que les principales caractéristiques de l'oscillation auto-entretenue du choc sont capturées par les simulations. De plus, la DDES prédit des fluctuations secondaires de l'écoulement qui n'apparaissent pas en URANS. L'étude de l'interface instationnaire RANS-LES montre que la DDES évite le MSD (modeled-stress depletion) pour les phases de l'écoulement attaché ou séparé. Le problème de la 'zone grise' et de son influence sur les résultats est considéré. Les conclusions de l'étude sur le profil supercritique est ensuite appliquées à l'étude numérique d'un profil transsonique laminaire. Dans ce contexte, l'effet de la position de la transition de la couche limite sur les caractéristiques de deux régimes d'interaction choc/couche limite sélectionnés est étudiée. En conditions de tremblement, les simulations montrent une forte influence du point de transition sur l'amplitude du mouvement du choc et sur l'instationnarité globale de l'écoulement.

Mots clefs : interaction onde de choc/couche limite ; tremblement transsonique ; simulation numérique ; modélisation de la turbulence ; méthodes hybrides RANS-LES ; URANS